Microwave Microfluidic Resonant Sensors and Applicators

A thesis submitted to the Cardiff University for the degree of Doctor of Philosophy

By

Hayder Miri Hamzah

May 2017

Department of Electrical and Electronic Engineering
Cardiff University

United Kingdom

Declaration

This work has not previously been accepted in substance for any degree and is not concurrently submitted in candidature for any degree.

Signed…….. (candidate) Date……

Statement 1

This thesis is being submitted in part fulfilment of the requirements for the degree of PhD.

Signed…….. (candidate) Date……

Statement 2

This thesis is the result of my own independent work/investigation, except where otherwise stated. Other sources are acknowledged by explicit references.

Signed…….. (candidate) Date……

Statement 3

I hereby give consent for my thesis, if accepted, to be available for photocopying and for inter-library loan, and for the title and summary to be made available to outside organisations.

Signed…….. (candidate) Date……

Acknowledgements

First of all, I thank the Almighty God for his infinite generosity and grace upon me to complete my Ph.D. study.

I would like to express my sincere gratitude to my supervisors Prof. Adrian Porch and Dr. Jonathan Lees for the continuous support of my Ph.D. study and related research, for their immense knowledge, guidance, and motivation and encouragement. Their guidance helped me in all the time of research and writing of this thesis. I could not have imagined having better advisors and mentors for my Ph.D. study. There are no words to express my thanks towards both of them.

Thanks to my country Iraq and ministry of higher education and scientific research for their support to fund my Ph.D. study.

I would also like to thank Dr. Nicholas Clark, Dr. Ali Abduljabar, Dr. Jerome Cuenca, Dr. Heungjae Choi, Prof. Les Baillie, Dr. Lovleen Joshi, Mr. Dmitry Malyshev, and Mr. Evans Ahortor for their valuable assistance and advice during my study.

Many thanks to the technicians in the electrical/electronic workshop, mechanical workshop, and IT team in the School of Engineering for their help and cooperation.

Last but not the least; I would like to thank my parents and family for supporting me spiritually throughout my study.

Abstract

Microwave sensors and applicators are of major interest in applications where no physical contact is possible or the use of active devices is impractical. Microwave sensors offer numerous advantages compared to traditional techniques, not least in terms of convenience and speed, since they do not require any markers. Furthermore, such microwave sensor methods can be designed to be fully compatible with lab-on-a-chip approaches.

In this work, the interaction between the microwave electric field and a microfluidic dielectric sample using resonant microwave sensors has been studied, and therefore the dielectric constant for sample materials can be measured by using perturbation theory when the sample is placed in the electric field.

Two forms of novel resonator for microfluidic sensing are proposed: a re-entrant microwave cavity (RMC) and split-ring resonator (SRR).

The RMC is one of the most useful forms of cavity for this purpose due to its simple geometry, wide frequency range tuning and high quality factor. It has been designed, machined, and evaluated experimentally with common liquids and different mixtures based on water and dielectric microspheres, in both static and flow situations.

Furthermore, we present a new approach for microfluidic sensing and microfluidic heating using a novel split ring resonator (SRR) for high sensing sensitivity and efficient heating of lossy dielectrics. The designed SRR shows very good performance experimentally in microfluidic sensing (pure liquids, chemical solutions, and saline concentration level), as well as in microfluidic heating where it is demonstrated how nearly all the microwave power is delivered to the sample under test.

Owing to its compact size and high efficiency, the SRR has been utilized in an important microbiological applications for rapid DNA release using low power levels (< 1 W). It is envisaged that this system is now suitable for incorporation within a rapid, hand-held, point-of-care detector for bacterial infections such as *Clostridium difficile*.

Table of contents

CHAPTER ONE
INTRODUCTION AND THESIS SUMMARY

1.1. Introduction

The ability to interrogate precisely the composition of liquid mixtures by non-contact techniques in both static and flow situations is highly desirable for a variety of industrial, analytical and quality control procedures. In this context, microwave resonators have a useful dual role. They provide sensitive characterisation of the dielectric polarisation and loss of a sample for small applied electric fields; the field amplitudes are necessarily small for characterisation since there is then no heating of a lossy dielectric sample, as temperature rise will change the dielectric properties (particularly so for polar liquids such as water). Conversely, they can also provide efficient volumetric heating of the same sample (if its dielectric loss is large enough to permit heating) for large applied electric fields. However, note that the structures for both sensor and applicator are the same; if one can sense, one can also heat if the loss tangent of the sample is large enough.

Accurate microwave methods for dielectric characterisation are useful for applications in industry, medicine, and in pharmaceuticals. Microwave resonators allow extremely precise and sensitive characterisation of the dielectric properties of dielectric materials due to their strong interaction with microwave electric fields. For very small sample volumes, the resonator perturbation technique is widely used for dielectric measurements on polar liquids when a sample is inserted within a region of high electric field of a microwave resonator.

In this research work, microwave resonators have been developed and utilized as microfluidic sensors for highly sensitive compositional analysis of two-component dielectric mixtures contained in capillaries. Firstly, the proposed microwave sensors have been evaluated with common liquids (water, methanol, ethanol, and chloroform), and the results (both simulation and experimental) indicate that the proposed microwave structures are very sensitive, sufficient for deployment for the characterisation of

different microfluidic mixtures in both static and dynamic situations. This is also the case when the compositions of the liquids are changing, for both miscible and immiscible liquids, and due to the concentration of dissolved species when dealing with solvents. During the development of the microwave resonators, the ability to both characterise and heat was borne in mind, to achieve maximum power delivery to the sample in addition to high sensitivity measurement. This will allow our sensors to be utilized in microfluidic heating applications.

1.2. Project Aims

The aims of this project were to study in detail the interaction between the electric field of microwaves with dielectric samples using a widely employed microwave cavity resonator (at the ISM frequency of approximately 2.5 GHz). This was followed by the development of new microwave microfluidic resonant sensors for dielectric property characterization and composition of liquid mixtures by non-contact techniques, in both static and flow situations, on the one hand, and heating applications on the other; the goal being maximum sensing sensitivity and maximum power transfer for the heating application. So, the research can be divided into two main parts: the sensing part (sensors) which is widely required in many industrial, chemical, and medical applications, and the heating part (applicator) with minimum power consumption and maximum power transfer, which can be used also in industrial and chemical applications. The specific application studied in detail here is microbiology, for the rapid DNA release of certain bacteria, allowing their timely detection.

The targets have been specified as listed below:

1) Maximize the sensor sensitivity and simultaneous miniaturisation by optimizing the sensor dimensions and materials.
2) Characterisation of liquids and micro-particle suspensions using the developed sensors.
3) Characterise impurity concentration levels in liquids, such as dissolved ionic species and detect pH by non-contact means.
4) Develop sensors and applicators to work with microfluidic samples in both static and dynamic situations.

5) Ensure the dual ability of sensor and applicator by controlling the microwave power level.
6) Design a miniaturized, resonant applicator to function at minimum power level (e.g. 1 W or less) which will allow its incorporation into a battery-operated, hand-held device. Specifically, this could be for point-of-care detection of DNA, for example.

1.3. Thesis Outline

The specific structure of this thesis is as follows:

- CHAPTER ONE (INTRODUCTION AND THESIS SUMMARY):
  This chapter presents a general introduction, the main project aims, and thesis outline.

- CHAPTER TWO (BACKGROUND AND LITERATURE SURVEY):
  This chapter gives a background on the relevant microwave technology and its ability to be used in sensing and, specifically, in dielectric property characterization. The main methods used in this field have been classified into resonant and non-resonant methods. Also thermal processing of materials using microwaves has been discussed and some application examples are presented in different fields within industry, medicine and pharmaceuticals. Furthermore some examples from the literature related to microwave cavities and split ring resonators have been presented for selected applications.

- CHAPTER THREE (DIELECTRIC MATERIALS INTERACTION WITH ELECTROMAGNETIC FIELD AT MICROWAVE FREQUENCIES):
  This chapter discusses the interaction between dielectric materials and the electromagnetic field at microwave frequencies. In this context, it presents the polarization and depolarization types, polarization mechanism and Debye model for some common solvents. Finally it characterizes the applicators and sensors according to the material interaction with the electric or magnetic field.

- CHAPTER FOUR (CYLINDRICAL MICROWAVE CAVITY):

  This chapter presents the most commonly used cylindrical microwave cavity, excitation devices, perturbation theory, and scattering parameters. These concepts have been employed in the design of a new re-entrant microwave cavity (RMC), which has been designed and machined in two types as shown in Figure 1.1 according to operating resonant frequencies of 900 MHz and 2.4 GHz. This chapter shows the sensing results (simulated and experimental) of these two cavities based on microfluidic sensing in a static situation, and mixture detection under flow conditions (in the form of micro-spherical beads dispersed in water, and a segmented flow of water and oil). An experimental system has been designed and implemented to control homogeneous and segmented flow through a motorized valve, microscopic camera, syringe pump, and laptop to control the system via a LabVIEW program.

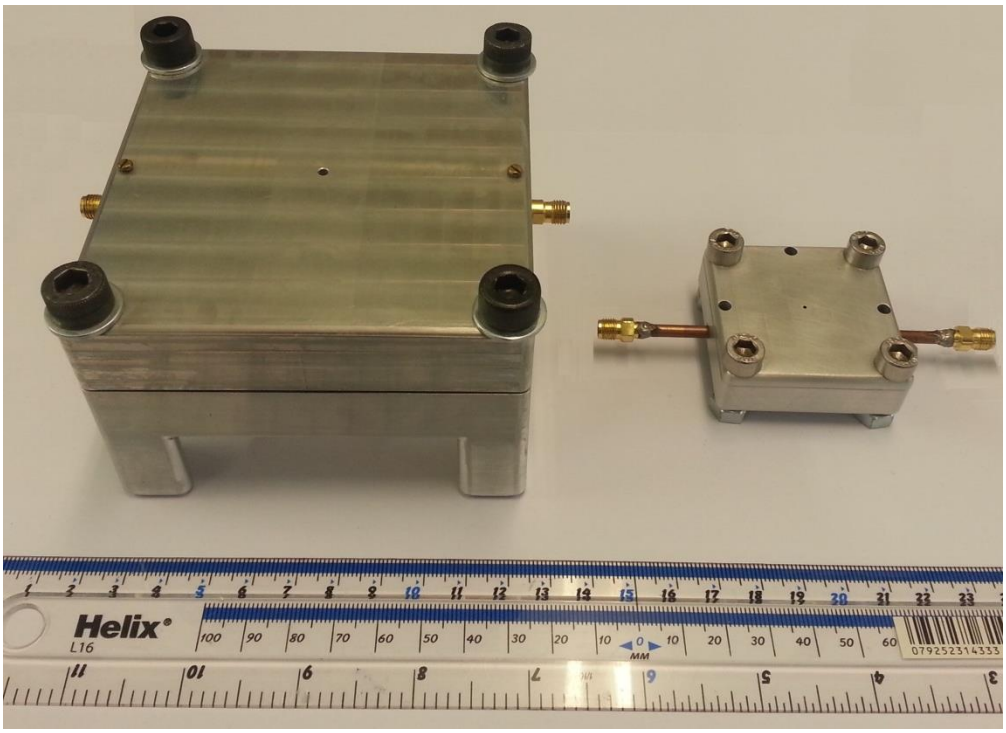

Figure 1.1 Re-entrant cavities.

- CHAPTER FIVE (SPLIT RING RESONATOR):

  A novel split ring resonator (SRR) is presented in this chapter, designed so that the electric field is parallel to the sample for maximum polarisation (i.e. sensitivity); it functions with higher sensitivity as a microfluidic sensor for solvents dielectric properties characterization on one hand, and concentration level detection for mixtures on the other. Furthermore, the designed split ring resonator is sensitive to pH change; it has been tested with HCl (acid) and NaOH (alkaline) with different pH values. Also the SRR has been considered as an applicator for efficient microwave heating and/or excitation under pulsed power.

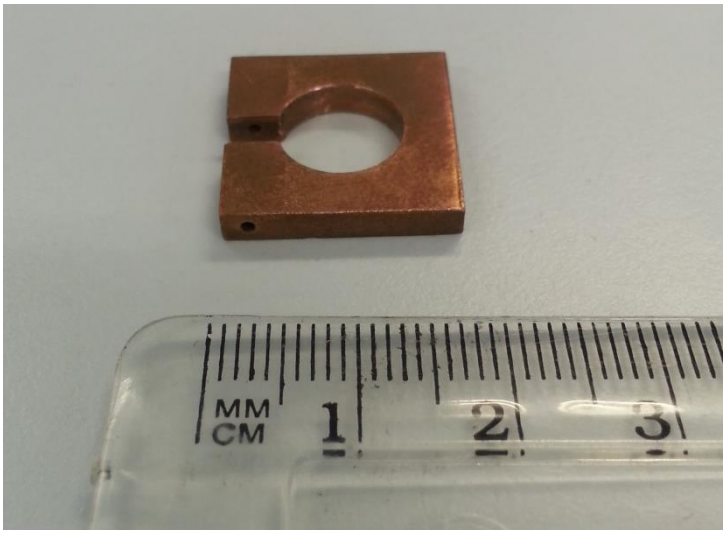

Figure 1.2 Split ring resonator

- CHAPTER SIX (HIGH POWER SYSTEM DESIGN):

  This chapter presents a high power microwave system for heating and thermal processing. It has been designed and built using modular components (derived from TELEMAKUS and Mini Circuits). The system has also been modified to include a programmable syringe pump to precisely control flow rate and keep it steady with time in dynamic situations. The results relating to maximum power transfer to the sample are highly promising for efficient, rapid and volumetric heating applications, especially of small (i.e. microlitre) volumes.

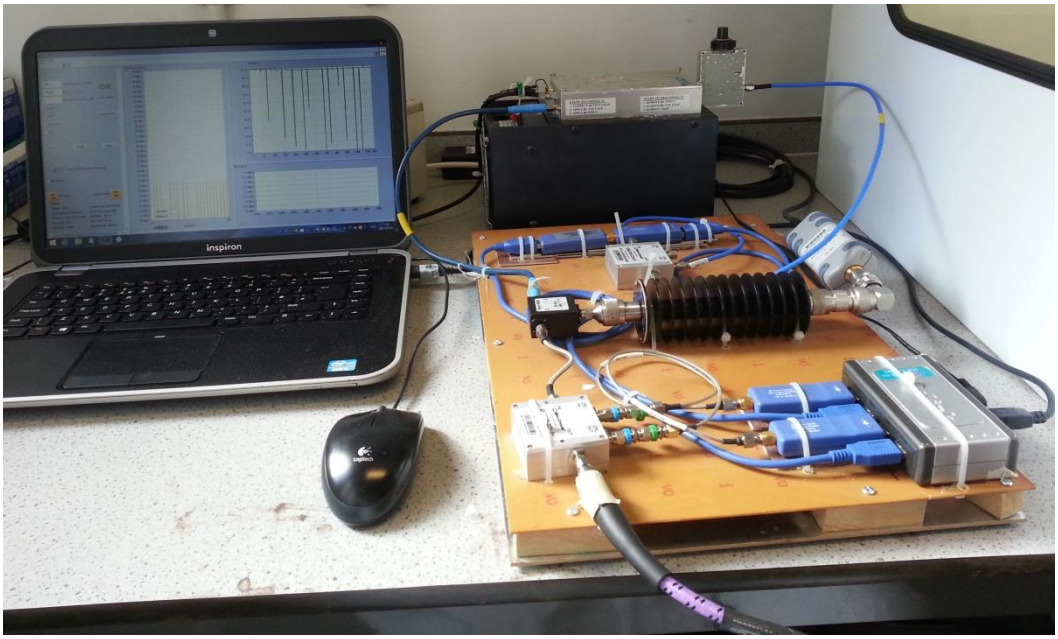

Figure 1.3 Microwave power generating and measurement system.

The enormous size benefit of scaling-down a single-mode cavity resonator to a SRR structure, whilst maintaining the same electric field magnitude within the sample, is shown in Figure 1.4, which then leads to the final application of the SRR as an actuator in Chapter 7.

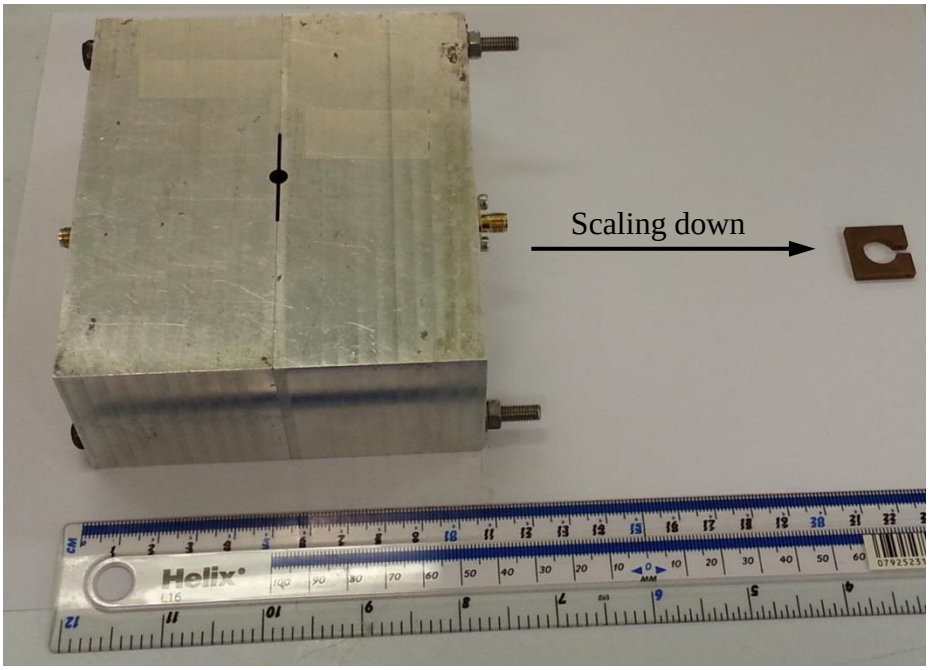

Figure 1.4 Scaling down microwave cylindrical cavity to split ring resonator.

- CHAPTER SEVEN (SPLIT RING RESONATOR FOR HEALTH CARE APPLICATIONS):

  This chapter presents the results of using the designed split ring resonator as a low-power applicator for the rapid liberation of the DNA from *C. difficile* bacteria. The whole microwaving system has been used as described in CHAPTER FIVE. The results showed that there is release of DNA due to microwave irradiation, with minimal heating (to retain sufficiently long fragments of DNA for its subsequent detection). Three microwaving scenarios have been applied: i) continuous microwaves, 100% duty cycle. ii) pulsed microwave at 10% duty cycle. iii) pulsed microwave at 3% duty cycle.

- CHAPTER EIGHT (CONCLUSIONS AND FUTURE WORK):

  Conclusions of the work are summarized in this chapter, and some recommendations are presented for future work.

CHAPTER TWO
BACKGROUND AND LITERATURE SURVEY

2.1. Introduction

Microwaves are radio waves with wavelengths ranging from as short as one millimetre (frequency of 300 GHz) to as long as one meter (300 MHz). The microwave frequency band allocation is shown in the context of the whole electromagnetic spectrum in Figure 2.1.

The wavelength in free space is equal to c/f, where c is speed of light in vacuum (3×10^8 m/s), and f is the frequency. However, in a medium other than free space, the velocity will be reduced by the factor $1/\sqrt{\varepsilon_r}$, where ε_r is the relative dielectric constant of the medium (for practical purposes the relative dielectric constant of air can be considered to be unity). So, the wavelength, λ, will be $\left(\frac{1}{\sqrt{\varepsilon_r}}\right)\left(\frac{c}{f}\right)$ which is also defined as the distance in which the phase changes by 2π radians (360^o) [1].

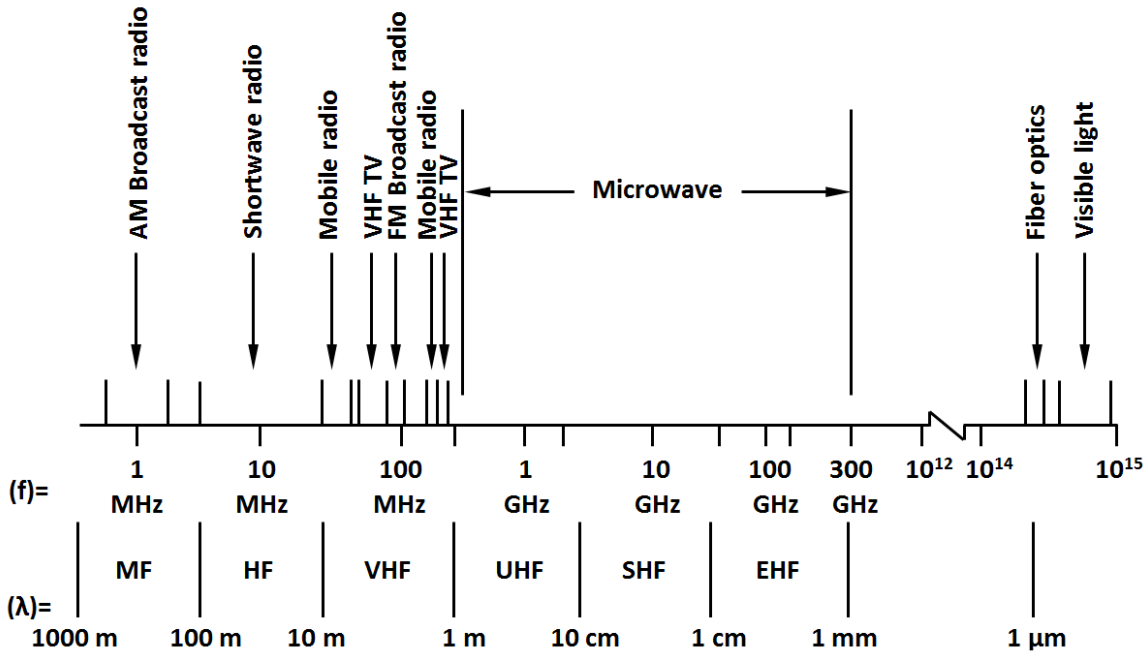

Figure 2.1 The electromagnetic spectrum for "electronic engineering" [2].

Transverse electromagnetic waves are composed of two oscillating wave fields, electric and magnetic, that oscillate perpendicular to each other and on the propagation direction as shown in Figure 2.2; microwaves are just one example of this.

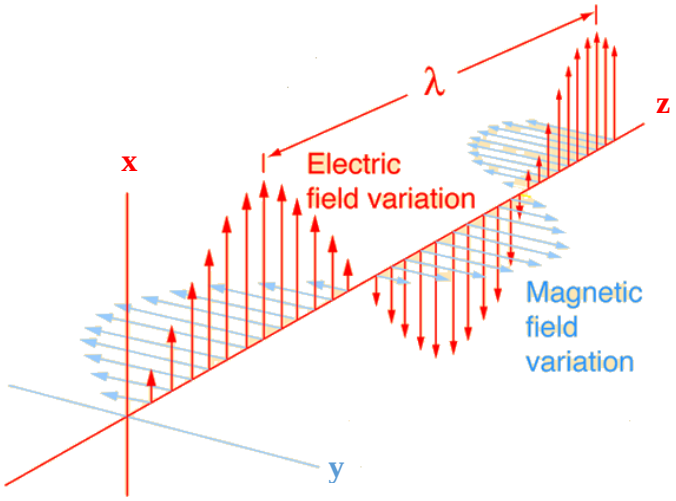

Figure 2.2 Electromagnetic waves transport energy through empty space, stored in the propagating electric and magnetic fields.

The wave has its electric field vector in the direction of the *x*-axis so that E_x has a finite value, but E_y and E_z are zero. Also, H_y has a finite value but H_x and H_z are zero. It can be noticed that there is no field component in the direction of propagation (z-axis); the wave is called transverse electromagnetic (TEM) because all the field components are transverse to its direction of travel [3].

The electric field component E_x and magnetic field component H_y vary sinusoidally in time and also in space, the wave is represented by:

$$E_x = E_0 \sin(\omega t - \beta z) \tag{2.1}$$

$$H_y = \frac{E_0}{Z_0} \sin(\omega t - \beta z) \tag{2.2}$$

where E_0 is the electric field amplitude, Z_0 is called the wave impedance and β is the wavenumber (rad/m) as expressed in equation (2.3) and (2.4) respectively:

$$Z_0 = \sqrt{\frac{\mu_0}{\varepsilon_0}} = 377\ \Omega \tag{2.3}$$

$$\beta = \frac{2\pi}{\lambda} \tag{2.4}$$

where μ_0 and ε_0 is permeability and permittivity of free space, respectively.

Microwave signals have various scientific and industrial applications in present day innovation. These include wireless communications, material processing, control and sensing, biomedical engineering, and pharmaceutical applications.

The question here is, why use microwave resonators in sensing and applications? Actually there are many answers to this question, such as:

1) No physical contact or active devices are required, so they offer numerous advantages compared with traditional techniques based on the dielectric/conducting properties of a sample under test (SUT).

2) These sensors do not require any markers or labels and so are therefore fast and non-invasive. Furthermore, such microwave sensors can be fully compatible with, and so can be embedded within, lab-on-a-chip type approaches.

3) Microwaves penetrate deeply inside materials (high penetration depth) except for metals. This provides reliable measurement results as the measurement is volumetric, and not restricted to the surface.

4) Microwave sensors are safe and non-destructive at low power levels.

This chapter will review microwave applications in three broad fields related to the work in this thesis: microwaves for sensing, microwaves for material thermal processing, and microwave technology in health care applications.

2.2. Fundamentals of Wave Propagation

The behaviour of wave phenomena is described by Maxwell's equations which are given below in their general form [4]:

$$\nabla \times \underline{H} = \underline{J} + \frac{\partial \underline{D}}{\partial t} = \underline{J} + j\omega \underline{D} = \sigma \underline{E} + j\omega\varepsilon \underline{E} = \underline{J} + \underline{J_d} \tag{2.5}$$

$$\nabla \times \underline{E} = -\frac{\partial \underline{B}}{\partial t} = -j\omega \underline{B} = -j\omega\mu \underline{H} \tag{2.6}$$

$$\nabla \cdot \underline{D} = \rho_v \tag{2.7}$$

$$\nabla \cdot \underline{B} = 0 \tag{2.8}$$

The quantities $\underline{E}$ (electric field intensity, V/m), $\underline{H}$ (magnetic field intensity, A/m), $\underline{D}$ electric flux density, C/m^2), $\underline{B}$ (magnetic flux density Wb/m^2), $\underline{J}$ (conduction current density, A/m^2), $\underline{J_d}$ (displacement current density, A/m^2) and ρ_v (volume charge density, C/m^3) are related to each other by the following relations:

$$\underline{D} = \varepsilon \underline{E} \tag{2.9}$$

$$\underline{B} = \mu \underline{H} \tag{2.10}$$

$$\underline{J} = \sigma \underline{E} \tag{2.11}$$

For free space $\mu = \mu_0 = 4\pi \times 10^{-7}$ H/m and $\varepsilon = \varepsilon_0 = 8.854 \times 10^{-12}$ F/m, and furthermore $\sigma = 0$, J = 0 and $\rho_v = 0$. Combining Maxwell's equations leads to another set of equations called wave equations. These wave equations for lossless and lossy media are:

$$\nabla^2 \underline{E} = \mu_0 \varepsilon_0 \frac{\partial^2 \underline{E}}{\partial t^2} \quad \text{(Lossless media)} \tag{2.12}$$

$$\nabla^2 \underline{H} = \mu_0 \varepsilon_0 \frac{\partial^2 \underline{H}}{\partial t^2} \quad \text{(Lossless media)} \tag{2.13}$$

$$\nabla^2 \underline{E} = \mu\sigma \frac{\partial \underline{E}}{\partial t} + \mu\varepsilon \frac{\partial^2 \underline{E}}{\partial t^2} \quad \text{(Lossy media)} \tag{2.14}$$

$$\nabla^2 \underline{H} = \mu\sigma \frac{\partial \underline{H}}{\partial t} + \mu\varepsilon \frac{\partial^2 \underline{H}}{\partial t^2} \quad \text{(Lossy media)} \tag{2.15}$$

In a wave travelling in an arbitrary direction *r*, the space variation is accounted for by multiplying all field quantities by a factor $e^{-\gamma r}$, where γ is called propagation constant.

This parameter may be written $\gamma = \alpha + j\beta$, where α is the attenuation constant or gain coefficient and β is the phase constant measured in rad/m. In the event that α is positive, then the wave decays in amplitude with distance and it is called attenuation constant. In the event that α is negative, then the wave grows, and α is called gain coefficient. The phase constant, β, is a measure of phase-shift per unit length. When $\alpha = 0$, $\beta \approx \omega\sqrt{\mu\varepsilon}$ is termed wavenumber. The value of β in free space $\beta_0 \approx \omega\sqrt{\mu_0\varepsilon_0}$ is referred to as the free space wave number.

2.3. Penetration Depth

The penetration depth, D_p, is a measure of the depth of microwave penetration in a dielectric material, which is defined as the distance from the surface to the place at which the magnitude of the field strength drops to 1/e = 0.368 of its value at the surface. It is mathematically defined as [5] and [3]:

$$D_p = \frac{\lambda}{2\pi\sqrt{2\varepsilon_1}} \times \frac{1}{\sqrt{\left(1 + \left(\frac{\varepsilon_2}{\varepsilon_1}\right)^2\right)^{0.5} - 1}} \tag{2.16}$$

where λ is the free space wavelength of incident radiation, ε_1, and ε_2 are the real and imaginary part of the material complex permittivity respectively ($\varepsilon_r = \varepsilon_1 - j\varepsilon_2$).
Equation (2.16) shows that penetration depth increases with an increase in the wavelength or a decrease in frequency. The penetration depth is also inversely proportional to the values of ε_1 and ε_2.

Due to the short wavelength of microwaves (of the order of centimetres), they penetrate quite deeply within non-metals, so keeping the resonator perturbation principle preserved, and also minimizing the radiation loss and, accordingly, the volumetric moisture content in a dielectric material can be determined as microwaves are not restricted to the surface of the tested material.
On the other hand, The skin depth, δ, of a conductor is expressed as [6] and [7]:

$$\delta = \sqrt{\frac{2}{\omega\mu\sigma}} = \sqrt{\frac{2\rho}{\omega\mu}} \tag{2.17}$$

where μ is the permeability of the material in H/m, $\mu = \mu_0\mu_r$, σ is the conductivity in S/m and ρ is the resistivity in Ωm. The skin depth according to equation (2.17) is a function of three variables; conductivity (or resistivity), permeability, and frequency of operation. Since $\mu_r \approx 1$ for most metals, the skin depth can be re-written as:

$$\delta = \sqrt{\frac{2}{\omega\mu_0\sigma}} = \sqrt{\frac{2\rho}{\omega\mu_0}} \tag{2.18}$$

At microwave frequencies, the skin depth for good conductors is extremely small (around 1μm), and so a very thin coating of a good conductor such as gold or silver is desired for low-loss microwave components [6].

2.4. Microwave for Sensing and Dielectric Constant Measurements

Precise measurement of material properties has received significant interest over the last decade. There is a growing need for wireless sensing for mission-critical industrial and military applications, and structural health monitoring [8] and [9].

Microwave sensors are interesting in applications in which no physical contact is applicable. Compared to traditional techniques, they offer advantages based on the dielectric/conducting properties of a sample under test (SUT). These sensors are fast and non-invasive as there is no need for markers or labels. [10].

The microwave methods for material property characterization generally can be divided into two groups: non-resonant methods, which are based on microwave propagation, and resonant methods which based on microwave resonance. Non-resonant methods are mainly used to get general information of electromagnetic properties over a wide frequency range, while resonant methods are utilized to get accurate information of dielectric properties at a single frequency or several discrete frequencies. Both non-resonant and resonant methods are often utilized in combination to get precise knowledge of material properties by modifying the general information over a certain frequency range obtained from non-resonant and resonant methods [11].

2.4.1. Non-Resonant Sensing Methods

Non-resonant sensing methods essentially include signal reflection and transmission/reflection measurements. In a reflection measurement, the material properties are extracted based on the signal reflection from the sample due to the impedance discontinuity introduced by the sample within a transmission line structure. In a transmission/reflection measurement, the material properties are extracted based on the signal reflected from the sample as well as the signal transmitted through the sample, and from the relevant scattering equations relating the scattering parameters of the segment of transmission line filled with sample material. Non-resonant methods need a way of directing the electromagnetic energy toward a sample material and then observing the reflection from the material, as well as the transmitted through it. Many types of transmission lines can be utilized to carry the electromagnetic wave such as coaxial line, waveguide, and free space [11].

A- Transmission/reflection method

A measurement using the Transmission/Reflection method includes placing a sample material under test (MUT) in a section of transmission line and measuring the two-port complex scattering parameters (s-parameters) with a vector network analyser (VNA) as shown in Figure 2.3. The method involves measurement of the transmitted (S_{21}) and reflected (S_{11}) signals. The relevant scattering parameters strongly relate to the complex permittivity and permeability of the MUT. The sample's electromagnetic parameters (permittivity ε^* and permeability μ^*) can then be extracted from the scattering matrix [12] and [13]. Since there are four experimental parameters (amplitude and phase of S_{11} and S_{21}) then, in principle, both real and imaginary parts of complex permittivity and permeability can be determined.

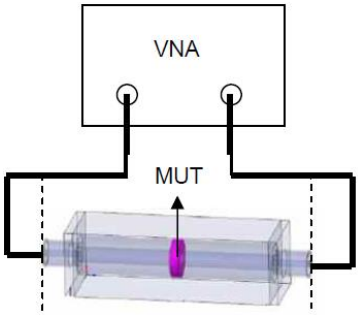

Figure 2.3 Measurement using transmission/reflection method with a waveguide [14].

The procedure firstly introduced by Nicolson, Ross and Weir (NRW) is derived from the following equations, which are applicable for the coaxial line cell (TEM propagation mode) and the rectangular waveguide cell (TE_{01} propagation mode) [12] and [15], [16]:

$$S_{11} = \frac{\Gamma(1 - T^2)}{1 - \Gamma^2 T^2} \tag{2.19}$$

$$S_{21} = \frac{T(1 - \Gamma^2)}{1 - \Gamma^2 T^2} \tag{2.20}$$

$$\Gamma = \frac{Z - Z_o}{Z + Z_o} \tag{2.21}$$

where S_{11} and S_{21} are the reflection and transmission scattering parameters; Γ and T are the first reflection and the transmission coefficients, Z_o and Z represent the waveguide impedances of the empty and filled cells, respectively. The NRW procedure includes the further relationships as shown in equation (2.22) to (2.27)

$$K = \frac{S_{11}^2 - S_{21}^2 + 1}{2S_{11}} \tag{2.22}$$

$$\Gamma = K \mp \sqrt{K^2 - 1} \tag{2.23}$$

$$T = \frac{S_{11} + S_{21} - \Gamma}{1 - (S_{11} + S_{21})\Gamma} \tag{2.24}$$

$$\frac{1}{\lambda^2} = \left[\frac{j}{2\pi d}\ln(T)\right]^2 \tag{2.25}$$

$$\mu^* = \frac{\lambda_{og}}{\lambda}\left(\frac{1 + \Gamma}{1 - \Gamma}\right) \tag{2.26}$$

$$\varepsilon^* = \frac{\lambda_o^2}{\mu^*}\left(\frac{1}{\lambda^2} + \frac{1}{\lambda_c^2}\right) \tag{2.27}$$

where λ_o and λ_c correspond to the free-space and the cut off wavelengths, and d is the sample length. The NRW procedure involves two steps: Firstly, Γ , T , and the $\frac{1}{\lambda}$ terms are calculated from the measured scattering parameters using equations (2.22) to (2.27). These parameters are determined from equations (2.19) and (2.20); secondly, both complex permittivity and permeability are calculated using equations (2.26) and (2.27). Equation (2.26) is dependent upon the parameter shown in equation (2.28):

$$\lambda_{og} = \frac{1}{\sqrt{\frac{1}{\lambda_o^2} - \frac{1}{\lambda_c^2}}} \tag{2.28}$$

which represents the guide wavelength in the empty cell.

An example application for this technique is proposed in [17] and [18] for characterization of the electric properties of textile materials and epoxy samples, respectively.

In [19], a coplanar waveguide sensor for the measurement of scattering coefficients of test specimens has been used to obtain dielectric properties represented by complex permittivity of thin samples and dielectric sheets. In [19] the authors discuss one of the major problems of planar RF sensors, which is the possible air gap between the device and the MUT. This problem is acute when there is a component of electric field perpendicular to such boundaries, especially for high permittivity materials. The authors also analyse the sensitivity in order to critically observe the effect of air gap between the test sample and the sensor, which required an analytical multilayered model to take into account the effect of the air gap and to accordingly provide the appropriate correction factor.
In [20], the technique is used to measure the permittivity of low-loss liquids such as crude oils using a single measurement cell in the broad frequency range 1 kHz to 6 GHz.

The advantages and disadvantages of Transmission/Reflection line method are listed below [14]:

Advantages:

- Waveguides are commonly used to measure samples with medium to high loss.
- It can be used to determine both the permittivity and permeability of the material under test.

Disadvantages:

- Measurement accuracy is limited by the air-gap effects.
- Accuracy is limited when the sample length is a multiple of one-half wavelength in the material (imposed by ill-conditioning from the NRW method).

B- Reflection method (the example of the open ended coaxial probe)

The open ended coaxial probe method has been used for years as a convenient, non-destructive method for dielectric sensing. In this method, the material is measured by immersing the probe into a liquid or by pressing it to the flat face of a solid (or compacted powder) material. The electric field at the open-circuit probe's end "fringe" into the material, as shown in Figure 2.4. The subsequent electric field interaction is measured via the reflection coefficient S_{11} using a vector network analyser and a suitable analytical model for the sample-loading of the probe's aperture is used to calculate the permittivity [21].

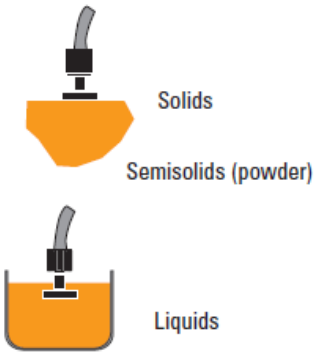

Figure 2.4 Measurement using coaxial probe method [21].

This technique was pioneered by Stuchly and Stuchly (1980). Since only amplitude and phase of S_{11} are measured, it is only possible to extract two material variables. The basic interaction here is with the probe's electric field, since in the first approximation, the magnetic field is zero at the open circuit end. Hence, the method is excellent for extracting real and imaginary parts of the complex permittivity of lossy dielectrics, but of no use for magnetic materials. While the method is easy to use and it is possible to measure the dielectric properties over a wide range of frequencies (500 MHz - 110 GHz), it is of limited accuracy, particularly with materials with low values loss (ε_2) [22].

The coaxial probe can be represented by an equivalent circuit consisting of the fringing capacitance between the inner and outer conductor of the coaxial structure and radiating conductance which represents propagation losses. The capacitance and conductance are

frequency and permittivity dependent and also dependent on the dimensions (of the inner and outer diameters) of the probe [23], [24]. The sensor can be modelled as a lumped admittance with capacitances as shown in Figure 2.5 (a) and (b).

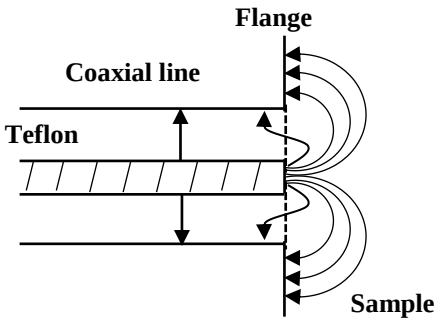

(a)

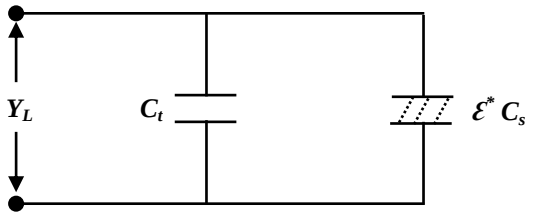

(b)

Figure 2.5 Coaxial line termination fringing fields (a), and sensor lumped equivalent circuit (b) with capacitances originating from the PTFE fringing field (C_t) and sample fringing field (C_s) [25].

The load admittance, Y_L^*, is given in terms of the voltage reflection coefficient, Γ^*, as [25]:

$$Y_L^* = Y_0 \frac{(1-\Gamma^*)}{(1+\Gamma^*)} \tag{2.29}$$

where Y_0 is the characteristic admittance of the line. In terms of the equivalent circuit model, the admittance is

$$Y_L^* = j\omega C_t + j\omega(\varepsilon_1 - j\varepsilon_2)C_s \tag{2.30}$$

where ω is the angular frequency. So, the real part of the relative permittivity is:

$$\varepsilon_1 = \frac{-2|\Gamma| sin\varphi}{\omega C_s Z_o (1 + 2|\Gamma| cos\varphi + |\Gamma|^2)} - \frac{C_t}{C_s} \tag{2.31}$$

and imaginary part is:

$$\varepsilon_2 = \frac{1 - |\Gamma|^2}{\omega C_s Z_o (1 + 2|\Gamma| cos\varphi + |\Gamma|^2)} \tag{2.32}$$

where $|\Gamma|$ and φ are the magnitude and phase of the reflection coefficient respectively, and Z_o is the characteristic impedance. The load admittance is also can be defined as:

$$Y_L^* = j\omega C_F^* \tag{2.33}$$

where C_F^* is the total complex fringing capacitance, $C_F^* = (C_s\varepsilon_1 + C_t) - jC_s\varepsilon_2$.

Open ended coaxial probe sensors are mainly used for non-destructive characterization of electromagnetic properties of solid state materials [26] and liquids (e.g. water, methanol, and dioxane-water mixtures [27]), and also in the field of biomedical engineering [28], e.g. utilized as a potential diagnostic tool for detection of skin cancers by measuring microwave properties of skin [29]. The published results of the measurements for normal and moistened skin showed that the water content of normal skin and benign and malignant lesions may cause significant differences among their reflection properties and subsequently render a malignant lesion detectable.

Furthermore, open ended coaxial probes have been employed in the detection of surface-breaking cracks in metals, which is an important issue in many industries, as presented by [30] and [31]. In this work, a crack is characterised by the relative phase of the reflected signal, where the reference phase is the value of the phase of the probe output signal when terminated with a perfect, flat conductor plane.

The advantages and disadvantages of the open ended coaxial probe method are listed below [14]:

Advantages:

- Requires no machining of the sample (easy sample preparation).
- Measurement can be achieved in a temperature controlled environment.

Disadvantages:

- Only reflection measurement available, so limited to dielectrics.
- Affected by air gaps for measurement on sample.

C- Free space method

The free space method allows measurements of materials under high temperatures or hostile environments. The approach works over a wide range of frequencies and the measurement requires the material sample to be large and flat. It usually utilizes two antennas (transmitting and receiving) placed facing each other and the antennas are connected to a network analyser, as shown in Figure 2.6 [14].

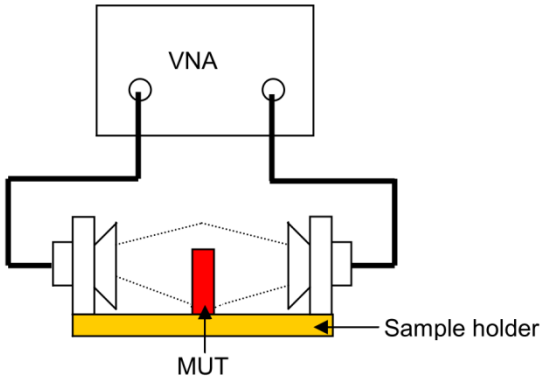

Figure 2.6 Measurement of a material sample using free space method.

High temperature measurements are easy to perform in free space as the sample is never touched or contacted. The MUT can be heated by placing it within a furnace that has "windows" of insulation material that are transparent to microwaves [21].

In a free-space transmission technique, when a sample is placed between a transmitting antenna and a receiving antenna, the attenuation and phase shift of the signal are measured. These can then be utilized to extract the material's dielectric properties, based on the NRW technique presented earlier. Accurate measurement of the permittivity over a wide range of frequencies can be carried out by free space techniques. In most measuring systems, the accuracy of the determined ε_1 and ε_2 depends mainly on the performance of the measuring system and the validity of the equations used for the calculation. The usual assumption made during this technique is that a uniform plane wave is normally incident on the flat surface of a homogenous material, and that the planar sample has infinite extent laterally, so that diffraction effects at the edges of the sample can be neglected [22].

In general, permittivity can be extracted from the following equations:

$$\varepsilon_1 = \left(\frac{\lambda_0}{2\pi}\right)^2 \left[\left(\frac{2\pi}{\lambda_c}\right)^2 - (\alpha^2 - \beta^2)\right] \tag{2.34}$$

$$\varepsilon_2 = \left(\frac{\lambda_0}{2\pi}\right)^2 (2\alpha\beta) \tag{2.35}$$

where λ_o and λ_c are the free-space and the cut off wavelength respectively.
The unknown values of the real and imaginary parts of the propagation coefficient (α and β) can be calculated using equation (2.36) for the transmission coefficient T, which is a measured quantity

$$T = \frac{(1 - \Gamma^2)e^{-\gamma L}}{1 - \Gamma^2 e^{-\gamma L}} \tag{2.36}$$

where L is the sample thickness, γ is the propagation coefficient given by $\gamma = \alpha + j\beta$, and Γ is the reflection coefficient given by $\Gamma = (Z - Z_0)/(Z + Z_0)$. Here Z and Z_0 are the characteristic impedance of the applicator with and without the test material, and are given by:

$$Z = \frac{2\pi\eta_0}{\lambda_0} \frac{\beta\left(1 + j\frac{\alpha}{\beta}\right)}{\alpha^2 + \beta^2} \tag{2.37}$$

$$Z_0 = \frac{2\pi\eta_0}{\lambda_0\beta_0} \tag{2.38}$$

$$\beta_0 = \frac{2\pi}{\lambda_0}\left[1 - \left(\frac{\lambda_0}{\lambda_c}\right)^2\right]^{1/2} \tag{2.39}$$

where η_0 is the wave impedance of air-filled applicator (377 Ω), and β_0 is the phase coefficient of the air-filled applicator.

Free space techniques have been used by [32] and [33] to determine the relative permittivity (dielectric properties) of planar samples, and by [34] for dielectric material characterization at THz frequencies within the frequency range 750–1100 GHz. Also, it has been employed in free-space measurement technique [35] for non-destructive noncontact electrical and dielectric characterization of nanocarbon (carbon nanotubes NCTs) composites in the Q-band frequency range of 30–50 GHz.

Another application using this technique has been presented by [36], where the dielectric properties of granular materials were determined by measuring the scattering transmission coefficient S_{21} in free space over a broad frequency range between 2 and 13 GHz. A pair of horn-lens antennas was used to provide a focused beam. Variations of the dielectric properties with frequency and physical properties such as bulk density, moisture content, and temperature were investigated. Both the dielectric constant and the loss factor decreased with frequency and increased linearly with bulk density, moisture content, and temperature.

Advantages and disadvantages of free space method are listed below [14] and [37]:

Advantages:

- Suitable for high frequency and high temperature sample measurement.
- Non-destructive and contactless measurement.
- Possible to measure the sample test in hostile environment.

Disadvantages:

- The inaccuracies in dielectric measurements are mainly due to diffraction effects at the edges of the sample and multiple reflections between the two transmitting and receiving antennas via the surface of the sample.

2.4.2. Resonant Methods

Resonant methods are used characterise the properties of a material with high accuracy and sensitivity in comparison with non-resonant methods. Resonant methods are usually based on the change in resonator properties (such as resonant frequency and quality factor) due to the interaction of the resonator's electromagnetic fields with the sample under test, often called generically the "cavity perturbation technique" [11].

There are many types of resonant structures available such as cavity resonators, re-entrant cavities, split cylinder resonators, etc., where the perturbation method is applied for complex permittivity measurements. Firstly, resonant frequency and quality factor measurements are made using an empty cavity. Secondly, the measurements are repeated after filling the cavity with the MUT. The permittivity or permeability of the

material can then be computed using the frequency, sample volume and Q-factor [14]. This will be discussed in detail in CHAPTER FOUR.
Different types of microwave cavities operating in different modes have been used by many researchers to measure the dielectric properties for various dielectric samples, all based on the cavity perturbation method [38]-[40].

For a cylindrical cavity with a sample placed on-axis, the most common modes used are TM_{010} for dielectric characterisation and TE_{011} for magnetic characterisation; furthermore, the re-entrant cavity can be used for a more concentrated electric field region for dielectric characterisation, and hence greater sensitivity for a fixed cavity volume. The TM_{010} mode usually has the lowest resonant frequency in a cylindrical cavity (otherwise TE_{111} if the length is longer than the diameter) and is then the most easily distinguishable mode, as shown in Figure 2.7 [41].

It is difficult to identify and reliably utilize more than two of TM_{0n0} modes as higher order modes resonant at higher frequencies, where the spectrum becomes cluttered and modes overlap in the transmission spectrum of the resonator. The last subscript '0' in TM_{010} indicates that the strength of the E and H fields do not change as one moves from top to bottom along the axis of the cavity. As one moves radially outwards, the axial E-field is at a maximum on the axis of the cavity and falls away to zero amplitude on the cylindrical side-wall, while the H-fields loop around the axis of the resonator as shown in Figure 2.8 [42]. Material samples are normally in solid rod form or tubes, which can be used for containing liquid dielectrics.

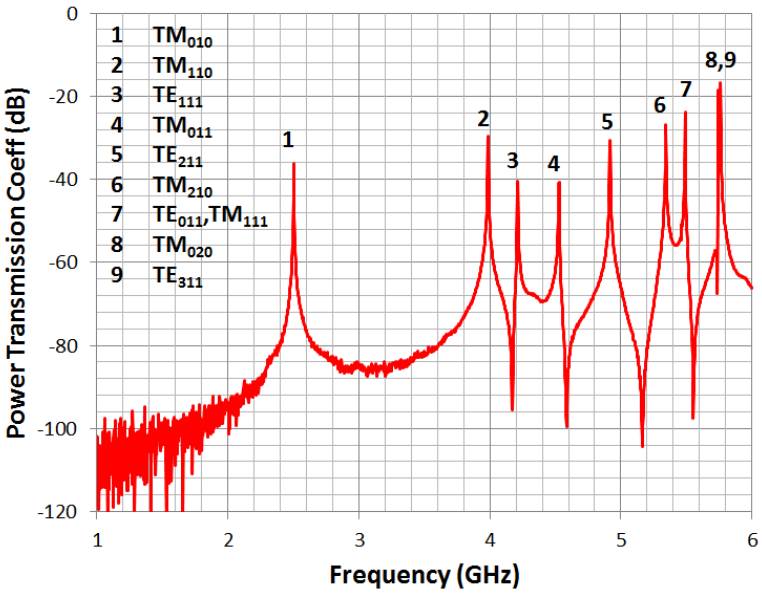

Figure 2.7 Cylindrical cavity modes for an aluminium cylinder of internal radius of 46 mm and length of 40 mm [41].

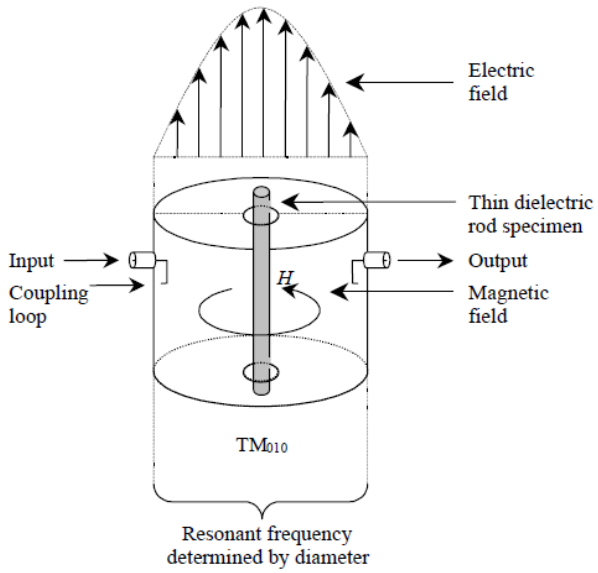

Figure 2.8 A TM_{010} mode cavity resonator containing a dielectric sample in rod form [42].

In the TE_{011} cylindrical cavity mode, the electric field lines are distributed circularly about the cavity axis, whilst the magnetic field is a maximum on axis, as shown in Figure 2.9. So, there is no current flowing between the sidewall and end wall, therefore, this mode does not require good electric contact between the sidewalls and end wall.

Due to its particular field distribution, this mode is suitable for the measurement of disc-shaped dielectric samples oriented parallel to the ends of the cavity, in the middle of the axis, to be in the maximum electric field.

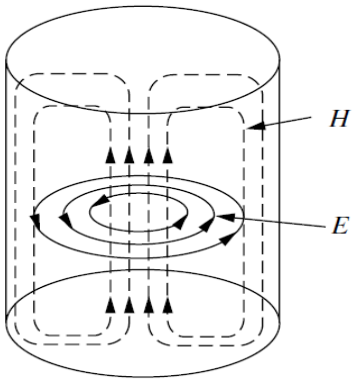

Figure 2.9 Field distribution of the cylindrical TE_{011} mode [11].

Re-entrant cavities can be considered as a special type of the TM_{010} cavity, where cylindrical conductors are modified to form two opposite internal posts making a gap capacitance between them where the electric field is highly concentrated. The magnetic field is distributed around the internal posts between the inner and outer cavity conductors as shown in Figure 2.10. The dielectric specimen is placed in the gap formed from the two parallel plates, where the electric field is concentrated strongly.

The re-entrant cavity has a high quality factor, frequency tuning capability, easy design and the possibility of localizing the electric field within a small gap region [43] and [44], which makes it very attractive for both telecommunication applications [45] and [46], and dielectric materials characterization [47].

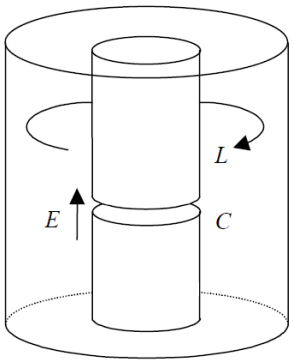

Figure 2.10 Fields distribution of a re-entrant cavity [42].

The application of cavity resonators for the measurement of dielectric properties of materials has been well known for more than half a century, and since that time they have become attractive and interesting for engineers and scientists to deploy or modify for a range of industrial and chemical applications.

In [48], researchers discussed the potential of using microwave techniques in the refinement of the heavy fraction of petroleum such as bunker oil. They presented measurements of the dielectric properties of heavy oils at 2.45 GHz using a highly sensitive resonant cavity at TM_{010}, and also over a broader frequency range (100 MHz to 8 GHz) using a coaxial probe technique. These cavity data are in excellent agreement with the coaxial probe data at the same frequency, and give confidence to predict the conversion efficiency if these samples were to be placed in a suitable microwave actuator.

Also, this mode TM_{010} of cylindrical cavity resonator has been used by [49], where the authors designed their cavity resonator to be suitable for noninvasively measuring the amount of water and its distribution within plant tissues.
Another example of TM_{010} mode of a cavity resonator has been shown by [50], they were able to extract the moisture content from the complex permittivity of cigarettes on the production line. The moisture content has an influence on both of the resonant frequency and quality factor.

A rectangular microwave cavity resonator has been presented by [51] as a tool for concentration measurements of liquid compounds. The sensing device is a rectangular

waveguide cavity tuned at 1.91 GHz. According to the type of substance inside the mixture, its concentration is conveniently related to the changes of the S_{21} scattering parameter (transmission coefficient). All measurements have been performed at the temperature of 27 °C using two solution mixtures; water/NaCl and water/sucrose solutions. The sensor was shown to be sensitive for assessing mixture concentrations. The rectangular cavity with its coupling elements and system measurement setup are shown in Figure 2.11 (a) and (b) respectively.

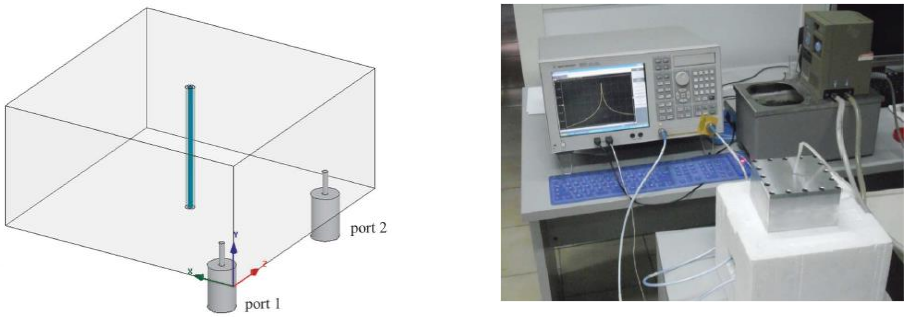

(a) (b)

Figure 2.11 (a) Schematic of a rectangular cavity, and (b) its system measurement setup [51].

In [52] a closed cylindrical cavity resonator is used to measure the dielectric constant and loss tangent of homogeneous isotropic samples in rod form. The measurements are made at the resonant frequency of the $TE_{01\delta}$ mode. The dielectric properties are computed from the sample dimension, resonant frequency, and unloaded quality factor of the resonator.

In [53] a cylindrical cavity resonant at 1040 MHz is used as a low power microwave sensor for analysis of lactic acid in water, and cerebrospinal synthetic fluid (CSF). It was observed that the measured relative reflected signal amplitude (S_{11}) was decreased when the concentration of lactic acid increased.

On the area of ring resonators, an improved split-ring resonator for microfluidic sensing has been proposed in [54], where a method of making low loss split-ring resonators for microfluidic sensing at microwave frequencies using silver coated copper wire is

presented. A simple geometric modification involving extending the conductor in the gap region provides a higher electric field in the capacitive region of the resonant sensor, as shown in Figure 2.12. The sensor sensitivity has been tested with some common liquids. A schematic view of this resonator setup is shown in Figure 2.13.

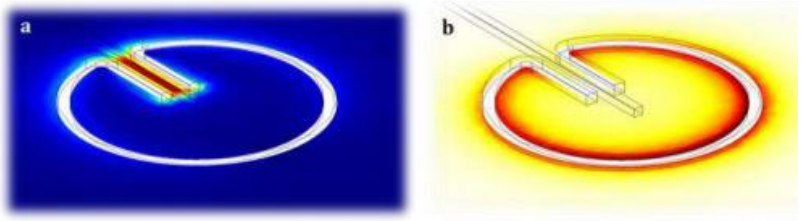

Figure 2.12 (a) Electric field colour map (blue = zero |E|, red = maximum |E|) and (b) magnetic field colour map (white = zero |H|, brown = maximum |H|) for a split ring resonator, with wire of square cross section to improve the sensitivity [54].

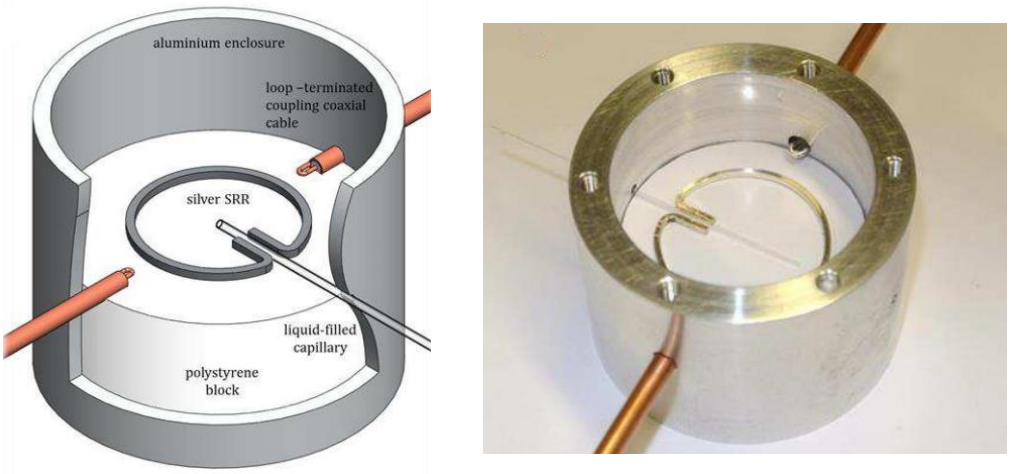

(a) (b)

Figure 2.13 (a) Cutaway schematic view and (b) photograph of a split-ring resonator perturbed with a liquid filled capillary [54].

In [55], researchers presented a microstrip double split ring resonator working at 3GHz as a microfluidic sensor to determine the dielectric properties of some common solvents based on perturbation theory, in which the resonant frequency and quality factor of the

microwave resonator depends on the dielectric properties of the resonator. A schematic of the sensor is shown in Figure 2.14. The extended arms in the two gap regions behave like two capacitors with high electric field which allow not only dielectric properties but also to measure properties such as fluid velocity and to interrogate multiphase flow.

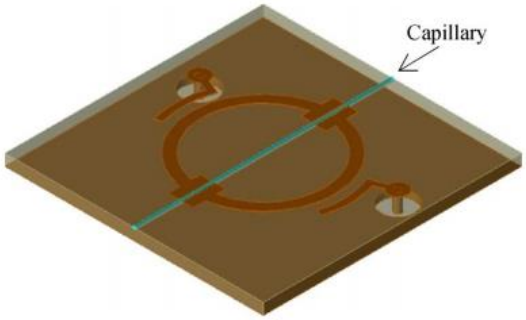

Figure 2.14 Schematic of the double microstrip split ring resonator and a capillary [55].

Generally speaking, the advantages and disadvantages of resonant methods are listed below:

Advantages:

- Able to measure very small size of test materials.

Disadvantages:

- High frequency resolution vector network analyser VNA is needed to perform these measurements.
- Limited to a narrow band of frequencies.

2.5. Microwaves for Material Thermal Processing

Microwave (MW) application for heating has been applied in various fields such as different drying processes (agricultural, and chemical), food production areas such as drying and cooking food, where the microwave oven has become popular in domestic kitchens as mass production of the magnetron became possible, and excitation in the chemical industry. Microwave applications also extend to broad areas such as incineration of medical wastes, treatment of sewage sludge and re-generation of spent

activated carbon and chemical residues of petrol industries. Heating is caused by a dielectric relaxation loss due to rotation of molecules, which is the result of the interaction between the MW electric field and the electric dipole of the molecules. Electric dipoles in liquid or gas experience relatively free rotational motion, compared to the dipoles within a solid [56].

Microwave heating offers a number of advantages such as: (i) energy transfer instead of heat transfer via conduction; (ii) selective material heating; (iii) volumetric heating; (iv) non-contact heating; (v) quick start and stop; (vi) heating from the interior of the material body; and (vii) safety, where the microwave energy is a nonionizing electromagnetic radiation since it has frequencies below 300 GHz [57], [58].
Microwave processing is a complicated process as it depends on many parameters such as dielectric properties, material volume and shape, and microwave system design. These factors are critical and influence microwave heating absorption in a material [59], [60].

At the point when electromagnetic waves experience a medium, the waves can be reflected, absorbed (microwave energy penetrates through the material and is converted into heat), transmitted or any mix of these three associations as shown in Figure 2.15 [58]. The electric field component of microwaves is responsible for the dielectric material heating, which in turn raises the temperature of the material such that the interior parts of the material are hotter than its surface since the surface loses more heat to the surroundings. This characteristic has the potential to heat large sections of the material uniformly. Also, dielectric heating is affected by means of two essential mechanisms; dipolar polarization and ionic conduction. In the polarization mechanism, a dipole is responsive to an external electric fields and tries to align itself with the field direction by rotation. At high frequencies, the dipoles do not have sufficient time to fully respond to the oscillating electric field and as a result of this phase lag, power is dissipated and heat generated in material owing to the interactions (usually chemical bonds) between the dipoles, e.g. hydrogen bonds in water and other polar solvents. The dipolar polarization mechanism is the origin of microwave dielectric heating that involves the heating of electrically insulating materials by dielectric loss, while in the conduction mechanism, any charge carriers (electrons, ions, etc.) move forward and backward through the material under the effect of the microwave electric field. The

resulting electric currents will cause Ohmic heating in the material sample resulting from electrical resistance caused by the collisions of charged particles with adjacent molecules or atoms [61] and [5].

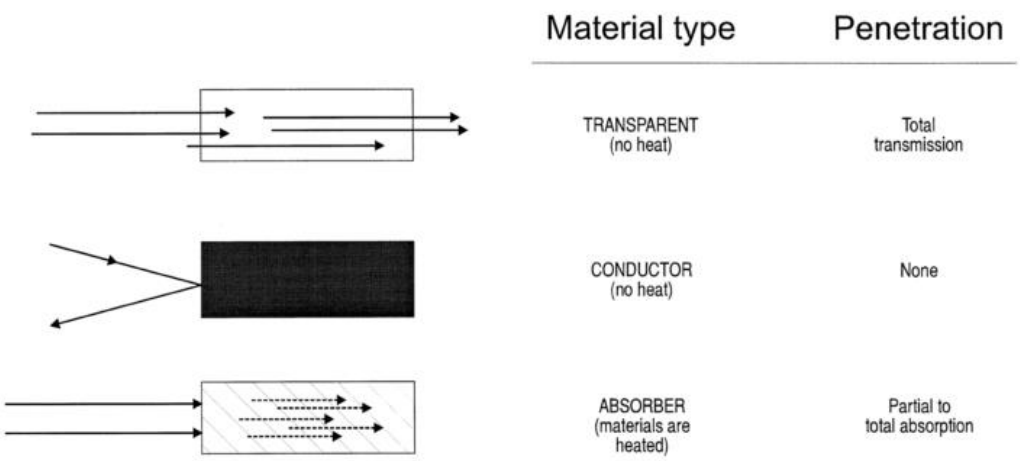

Figure 2.15 Interaction of microwave with materials [58].

There is a wide range of applications for using the microwaves in drying in industrial, chemical, and food heating.

2.6. Microwave Technology for Health Care Applications

There is also wide range of microwave applications in health care applications, ranging from low power levels used for sensing to higher power levels for diagnostics and treatment. Different microwave structures and devices are used based on the application requirements, and some applications will be reviewed in the next two subsections.

2.6.1. Microwaves for Medical Applications

As already mentioned, microwaves present a completely non-ionizing tomographic technique owing to the low photon energies involved. Microwaves energy can be very safe to apply and as a result is widely used in medicine, especially in the field of diagnosis by MRI (Magnetic Resonance Imaging) [62]. There are very many research

activities concerned with medical diagnostics and treatment based on electromagnetic wave technologies, especially during the last twenty years, specifically those coming out from the theory and technique of microwaves, antennas and electromagnetic wave propagation. Microwave applicators for medical diagnostics and therapy are, when considering the working principle, very similar each to other. They can be derived from various microwave technologies, for instance waveguides, planar and coaxial structures and others. Wide utilization of microwave thermotherapy can be observed in most worldwide countries. The electromagnetic wave propagation from applicator into the treated tissue depends on the dielectric properties, such as permittivity ε and conductivity σ of that tissue [63]. Many microwave structures have been proposed and presented by researchers for this purpose, such as: antenna needle [64], open ended coaxial probe as shown in Figure 2.16 [29],[65], antenna arrays [66],[67], re-entrant resonant cavity [68], and open-ring applicator [69].

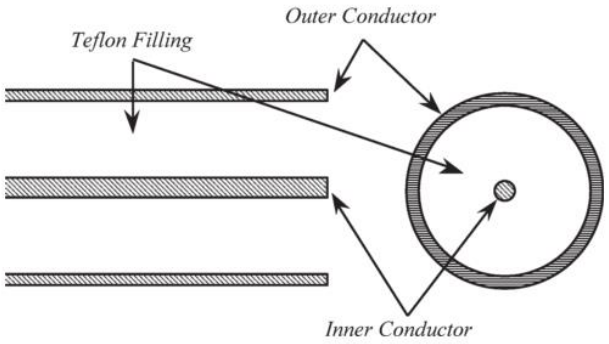

Figure 2.16 Cross-sectional and plan views of an open-ended coaxial probe, it is used to measure the reflection properties. The outer diameter is 3.62 mm and inner conductor diameter of 1.08 mm [29].

2.6.2. Microwaves for Biological Applications

Interactions between different types of electromagnetic radiation and living organisms have received the attention of scientists since the introduction of technical devices that operate using electromagnetic waves. The published results demonstrated that microwaves produce significant effects on the growth of microbial cultures, which differ from the killing of microorganisms to enhancement of their growth. The nature

and degree of the effect depend on the frequency of the microwaves and the total energy absorbed by the microorganisms. Low energy, low frequency microwaves can enhance the growth of microorganisms, whereas high energy, high frequency microwaves will damage the microorganisms. When applying microwaves to living organisms, two types of effects will be produced: thermal and non-thermal. Thermal effects are the result of absorption of microwave energy by cell molecules, causing them vibrate much faster and producing general heating of the cell. The extent of microwave absorption within a cell depends on its dielectric constant and electrical conductivity [70].

Wu et al. [71] made a series of experiments to determine the effect of microwave energy using the system shown in Figure 2.17 on several types of bacteria such as *Bacillus subtilis var. niger*, *Bacillus stearothermophilus*, *Bacillus pumilus E601*, *Staphylococcus aureus* and *Bacillus cereus*. Under the conditions of different exposure duration and unequal microwave power irradiation onto the bacteria, a valuable result of killing bacteria has been obtained. He concluded that the conditions for killing or damaging of all bacteria depend not only on the duration and the frequency, but on the microwave power intensity as well as the types of bacteria. As long as the *Bacillus subtilis var. niger* is killed by microwave energy, then under the same conditions, all other types of bacteria can be killed. *Bacillus subtilis var. niger* can therefore be considered as an ideal marker bacterium for disinfection by microwave energy. This conclusion provided important evidence for choosing a marker or indicator bacterium for disinfection by microwave as a new technical standard [71].

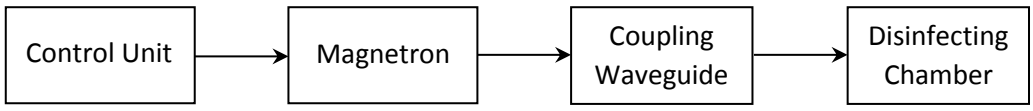

Figure 2.17 A block diagram of microwave disinfector, it uses a magnetron with an output frequency of 2450±30 MHz. The maximum output power of the magnetron is as high as 650 W, the circuit is similar to that of a home microwave oven [71].

CHAPTER THREE
INTERACTION OF DIELECTRIC MATERIALS WITH ELECTROMAGNETIC FIELDS AT MICROWAVE FREQUENCIES

3.1. Introduction

Dielectric properties are the main parameters that provide information about how materials interact with electromagnetic energy during dielectric heating [72]. One of the most important of these is the complex relative permittivity $\varepsilon_r = \varepsilon_1 - j\varepsilon_2$, where ε_1 is the real part (generally known as permittivity or dielectric constant) and ε_2 is the imaginary part (or the loss factor) [73].

In recent years, there has been a growing demand to obtain the dielectric properties of materials, since the dielectric properties measurements are widely required for the numerous applications in industry, medicine and pharmaceuticals [74], [75] as discussed in Chapter 2.

Understanding of field-material interactions is essential in the design of high frequency sensors and applicators, because the electrical properties of the material of interest will become a part of the device's functionality. This fact is a unique feature of these devices [76].

In terms of liquid polarity, there are two types of liquids, polar and non-polar. Polar liquids are those whose molecules have permanent electric dipole moments, while non-polar liquids have molecules that only develop a net electrical polarisation upon application of an external electric field (thus exhibiting electronic or ionic polarisation). The permittivity, ε_1, of polar liquids is much higher than non-polar liquids, lying typically in the range from 10 to 100. Also, the dielectric loss of polar liquids at microwave frequencies is comparatively high, with loss tangent $tan\delta = \varepsilon_2/\varepsilon_1$ typically in the range of 0.1 to 1 [77].

Conversely, non-polar liquids have a low relative permittivity, typically between 2 and 3, which changes little over a frequency range of several decades. They also have low loss, with $tan\delta$ typically less than 0.001 [77].

The characterisation of polar dielectric liquids is receiving wide interest for different reasons. For example, the dielectric relaxation behaviour of polar liquids provides information about their molecular structure. Also, biomedical applications of polar liquids have become prominent because of the good match of their complex permittivity over the frequency range from 300 MHz to 6 GHz to that of biological tissues. This is the region of the spectrum that is widely used for mobile and local area telecommunications [77].

3.2. Polarization Mechanism

When an electric field is applied to a material, dipoles will be induced within the atomic or molecular structure and become aligned with the applied field direction. Furthermore, any permanent dipoles which already exist in the material are aligned with the field. The material will then become polarised. Generally, there are three main types of polarisation exhibited by dielectrics [78], [79]:

- Electronic polarisation: this is often weak and occurs in all materials, where the relative permittivity ε_r is small, as shown in Figure 3.1. When an external electric field is applied to neutral atoms, the electron cloud of the atoms will be distorted, resulting in electronic polarisation. It is the only polarisation in hydrocarbons, hexane is an example [11], [78], [80].

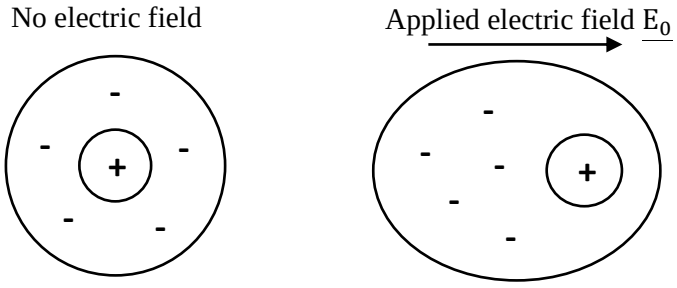

Figure 3.1 Electronic polarization in a dielectric material.

- Ionic polarisation: this is when two different atoms join together to construct an ionic bond, there is a transfer of electrons from one atom to another resulting in excess positive or negative charge on some of the atoms in a molecule. Sodium chloride NaCl is a typical ionic compound example. So, this type of polarisation occurs in crystalline solids, ion displacement by the applied $\underline{E_0}$ often gives strong polarisation (large ε_r), as shown below in Figure 3.2 [78], [81].

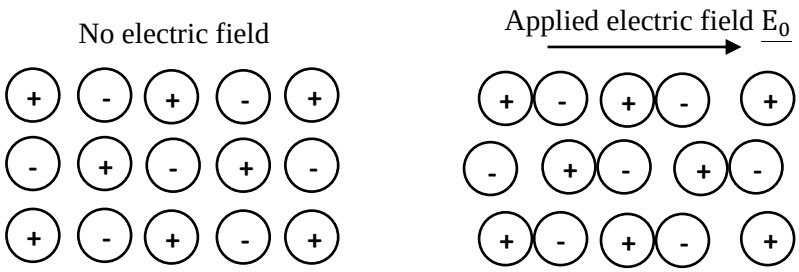

Figure 3.2 Ionic polarizations in a dielectric material.

- Orientation polarisation: this type of polarisation occurs in materials (liquids or gases) which are constructed from molecules known as "polar molecules" that have a permanent dipole moment even if there is no applied electric field because there is charge asymmetry within the molecule. When the electric field is applied, the molecular dipoles will be aligned with direction of electric field; water is a classic example. Figure 3.3 shows orientation polarisation [82], [83].

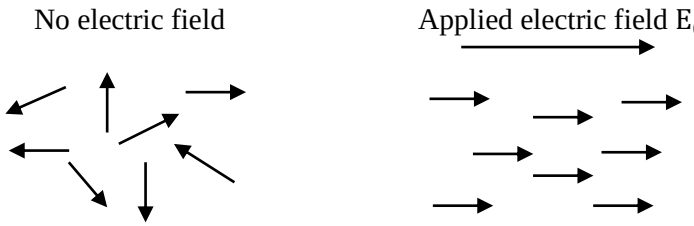

Figure 3.3 Orientation polarization in a polar dielectric material.

3.3. Dielectric Materials

The typical qualitative behaviour of permittivity (ε_1, and ε_2) is shown in Figure 3.4 as a function of frequency. The permittivity of a material is related to a variety of physical phenomena. Ionic conduction, dipolar relaxation, atomic depolarization, and electronic polarization are the main mechanisms that contribute to the permittivity of a dielectric material. In the low frequency range, ε_2 is dominated by the influence of ionic conductivity. The variation of permittivity in the microwave range is mainly caused by dipolar relaxation, and the absorption peaks in the infrared region and the above is mainly due to atomic and electronic polarizations [11].

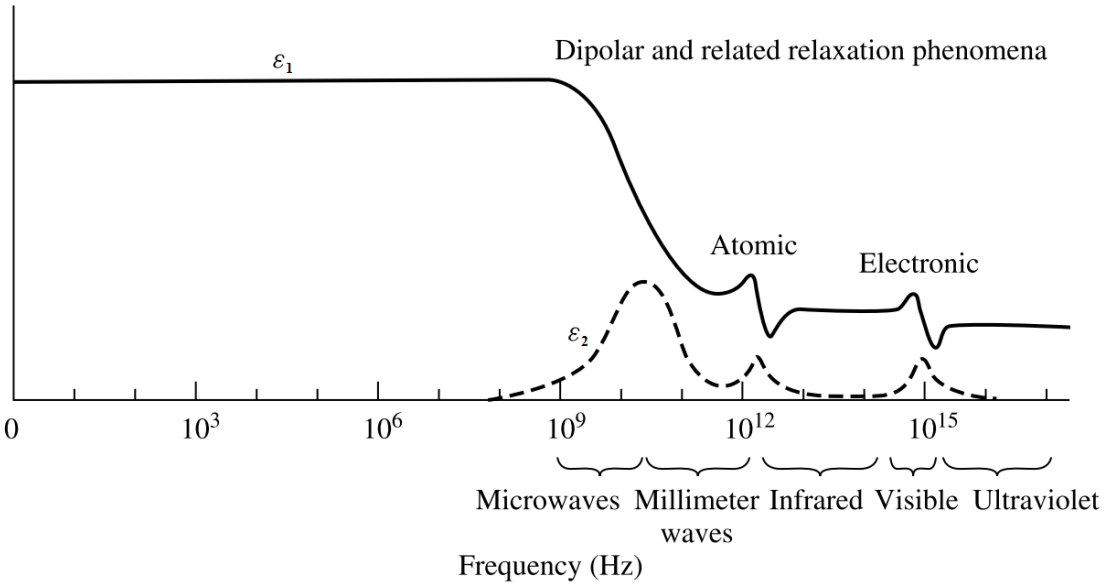

Figure 3.4 Frequency dependence of permittivity for a hypothetical dielectric [11].

3.4. The Polarization and Depolarization of a Dielectric Sample

When a dielectric material block, which contains no conduction electrons, is placed in a uniform $\underline{E_0}$ its electrons stay bound to its atoms but the electron cloud of each distorts. The dielectric thus becomes polarised (i.e. an electric dipole is induced on each atom), as shown in Figure 3.5 [78].

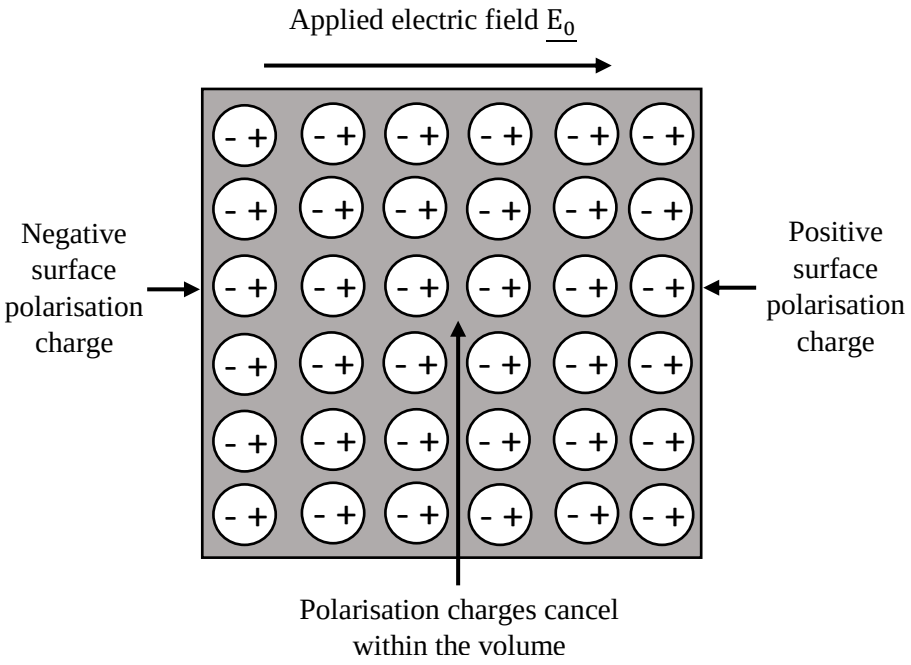

Figure 3.5 The polarisation of a dielectric material when placed in a uniform electric field.

The surfaces perpendicular to $\underline{E_0}$ develop polarisation charges and the internal electric filed $\underline{E_{in}}$ inside the dielectric material is reduced due to the depolarising field. So, the net electric field inside the dielectric is the difference between the applied electric field and the depolarised electric field $\underline{E_d}$ as shown in Figure 3.6 and described below in equation (3.1).

$$\underline{E_{in}} = \underline{E_o} - \underline{E_d} \tag{3.1}$$

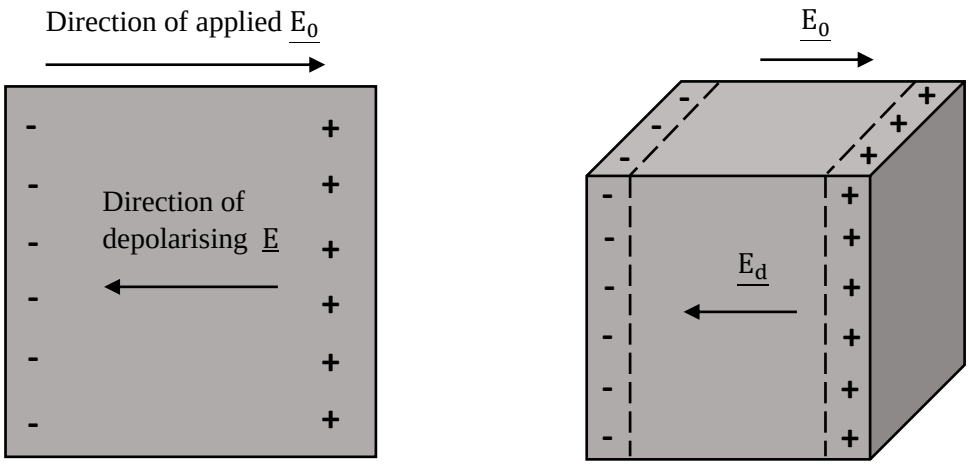

Figure 3.6 The direction of depolarising electric field is opposite to the applied field.

If there are n atoms per unit volume, each of dipole moment $\underline{p}$, the polarisation (dipole moment per unit volume) is

$$\underline{P} = n\underline{p} \tag{3.2}$$

The surfaces of the cube shown in Figure 3.4 develop surface polarisation charges $Q_{pol} = PS$ (S is the surface area of the cube ends) [78].

When an electric field $\underline{E_0}$ is applied to a dielectric material, the interaction between the material and field is described by the material's relative permittivity ε_r. The polarization per unit volume $\underline{P}$ is directly proportional to the internal electric field $\underline{E_{in}}$ via the relationship [84], [85], [86]

$$\underline{P} = (\varepsilon_r - 1)\varepsilon_0\underline{E_{in}} \equiv \chi_e\varepsilon_0\underline{E_{in}} \tag{3.3}$$

The quantity $\chi_e = (\varepsilon_r - 1)$ is a dimensionless quantity called the electric susceptibility of the dielectric, and quantifies how strongly a dielectric will polarize when placed in an applied $\underline{E_0}$ field. Losses can be considered by writing ε as the complex quantity

$$\varepsilon_r = \varepsilon_1 - j\varepsilon_2 \tag{3.4}$$

The quantity$(\varepsilon_r - 1)$ is proportional to the material's polarization and ε_2 to the power dissipation.

The magnitude of the internal electric field can be written

$$E_{in} \approx \frac{E_0}{1 + N\,\chi_e} \tag{3.5}$$

By substituting $\chi_e = (\varepsilon_r - 1)$ in above,

$$E_{in} \approx \frac{E_0}{1 + N(\varepsilon_r - 1)} \tag{3.6}$$

N is a dimensionless number called the depolarization factor, which depends on the object's shape and the direction of the applied field.

Assuming a uniform internal electric field and an external field consisting of the applied field plus a dipole term, the depolarization factor for a cylindrical shape is [87]:

1. N ≈ zero, when the applied electric field is parallel to the axis of a long cylinder.

So, the internal electric field is approximately equal to the applied electric field $E_{in} \approx E_0$ as shown in Figure 3.7 (a).

2. N $\approx \frac{1}{2}$, when the applied electric field is perpendicular to the axis of a long cylinder.

   So, the internal electric field is reduced to $E_{in} \approx \frac{2E_0}{1+\varepsilon_r}$. For water ($\varepsilon_r = 78$), then $E_{in} \approx 0.025E_0$, as shown in Figure 3.7 (b). i.e. the magnitude of internal electric field is much smaller than applied field E_0 when the relative permittivity ε >>1.

(a) (b)

Figure 3.7 The depolarization effects in dielectric cylindrical shape.

Hence, it is desirable to apply E along the long dimension of the material sample in applications that require maximum internal electric field inside material. Only in these instances is there maximum polarisation, and so maximum interaction between the applied electric field and the sample.

3.5. Ionic Conductivity

Ionic conductivity usually introduces losses into a material. The dielectric loss of a material can be described as a function of both dielectric loss (ε_{2d}) and conductivity (σ):

$$\varepsilon_2 = \varepsilon_{2d} + \frac{\sigma}{\omega\varepsilon_0} \tag{3.7}$$

The conductivity of a material may consist of many components due to different conduction mechanisms; the most common one in moist materials is the ionic conductivity. ε_2 at low frequencies is dominated by the effect of electrolytic conduction caused by free ions in the presence of a solvent, salt water being an example. As

presented by equation (3.7), the effect of ionic conductivity on the loss term is inversely proportional to operating frequency [11].

3.6. Debye Theory

Dipolar polarization results from the alignment of the molecule dipolar moment due to an applied filed. The dipolar polarization reaches its saturation value only after some time, quantified by a time constant called relaxation time τ [84].

According to Debye theory, the complex permittivity of a dielectric can be expressed as [11]:

$$\varepsilon_r = \varepsilon_{r\infty} + \frac{\varepsilon_{r0} - \varepsilon_{r\infty}}{1 + j\beta} \tag{3.8}$$

With

$$\varepsilon_{r\infty} = lim_{\omega\to\infty}\varepsilon_r \tag{3.9}$$

$$\varepsilon_{r0} = lim_{\omega\to 0}\varepsilon_r \tag{3.10}$$

$$\beta = \omega\tau \tag{3.11}$$

where τ is the relaxation time and ω is the operating angular frequency. Equation (3.8) shows that the dielectric permittivity due to Debye relaxation is mainly determined by three parameters ε_{r0}, $\varepsilon_{r\infty}$, and τ. At high frequencies, as the period of electric field $\boldsymbol{E}$ is much smaller than the relaxation time of the permanent dipoles; then the orientations of the dipoles are not affected by electric field $\boldsymbol{E}$ and remain random, so the permittivity at infinite frequency $\varepsilon_{r\infty}$ is a (small) real number. As $\varepsilon_{r\infty}$ is mainly due to electronic and atomic polarization, ε_{r0} is a real number. The static permittivity ε_{r0} decreases with increasing temperature because of the increasing disorder, and the relaxation time τ is inversely proportional to temperature as all the movements become faster at higher temperatures.

The real and imaginary parts of the permittivity are [84]:

$$\varepsilon_1 = \varepsilon_{r\infty} + \frac{\varepsilon_{r0} - \varepsilon_{r\infty}}{1 + \omega^2\tau^2} \tag{3.12}$$

$$\varepsilon_2 = \frac{(\varepsilon_{r0} - \varepsilon_{r\infty})\omega\tau}{1 + \omega^2\tau^2} \tag{3.13}$$

3.7. Equivalent Circuit of Debye Relaxation

The Debye relaxation model is the simplest model of dielectric relaxation behaviour according to equation (3.14). This behaviour is precisely similar to that of equivalent circuit shown in Figure 3.8 with relaxation frequency $f_r = 1/2\pi RC_1$. The Debye relaxation parameters of water at 25 ^{o}C are [88], [42]:

ε_{r0}=78.36

$\varepsilon_{r\infty}$=5.2

τ=8.27 ps

f_r=19.24 GHz, where $f_r = 1/2\pi\tau$

Assuming that there is a small capacitance cell with fixed electrodes and its capacitance is 1 pF when it is filled with air dielectric, when it is filled with de-ionized water, then the admittance of the cell as a function of frequency will be described over a wide band of frequencies by the equivalent circuit in Figure 3.8. This circuit is described by equation (3.14) when the above values for Debye relaxation parameters are substituted into it. So, the circuit is an analogue of the Debye relaxation of water, $C_1 \equiv (\varepsilon_{r0} - \varepsilon_{r\infty}) = 73.16$ pF, $C_2 \equiv \varepsilon_{r\infty} = 5.2$ pF, $R = 0.113\Omega$.

$$\varepsilon_r = \varepsilon_{r\infty} + \frac{\varepsilon_{r0} - \varepsilon_{r\infty}}{1 + jf/f_r} \tag{3.14}$$

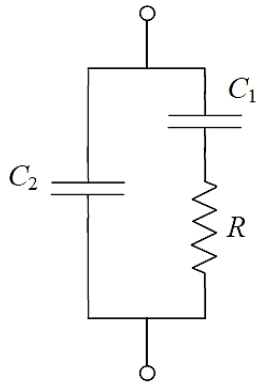

Figure 3.8 An equivalent circuit of Debye Relaxation.

In a linear and isotropic medium, the volume density of polarization is directly related to the applied electric field intensity as given in equation (3.3). Electric flux density $\underline{D}$, is related to the polarization per unit volume $\underline{P}$ and the electric field intensity $\underline{E}$ as follows [89]:

$$\underline{D} = \varepsilon_o \underline{E} + \underline{P} = \varepsilon \underline{E} = \varepsilon_o \varepsilon_r \underline{E} \tag{3.15}$$

A time-varying electric field induces two various types of currents in a material medium. Conduction current is produced by a net flow of free charges, and displacement current which is generated from the bound charges. The former is related to the electric field intensity by Ohm's law as follows:

$$\underline{J_c} = \sigma \underline{E} \tag{3.16}$$

where $\underline{J_c}$ is the conduction current density which is expressed in A/m, and σ is the material conductivity in S/m, while the displacement current is related to electric flux density by:

$$\underline{J_d} = j\omega \underline{D} \tag{3.17}$$

The total current density $\underline{J_T}$ is the sum of conduction and displacement current densities:

$$\underline{J_T} = \sigma \underline{E} + j\omega\varepsilon \underline{E} \tag{3.18}$$

$$\underline{J_T} = j\omega \underline{E}(\varepsilon_o \varepsilon_r - j\frac{\sigma}{\omega}) \tag{3.19}$$

$$\varepsilon = \varepsilon_1 - j\varepsilon_2 = \varepsilon_o \varepsilon_r - j\frac{\sigma}{\omega} \tag{3.20}$$

The permittivity for several common liquids (water, methanol, ethanol, and chloroform) has been plotted with the aid of equations (3.12) and (3.13) and Table 3.1 for Debye relaxation parameters [90], and [91] as shown in Figures 3.9, 3.10, 3.11, and 3.12 respectively.

Table 3.1

Debye relaxation model parameters of several liquids

Liquid	Temperature (^{0}C)	ε_{r0}	$\varepsilon_{r\infty}$	τ (ps)
Water	25	78.36	5.16	8.27
Methanol	25	32.5	5.6	51.5
Ethanol	25	24.3	4.2	163
Chloroform	25	4.7	2.5	7.96

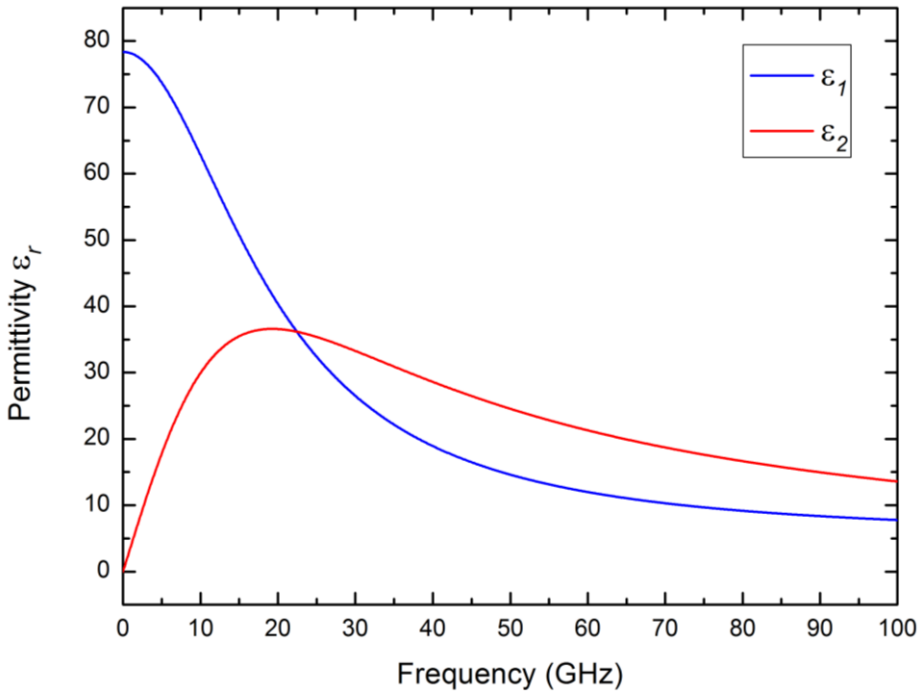

(a)

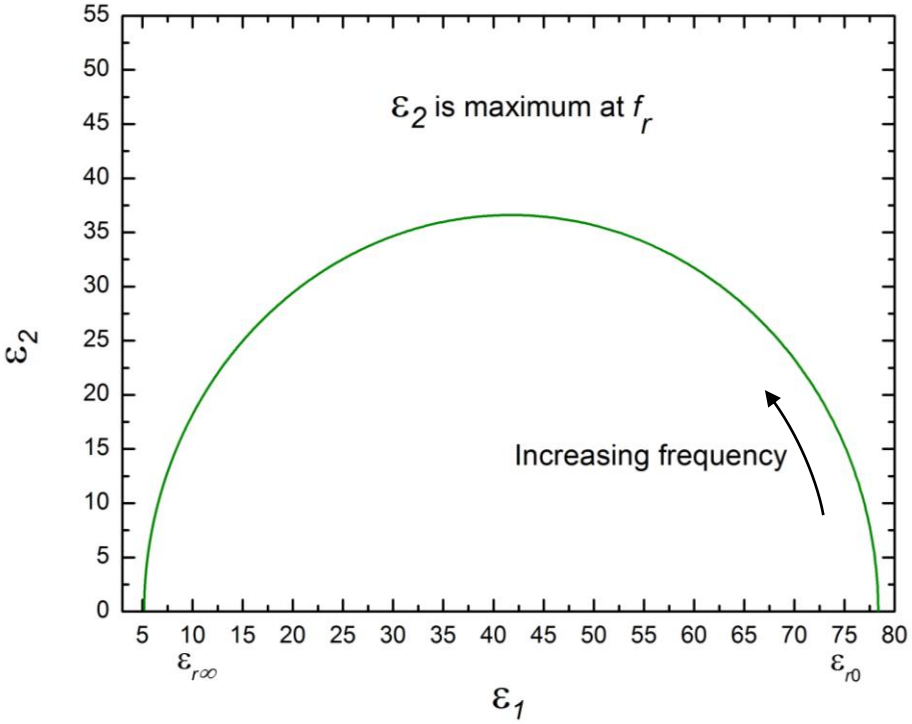

(b)

Figure 3.9 (a) A typical Debye relaxation response for water, (b) A 'Cole-Cole Plot' ε_2 is against ε_1 giving a semi-circular trace, frequency increases when moving anticlockwise around the trace.

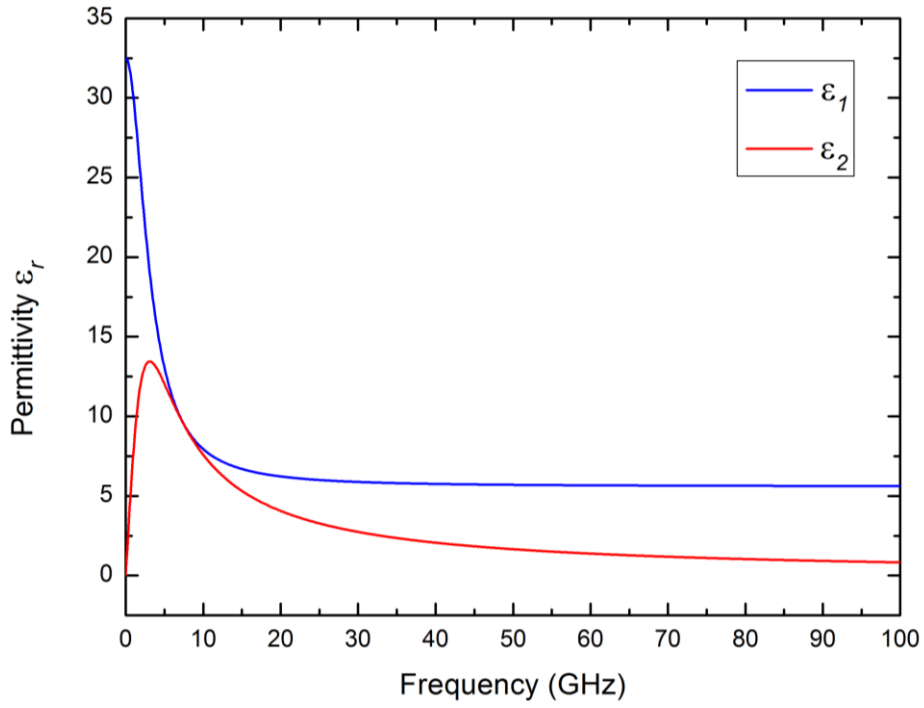

(a)

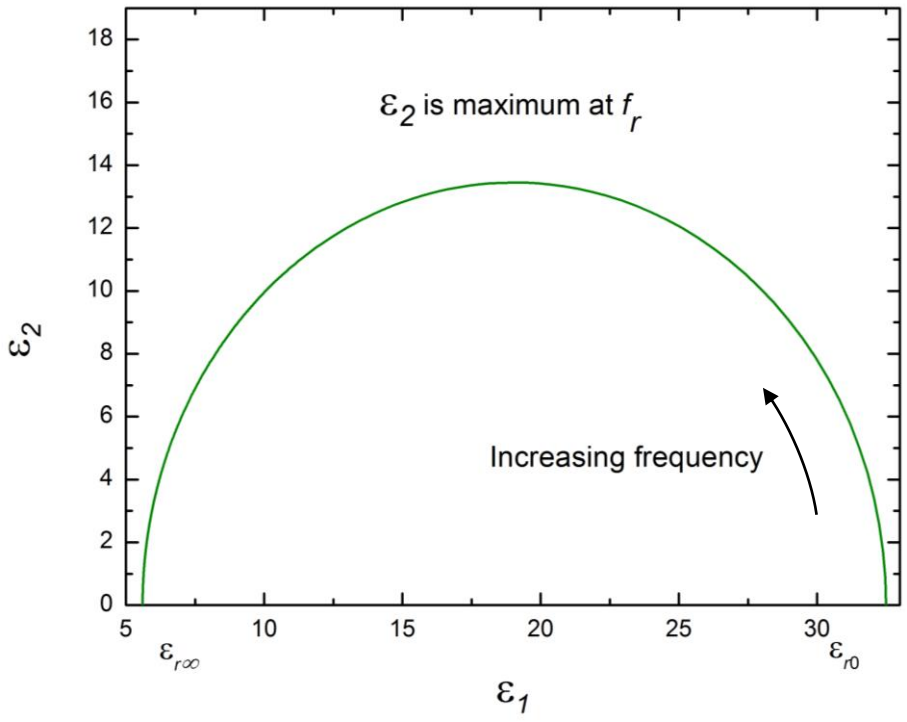

(b)

Figure 3.10 (a) A typical Debye relaxation response for methanol, (b) A 'Cole-Cole Plot' ε_2 is against ε_1 giving a semi-circular trace, frequency increases when moving anticlockwise around the trace.

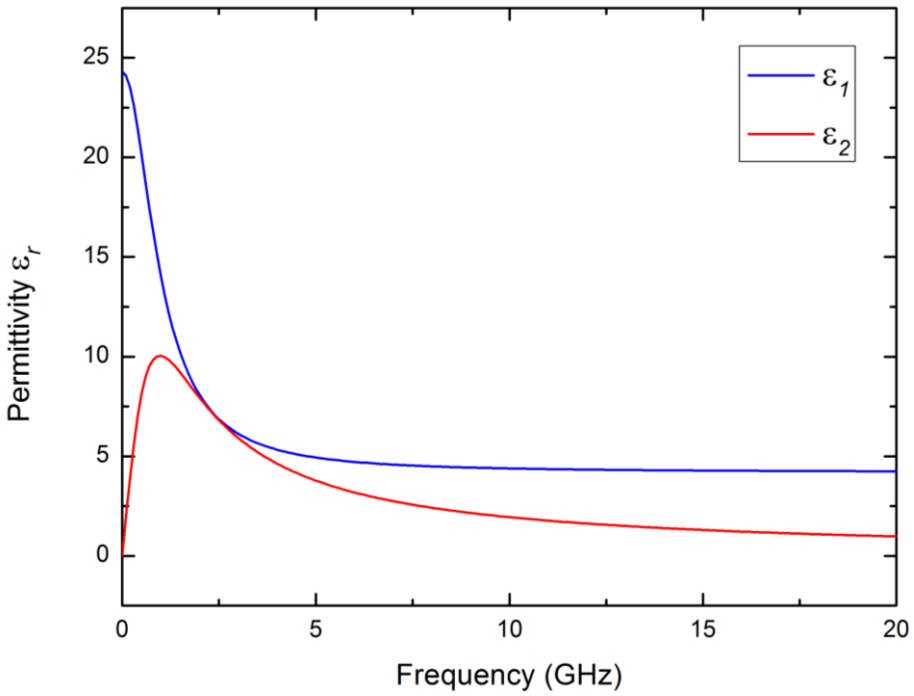

(a)

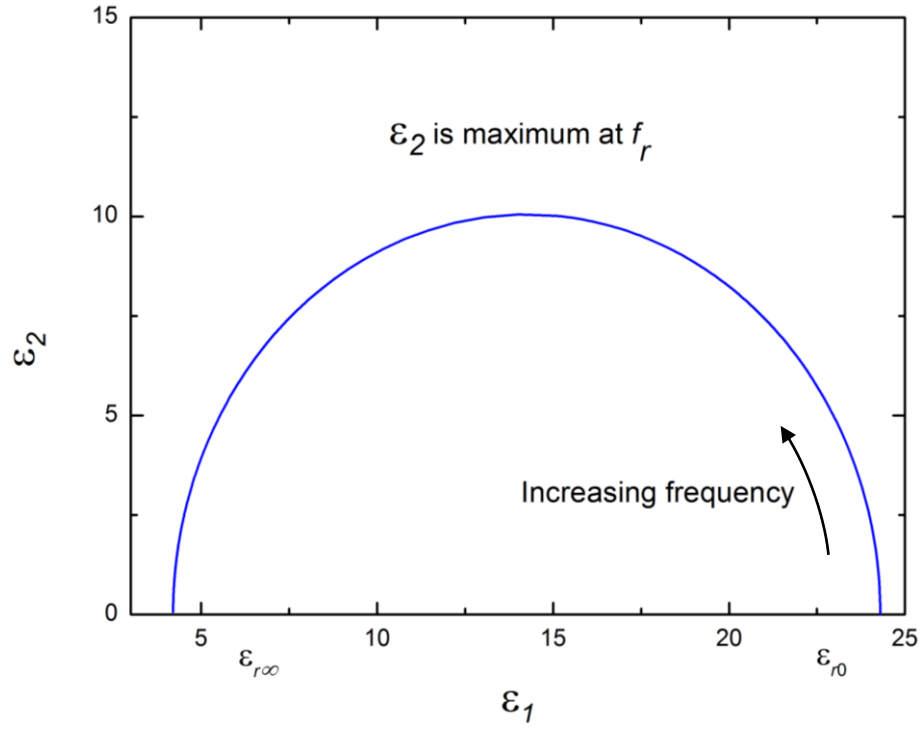

(b)

Figure 3.11 (a) A typical Debye relaxation response for ethanol, (b) A 'Cole-Cole Plot' ε_2 is against ε_1 giving a semi-circular trace, frequency increases when moving anticlockwise around the trace.

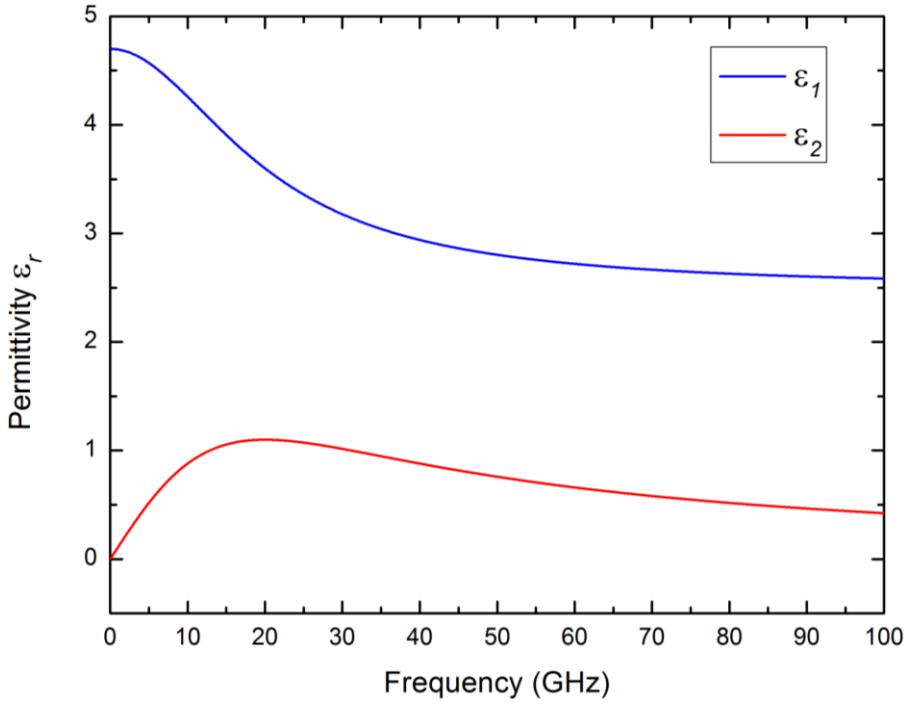

(a)

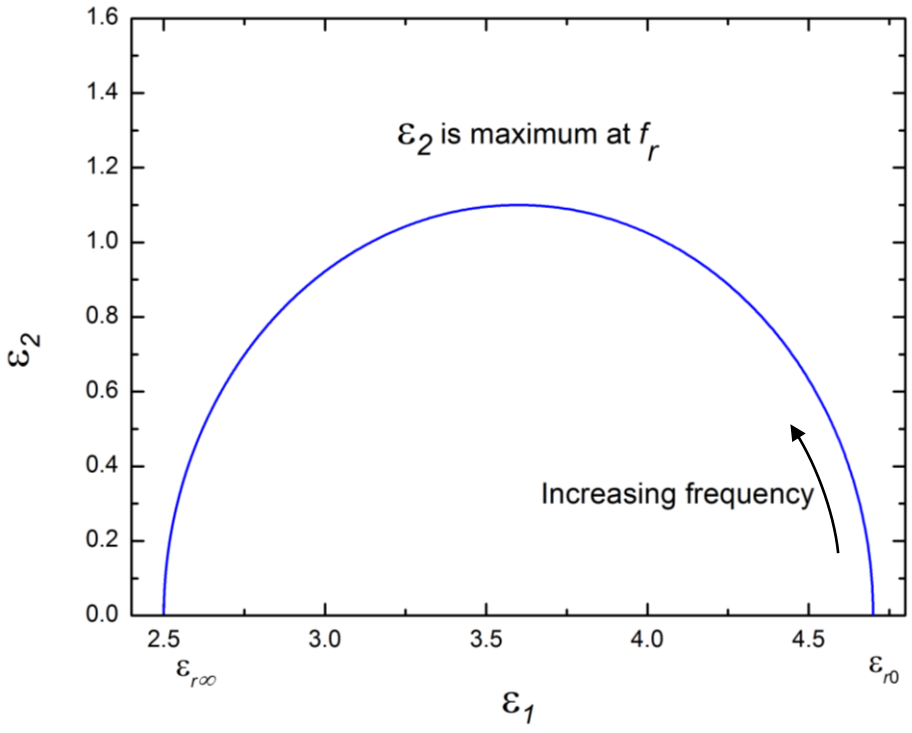

(b)

Figure 3.12 (a) A typical Debye relaxation response for chloroform, (b) A 'Cole-Cole Plot' ε_2 is against ε_1 giving a semi-circular trace, frequency increases when moving anticlockwise around the trace.

3.8. Categorization of Applicators and Sensors

Let's first distinguish between applicator and sensor; the first term is utilized for a device that applies RF or microwave energy into a material volume at a level sufficient to create either a permanent or temporary change in a material parameter or property. The change could be a rise in temperature, excluding moisture, improving a chemical reaction, ablation of a biological tissue, breakdown of gases to form plasmas, etc.; while the second term, sensor or probe, is used when the reason of the field interaction is just to obtain information from the material. Typically, the signal strength is far below the level needed to heat or excite the material [76].

Applicators and sensors can be categorized by useful field type, electric field (E-field) or magnetic field (H-field). Any high frequency applicator must contain both field types to satisfy Maxwell equations, but usually only one type of field is useful for the required purpose. Efforts to maximize the useful field type and minimize the unnecessary field type are sometimes a part of the design process. The absorbed power by a dielectric material is directly proportional to the electric field intensity inside material, so the electric field must be maximized for best power absorption. On the opposite side, there are many applications that require the maximum magnetic field in order to have the desired field interactions; these include eddy current induction, and magnetic hysteresis effect.

The simplest form of electric field applicator is the parallel plate, which is shown in Figure 3.14 (a) and its simplified equivalent circuit Figure 3.14 (b). This applicator is usually used for interfacing dielectrics and generally low conductivity materials with electric fields. Here, the electric field is set up always perpendicular to the two plates, while the magnetic field pattern circulates around the E-field.

On the other hand, the simplest form of magnetic field applicator/sensor is a current loop, which is shown in Figure 3.15 (a) and its equivalent circuit Figure 3.15 (b) which is represented by the inductance (varied slightly by the existence of the material load), and two resistors (one represents the resistance of the coil applicator, and the other one represents the material load loss). The magnetic field is generated from the flowing current in the applicator. There are many applications for magnetic field applicators

such as induction heating of conductive materials, hysteresis heating of ferrous metals at low (kHz) level frequencies, and magnetic heating of materials with magnetic loss. Furthermore, magnetic field sensors are used in different applications such as eddy current sensors, nuclear magnetic resonance (NMR), and magnetic resonance imaging (MRI) [76].

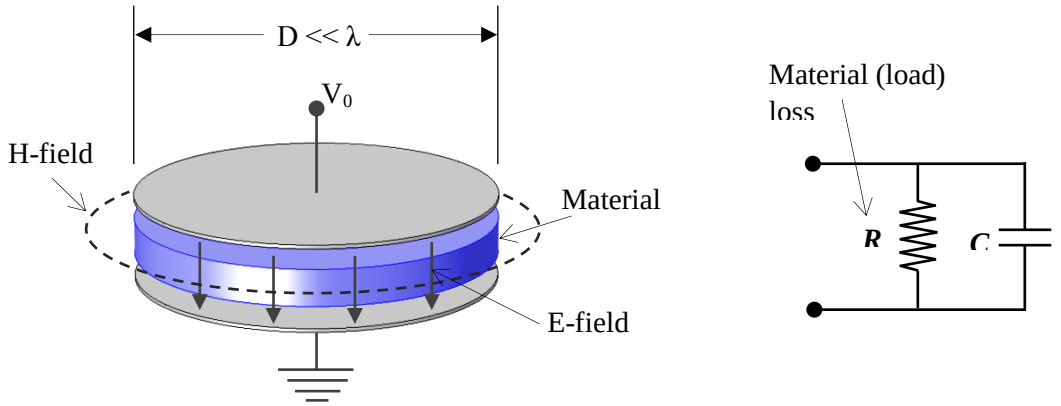

Figure 3.14 (a) Schematic of simple electric field applicator (parallel-plate applicator), (b) its equivalent circuit.

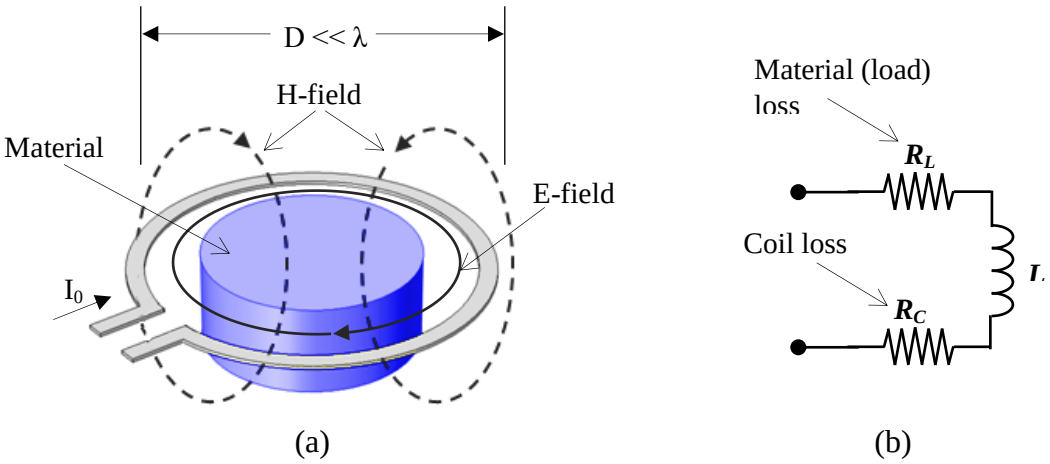

Figure 3.15 (a) Schematic of simple magnetic field applicator (single current loop), (b) its equivalent circuit.

CHAPTER FOUR
CYLINDRICAL MICROWAVE CAVITIES

4.1. Introduction

The most practical method of developing a high frequency and high quality resonator is to enclose the fields within a body whose dimensions are related to the desired wavelength of operation. Such a device is normally referred to as a resonant cavity, and it will support a series of modes, each corresponding to a unique distribution of fields. Most resonators are constructed from highly conducting materials. For ease of construction, one is generally limited to cylindrical or rectangular cavities, and in these cases one can easily determine the field distribution within the resonator [92].
Generally, a cylindrical cavity resonator can be constructed from circular waveguide shorted at both ends or built by a metallic closed cylindrical box. The basic concept of the circular waveguide and the cylindrical cavity resonator are similar [6]. The frequency which resonance occurs depends on the shape and size of the enclosed cavity [93].

Electric and magnetic energy is stored within the cavity, and power is dissipated in the metallic walls of the cavity as well as in the dielectric material that may fill the cavity. The dielectric material will affect the resonant frequency and Q-value and as a result, the microwave cavity resonator is the favourite structure used for dielectric or liquid materials permittivity measurements. This technique of material properties measurement is based on perturbation theory [6], [93]. The transverse modes used in the cavity resonators are the TE and TM modes, which will provide the different dimensions, resonant frequencies and Q-values.

Figure 3.1 shows the geometry of a cylindrical cavity, which implies that the waveguide must be an integer number of half-guide wavelengths long. A coupling device is needed to excite the microwave cavity where the energy is transmitted from external equipment to the cavity.

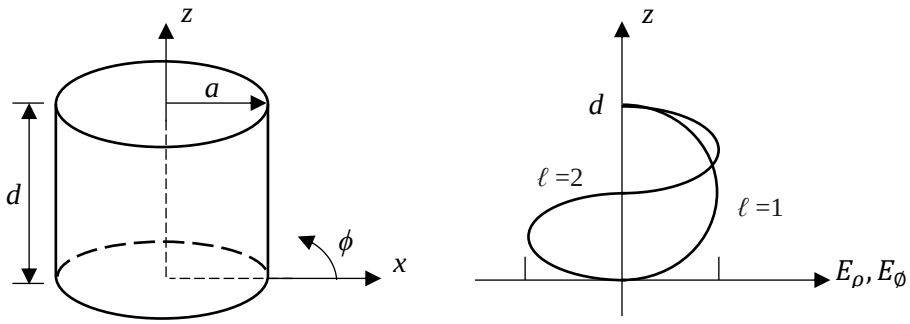

Figure 4.1 Cylindrical resonant cavity, and the electric field distribution for resonant modes with longitudinal mode number ℓ= 1 or ℓ= 2 [6].

4.2. The Microwave Cavity for the Electromagnetic Characterisation of Materials

The accurate characterization of a material's electromagnetic properties at microwave frequencies provides critical information needed for material and circuit design, modeling, manufacturing, research and quality control. Many measurement methods exist (parallel plates, coaxial probe, transmission line and free space, and resonant cavity), but which technique is best to use? The answer to this question depends upon many parameters [94] such as:

- Frequency of interest
- Expected value of ε_r
- Required measurement accuracy
- Material properties (homogeneous, isotropic)
- Material form (liquid, powder, solid, sheet)
- Sample size restrictions
- Destructive or non-destructive
- Contacting or non-contacting
- Temperature

A rectangular cavity has been used for determination of complex permittivity of dielectric samples placed in the E-plane [38].

4.3. Analysis of Cylindrical Microwave Cavity

Consider a cylindrical cavity of radius a and height d described by a cylindrical coordinate system (r, ϕ, z). Metallic boundaries that construct the cylindrical cavity have conductivity σ and the space bounded by them is filled by a dielectric medium with permittivity Ɛ and permeability μ. In a waveguide, Maxwell's equations are [6]:

$$\nabla \times \underline{E}(r,\omega) = -j\omega\mu\underline{H} \tag{4.1}$$

$$\nabla \times \underline{H}(r,\omega) = j\omega\varepsilon\underline{E} \tag{4.2}$$

where E is the vector electric field, H is the vector magnetic field, ω is the angular frequency, μ is the permeability and ε is the permittivity.

The dominant mode for short cylinders is the TM_{010} mode, but there are an infinite number of other modes at higher frequencies. Figure 4.2 illustrates some other transverse modes and resonant frequencies using a mode chart. Basically, the resonant frequency is related to the dimension of the cavity and the dielectric properties of the filling materials. The transverse electric fields $E_\rho, E_\emptyset$ of the TE_{nm} or TM_{nm} circular waveguide mode can be written as

$$\underline{E_t}(\rho,\emptyset,z) = \bar{e}(\rho,\emptyset)(A^+e^{-j\beta_{nm}z} + A^-e^{j\beta_{nm}z}) \tag{4.3}$$

where $\bar{e}(\rho,\emptyset)$ represents the transverse variation of the mode, and A^+ and A^- are arbitrary amplitudes of the forward and backward traveling waves. The propagation constant of the TE_{nm} mode is

$$\beta_{nm} = \sqrt{k^2 - \left(\frac{p'_{nm}}{a}\right)^2} \tag{4.4}$$

And the propagation constant of the TM_{nm} mode is

$$\beta_{nm} = \sqrt{k^2 - \left(\frac{p_{nm}}{a}\right)^2} \tag{4.5}$$

where $k = \omega\sqrt{\mu\epsilon}$ and

$$\beta_{nm}d = \ell\pi \tag{4.6}$$

for ℓ=0, 1, 2, 3, ……

The resonant frequency of the $TE_{nm\ell}$ mode is

$$f_{nm\ell} = \frac{c}{2\pi\sqrt{\mu_r \varepsilon_r}} \sqrt{\left(\frac{p'_{nm}}{a}\right)^2 + \left(\frac{\ell\pi}{d}\right)^2} \tag{4.7}$$

and the resonant frequency of the $TM_{nm\ell}$ mode is

$$f_{nm\ell} = \frac{c}{2\pi\sqrt{\mu_r \varepsilon_r}} \sqrt{\left(\frac{p_{nm}}{a}\right)^2 + \left(\frac{\ell\pi}{d}\right)^2} \tag{4.8}$$

$f_{nm\ell}$ is the operation frequency of the cylindrical cavity resonator.

c is the speed of light= 3×10^8 m/s

μ_r is the relative permeability of the material inside the cylindrical cavity resonator

ε_r is the relative permittivity of the material inside the cylindrical cavity resonator

d is the height of the cylindrical cavity resonator

and a is the radius of the cylindrical cavity resonator.

The values of $p_{nm}$and p'_{nm} are listed below in Table 4.1 and Table 4.2 respectively [6].

Table 4.1

Values of p_{nm}

n	1	2	3	4
0	2.4048	5.5201	8.6537	11.7915
1	3.8317	7.0156	10.1735	
2	5.1356	8.4172	11.6198	
3	6.3802	9.761		
4	7.5883	11.0647		
5	8.7715			
6	9.9361			
7	11.0864			

Table 4.2

Values of p'_{nm}

n	1	2	3	4
0	3.8317	7.0156	10.1735	13.3237
1	1.8412	5.3314	8.5363	11.706
2	3.0542	6.7061	9.9695	
3	4.2012	8.0152	11.3459	
4	5.3175	9.2824		
5	6.4156	10.5199		
6	7.5013	11.7349		
7	8.5778			
8	9.6474			
9	10.7114			
10	11.7709			

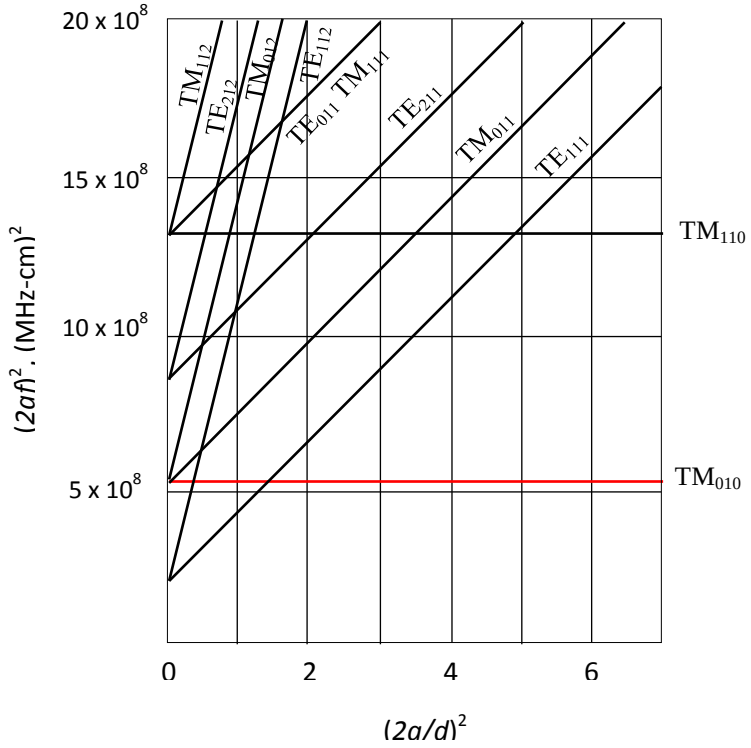

Figure 4.2 Resonant mode chart for a cylindrical cavity.

4.4. Excitation Devices

The excitation or coupling devices are used to transfer energy from the feedline to the resonator. The required coupling level between a resonator and its attached circuitry depends on the application. For example, a waveguide cavity used as a frequency meter is usually loosely coupled to its feed guide in order to keep high Q and good accuracy. A resonator used in an oscillator or tuned amplifier may be strongly coupled in order to achieve maximum power transfer [6].

The ratio of the absorbed power at the resonant frequency to the reflected power is defines as the strength of the coupling. The coupling strength can be adjusted by varying the size and/or shape of the device. Increasing the coupling increases the radiation loss, decreasing the cavity quality factor Q and sensitivity [92].
The coupling methods, coupling holes, coupling probe, and coupling loop will be introduced below:

Aperture coupling: these structures are typically designed using a waveguide as the feeding transmission line, as shown in Figure 4.3. The tangential magnetic field or normal electric field will penetrate the aperture and couple to the resonant mode depending on the location of the aperture in the waveguide. The coupling strength depends upon the location of the aperture with respect to the field of the resonant mode and the orientation of the field lines.

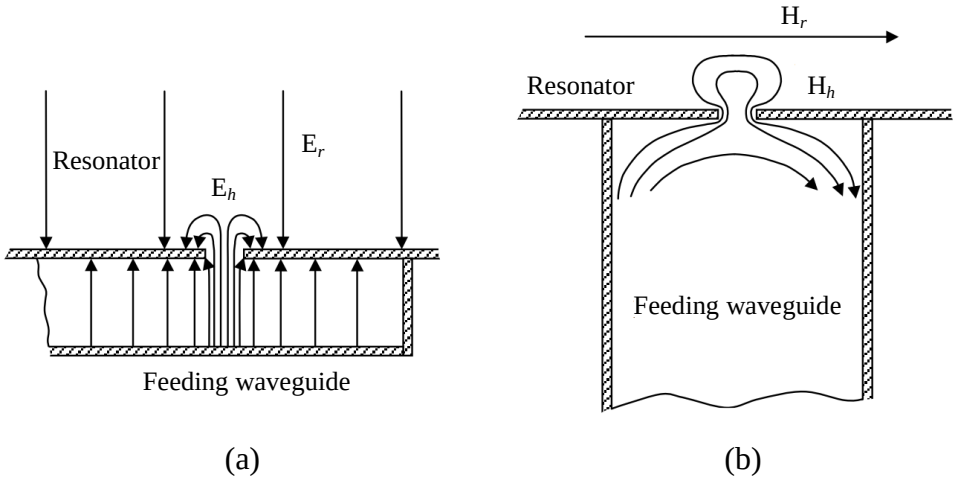

Figure 4.3 Aperture coupling, (a) electric, (b) magnetic [95].

Probe coupling: this is performed by extending the centre conductor of a feeding coaxial cable a small distance into the cavity resonator, which is shown in Figure 4.4. The length of the probe should be small compared to the wavelength, and the input impedance is therefore nearly equivalent to that of an open circuit. The current in the probe is small, but the voltage creates an electric field between the probe and the adjacent wall of the resonator. The field radiates energy into the resonator like a small monopole antenna. The probe couples to the electric field that is perpendicular to the wall at the location of the probe. The coupling is stronger the closer to a field maximum the probe is located.

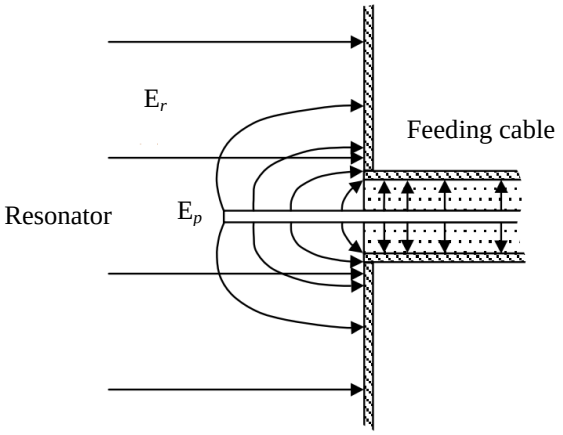

Figure 4.4 Probe coupling [95].

Loop coupling: thus is performed by extending the centre conductor of a feeding coaxial cable and forming a short circuit loop, either with the cavity wall or the outer conductor of the cable, as shown in Figure 4.5 for loop coupling to a cavity resonator. The strength of the coupling depends on the surface area of the loop in the plane perpendicular to the H-field lines on the inner surface of the cavity [76].

The radius of the loop is small compared to the wavelength, therefore the voltage induced across it is nearly zero but the current is large, and the input impedance is nearly equivalent to that of a short circuit. The current generates a magnetic field that radiates like a magnetic dipole tangential to the wall. The radiation couples to the magnetic field of a resonance mode that is tangential to the wall and perpendicular to the plane of the loop. Therefore the orientation of the loop is also important.

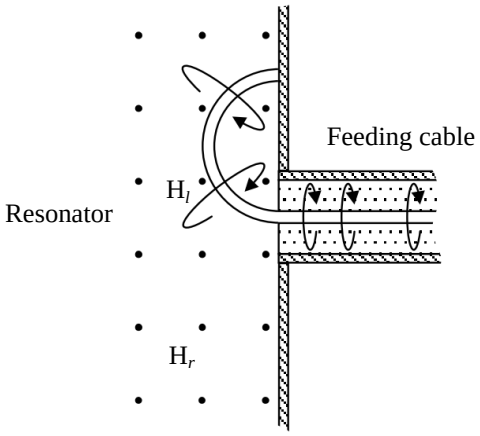

Figure 4.5 Loop coupling [95].

4.5. The Coupling Coefficient

The coupling coefficient is a dimensionless quantity that is a measure of the level of coupling between a resonator and a feed. The maximum power transfer between a resonator and a feed line is achieved by matching them at the resonant frequency; the resonator is then said to be critically coupled to the feed. These concepts will be illustrated by considering the series resonant circuit shown in Figure 4.6 [6].

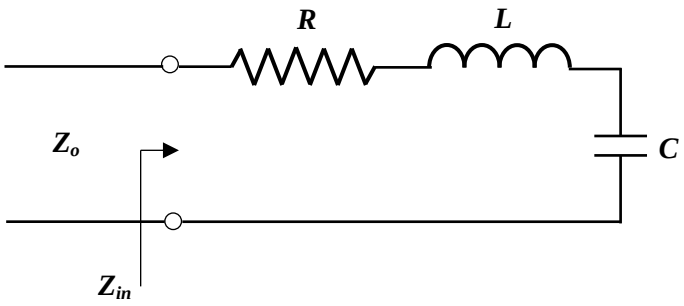

Figure 4.6 A series resonant circuit coupled to a feedline.

The input impedance near resonance of the series resonant circuit is given by

$$Z_{in} = R + j2L\Delta\omega = R + j\frac{2RQ\Delta\omega}{\omega_o} \tag{4.9}$$

The unloaded Q is

$$Q = \frac{\omega_o L}{R} \tag{4.10}$$

At resonance, $\Delta\omega = 0$, so the input impedance is $Z_{in} = R$. In order to match the resonator to the feedline of characteristic impedance Z_0, we should have:

$$R = Z_o \tag{4.11}$$

In this case the unloaded Q is

$$Q = \frac{\omega_o L}{Z_o} \tag{4.12}$$

The external Q is defined to be

$$Q_e = \frac{\omega_o L}{Z_o} = Q \tag{4.13}$$

This shows that the external Q and unloaded Q are equal under the condition of critical coupling.

The coupling coefficient, g, can be defined as:

$$g = \frac{Q}{Q_e} \tag{4.14}$$

This can be applied to both series ($g = Z_o/R$) and parallel ($g = R/Z_o$) resonant circuits, Three cases can be distinguished:

1. $g < 1$: The resonator is said to be under-coupled to the feedline.
2. $g = 1$: The resonator is critically coupled to the feedline.
3. $g > 1$: The resonator is said to be over-coupled to the feedline.

The dimensionless coupling coefficients are defined as [96]:

$$g_1 = f_o k_1^2 Q \tag{4.15}$$

$$g_2 = f_o k_2^2 Q \tag{4.16}$$

where K_1 and K_2 are constants, which depend on the geometrical properties of the coupling structures. Usually symmetric coupling is assumed (identical input and output coupling structure, that means, $g = g_1 = g_2$), to simplify the correction procedures needed to account for the effects of coupling.

4.6. Cavity Perturbation

Cavity perturbation is defined as changing of a cavity's resonant frequency and quality factor owing to some extrinsic effect, e.g. when the cavity resonator volume changes or when introducing a small dielectric sample [6], [97]. From this phenomenon, the electric and magnetic properties can be measured for a certain sample by inserting it into the cavity and by measuring the change in the cavity resonance frequency and quality factor [39]. As described by Maxwell's equations below, $\bar{E}_o$ and $\bar{H}_o$ represents the electric field and magnetic field respectively of the original cavity, $\bar{E}$ and $\bar{H}$ represents the fields of the perturbed cavity [6], [39], [98]:

$$\nabla \times \underline{E_o} = j\omega_o \mu \underline{H_o} \tag{4.17}$$

$$\nabla \times \underline{H_o} = j\omega_o \varepsilon \underline{E_o} \tag{4.18}$$

$$\nabla \times \underline{E} = -j\omega(\mu + \Delta\mu)\underline{H} \tag{4.19}$$

$$\nabla \times \underline{H} = -j\omega(\varepsilon + \Delta\varepsilon)\underline{E} \tag{4.20}$$

where ω_o and ω are the resonant frequency of the original cavity and the perturbed cavity, while $\Delta\varepsilon$ and $\Delta\mu$ are the change in in permittivity and permeability.

The final equation for the change in resonant frequency due to material perturbations is obtained by assuming $\Delta\varepsilon$ and $\Delta\mu$ are small, then the change in resonant frequency can be expressed as [6]:

$$\frac{\omega - \omega_o}{\omega_o} = \frac{-\int_{V_o}(\Delta\varepsilon \left|\underline{E_o}\right|^2 + \Delta\mu \left|\underline{H_o}\right|^2)dv}{\int_{V_o}(\varepsilon \left|\underline{E_o}\right|^2 + \mu \left|\underline{H_o}\right|^2)dv} \tag{4.21}$$

Also, the quality factor is defined as

$$Q = \frac{2\pi \times average \text{ energy stored in the resonator}}{average\ energy\ dissipated\ during\ one\ cycle} \tag{4.22}$$

$$Q = \frac{\omega \times \text{stored energy}}{\text{power dissipated}} \tag{4.23}$$

i.e.

$$Q = \frac{\omega \mathrm{U}}{P} \tag{4.24}$$

So, the change in Q is expressed as the difference between quality factor before cavity perturbation and after perturbation when the sample is present.

$$\Delta Q = Q_o - Q \tag{4.25}$$

$$\Delta Q = \frac{\omega_o U_o}{P_o} - \frac{\omega\, U}{P} \tag{4.26}$$

However, the change in resonant frequency is proportional to sample permittivity and sample polarisability, where the perturbation theorem (in electric or magnetic field) is dependent on several parameters, specifically the mode of excitation, the resonator geometry, and the sample polarisability which is affected by both its dielectric properties and its shape as discussed in CHAPTER THREE.

4.7. Scattering Parameters

Scattering parameters are widely used at RF and microwave frequencies for component modelling, component specification and circuit and network design [99]. The response of any network to external stimulus can be represented by the diagram shown in Figure 4.7. The waves incident at port 1 and port 2 are indicated as a_1 and a_2 respectively, and the waves reflected or emerging from port 1 and port 2 are indicated as b_1 and b_2 respectively. The parameters (a_1, a_2, b_1, and b_2) can be voltage or current, the relationship between the incident wave [a] and reflected wave [b] are normally represented by scattering parameters [S] [11]:

$$[b] = [S]\,[a] \tag{4.27}$$

where $[a] = [a_1, a_2]^{\mathrm{T}}$, $b = [b_1, b_2]^{\mathrm{T}}$, and the scattering matrix [S] is described as:

$$[S] = \begin{bmatrix} S_{11} & S_{12} \\ S_{21} & S_{22} \end{bmatrix} \tag{4.28}$$

For a scattering parameter S_{ij}, if a_i=0 ($i \neq j$), according to equation (4.27), then:

$$S_{jj} = \frac{b_j}{a_j} \qquad (j = 1, 2) \tag{4.29}$$

Equation (4.29) shows that when port *j* is connected to a source and the other port is connected to a matched load, the reflection coefficient at port *j* is equal to S_{jj}:

$$\Gamma_j = S_{jj} = \frac{b_j}{a_j} \tag{4.30}$$

On the other hand,

$$S_{ij} = \frac{b_i}{a_j} \qquad (i \neq j; i = 1, 2; j = 1, 2) \tag{4.31}$$

Equation (4.31) shows that when port *j* is connected to a source and the other port is connected to a matched load, the transmission coefficient from port *j* to port *i* is equal to S_{ij}:

$$T_{j \to i} = S_{ij} = \frac{b_i}{a_j} \tag{4.32}$$

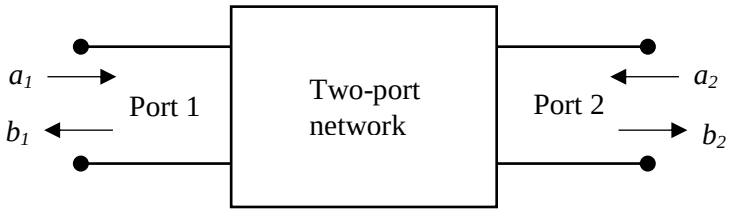

Figure 4.7 A two-port network

Electromagnetic energy can be coupled to the cavity resonator (which represents an impedance) either to the electric field using an open circuit transmission line (capacitive coupling) or to the magnetic field by a short circuit transmission line (inductive coupling).

Figure 4.8 shows the equivalent circuit for a cavity resonator. It is coupled inductively where L_1 and L_2 are mutual inductances, and Z_0 is the characteristic impedance of the coupling lines which is usually 50 Ω [96].

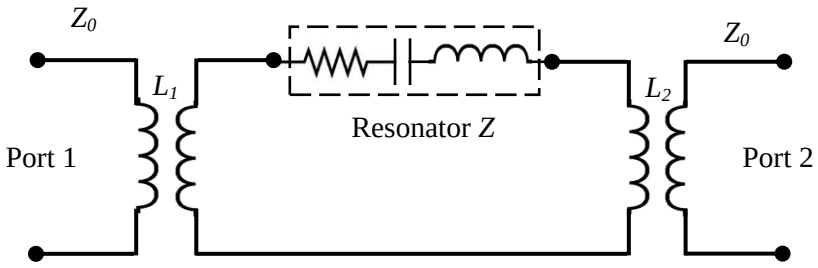

Figure 4.8 Cavity resonator equivalent circuit, inductive coupling with L_1 and L_2 mutual inductances.

Generally, loop coupling is used and the mutual inductance is determined by the geometrical dimensions of the coupling loops. For this circuit:

$$S_{21}(f) = \frac{2\sqrt{g_1 g_2}}{1 + g_1 + g_2 + j2Q_o \frac{f - f_o}{f_o}} \tag{4.33}$$

where g_1, and g_2 are the dimensionless coupling coefficients and can be defined as $\frac{\omega_0^2 L_1^2}{Z_0 R} = \frac{\omega_0 L_1^2 Q_0}{L}$, and $\frac{\omega_0^2 L_2^2}{Z_0 R} = \frac{\omega_0 L_1^2 Q_0}{L}$ respectively and f_o is the resonant frequency.

The power transmission coefficient is

$$P_{tr}(f) = |S_{21}|^2 = \frac{4g_1 g_2}{(1 + g_1 + g_2)^2 + 4Q_o^2 \left(\frac{f - f_o}{f_o}\right)^2} \tag{4.34}$$

For single port measurements, the equivalent resonator circuit is shown in Figure 4.9, where the cavity is only coupled to by a single port and reflection measurements are taken.

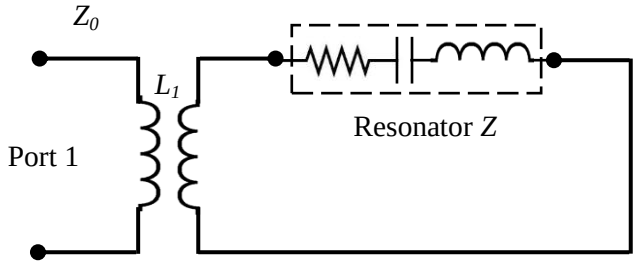

Figure 4.9 Cavity resonator equivalent circuit for single port measurements.

The voltage reflection coefficient is then

$$S_{11}(f) = \frac{1 - \mathrm{g} + j2Q_o\left(\frac{f - f_o}{f_o}\right)}{1 + \mathrm{g} + 2jQ_o\left(\frac{f - f_o}{f_o}\right)} \tag{4.35}$$

The power reflection coefficient is

$$P_{re}(f) = |S_{11}|^2 = \frac{(1 - \mathrm{g})^2 + 4Q_o^2\left(\frac{f - f_o}{f_o}\right)^2}{(1 + \mathrm{g})^2 + 4Q_o^2\left(\frac{f - f_o}{f_o}\right)^2} \tag{4.36}$$

4.8. Cylindrical Microwave Cavity Simulation

COMSOL Multiphysics® 4.4 was used to perform 3D simulations of the cylindrical cavity microwave fields according to the dimensions in Figure 4.10, a = 46 mm, d = 40 mm, and axial sample hole radius r = 3 mm. Aluminium has been used for the cavity construction material for simulation as well as all experimental cavities.

The wave equation in the frequency domain was computed in the electromagnetic wave model as described in the software as:

$$\nabla \times \mu_r^{-1}\left(\nabla \times \underline{E}\right) - k_0^2\left(\varepsilon_r - \frac{j\sigma}{\omega\varepsilon_0}\right)\underline{E} = 0 \tag{14}$$

where μ_r is the relative permeability, ε_r the relative permittivity and σ the electric conductivity of the material; ε_0 is the permittivity of the vacuum, k_0 is the wave number in free space, and ω the wave angular frequency. The impedance boundary condition is used for the aluminium surfaces in order to calculate their losses. The simulation boundary is the inside surface of the aluminium outer cavity. Coaxial ports were used to feed the electromagnetic energy to the resonator.

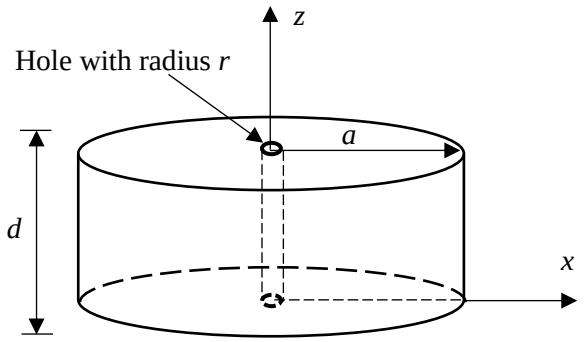

Figure 4.10 Schematic of a cylindrical cavity resonator which has been simulated using COMSOL software.

Figure 4.11 shows the flowchart for the model simulation procedures used in COMSOL.

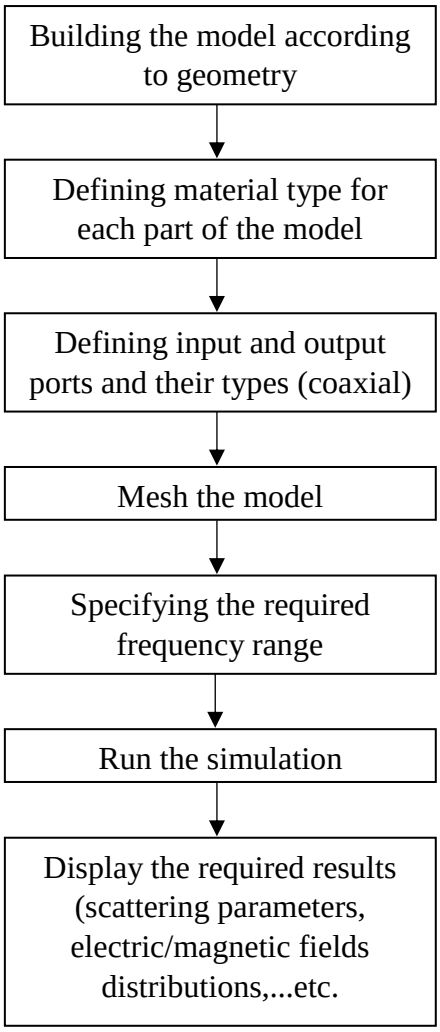

Figure 4.11 Flowchart for the model simulation using COMSOL software.

Figure 4.12 shows the simulation results for the electric (E) field (a) 3D view and (b) side view, and the magnetic (H) field (c) 3D view and (d) side view for the dominant mode TM_{010}. The operating resonant frequency is 2.494 GHz, which agrees perfectly with the theoretically calculated value.

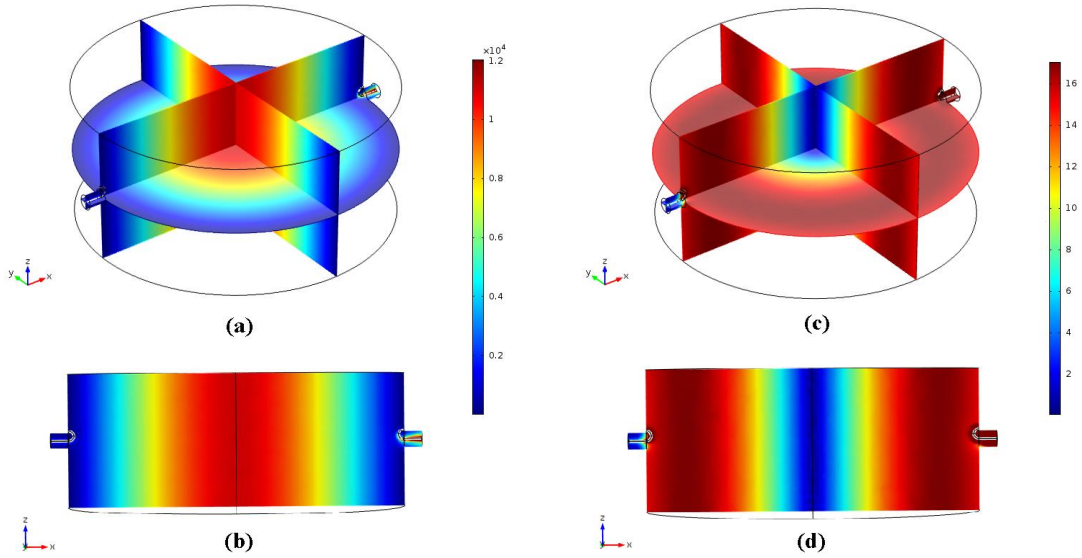

Figure 4.12 Simulation of the cylindrical cavity resonator TM_{010}, E-Field V/m (a) 3D view and (b) side view, H-Field A/m (c) 3D view and (d) side view.

The material under test MUT is inserted vertically through an access hole on the top surface on the cavity, where the electric field is at a maximum. As a result, the resonant frequency will be shifted and the quality factor will reduced as discussed in section 4.6. Figure 4.13 presents the COMOSL simulation S_{21} for the cylindrical cavity resonator before and after insertion of a PTFA tube (outer diameter is 2 mm and inner diameter is 1.2 mm) filled with water.

The real and imaginary values of the complex permittivity can be extracted from the change in both resonant frequency and quality factor using the two equations 4.37 and 4.38 below [100], [101], which are derived from the cavity perturbation equations for a sample on axis, with its length aligned parallel with the electric field (as for the TM_{010} mode):

$$\varepsilon_1 - 1 = \left(\frac{f_o - f_s}{f_o}\right)\left(\frac{2V_{eff}}{V_s}\right) \tag{4.37}$$

$$\varepsilon_2 = \Delta\left(\frac{1}{Q}\right)\left(\frac{V_{eff}}{V_s}\right) \tag{4.38}$$

where f_o and f_s are the resonant frequencies without and with sample respectively, V_s is the sample volume within the cavity and V_{eff} is the effective cavity volume. This latter quantity is the effective space filled by the electric field energy, and for the TM_{010} mode can be shown to be about 26.9% of the cylinder volume.

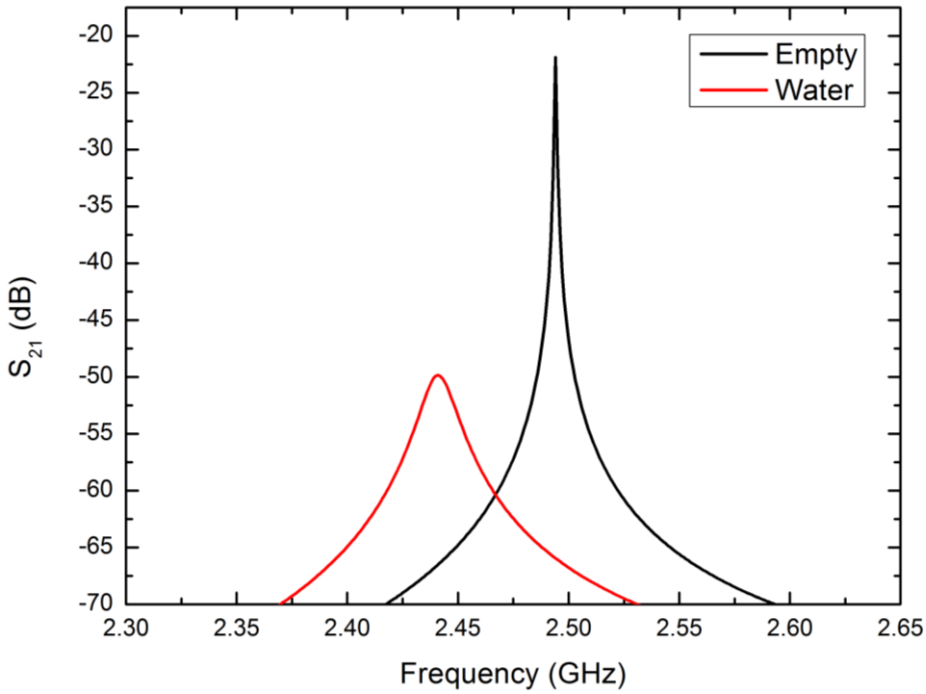

Figure 4.13 Simulated $|S_{21}|$ of the cylindrical cavity when it is empty and when with a PTFA tube filled with water (using COMSOL Software).

4.9. Re-entrant Microwave Cavity

The re-entrant microwave cavity (RMC) is a very attractive sensor for dielectric characterisation of small liquid volumes (ml to µl volumes) due to the high concentration of electric field in its gap region. The structure is also easy to manufacture, and retains a high quality factor Q (~3000) even when machined from

metals such as aluminium. Whilst the electric field is very high in the narrow gap region, the associated magnetic field is small and spread over a much larger volume, leading to low surface loss on the exposed metal surfaces, hence the high Q. These desirable features (high Q, high concentration of electric field in the gap) contribute to a high performance dielectric sensor, as we will now demonstrate.

A re-entrant cavity is a three-dimensional structure whose metallic boundaries extend into the interior of the cavity [4]. The general type of re-entrant cavity is circular cylindrical cavity with a small gap in the interactive region at the central part of the cavity. A cross section of the re-entrant cavity is shown in Figure 4.14 (a) The resonator could also be designed in the form of a double re-entering cavity as shown in Figure 4.14 (b). All the relationships for the single re- entering cavity can be easily adapted to the double re-entering case, but the practical realisation of the single re-entering resonator is much easier [102], [103].

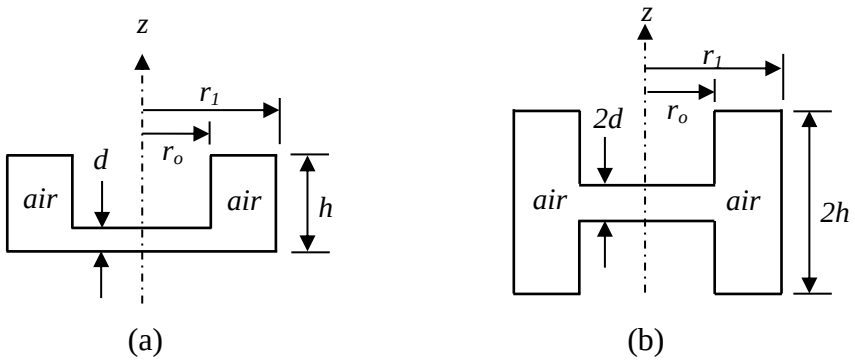

Figure 4.14 Re-entrant cavities [102], the air space is bounded by the cavity metal.

Re-entrant cavities have been studied and used widely for a variety of applications, in radio and microwave communications systems, dielectric properties measurements, and medical applications [45], [104]-[107] due to their simple mechanical construction and wide tuning range, with the narrow gap having the effect of reducing the frequency and focusing the electric field [108].

4.10. Modelling Circuit Parameters for Re-entrant Cavity

As can be seen from the schematic field distributions of Figure 4.15, there is excellent separation between the regions of maximum electric and magnetic fields in a RMC. Re-entrant cavities can be modelled using a lumped-element approximation. The electric field concentrates in the gap between the centre post and the cavity wall and its direction from the inner post points to the cavity wall. If the gap region is small, then the electric field in the gap will be approximately uniform and the magnetic field will be infinitesimally small there, increasing linearly with distance off-axis. This region looks like a parallel-plate capacitor; its capacitance being inversely proportional to the gap width. The purely circumferential magnetic field is generated from surface currents flowing in the directions shown in Figure 4.15, with a displacement current across the gap. The largest magnetic field strength is near the short-circuit-end, at the opposite end of the gap (as shown in Figure 4.15) [4], [102], and [109].

An accurate analysis can be made in the limit when the gap dimension is small compared with the other dimensions of the cavity and with the resonant wavelength λ_o. In this case the concept of lumped circuit elements becomes meaningful. In our re-entrant cavity, we position the hole for the sample tube to be axial, though the post and passing through the gap region where the electric field magnitude is highest, to ensure the greatest sensitivity for dielectric measurement.

As noted, the electric field concentrates in the gap between the centre post and the cavity wall and is directed perpendicular to the gap regions. If the gap region is small, then the electric field in the gap will be approximately uniform and the magnetic field will be infinitesimally small near the axis.

The equivalent circuit of the lumped element mode of the RMC is shown in Figure 4.16, with C_0 being the capacitance of the gap region and C_1 the capacitance associated with charge leakage onto the outside surface of the central post [109].

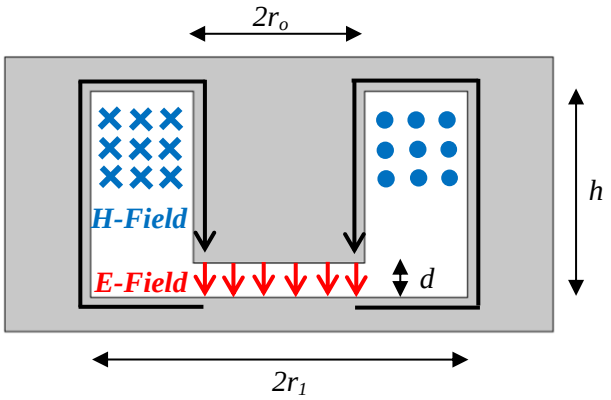

Figure 4.15 Cross section of a re-entrant cavity, showing schematically the distribution of electric and magnetic fields.

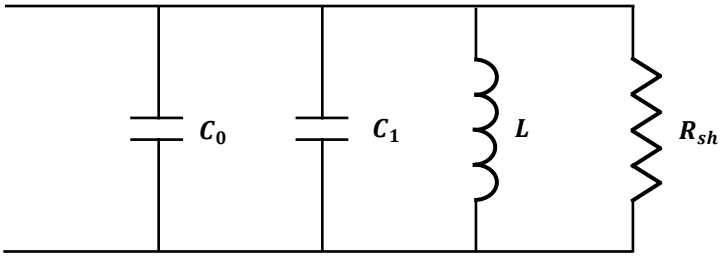

Figure 4.16 Equivalent lumped circuit for re-entrant cavity

The total equivalent capacitance of the cavity is operating in its lumped element mode is then:

$$C = C_0 + C_1 \tag{4.39}$$

where C_0 is the gap capacitance, and C_1 is the capacitance of the toroidal section.

$$C_0 \approx \frac{\pi r_0^2 \varepsilon_0}{d} \tag{4.40}$$

$$C_1 \approx 4 r_0 \varepsilon_0 ln\left(\frac{\sqrt{(r_1 - r_0)^2 + h^2}}{2d}\right) \tag{4.41}$$

while the inductance L is:

$$L \approx \frac{\mu_0 h}{2\pi} ln\frac{r_1}{r_0} \tag{4.42}$$

The equivalent shunt resistance is

$$R_{sh} \approx \frac{2\pi\delta\sigma\omega^2 L^2}{(\frac{h-d}{r_0} + \frac{h}{r_1} + 2ln\frac{r_1}{r_0})} \tag{4.43}$$

where σ is the metal conductivity and δ is the skin depth, given by equation (2.18)

The resonant frequency f_r is:

$$f_r = \frac{1}{2\pi\sqrt{LC}} \tag{4.44}$$

The unloaded quality factor Q is expressed by

$$Q = \omega C R_{sh} \tag{4.45}$$

4.11. Power Dissipation and Quality Factor

The average total stored energy (U) within an empty cavity is the integral over the volume of the cavity of the energy density [110].

$$U = \frac{1}{4}(\varepsilon_o E^2 + \mu_o H^2)V_{eff} \tag{4.46}$$

where, E and H are the electric and magnetic field magnitudes respectively. The cavity has been assumed to be empty. In the time domain, the total energy U in a particular mode decreases exponentially in time according to the expression,

$$U = U_o e^{\frac{-\omega_o t}{Q}} \tag{4.47}$$

where, $\omega_o = 2\pi f_o$

Since at resonance the energy stored in the electric field equals that in the magnetic field (but 90 degrees out of time phase) [111], equation (4.46) can be written as,

$$U = \frac{1}{2}\varepsilon_o E^2 V_{eff} = \frac{1}{2}\mu_o H^2 V_{eff} \tag{4.48}$$

When the empty cavity is excited, a surface current will be flowing on the walls and it is where the energy is dissipated in form of heat. The power dissipated P_d because of the cavity wall [11] is

$$P_d = \frac{R_s}{2}\iint |H|^2 ds \tag{4.49}$$

The surface resistance $R_s$of the cavity wall is given by:

$$R_s = \frac{\omega_o \mu \delta}{2} \tag{4.50}$$

where, μ is permeability of the conductor and δ is the skin depth of the conductor.

When a dielectric material is inserted into the active region of the re-entrant cavity, which is the gap between the post and the cavity wall as shown in Figure 4.17, a new perturbed capacitance C_o' will be obtained [112]. The gap capacitance is that of two concentric cylindrical regions, the inner region is containing a dielectric material with a dielectric constant ε_r and radius r_d while the outer one is containing air.

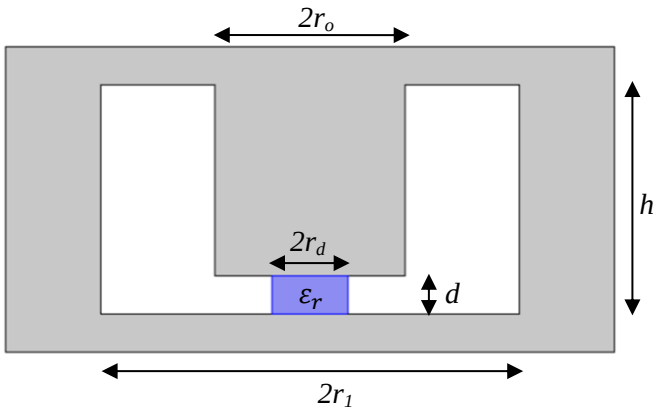

Figure 4.17 Re-entrant cavity with a gap partially filled with a dielectric

In the gap region where the sample is placed, the new capacitance value with the sample are given by [113]:

$$C_o' \approx \frac{\pi \varepsilon_o}{d}[(r_d^2(\varepsilon_r - 1) + r_o^2) + 4\varepsilon_o r_o ln(r_o - r_1)] \tag{4.51}$$

The resonance frequency will be shifted from f_o to f , due to change in gap capacitance according to below equation [112]:

$$\frac{f - f_o}{f_o} = \sqrt{\frac{C_o + C_1}{C_o' + C_1}} - 1 \tag{4.52}$$

The Q-factor of a dielectric loaded cavity is expressed as [113]:

$$\frac{1}{Q} = \frac{1}{Q_c} + \frac{1}{Q_d} \tag{4.53}$$

where, Q_c is the cavity quality due to the wall loss, and Q_d is the cavity quality due to the dielectric loss.

$$Q_c = \frac{\omega U_E}{P_w} \tag{4.54}$$

And,

$$Q_d = \frac{U_E}{U_d tan\delta} \tag{4.55}$$

where U_E and U_d are the stored energy in the whole cavity and in the dielectric sample, respectively. P_w is the dissipated power on the cavity walls which is inversely proportional to the square root of the wall conductivity σ.

4.12. Re-entrant Microwave Cavity Design

Two re-entrant cavities were designed and tested. The lowest frequency one works at 980 MHz and has been designed using COMSOL Multiphysics software and then machined. Figure 4.18 shows the schematic design, with r_1=40 mm, r_o=15 mm, h=30 mm, with an active gap between the two opposite posts of 2 mm. A hole with diameter ϕ =2.5 mm has been made to allow tube insertion through the cavity's posts to place the MUT in the active electric field gap area. SMA connectors have been used to loop couplings for cavity excitation via the magnetic field.

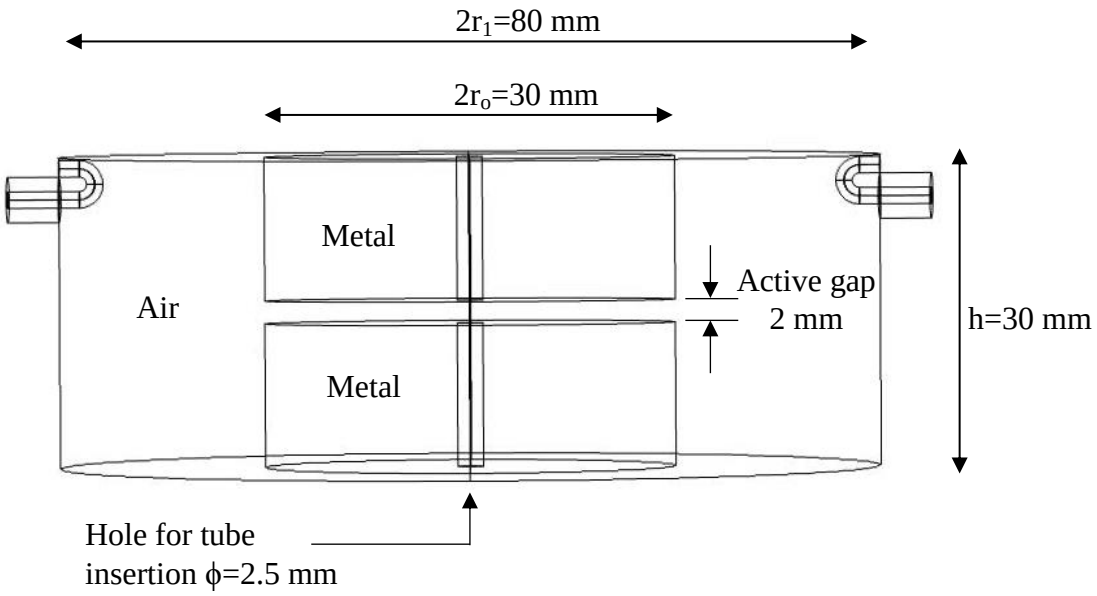

Figure 4.18 Re-entrant cavity design dimensions.

Figure 4.19 shows the machined re-entrant cavity made from aluminium in two parts, top and bottom (a) inside view, and the whole cavity (b). Two holes have been drilled towards the top of the cavity's side wall for the loop coupling SMA connectors. The coupling coefficients at both ports 1 and 2 are made equal by small adjustments to the loop angles, so making the response of S_{11} and S_{22} at resonance equal. Also, the bottom part of the resonator has been designed to stand on four legs which facilitates the collection of fluid for sensing under flow conditions. Four bolts are used to fix the two parts together.

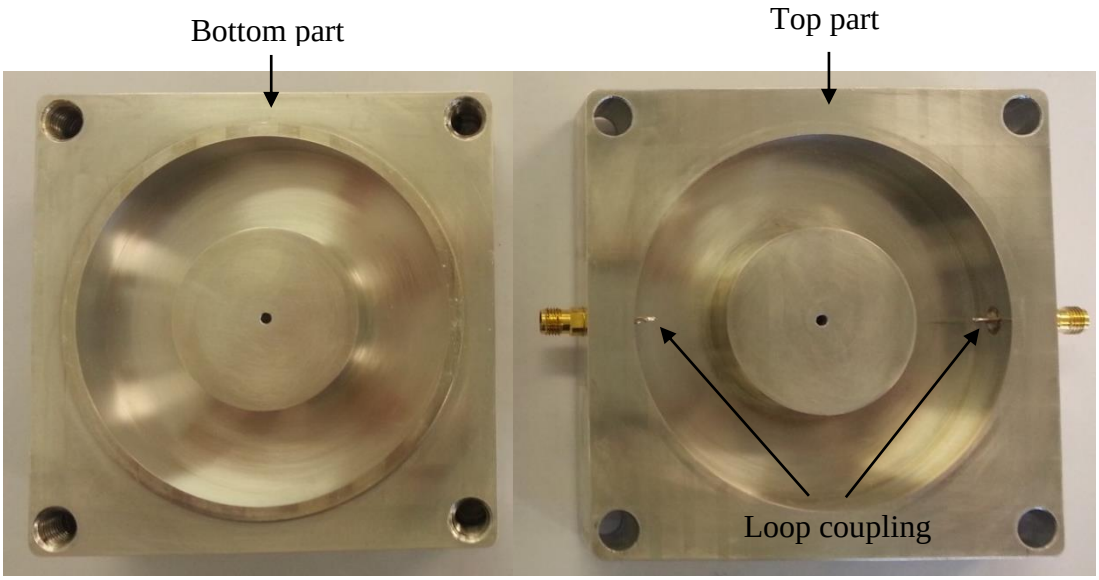

(a)

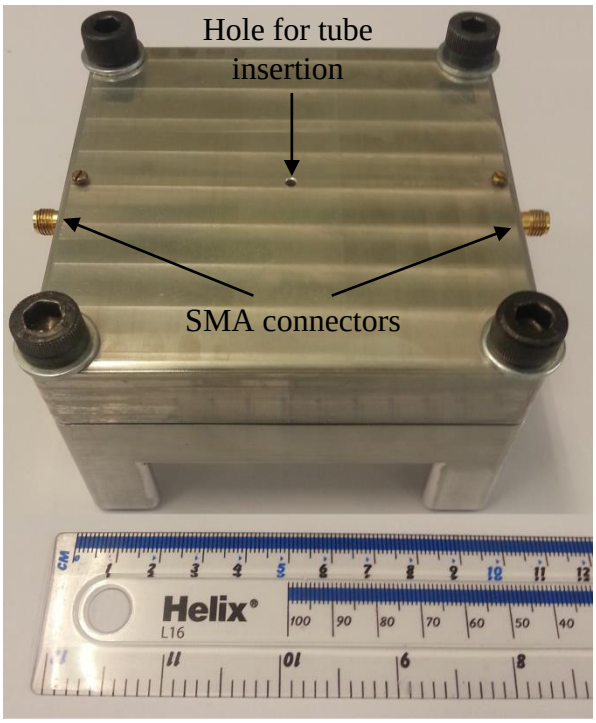

(b)

Figure 4.19 Photograph of the machined aluminium re-entrant cavity: (a) in two separated parts, and (b) the whole cavity where the two parts are held together using bolts.

4.13. Re-entrant Microwave Cavity Simulation Results

COMSOL multiphysics software has been used to simulate the behaviour of the re-entrant cavity according to simulation flowchart in Figure (4.11). Figure 4.20 (a) shows the E-field in the presence of an empty quartz tube; 1.7 mm outer diameter and 1.3 mm inner diameter. Figure 4.20 (b) shows an enlarged plot of the active gap area when the tube is empty, where it can be seen that the direction of the electric field is from top to bottom in parallel with the material under test. Figure 4.20 (c) shows the depolarising effect when the tube is filled with water. When empty, the cavity has an operating resonant frequency of 980.45 MHz and the quality factor Q is 1288 which changes to (964.6 MHz resonant frequency and 490 quality factor Q) when the tube filled with water.

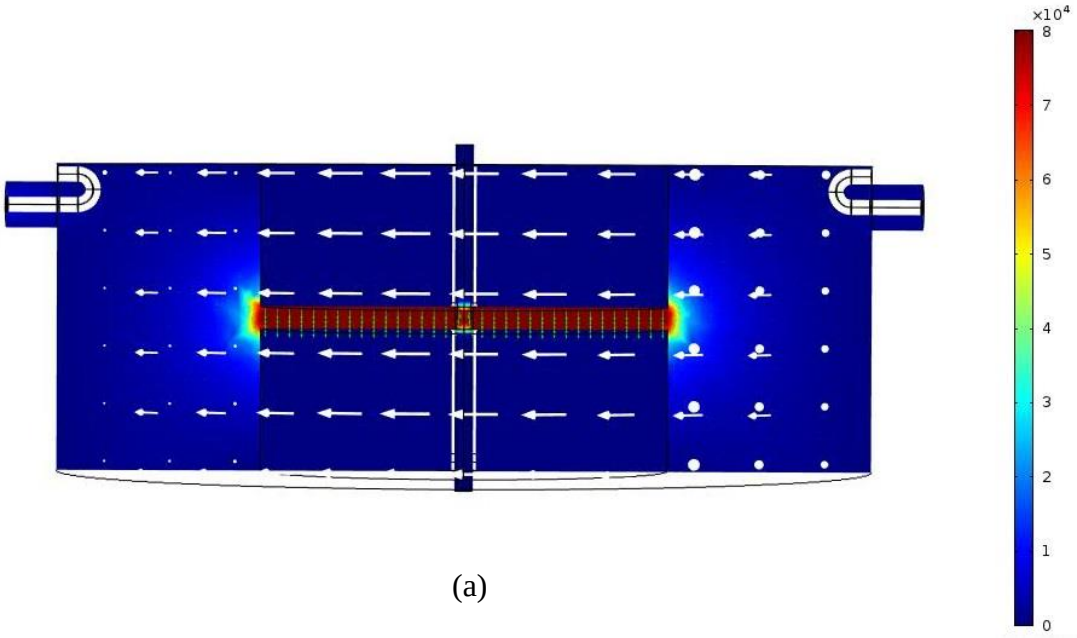

(a)

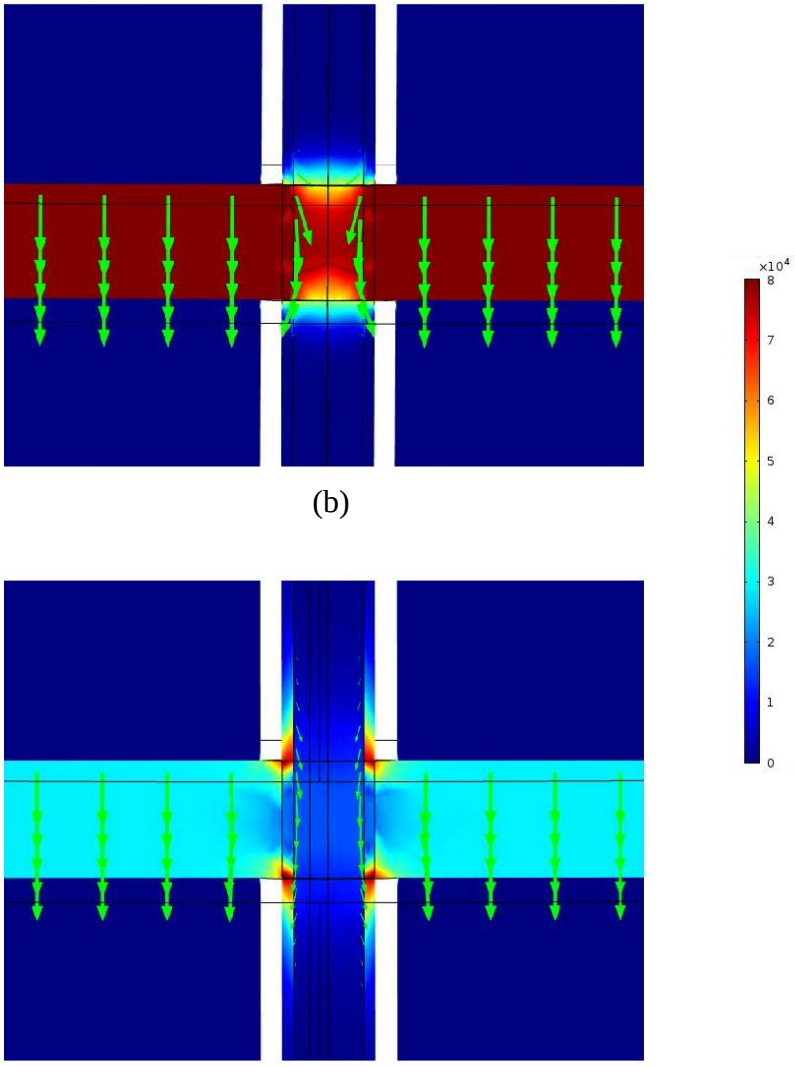

(b)

(c)

Figure 4.20 Simulation results showing the electric field (V/m) (a) when the quartz tube is empty with the magnetic field around the internal post (white arrows), (b) for an enlarged gap region with the direction of the electric field shown by green arrows and (c) when filled with water.

4.14. Microfluidic Experimental and Simulation Results

The re-entrant cavity has been tested experimentally with some common liquids (water, methanol, ethanol, and chloroform) using a network analyser (Agilent E507IB). Also, the cavity response for these fluids has been simulated by COMSOL software. The

Debye model equation (4.56) has been coded into COMSOL to prepare these simulation results for water, methanol, ethanol, and chloroform

$$\varepsilon(\omega) = \varepsilon_{\infty} + \frac{\varepsilon_s - \varepsilon_{\infty}}{1 + j\omega\tau} \tag{4.56}$$

where, ε_s is the permittivity for a static field, $\omega\tau << 1$, ε_{∞} is the permittivity for VHF (very high frequency), $\omega\tau >> 1$, and τ is the relaxation time. ε_s, ε_{∞}, and τ are considered as in Table 3.1 in CHAPTER THREE. There is excellent agreement between simulated and experimental results as shown in Figure 4.21.

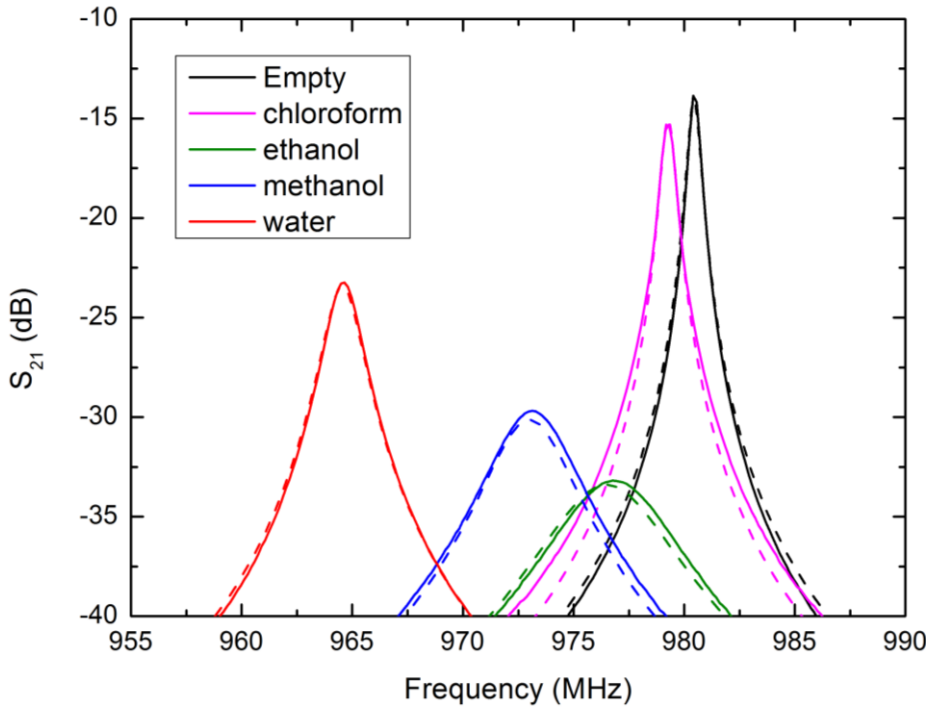

Figure 4.21 Measured (solid) and simulated (dashed) $|S_{21}|$ for several solvents at 25ºC.

Table 4.1, presents the simulated and experimental values for resonant frequency, quality factor, and insertion loss for the sensor when the capillary is empty and when filled with the mentioned solvents.

Table 4.1
Summary of results

Resonator	Simulated fr (MHz)	Measured fr (MHz)	Simulated Quality	Measured Quality	Simulated IL (dB)	Measured IL (dB)
Empty	980.45	980.40	1288	1280	-14.075	-13.861
Water	964.60	964.65	490	484	-23.403	-23.235
Methanol	973.00	973.12	263	250	-30.122	-29.692
Ethanol	976.50	976.75	212	208	-33.392	-33.183
Chloroform	979.30	979.31	1253	1250	-14.993	-15.296

4.15. Microspheres Detection

During the production of high-quality bulk materials, undesirable metallic and/or non-metallic impurities may occur and reduce the quality of the final product. In the case of food materials this could cause serious health problems, where as in the case of granulated intermediate products used for example in plastics industry, the performance of a final structural element may suffer significantly. The real issue of detecting such impurities is the way in which many bulk materials are moved as a dense material agglomeration during production, so that the detection within the bulk cannot be performed by optical or infrared means due to insufficient penetration capability. Ultra-sound techniques may be of restricted use in light of uncontrolled production noise. X-ray techniques are mostly prohibited because of environmental safety issues. Additionally, a suitable detection system must be able to fit into existing production infrastructure to keep cost as low as possible. Recently, microwave technology has provided an attractive method for solving issues [114].

In the field of microfluidic sensing, characterization of liquid and biological samples is significant in research and progressively required in control, chemistry, bio-chemistry, biology, medicine and clinical applications. Electromagnetic characterization is standing out as an alternative to typical chemical and photonic detection schemes. One promising

electromagnetic detection technique is dielectric spectroscopy, which characterizes the permittivity of a fluid as a continuous function of frequency providing important information on composition of liquids and cell suspensions, for example, cell structure, orientation of molecular dipoles, and surface conductance [115], [116].

4.16. Sensitivity of RMC to Polystyrene Microspheres

Analysis of mixtures of materials began at the early days of electromagnetics by modelling the in-homogeneities as spherical inclusions in a homogeneous material. Spherical shape objects were the choice to test. The mixture shown in Figure 4.22 shows spherical objects with permittivity ε_r distributed randomly in a medium with permittivity ε_m.

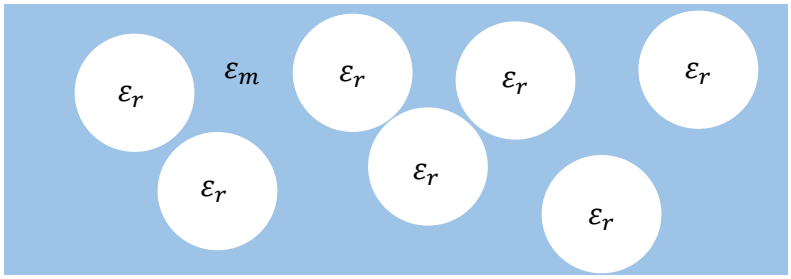

Figure 4.22 Dielectric spheres are distributed randomly in a dielectric medium.

Polarisability α is an important parameter in electromagnetics; it is the relation between the electric field E and the dipole moment p that is induced in the object by this field, so that the dipole moment p is defined as [117].

$$p = \alpha\, E \tag{4.57}$$

The polarisability for a spherical object with relative permittivity ε_r in a medium with relative permittivity ε_m, which is DI-water in our experiments, is expressed as [118]:

$$\alpha = 3\varepsilon_m V \frac{\varepsilon_r - \varepsilon_m}{\varepsilon_r + 2\varepsilon_m} \tag{4.58}$$

where V is the volume of the sphere.

If there are several spheres in the medium, the average dipole moment density and sometime called (average polarization) is:

$$P_{av} = np \tag{4.59}$$

where n in the unit volume.

By substituting equation (4.57) into equation (4.59):

$$P_{av} = n\alpha\, E \tag{4.60}$$

For a mixture, the relationship between the electric field E and the electric flux density D is related by the effective permittivity ε_{eff} of that mixture:

$$D = \varepsilon_{eff}\, E \tag{4.61}$$

$$D = \varepsilon_m\, E + P_{av} \tag{4.62}$$

From Equations (4.61) and (4.62), we can get:

$$P_{av} = (\varepsilon_{eff} - \varepsilon_m\,)E \tag{4.63}$$

By equating equations (4.60) and (4.63), the effective permittivity and the medium permittivity will be related to each other by:

$$(\varepsilon_{eff} - \varepsilon_m\,) = n\alpha \tag{4.64}$$

Now, substituting the polarisability α in equation (4.58) into (4.64):

$$\varepsilon_{eff}\ = \left[3v\left(\frac{\varepsilon_r - \varepsilon_m}{\varepsilon_r + 2\varepsilon_m}\right) + 1\right]\varepsilon_m \tag{4.65}$$

where v is the volume fraction of microspheres= nV.

The sensitivity of the 980 MHz re-entrant cavity has been tested in terms of changing the resonant frequency and quality factor Q when polystyrene beads dispersed in water are flowing through the active gap. The resonant frequency changed according to the concentration and inhomogeneity of clusters of the flowing beads through the active gap via PFA (Perfluoroalkoxy) tube (2.3 mm outer diameter × 2.1 mm inner diameter) using

a syringe and programmable syringe pump (KDScientific) to keep a constant flow rate. The properties of this sensor like higher sensitivity, compact and simple mechanical shape provides many possibilities for use in many industrial and pharmaceutical applications.

Firstly, the resonant frequency, and quality factor Q have been recorded with just DI-water passing though the active gap region, using (Agilent PNA-L network analyser N5232A) and LabVIEW program with a sweep points of 401, span 100 MHz and time per measurement is approximately 0.038 s. The results are shown in Figure 4.23.

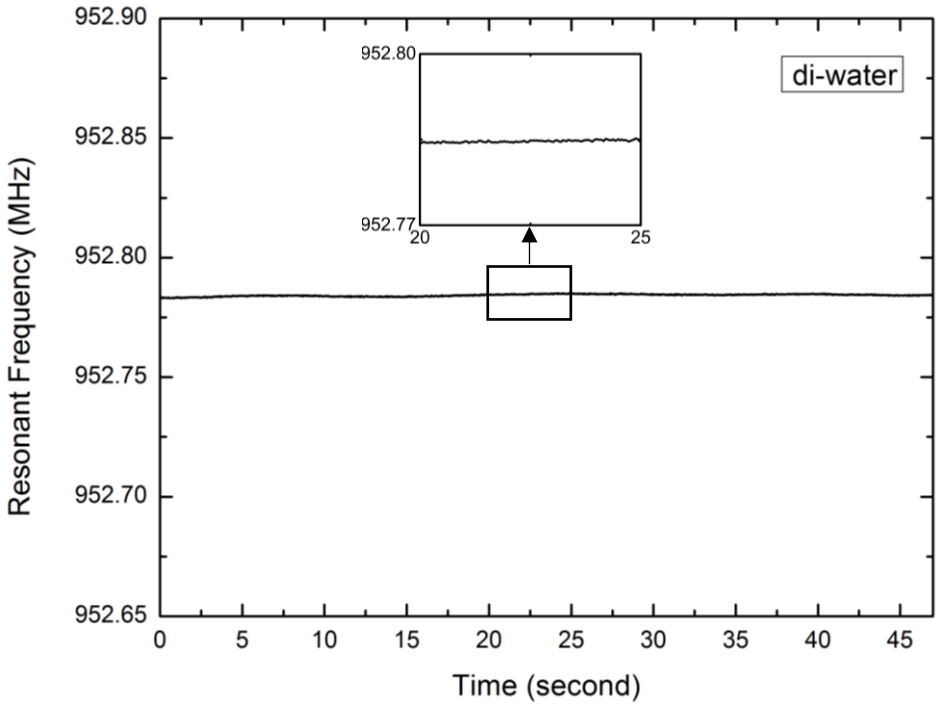

(a)

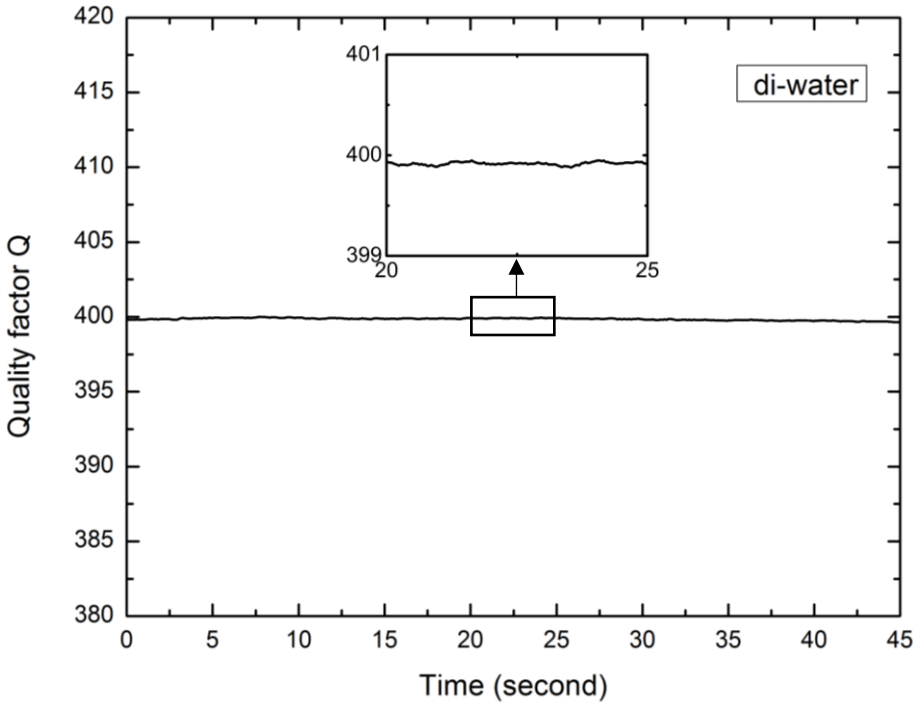

(b)

Figure 4.23 Resonant frequency vs time (a), and quality factor vs time (b) when di-water flowing through the active gap region of the RMC. The vertical scale on the graphs is chosen to be the same as those used in later graphs, where there is solid phase present, to properly illustrate the differences.

Polystyrene latex microspheres were used, of 50 micron average diameter, with concentration of 2.5 wt% dispersed in water. Flow rates has been controlled via syringe pump and set to 10 ml/hr. Microwave measurements have been recorded under continuous flow, and the time dependence of the resonant frequency and quality factor Q are shown in Figure 4.24. Note that the resonant frequency and quality factor change according to the density of polystyrene particles in the gap region, and also on whether particles are either dispersed or in clusters. Low polystyrene concentration is indicated by a lower resonant frequency and quality factor since the relative permittivity of the polystyrene beads is very low ($\varepsilon_r \approx 2.1$) compared with water. In other words, polystyrene particles decrease the mixture permittivity and accordingly this behaviour allowed our microwave sensor to detect the change in micro polystyrene impurities concentration within a solution.

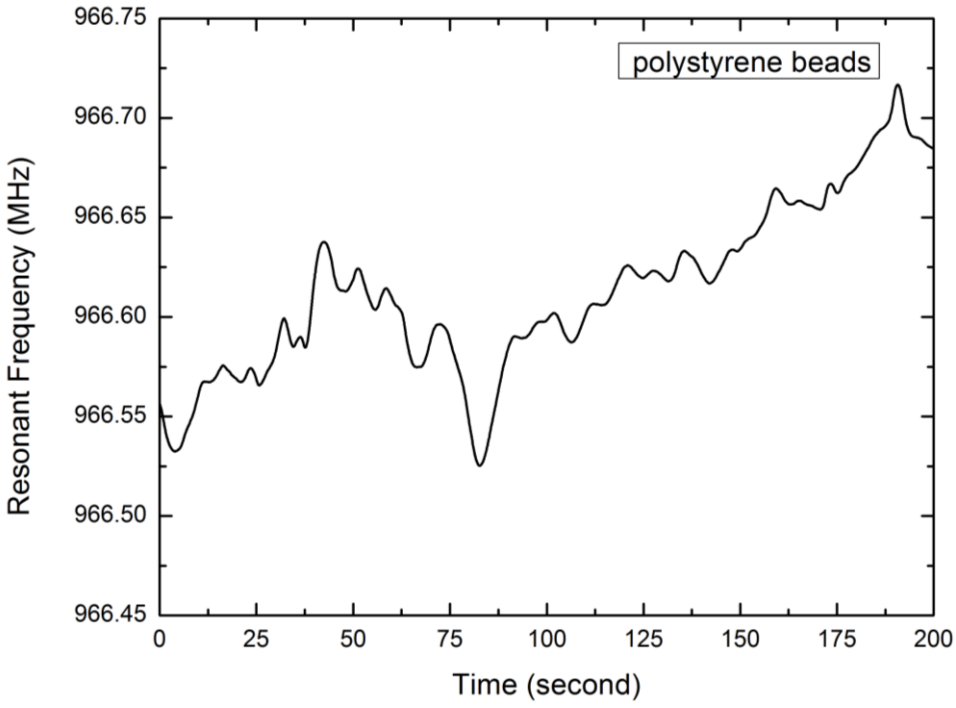

(a)

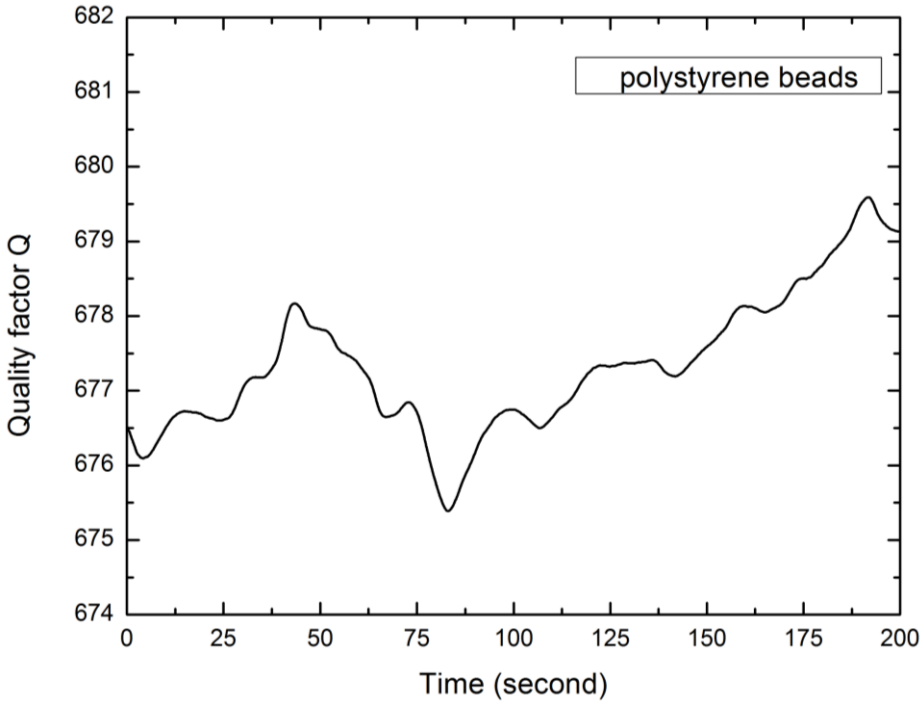

(b)

Figure 4.24 Resonant frequency vs time (a), and quality factor vs time (b) when polystyrene beads in DI-water flow through the active gap region of the RMC.

COMSOL Multiphysics was used to perform 3D simulations of the electromagnetic fields of the re-entrant cavity sensor with and without polystyrene spheres in water at 25 ^{0}C. The complex relative permittivity of water ($\varepsilon_1 - j\varepsilon_2$) was coded into COMSOL via the Debye model equation (4.56) to calculate the exact permittivity value at each frequency step; the static permittivity, infinite permittivity, and relaxation time are considered as listed in Table 3.1 in CHAPTER THREE as the relative permittivity of water is frequency dependent. Figure 4.25 shows the simulation results for the electric field. The resonant frequency shifted from 952.8 MHz (when there is just water) to 953.0 MHz due to the polystyrene beads shown.

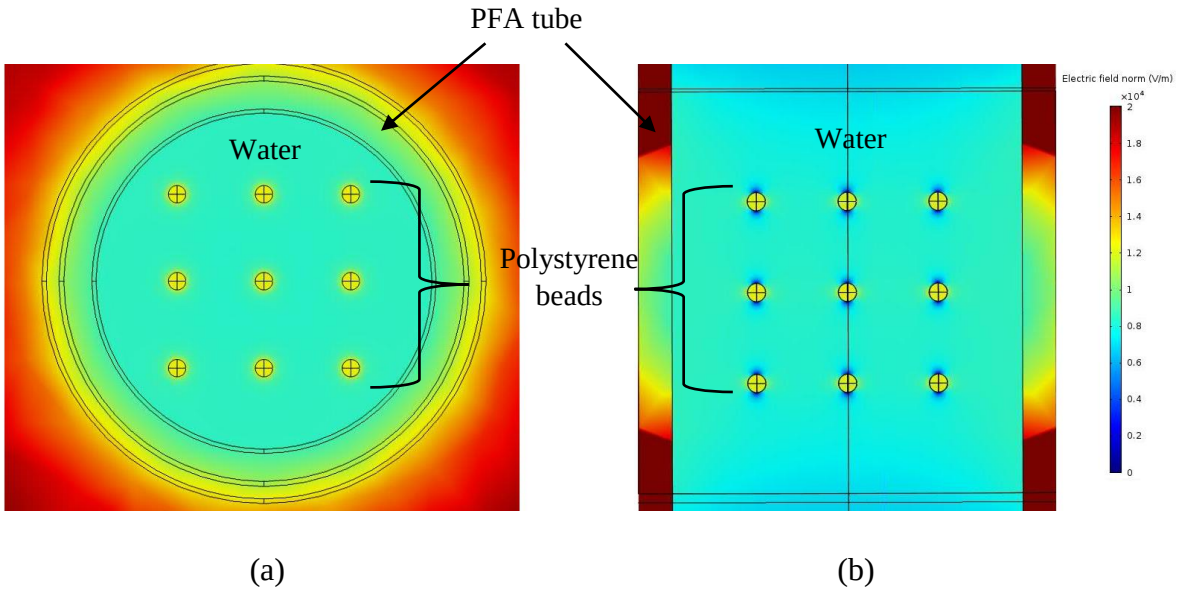

Figure 4.25 Simulation results for the electric field (V/m) when there are polystyrene beads dispersed in water, (a) top view, (b) cross section view.

It can be seen that the electric field inside the polystyrene beads is greater than the mean value in the water, as expected due to the high contrast in the relative permittivities and the depolarization effect with depolarization factor N = 1/3 for spheres.

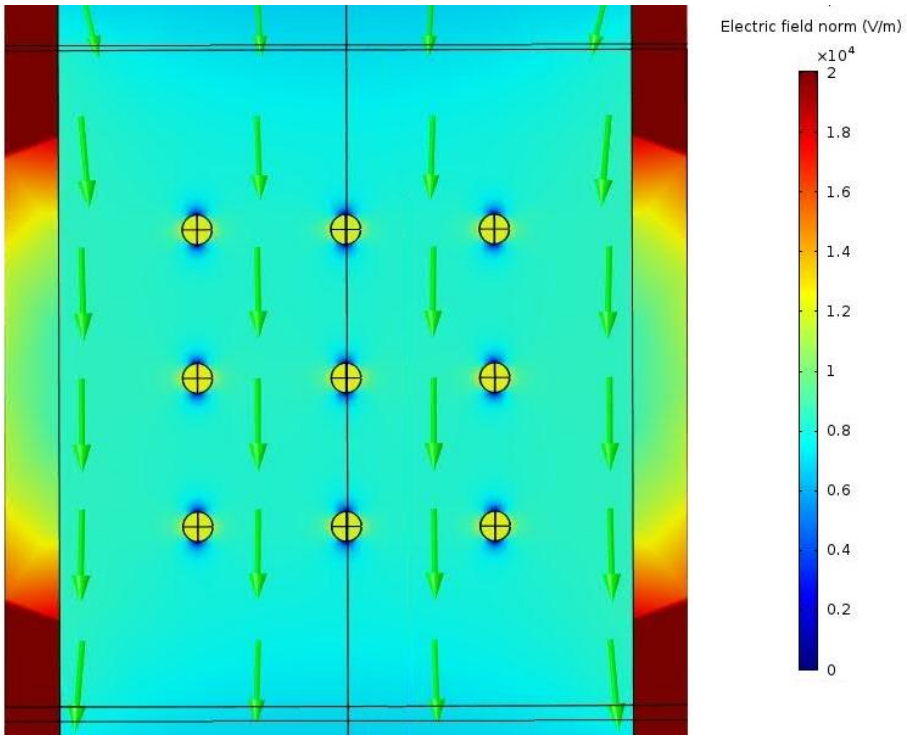

Figure 4.26 Simulation results for the electric field (V/m) and its direction when there are polystyrene beads dispersed in water.

Statistical results are summarized in Table 4.2, showing the average value of the resonant frequency, quality factor, S_{21}, and the standard deviation (SD) for each parameter for two cases; di-water, and dispersed polystyrene beads in water. Such variations can be used to study inhomogeneous flow processes involving these particles.

Table 4.2
Water, and polystyrene results

Solution	Average Frequency (MHz)	SD in frequency (KHz)	Average Quality factor	SD in quality factor	Average S_{21} (dB)	SD in S_{21} (dB)
Water	952.78	0.4744	399.85	0.0956	-24.682	0.0070
Polystyrene	966.61	42.708	677.33	0.9293	-19.003	0.0152

4.17. Miniaturized Re-entrant Microwave Cavity Design

COMSOL Multiphysics has been used in the cavity design of a compact RMC, to confirm a resonant frequency of approximately 2.4 GHz with sample loaded, and in the determination of the fields needed to develop a more precise model for cavity perturbation. In our constructed cavity, referring to Figure 4.27, the final dimensions chosen were d = 1 mm (the active gap width), r_1 = 18 mm, r_o = 5 mm and h = 10 mm. Also, a 1 mm diameter (ϕ) hole has been drilled through the whole length of the central pillar to take a sample tube. Note the much smaller dimensions of the RMC compared to, for example, a cylindrical TM_{010} cavity, which would need to have an internal diameter of about 92 mm for a similar resonant frequency. The RMC has a much smaller effective volume of two orders of magnitude smaller, about 0.8 cm^3, compared with around 80 cm^3 for the TM_{010} cylindrical cavity.

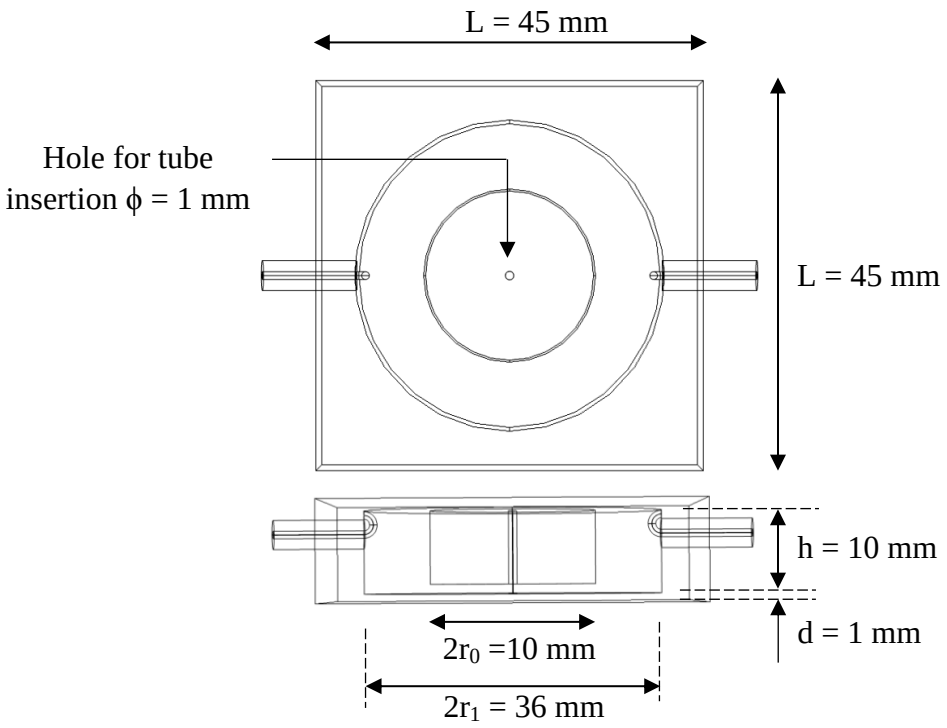

Figure 4.27 Miniaturized re-entrant cavity dimensions.

Figure 4.28 shows the constructional diagram of the manufactured aluminium re-entrant cavity, showing the base and lid. Two holes (3.6 mm diameter) have been made on the

side surface for inserting the coaxial feed lines, made from RG402 coaxial cable with SMA connectors. The feedlines are terminated in small coupling loops. The magnetic field in the resonant mode is excited in the cavity when current flows in one of the loops, whose excitation can be described as a magnetic dipole tangential to the cavity wall [6], [119]. The coupling coefficients at both ports 1 and 2 are made equal by small adjustments to the loop angles, so making S_{11} and S_{22} at resonance equal.

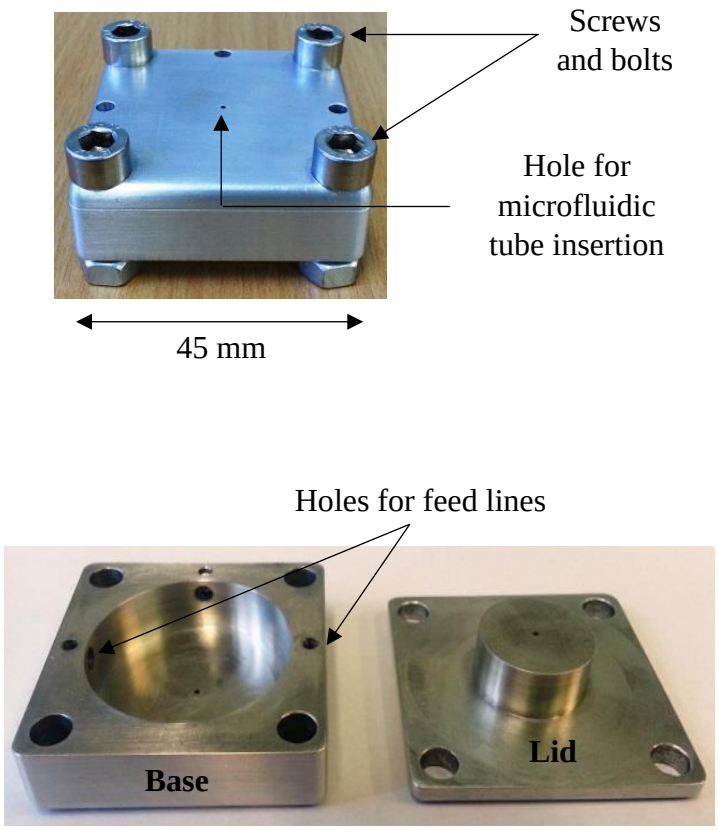

Figure 4.28 Photograph of machined miniaturized re-entrant cavity; the lid covers the cavity base and is tightened using screws and bolts.

4.18. Simulation and Experimental Results of Miniaturized RMC

COMSOL Multiphysics has been used in simulation and measurements. Figure 4.29 shows the result when an empty (Fluorinated Ethylene Propylene) FEP tube is fully inserted into the sensor cavity. It can be seen that, as expected, the electric field is concentrated in the gap area between the cavity post and end wall, while the magnetic field is around the post.

The simulated fields for a water-filled FEP tube of 0.77 mm O.D. × 0.4 mm I.D. are shown in Figure 4.30. The absorbed power P per unit volume (W/m3) by a dielectric material is given by the frequency f of the applied electric field, the electric field strength E within material, the material loss factor ε_2, and the free space permittivity ε_0 [120], [121].

$$P = 2\pi f E^2 \varepsilon_0 \varepsilon_2 \tag{4.66}$$

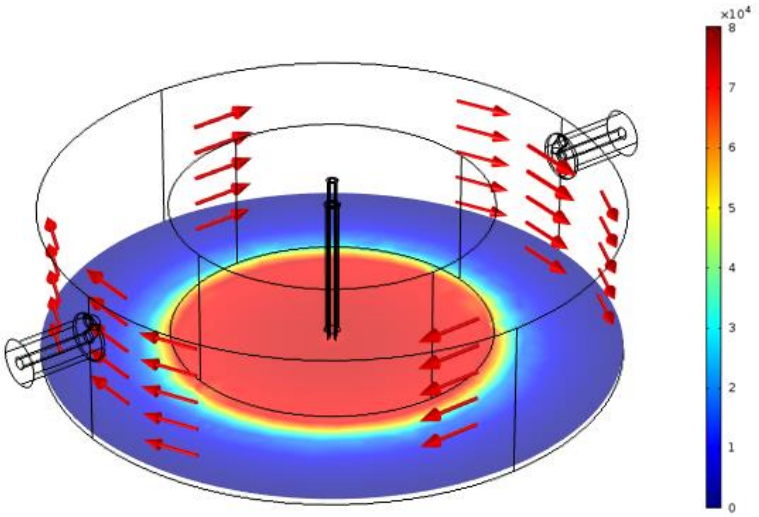

Figure 4.29 Simulation result for the electric field (V/m) when the FEP is empty, with the magnetic field around the internal post (red arrows).

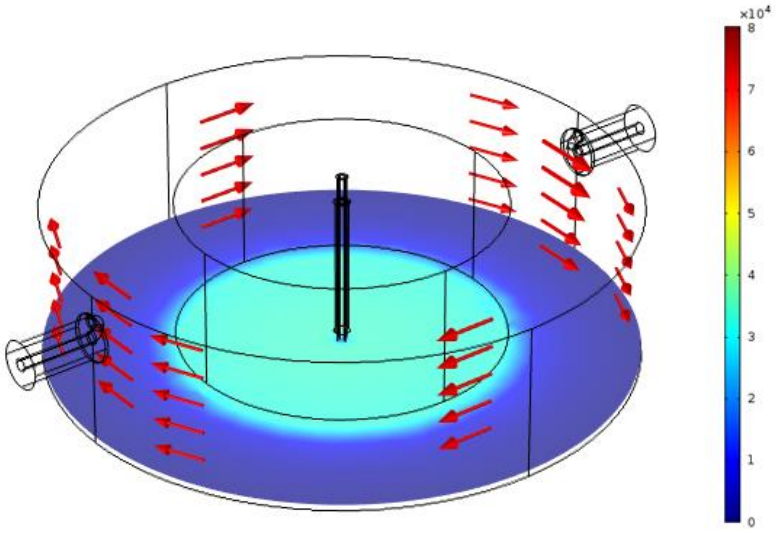

Figure 4.30 Simulation result for the electric field (V/m) when there is water in the FEP tube in the active gap area.

An expanded view of the cavity's cross sectional area is shown in Figure 4.31, (a) when the cavity is empty, and (b) when there is water in the tube. A schematic of the resulting electric field lines are shown in Figure 4.32. The parallel component of electric field along the tube is continuous across the boundaries, and this boundary condition gives rise to a large electric field inside the water sample for large cavity perturbations, leading to a sensitive measurement of sample dielectric properties.

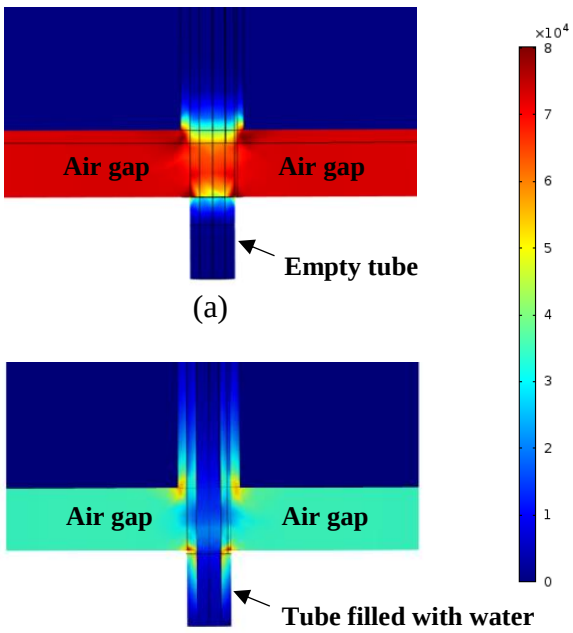

Figure 4.31 Cross sectional view when FEP tube is empty (a), and when there is water in tube in the active gap area (b).

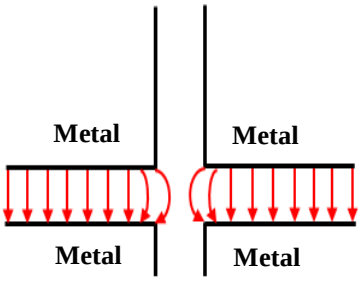

(a)

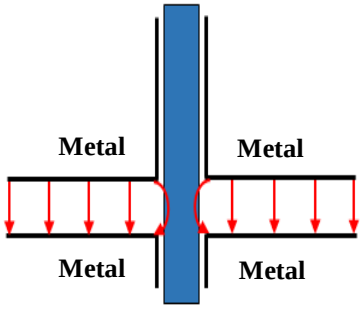

(b)

Figure 4.32 Electric field lines have a slightly curving trajectory in within the sample tube, when the cavity is empty (a), and when there is water (b).

For a narrow gap *d*, assumed to be much smaller than the central pillar radius r_0, the increased capacitance due to the presence of a sample can be calculated quite simply by application of the parallel plate capacitor formula for a composite capacitor. Assuming that the dielectric has a complex permittivity $\varepsilon = \varepsilon_1 - j\varepsilon_2$, simple approximate formulae for the cavity perturbation [100] by the sample can be derived, namely

$$\frac{\Delta f}{f_r} \approx -\frac{1}{2}(\varepsilon_1 - 1)\frac{V_s}{V_{eff}} \tag{4.67}$$

$$\Delta\left(\frac{1}{Q}\right) = \frac{\Delta f_B}{f_r} = \varepsilon_2 \frac{V_s}{V_{eff}} \tag{4.68}$$

where Δf, Δf_B are the change in resonant frequency and bandwidth, respectively, owing to the presence of the sample and f_r is resonance frequency when the cavity is empty. The quantity V_s is the sample volume and V_{eff} is the mode volume of the cavity. This is the effective volume occupied by the electric field energy, which in the first approximation is the volume of the gap region but in practice is larger owing to the charge on the lower part of the central pillar (i.e. the "fringing field").

Figure 4.33 shows good agreement between experimental (solid) and simulated (dashed) results when the resonator is empty and with some common liquids. The Debye model equation (4.56) has been coded into COMSOL to prepare these simulation results for water, methanol, ethanol, and chloroform. Debye model parameters (ε_s, ε_∞, and τ) are considered as in Table 3.1 in CHAPTER THREE.

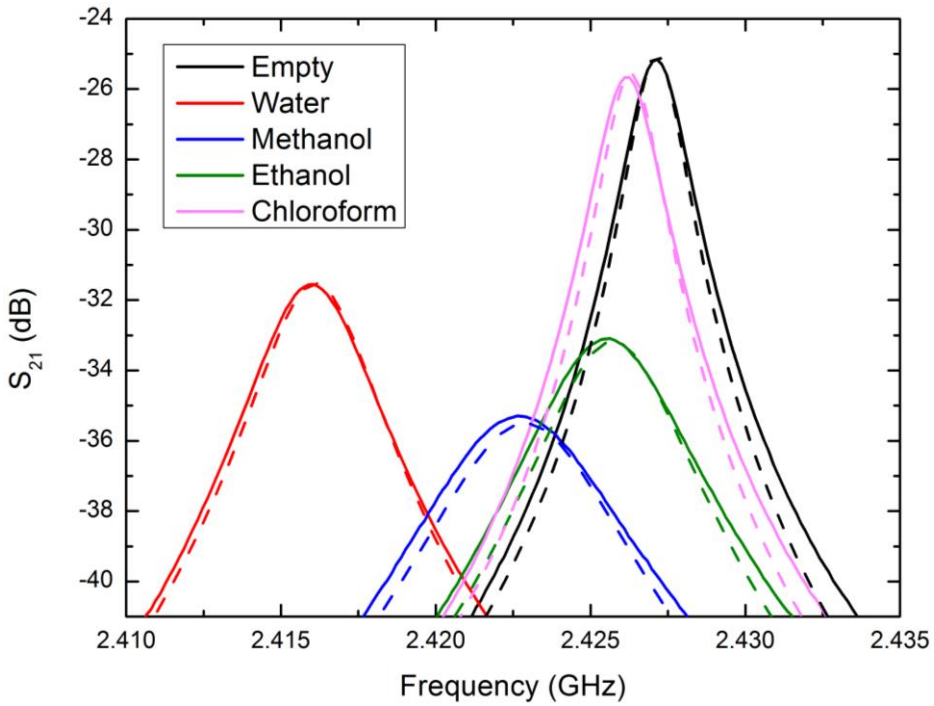

Figure 4.33 Measured (solid) and simulated (dashed) $|S_{21}|$ for several solvents at 25ºC.

Table 4.3 illustrates the simulated and experimental values for resonant frequency, quality factor and insertion loss for a RMC with a FEP sample tube filled with a selection of common solvents. From these measured values, the relative permittivity has been extracted using COMSOL and compared with simulated values. The small error ratios obtained show that the RMC system is accurate in measuring both absolute values, and small changes in the complex relative permittivity of liquids at microwave frequencies.

Table 4.3

Simulated and experimental values for resonant frequency, quality factor, and insertion loss for water, methanol, ethanol, and chloroform

Resonator	Simulated fr (GHz)	Measured fr (GHz)	Simulated Quality	Measured Quality	Simulated IL (dB)	Measured IL (dB)	Simulated Permittivity	Measured Permittivity	Error (%)
Empty	2.4271	2.4271	1190	1187	-25.020	-25.153			
Water	2.4161	2.4160	615	613	-31.527	-31.578	77.23-j9.04	77.85-j9.10	0.8
Methanol	2.4229	2.4227	385	381	-35.509	-35.296	22.27-j13.06	22.84-j12.87	1.5
Ethanol	2.4257	2.4255	483	480	-33.169	-33.117	7.01-j6.97	7.27-j6.96	1.7
Chloroform	2.4263	2.4261	1125	1125	-25.557	-25.663	4.69-j0.27	4.81-j0.30	2.5

From the simulation results, the changes in resonant frequency (Δf) and the change in bandwidth (Δf_B) both normalised by the unperturbed resonant frequency, have been plotted as functions of real and imaginary parts of the complex permittivity; the results are shown in Figure 4.34 (a) and Figure 4.34 (b), respectively. The fact that the plot of Δf continues to increase, almost linearly, with increasing real part of the permittivity is an important result that validates the use of first order perturbation theory for the RMC, and is a consequence of the electric field being mostly parallel to the sample length within the gap region (i.e. very little depolarisation is occurring).

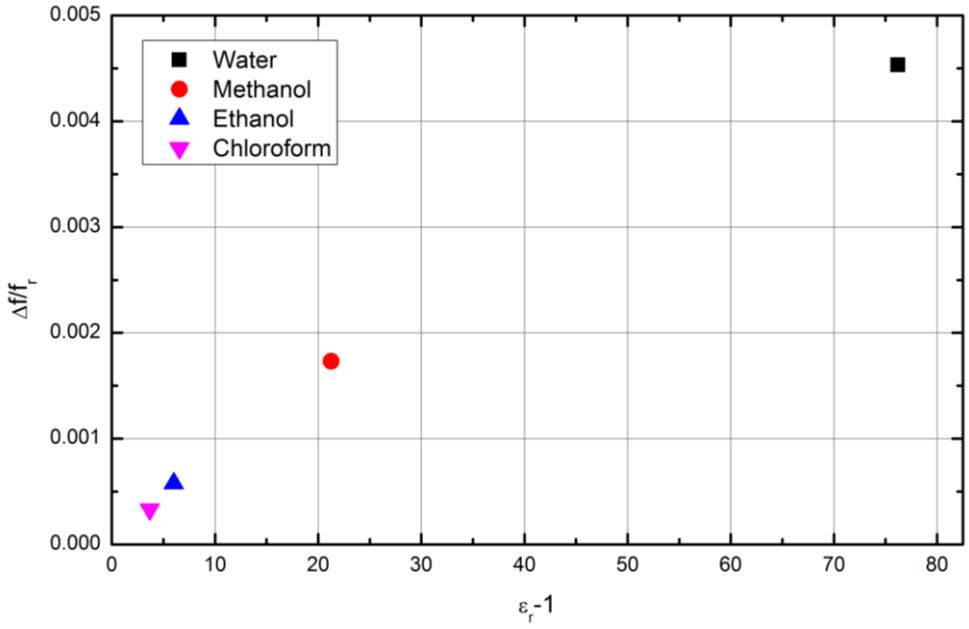

(a)

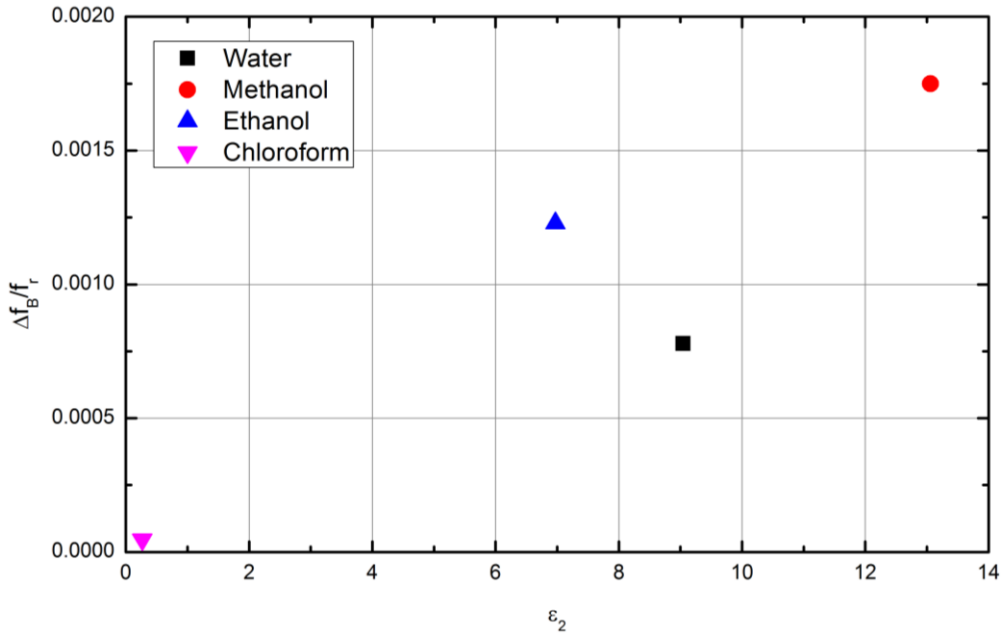

(b)

Figure 4.34 ($\Delta f/f_r$) for water, methanol, ethanol, and chloroform vs ε_1-1 (a), and ($\Delta f_B/f_r$) for the same solvents vs ε_2 (b).

4.19. Microfluidic System Design and Segmented Flow Results

To get discrete and controlled multi-phase segments flowing through a tube, a special system has been design to control the whole operation. FEP tubing (Fluorinated Ethylene Propylene), 0.77 mm O.D. × 0.4 mm I.D. has been used for the liquid sample flow. A programmable, two syringe pump (KDScientific) with a motorized valve (MXX777-601) was used to control flow of water and oil segments. Microwave measurements are performed by using a network analyser (Agilent E507IB), with all equipment controlled by laptop via LabVIEW code. The whole system connection is shown in Figure 4.35.

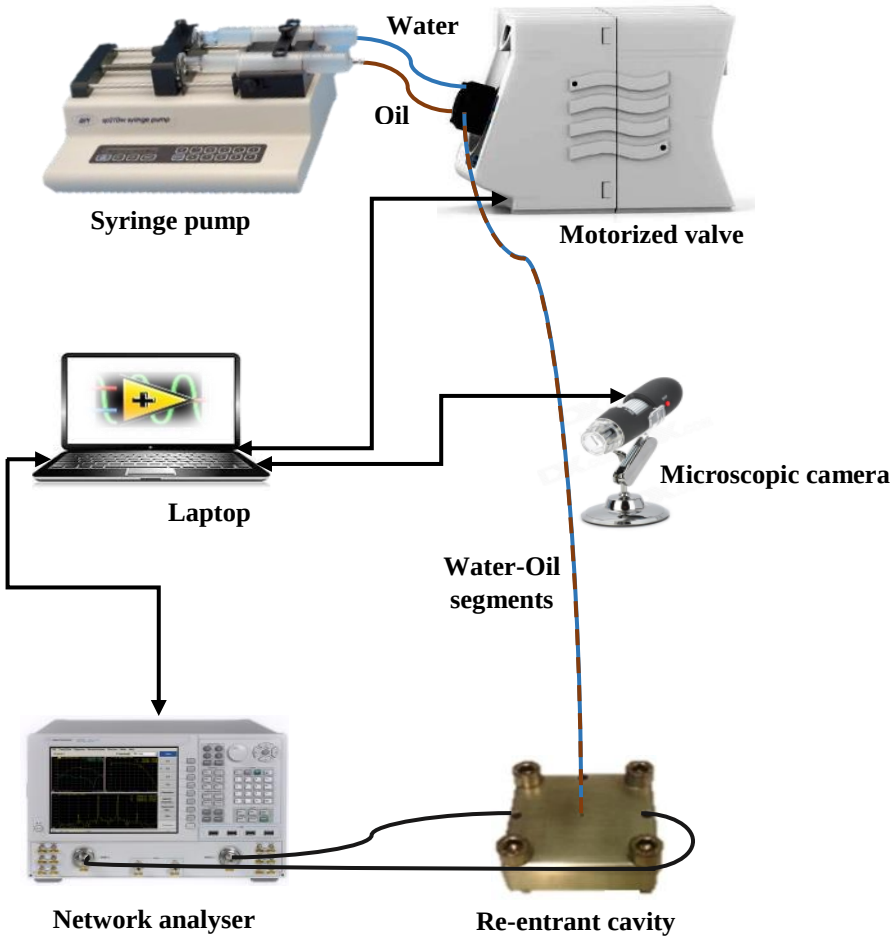

Figure 4.35 The complete microfluidic system connected to the RMC cavity sensor and controlled via LabVIEW code; the microscopic camera has been used for video recording.

The compact RMC has been tested for a flow involving different lengths of segments of water and oil. Figure 4.36 shows how the resonant frequency, bandwidth (BW), and insertion loss (IL) vary with the segment type present within the gap region (water segment length is 18.5 mm, and oil segment length is 35.5 mm). There is excellent contrast between the segment materials, in all three of these resonator parameters. Note that there are only two independent measurement variables here, since BW and IL both quantify the same thing (i.e. microwave loss, or ε_2).

By using a microscopic camera, the segment lengths and times required to travel through the gap region have been recorded. The length of segment can be calculated

from the velocity and the required time to pass through the active gap as shown in Table 4.4.

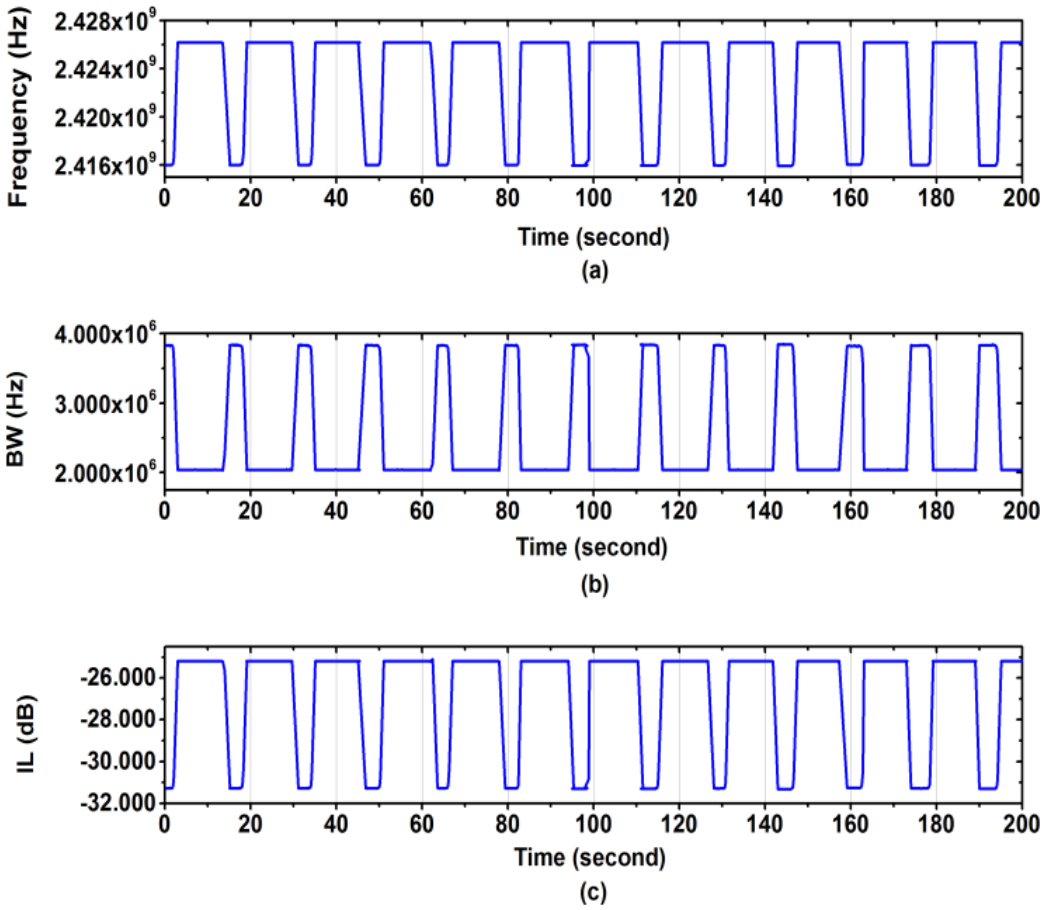

Figure 4.36 Effects of segment type on resonant frequency (a), frequency drops to 2.416GHz when water is present in the gap region, then increases to 2.426 GHz when oil is present, the corresponding BW (b), and insertion loss (c).

Table 4.4

Water and Oil Segment Length Measurement by Camera and Cavity

Segment Type	Velocity (mm/sec.) measured by camera	length (mm) from camera	length (mm) from cavity
Water	3.4±0.2	18.5±1.2	18.2±0.9
Oil	3.4±0.2	35.5±1.2	33.6±1.6

CHAPTER FIVE
SPLIT RING RESONATOR

5.1. Introduction

Split rings were among the first microwave resonators designed to be small in size relative to the wavelength, where the resonant frequency is a function of ring radius and the geometry parameters. Basically, they are composed in two forms, square or circular shape. The most important property of any resonator is its resonant frequency. Nowadays, there are many software packages that could be used to obtain the resonant frequency for the designed structure. Nevertheless it still important to have an approximate analytical expression for the resonant frequency, based on the understanding of the physics [122].

The basic geometry for the split ring resonator is shown in Figure 5.1. The parameters are: inner radius of the split ring *r*, thickness *w*, height *h*, and the gap width *g*.

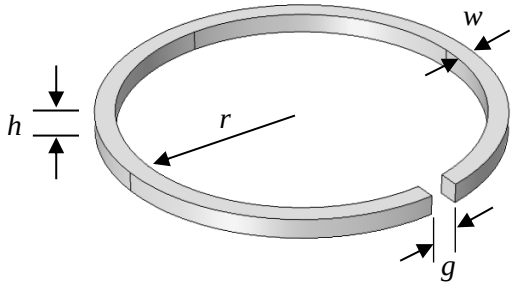

Figure 5.1 Split ring resonator geometry

The split-ring resonator can be represented by an equivalent parallel *LC* circuit. The inductance *L*, is due to flux linkage through the ring area of a single turn loop, and the capacitance *C*, is equivalent to the gap capacitance between the two parallel faces as shown in Figure 5.2.

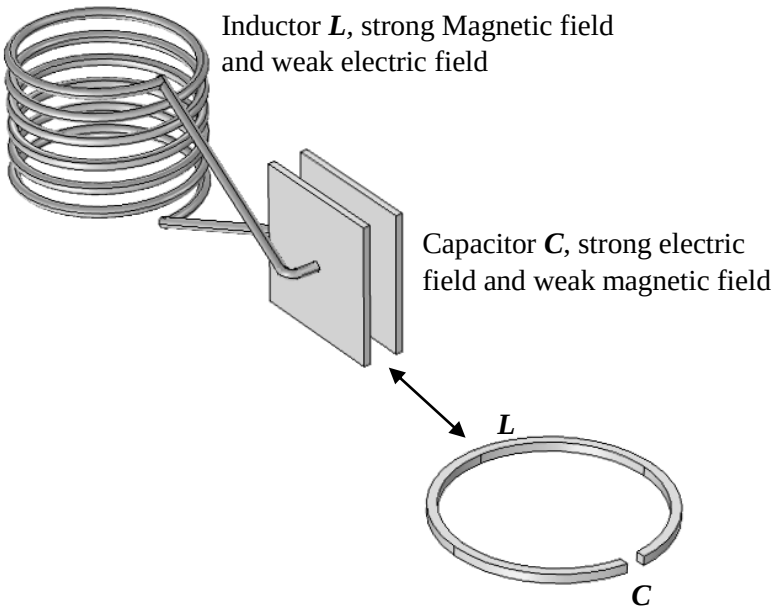

Figure 5.2 Split ring resonator as an *LC* circuit

Large values of capacitance can be achieved in the resonators due to the ability to construct small gaps; the capacitance is inversely proportional to the resonant frequency of the split ring.

5.2. Basic Concept of Resonance Frequency of the Split Ring

Resonant frequency, Quality factor, electric field and magnetic field of a split ring resonator as shown in Figure 5.3 depend on its geometry.

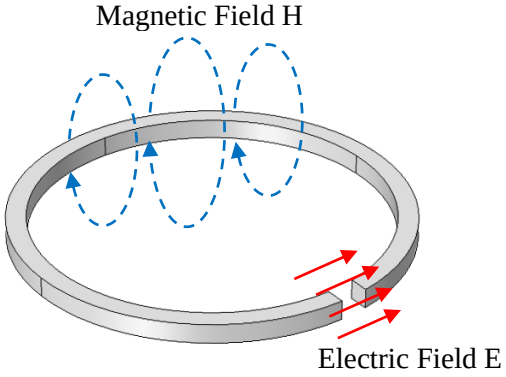

Figure 5.3 Schematic of split ring resonator

The geometry of the split ring resonator includes the mean radius of the ring (r), the thickness (w), the height (h), and the gap width (g). These give rise to an effective inductance (L_{eff}) and effective capacitance (C_{eff}), in terms of which the resonance frequency f_0 is [122]:

$$f_0 = \frac{1}{2\pi\sqrt{L_{eff}C_{eff}}} \tag{5.1}$$

The effective inductance can be approximated as:

$$L_{eff} \approx \mu_0 r\left(log\frac{8r}{h+w} - \frac{1}{2}\right) \tag{5.2}$$

Here, there are two capacitances, the gap and the surface capacitances. The former is appoximately

$$C_g \approx \varepsilon_0\frac{hw}{g} + \varepsilon_0(h+g+w) \tag{5.3}$$

where d is dielectric substrate height and w is conductor width.

The capacitance associated with the surface charges outside of the gap region is expressed by the surface capacitance (C_s) parameter

$$C_s \approx 2\varepsilon_0\frac{(h+w)}{\pi} \tag{5.4}$$

So, the effective capacitance is a sum of these two terms:

$$C_{eff} = C_g + C_s \tag{5.5}$$

5.3. Split Ring Design Considerations

It is well known that presenting a dielectric material to the high electric field area of a split ring resonator will change both resonant frequency and quality factor, and these changes depend on the complex relative permittivity of that dielectric material.

In terms of the phasor electric field E_0 applied to the sample, and the induced electric dipole moment p , the normalized changes in centre frequency and bandwidth can be expressed using perturbation theory, this time more conveniently expressed in the dipole moment of the sample since it allow the sample to be placed at an arbitrary angle relative to the applied electric field [54]:

$$\frac{\Delta f_0}{f_0} = \frac{Re(pE_0^*)}{4U} \tag{5.6}$$

$$\frac{\Delta f_B}{f_0} = \frac{-Im(pE_0^*)}{2U} \tag{5.7}$$

In these equations, U is the time-averaged stored energy, and p is induced electric dipole moment of the microfluidic sample are given below respectively

$$U = \frac{1}{2}\varepsilon_0 \int E^2 dV \tag{5.8}$$

$$p = \alpha\, \varepsilon_0\, E_0\, V_s \tag{5.9}$$

where α is sample polarisability and V_s is the volume of the electric field occupied by the sample. By substituting equations (5.8) and (5.9) into equation (5.6), we find the following results:

$$\frac{\Delta f_0}{f_0} = \frac{Re(\alpha\, \varepsilon_0\, E_0^2\, V_s)}{4\frac{1}{2}\varepsilon_0 \int E^2 dV} \tag{5.10}$$

$$\frac{\Delta f_0}{f_0} = \frac{Re(\alpha)V_s}{2\int \frac{E^2}{E_0^2} dV} \tag{5.11}$$

$$\frac{\Delta f_0}{f_0} = \frac{Re(\alpha)V_s}{2V_{eff}} \tag{5.12}$$

And in the same way, substituting equations (5.8) and (5.9) into equation (5.7), gives:

$$\frac{\Delta f_B}{f_0} = \frac{Im(\alpha)V_s}{\int \frac{E^2}{E_0^2} dV} \tag{5.13}$$

$$\frac{\Delta f_B}{f_0} = \frac{Im(\alpha)V_s}{V_{eff}} \tag{5.14}$$

where V_{eff} is effective volume=$\int \frac{E^2}{E_0^2} dV$, having the same definition as encountered previously, namely the mean volume occupied by the electric field energy.

Now, two cases for the orientation of the sample will be discussed here:

I. If the microfluidic sample is presented in perpendicular position with the electric field of the split ring resonator, then $E_{in} \approx \frac{2E_0}{1+\varepsilon_r}$. By substituting E_{in} into sample dipole moment $p = (\varepsilon_r - 1)\, \varepsilon_0\, E_{\text{in}}\, V_s$ the result is:

$$p \approx 2\, \frac{\varepsilon_r - 1}{\varepsilon_r + 1}\, \varepsilon_0\, E_0\, V_s \tag{5.15}$$

By comparing equation (5.15) with the general form of dipole moment given in equation (5.9), shows that the macroscopic polarisability of a cylindrical sample placed in perpendicular position with the applied electric field is [54]:

$$\alpha \approx 2\, \frac{\varepsilon_r - 1}{\varepsilon_r + 1} \tag{5.16}$$

II. If the microfluidic sample is presented in parallel position with the electric field of the split ring resonator, then $E_{in} \approx E_0$. By substituting E_{in} into sample dipole moment $p = (\varepsilon_r - 1)\varepsilon_0 E_{\text{in}} V_s$ the result is:

$$p = (\varepsilon_r - 1)\, \varepsilon_0\, E_0\, V_s \tag{5.17}$$

And by the same comparing, equation (5.17) with equation (5.9), α will be:

$$\alpha \approx \varepsilon_r - 1 \tag{5.18}$$

It should be noted that in case (I), the measurements of high values of ε_1 would be insensitive because the depolarization is almost complete, and increases in ε_1 do not

result in much of an increased dipole moment. So, it is essential to avoid the depolarization effect to increase the split ring sensitivity, as shown in case (II). This can be done by placing the microfluidic sample in parallel with applied electric field, and this is exactly what is considered in the split ring design as will be presented in next section.

Hence, the specially designed split-ring resonator is suitable for greatly increasing the efficient use of microwave power, in terms of maximising the electric field generated for a given input power. This is mostly down to the very small effective volume for electric energy, since from the fundamental definition of Q, the maximum electric field for a critically coupled resonator is

$$E_{max}^2 \approx \frac{2QP_{in}}{\omega_0 \varepsilon_0 V_{eff}} \tag{5.19}$$

This would allow simultaneous material characterisation and heating, which provide and facilitate the use in biomedical and chemical synthesis applications.
Practically, this can be achieved by changing the coupling gap distance by moving the coupling feed lines closer the split ring resonator until a specified value of insertion loss was achieved.

5.4. Split Ring Resonator Design

A split ring microwave resonator (SRR) has been designed and machined for dielectric properties measurements of common solvents. A novel aspect of our system is that the sample liquid will be placed in parallel to the electric field, to negate depolarization effects and so to maximise the sample's electric dipole moment by maximising the internal electric field. These, together with ensuring a small gap volume, are the crucial aspects and novelty of our SRR design. A schematic of the designed SRR is shown in Figure 5.4. It is machined from solid copper and has a pair of RG402 feedlines (Figure 5.4 (a)), terminated in open circuits (so coupling to the electric field) and arranged for

symmetric coupling. The sample tube is introduced as in Figure 5.4 (b), parallel to the electric field in the gap region of the SRR.

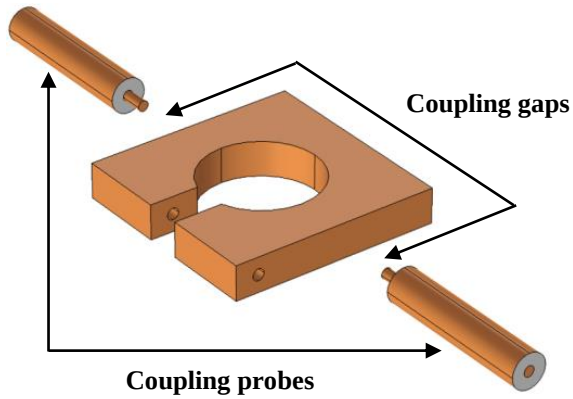

(a)

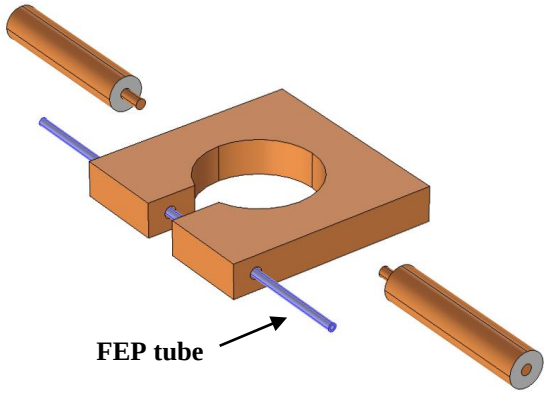

(b)

Figure 5.4 Schematic of split ring resonator (a) with its coupling probes and coupling gaps and (b) with microfluidic FEP tube.

Figure 5.5 shows the labels for the dimensions of the split ring resonator (L = 18 mm, radius *r* = 5 mm, gap distance g = 3 mm, height or thickness of the split ring h = 3 mm, and diameter ϕ of the hollow for tube insertion = 1 mm). Copper metal has been chosen for the high quality factor requirements. The resonant frequency when empty is 2.5 GHz, and the quality factor Q when empty is around 1860.

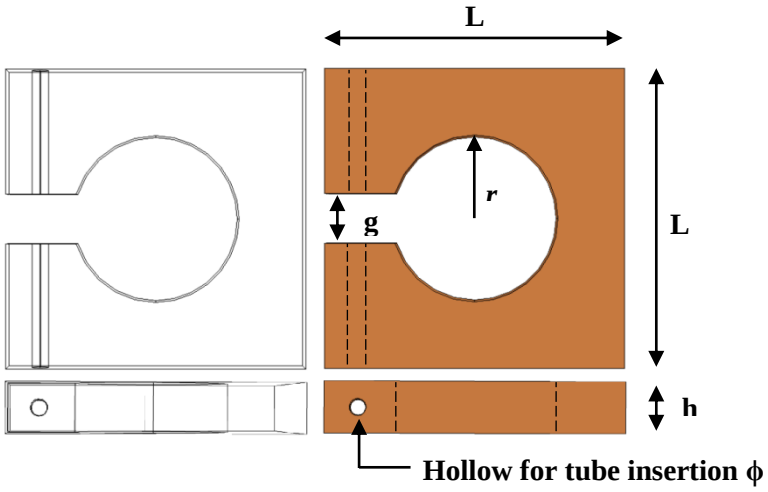

Figure 5.5 Labels for the dimensions of the split ring resonator.

By applying symmetric input and output feed lines on the on the split ring resonator, the positions of maximum electric field are shown in Figure 5.6. Adding to the capacitances described in section 5.2 which depend on split ring dimension and on the gap dimensions, there are extra coupling capacitances that need to be considered resulting from the gaps between the ends of the split ring resonator and coupling probes.

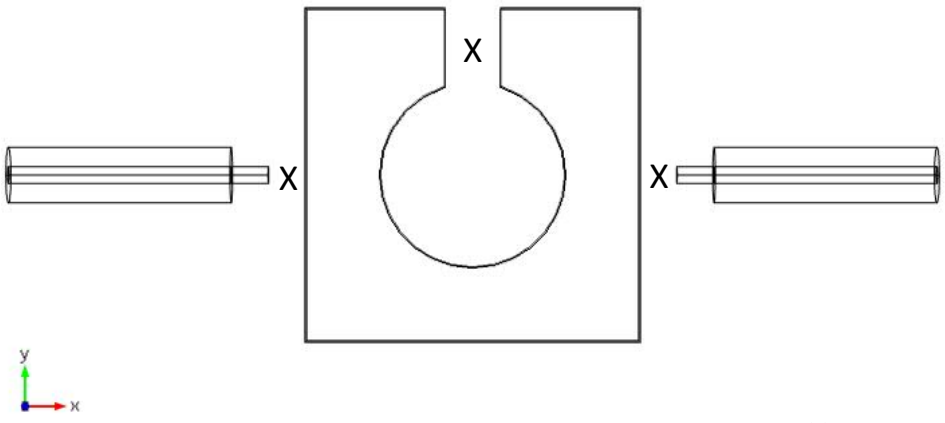

Figure 5.6 Maximum electric field points denoted by ×

Capacitive coupling is achieved by the capacitance resulting mainly from the gap capacitance between the edge of the resonator and the coupling probe, which is inversely proportional with this gap width.

Figure 5.8 shows a one-port ring equivalent circuit. The coupling gap between the feed line and the ring is represented by a L-network gap capacitance C_{g} and fringing capacitance C_f. The lossless ring resonator is represented by a shunt circuit of inductance L_r and capacitance C_r. In addition, comparing C_{g} and C_f, the coupling gap is significantly dominated by C_{g}. To ease the calculation of the input impedance, the fringe capacitance C_f can be neglected as shown on the right of Figure 5.8. The total input impedance obtained from the simple equivalent circuit is given by [123]:

$$Z_{in} = \frac{j[\omega^2 L_r(C_r + C_g) - 1]}{\omega C_g(1 - \omega^2 L_r C_r)} \tag{5.20}$$

where ω is the angular frequency. Z_{in}=0 (at resonance), the resonant angular frequency can be found as

$$\omega_0 = \frac{1}{\sqrt{L_r(C_r + C_g)}} \tag{5.21}$$

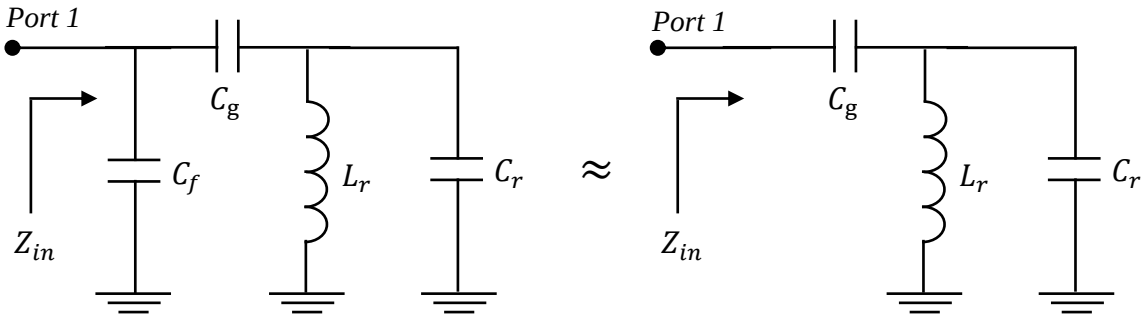

(a) (b)

Figure 5.8 One-port ring equivalent circuit (a) with the fringe capacitance C_f (b) the fringe capacitance is neglected.

According to equation (5.21), if the coupling gap size is decreased, C_{g} will increase, and the resonant frequency will decrease as a result. Also, the coupling gap size affects the insertion loss, which can be seen from the two port ring circuit shown in Figure 5.9.

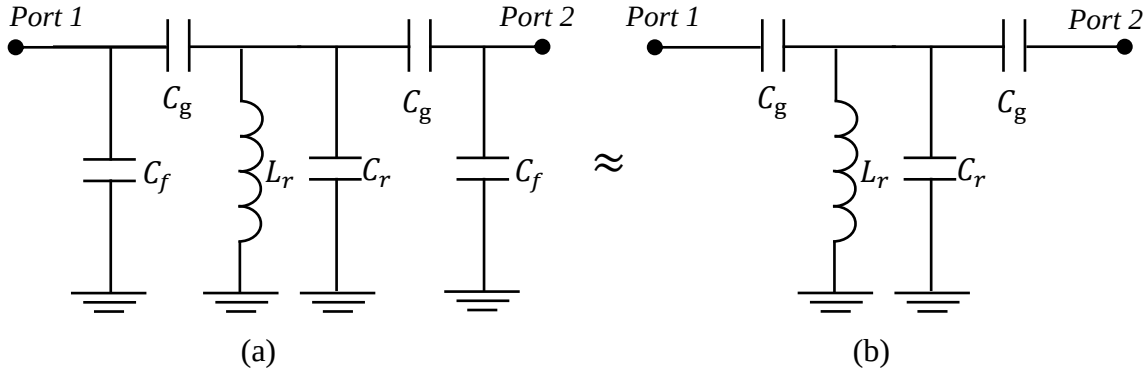

Figure 5.9 Two-port ring equivalent circuit (a) with the fringe capacitance C_f (b) the fringe capacitance is neglected.

S_{21} of the simplified equivalent circuit on the right of Figure 5.9 is given by

$$S_{21}|_{\omega=\omega_0} = \frac{2}{2(1+Z_gY) + Z_g(2+Z_gY)/Z_0 + YZ_0} \tag{5.22}$$

where $Z_g = \frac{1}{j\omega_0 C_g}$, $Y = \frac{j(\omega_0^2 L_r C_r - 1)}{\omega_0 L_r}$, and Z_0 is the characteristic impedance.

Capacitive coupling probes have been used to transfer energy from the feedline to the resonator by extending the feeding coaxial cable by a small distance, as shown in Figure 5.10. The length of the probe should be small compared to the wavelength, and its input impedance is therefore nearly equivalent to that of an open circuit. Each probe couples to the electric field that is perpendicular to the wall at the probe's location. The coupling strength is adjusted by simply moving the probe closer to the SRR. Lengths of standard semi-rigid RG402 coaxial cable have been used for each coupling probe, with female SMA connectors. All dimensions are shown in Figure 5.10.

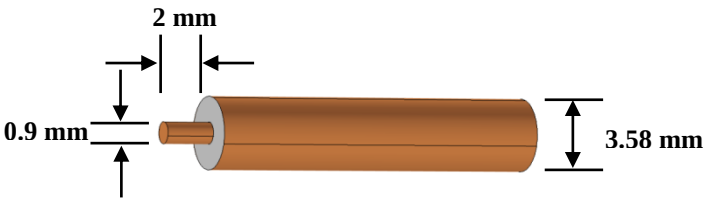

Figure 5.10 Coupling probe dimensions

The strength of the coupling at each of the SRR's coupling ports is quantified using the dimensionless coupling coefficients g_1 and g_2. We use the SRR reported here in two main configurations. One of these is for microwave excitation of a sample, where maximum power transfer is needed between microwave source and SRR. This is achieved by careful adjustment of the position of one of the coupling probes to achieve critical coupling, i.e. g = 1 at the port of interest, giving almost zero reflected power at that port at the resonant frequency. For the sensor configuration we keep the coupling weak to reduce the error in the calculation of the unloaded Q, as will now be explained. Circuit analysis yields the formula for the voltage transmission coefficient $S_{21} = \frac{2\sqrt{g_1 g_2}}{1+g_1+g_2+2jQ\Delta f/f_0}$, where the coupling coefficients can be written as $g_1 = f_o k_1^2 Q$, $g_2 = f_o k_2^2 Q$.

Here k_1 and k_2 are constants, which depend on the geometrical properties of the coupling structures (i.e. position and length of the probes). To simplify the analysis for the extraction of unloaded Q from the loaded (i.e. measured) Q, denoted Q_L, we mechanically adjust the coupling to ensure that the coupling is symmetric, by ensuring that the values of S_{11} and S_{22} measured at resonance are approximately equal. Then $g = g_1 = g_2$. Defining S to be the value of $|S_{21}|$ at resonance, unloaded Q is then simply equal to $Q_L/(1-S)$. To reduce uncertainty in the extraction of unloaded Q we keep the couplings weak.

For example, the typical insertion losses at resonance of the empty and sample filled resonators are -20 dB and -40 dB typically; these give values of S of 0.1 and 0.01, respectively, meaning that only 10% and 1% correction factors have to be applied in correcting loaded Q to unloaded Q.

5.5. Resonator Packaging

A PTFE dielectric platform has been designed for the split ring resonator to be mounted as shown in Figure 5.11. The dielectric constant and loss of PTFE is very low and has little effect on the microwave frequency measurements.

The SRR and its PTFE platform sit within a special designed aluminium outer cavity with lid and holes drilled in the sides of the cavity for coupling probes to be inserted through them. After adjustment, the latter are pinned into place with the aid of two grub screws. The aluminium outer is shown in Figure 5.12, and the full assembly (sketched ready for simulation) is shown in Figure 5.13. The sample tube is made from FEP (Fluorinated Ethylene Propylene), of outer diameter of 0.77 mm and inner diameter of 0.4 mm. This can be connected to a pump to study flowing liquids. This type of design allows the required coupling level from weak to strong coupling to be attained by changing the distance between coupling probes and the side surface of the split ring resonator. Also, small slots have been made for the tube to be inserted through the cavity passing through the split ring and exiting from the opposite side. These slots provide more flexibility for the tube insertion than holes, as the whole structure is completely enclosed as shown in Figure 5.13.

The outer cavity was designed so that its lowest mode was above that of the split-ring resonator to avoid frequency overlapping between the split ring resonator and the cavity. Furthermore, the outer cavity provides very good isolation for the split ring resonator from external interferences where it is completely shielded (to reduce radiation losses so to maintain the highest possible Q). If the lid were to be removed, there was a slight decrease in the resonant frequency while the quality factor dropped significantly to a few hundred (around 700). Therefore, it was necessary to retain the lid during experiments to retain the highest Q factor, for highest sensitivity results.

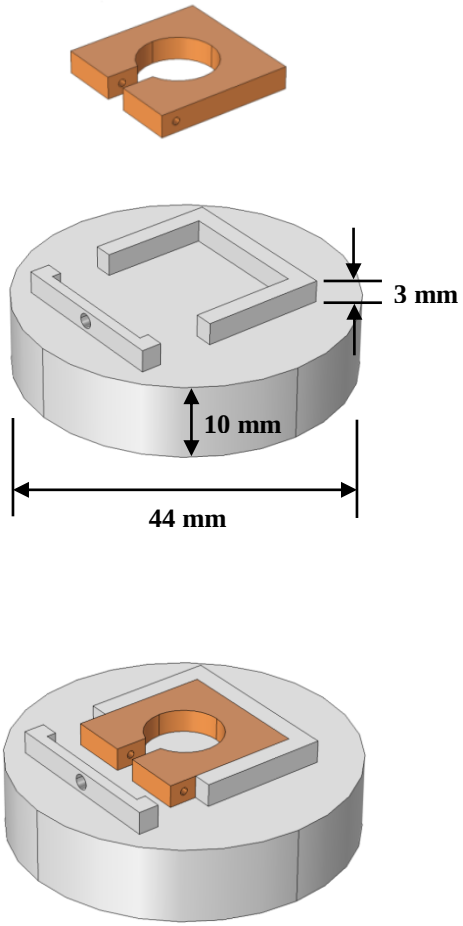

Figure 5.11 The split ring resonator and its PTFE platform.

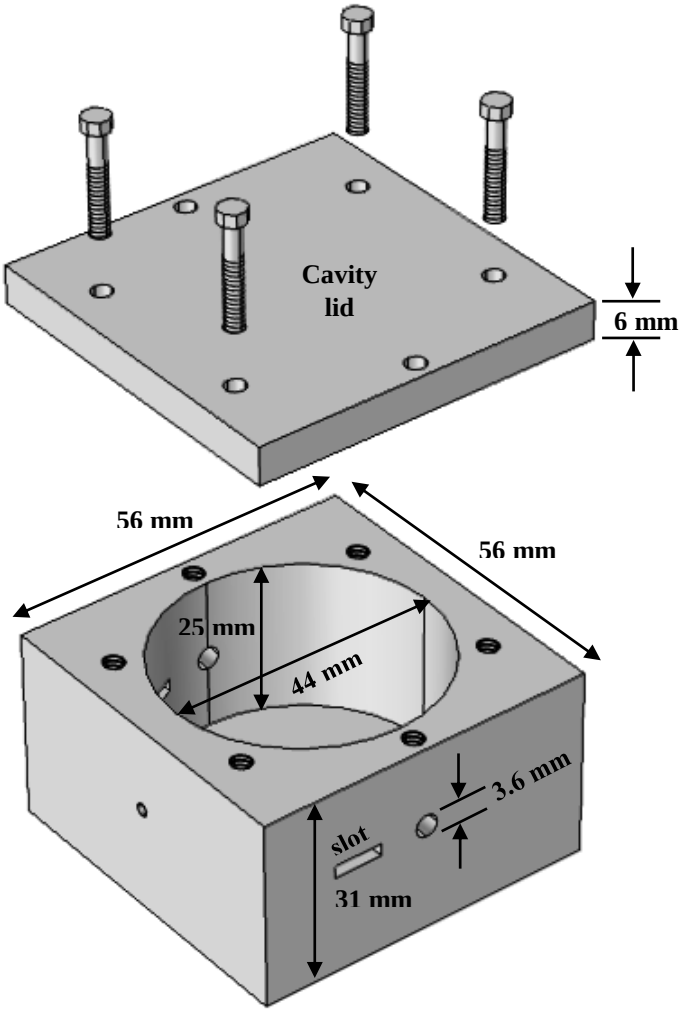

Figure 5.12 Cavity housing: base, lid, and screws.

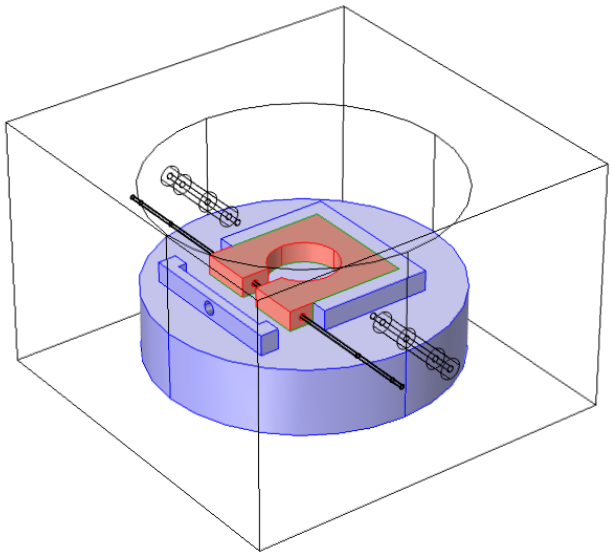

Figure 5.13 The split ring resonator, PTFE dielectric base, outer cavity position, coupling probes, and microfluidic FEP tube.

5.6. Simulation Results

COMSOL Multiphysics® 4.4 software has been used for all electromagnetics simulations. The impedance boundary condition is used for the copper and aluminium surfaces in order to calculate their losses. The simulation boundary is the inside surface of the aluminium outer cavity. Coaxial ports were used to feed the electromagnetic energy to the resonator. Figure 5.14 shows the electric field (E-field) (a), which is concentrated in the gap which is the active part for materials measurement, while the magnetic field (H-field) (b) is concentrated on the opposite side of the split ring gap. There is excellent spatial separation between these two field components.

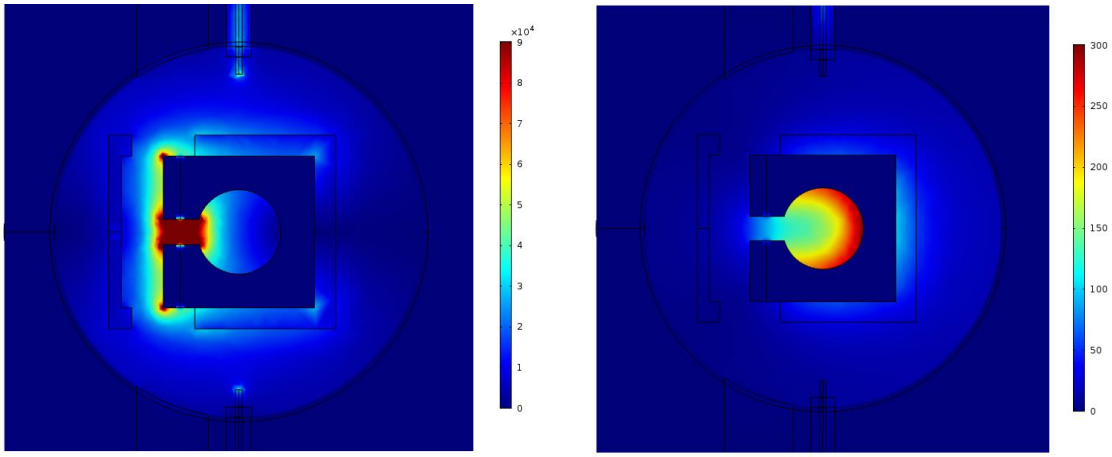

(a) (b)

Figure 5.14 COMSOL simulation results for the (a) electric field (V/m), and (b) magnetic field (A/m) distribution.

Figure 5.15 shows a magnified plot of the E-field in the gap region and its direction when the resonator is empty. The maximum internal electric field occurred when sample is in parallel with the applied electric field. So, this configuration allows maximum power to be absorbed by a lossy dielectric, e.g. for the water sample shown in Figure 5.16.

All microwave measurements of the SRR have been performed using a vector network analyser (Agilent E507IB) operating in the frequency domain under computer control

(LabVIEW, National Instruments), as seen in Figure 5.17. There is very good agreement between simulated and experimental results as listed in Table 5.1, which shows simulated and experimental results for the resonance frequency (f_0), Q factor, and the insertion loss (IL). This data also demonstrates the huge increase in sensitivity that is achieved by choosing the correct sample orientation for highly polar liquids like water.

Table 5.1

Simulated and experimental results

Resonator	Simulated f_0 (GHz)	Measured f_0 (GHz)	Simulated Q factor	Measured Q factor	Simulated IL (dB)	Measured IL (dB)
Empty	2.527	2.528	1861	1858	-19.785	-19.961
Water-perpendicular	2.521	2.520	1480	1476	-20.706	-21.737
Water-parallel	2.467	2.467	258	250	-41.381	-40.886

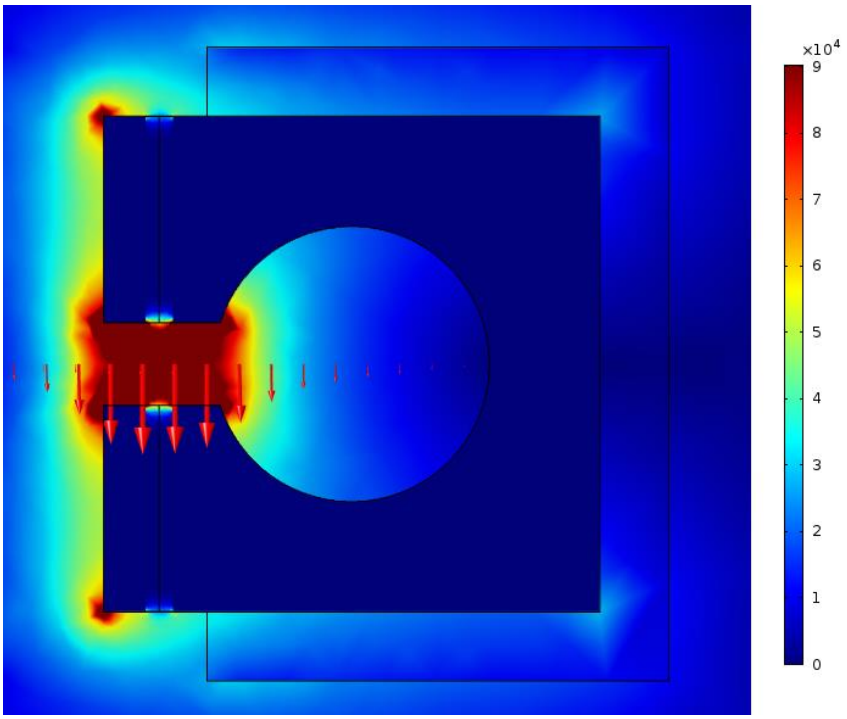

Figure 5.15 Cross sectional top view for the electric field (V/m) and direction for the microwave cavity-split ring resonator.

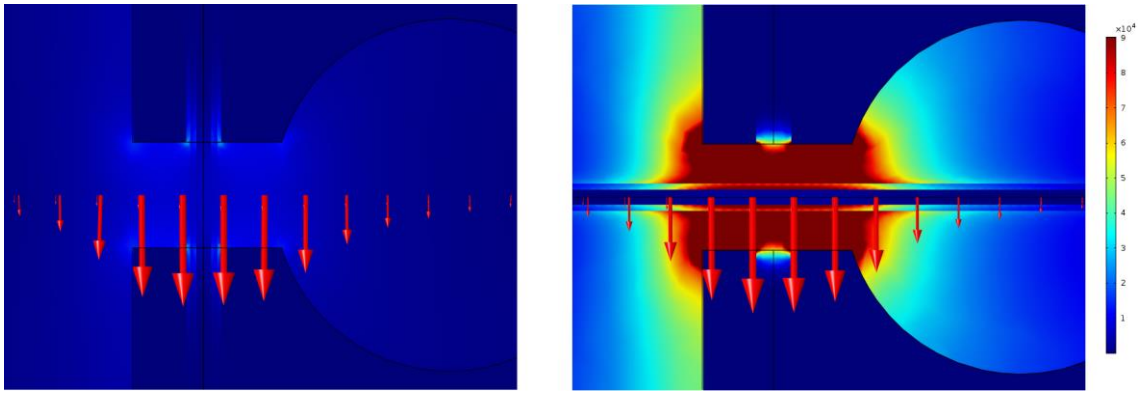

(a) (b)

Figure 5.16 Simulation results for the electric field (V/m) when FEP tube filled by water presented in two positions, horizontal (a) and vertical (b) with applied electric field in the gap of the split ring resonator.

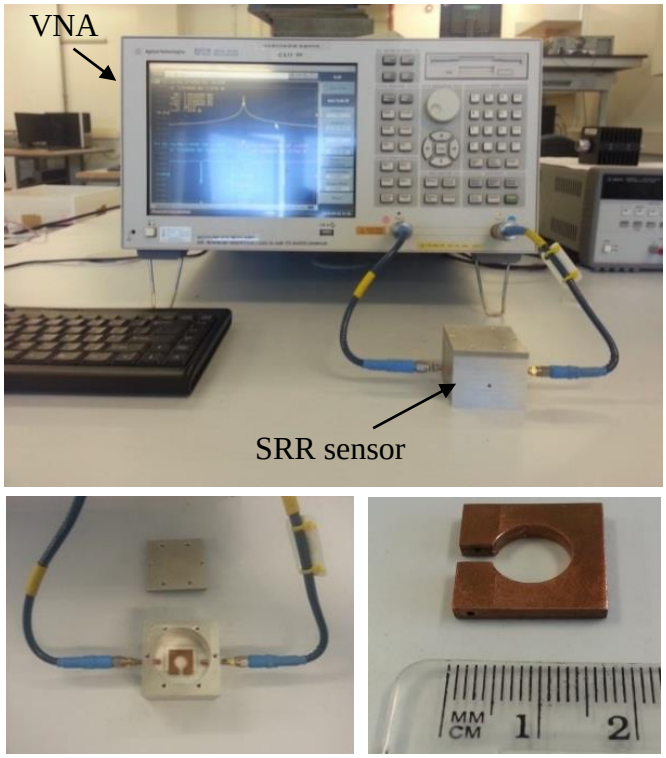

Figure 5.17 Cavity-split ring resonator connected the VNA.

Figure 5.18 shows transmission coefficient S_{21}, measured (solid) and simulated (dashed) for the three cases, when the resonator is empty (no sample), and when the FEP tube is filled with water and inserted in two positions: vertical (V) and horizontal (H) with respect to the electric field in the split ring gap.

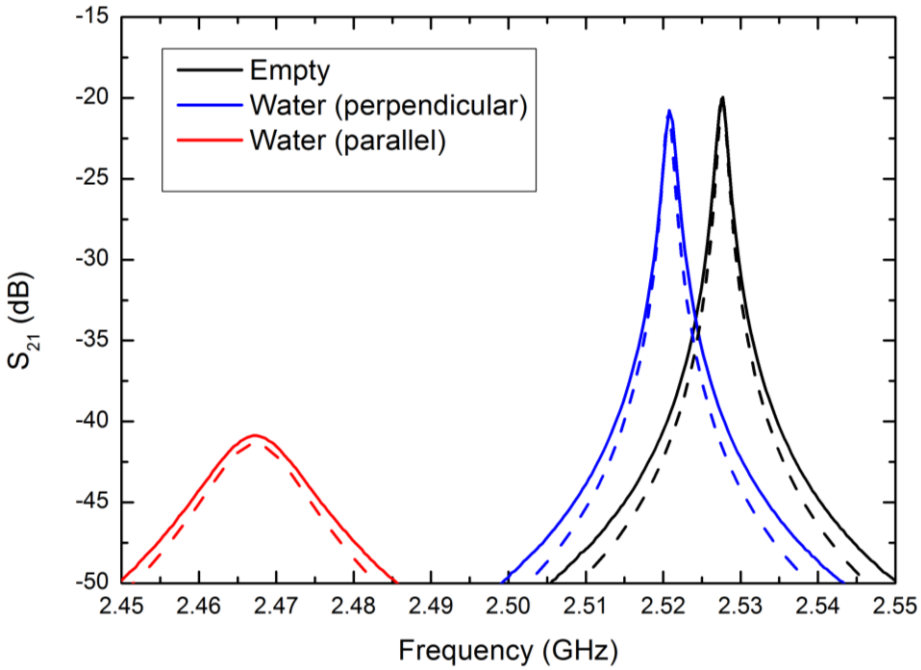

Figure 5.18 Measured (solid) and simulated (dashed) transmission coefficient $|S_{21}|$, with and without water sample in the vertical position with the electric field (sample perpendicular to the electric field), and in the horizontal position (sample parallel to the electric field).

It is obvious from Figures 5.16 and 5.18 that placing a microfluidic tube sample in parallel with the electric field results in higher power absorption by the dielectric sample and increases the sensor sensitivity for the material under test (MUT), since the internal electric field inside the dielectric sample is approximately equal to the applied electric field, as shown in Figure 5.19.

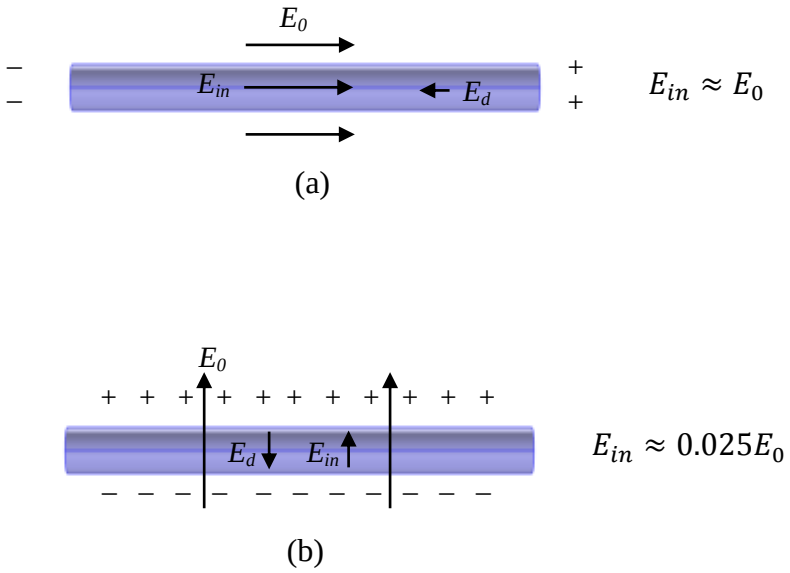

Figure 5.19 The depolarized field E_d affects in a water sample of cylindrical shape, (a) when the applied electric field in parallel to the sample, (b) when the applied electric field is perpendicular to the sample.

5.7. Liquids Test Results

The solvents measured were deionised water, methanol, ethanol, and chloroform, from which complex permittivity values were extracted. The Debye model equation (4.56) was coded into COMSOL for the parallel simulations. ε_s, ε_∞, and τ are considered as in Table 3.1 in CHAPTER THREE.

Figure 5.20 shows the simulated and measured voltage transmission coefficient $|S_{21}|$. From equations (5.12) and (5.14) we can write that for the parallel orientation

$$\Delta f \approx -\gamma(\varepsilon_1 - 1) \tag{5.23}$$

$$\Delta\left(\frac{1}{Q}\right) \approx 2\gamma\varepsilon_2 \tag{5.24}$$

where γ is a dimensionless constant, approximately equal to $V_s/2V_{eff}$, where V_s is the sample volume in the gap region and V_{eff} is the effective volume of the gap region, accounting also for field fringing effects. We can calculate γ for the SRR using the COMSOL simulations, which can then be used to convert resonant frequency and Q

factor data into real and imaginary parts of complex permittivity ε, respectively. Table 5.2 presents simulated and experimental results for the above liquids in terms of the SRR's resonant frequency, quality factor, and insertion loss for the sample in the parallel geometry. There is very good agreement between simulated and experimental data, with results indicating that our split ring is very sensitive to liquid type.

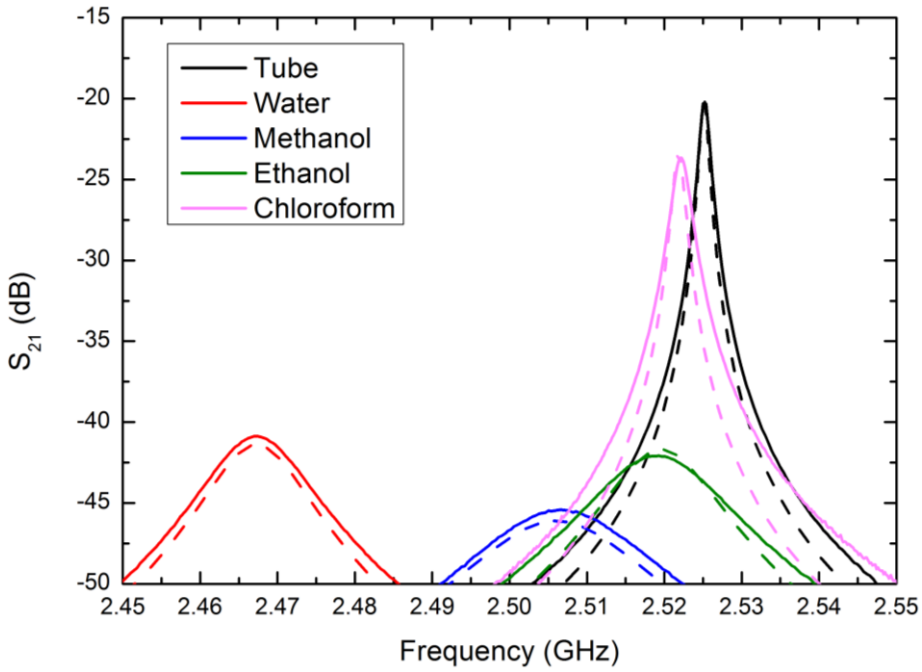

Figure 5.20 Measured (solid) and simulated (dashed) $|S_{21}|$ for several solvents at 25ºC.

Table 5.2

Summary of simulated and measured values for the complex permittivity

Resonator	Simulated f_0 (GHz)	Measured f_0 (GHz)	Simulated Q	Measured Q	Simulated IL (dB)	Measured IL (dB)	V_s/V_{eff}	Simulated Permittivity	Measured Permittivity	Error
Empty (tube)	2.525	2.525	1855	1848	-20.036	-20.313				
Water	2.467	2.467	258	250	-41.381	-40.886	0.0006051	77.18-j9.23	77.18-j8.09	0.9%
Methanol	2.506	2.507	122	110	-46.102	-45.425	0.0007298	21.84-j13.16	20.75-j11.74	1.6%
Ethanol	2.520	2.519	151	141	-41.691	-42.089	0.0007744	6.83-j6.78	7.34-j8.46	1.8%
Chloroform	2.521	2.522	958	943	-23.348	-23.672	0.0007092	4.69-j0.28	4.57-j0.732	2.4%

5.8. HCl and NaOH Test Results

The measurement of pH plays a very important role in wide range of industrial, chemical, and biological applications. These include water conditioning to specific process-related measurements to waste treatment and especially in chemical processing where reactions influenced by acidity. A sensitive, non-invasive method to measure pH, without the use of electrodes, would be very attractive to all of these applications.

Acidity and alkalinity are related terms. Acidity is produced by substances that liberate or contribute hydrogen ions in a solution while alkalinity is produced by substances that liberate or contribute hydroxide ions in a solution. Acidity is a net effect of the existence of several constituents, including dissolved carbon dioxide, dissolved multivalent metal ions, strong mineral acids such as sulfuric, nitric, and hydrochloric acids, and weak organic acids such as acetic acid. Like acidity, alkalinity is a net effect of the presence of several constituents such as bicarbonate (HCO_3^-), carbonate (CO_3^{2-}), and hydroxide (OH^-) ions. Alkalinity is often taken as an indicator for the concentration of these constituents. There are other, usually minor, contributors to alkalinity, such as ammonia, phosphates, borates, silicates, and other basic substances [124] - [125].

The pH scale measures the concentration of hydrogen ions in a solution, where the pH value or hydrogen ion concentration is a measure of the acidity or alkalinity of a substance. Acidity is caused in the solution if $[H^+]$ ions are in excess over $[OH^-]$ ions and alkalinity when the reverse happens. pH value is expressed as:

$$pH = \log\left[\frac{1}{H^+}\right] \tag{5.28}$$

where H^+ is hydrogen ion concentration in mol/L.

At pH = 7, the ratio of (H^+) to (OH^-) is equal and hence the solution is neutral, the pH scale is ranged from 0 (strong acid) to 14 (strong alkaline or basic) as shown in Figure (5.22) [125].

Microwave resonators like our SRR are very appropriate for the determination of moisture and density of chemical ingredients in liquids via dielectric property

measurement. Owing to their penetration into aqueous media by a few cm, microwaves can be used not only to assess the surface moisture of the material under test, but also the moisture in the core of that material [126], [127].

Our aim here is to assess our SRR's application to sensitive measurements of small changes in pH of an aqueous solution. Hydrochloric acid (HCl) and sodium hydroxide (NaOH) were used in the test. Samples have been prepared for different pH levels for each chemical solution by diluting them with de-ionised water and checking using a conventional pH meter.

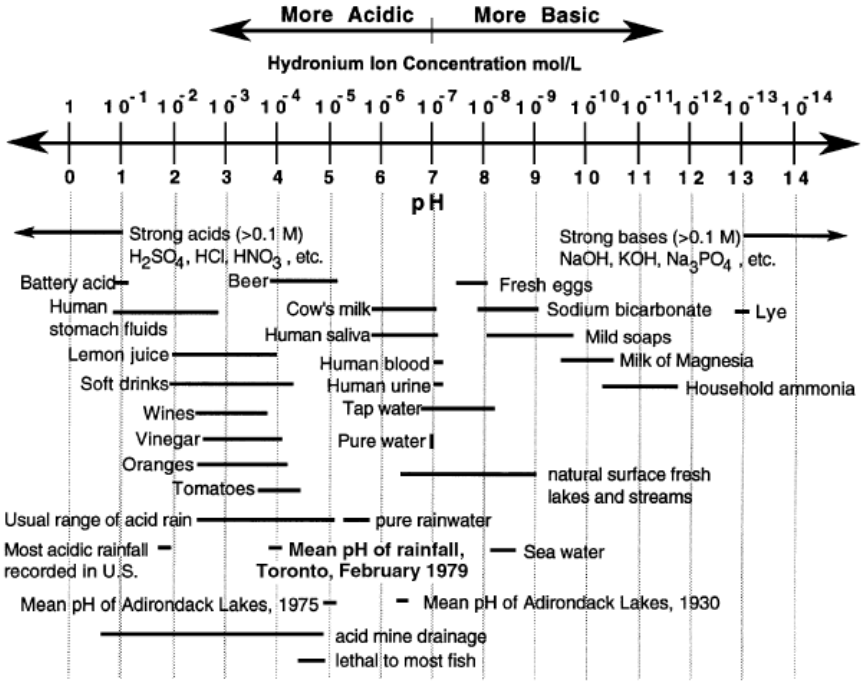

Figure 5.22 pH scale and typical pH values of some common substances [125].

Pure water always contains a small number of molecules that have dissociated into hydrogen ions $[H^+]$ and hydroxide ions $[OH^-]$ and they are equal at 25^0C, $[H^+] = [OH^-] = 1 \times 10^{-7}$ mol/L, as shown in equation (5.29). The hydrogen ions and hydroxide ions can be seen in equations (5.30) and (5.31) for hydrochloric acid (HCl) and sodium hydroxide (NaOH) respectively.

$$\underset{\text{water}}{H_2O} \leftrightarrow \underset{\text{hydrogen ion}}{H^+} + \underset{\text{hydroxide ion}}{OH^-} \tag{5.29}$$

$$\underset{\text{Hydrochloric acid}}{HCl} \rightarrow \underset{\text{hydrogen ion}}{H^+} + \underset{\text{chloride ion}}{Cl^-} \tag{5.30}$$

$$\underset{\text{sodium hydroxide}}{NaOH} \rightarrow \underset{\text{sodium ion}}{Na^+} + \underset{\text{hydroxide ion}}{OH^-} \tag{5.31}$$

The SRR was found to be very sensitive for detecting pH changes and was able to indicate the acidity or alkalinity of the tested substances listed in Table 5.3. Whereas the resonant frequency was found not to be sensitive to the pH level for HCl, as shown in Figure 5.23, the quality factor (Q) was found to be sensitive and increased with pH level towards low acidity, as shown in Figure 5.24. One would expect these observations, since the presence of $[H^+]$ ions increases the ionic conductivity σ of the solution which increases ε_2 to first order owing to the additive contribution $\sigma/\omega\varepsilon_0$, but with little effect on ε_1.

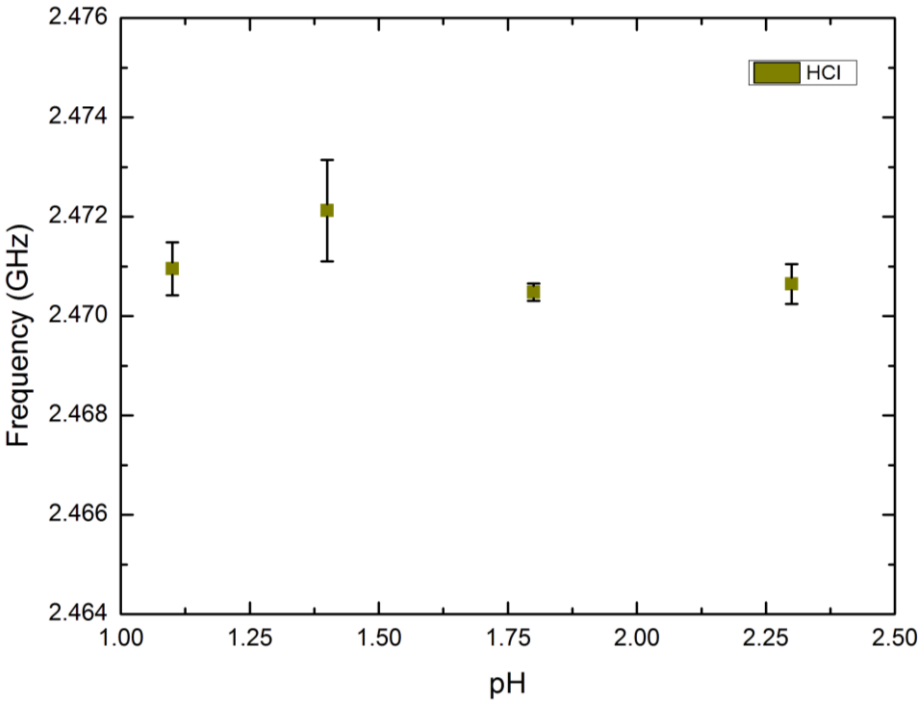

Figure 5.23 Resonant frequency response vs. pH for HCl

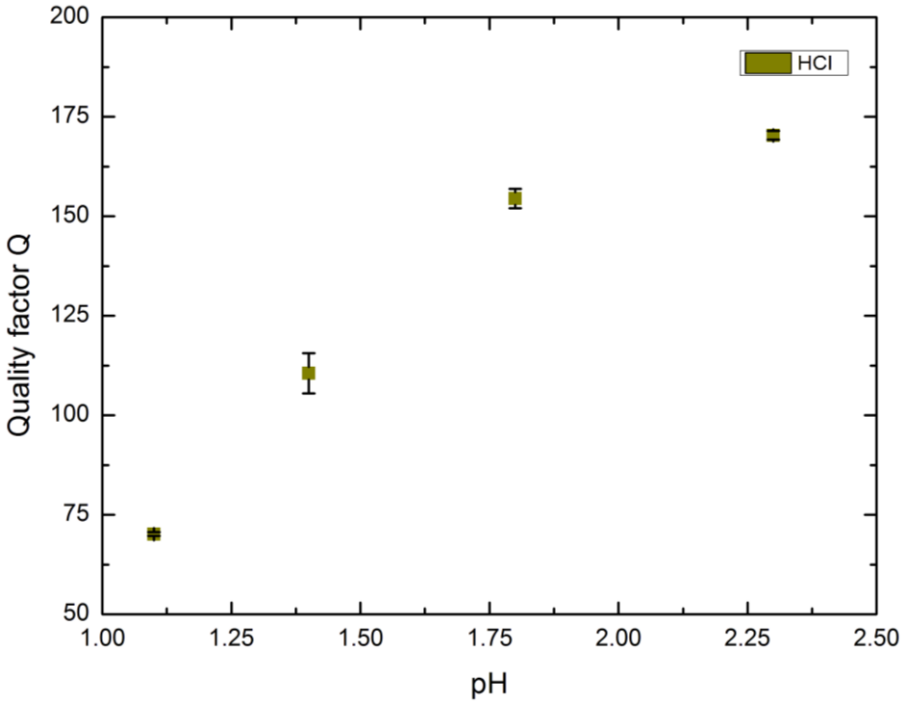

Figure 5.24 Quality factor Q change vs. pH for HCl

In Figure 5.25, the dimensionless parameter $\Delta f/\Delta f_B$ has been plotted as a function of pH, which from Equations (5.23) and (5.24) removes any small uncertainty owing to sample volume. Significance testing of this correlation using SPSS yields a p-value of less than 0.05, indicative of the excellent correlation.

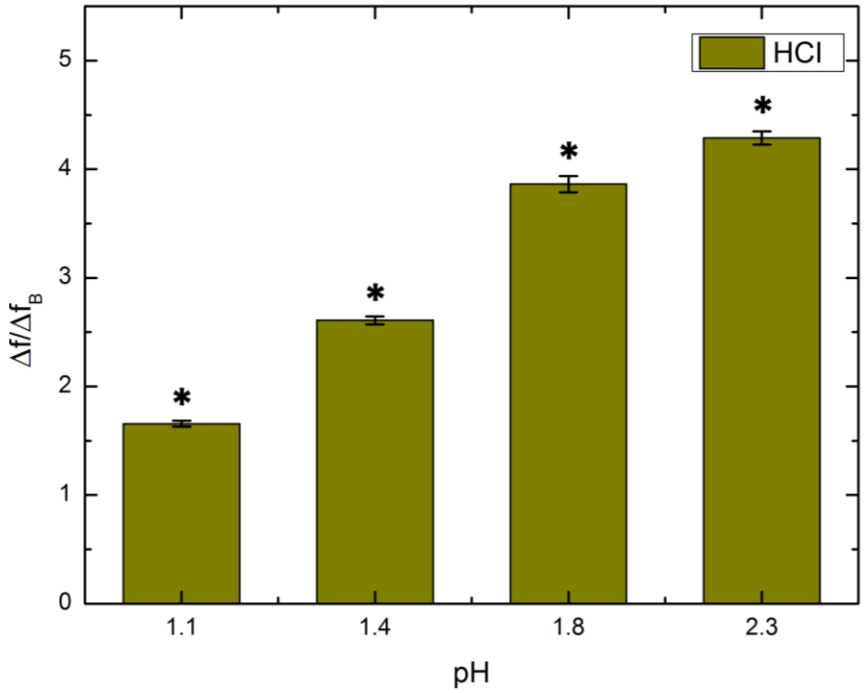

Figure 5.25 Δf/ΔBW vs. pH for HCl. (*) means the difference is significant ($p < 0.05$) between the pH groups.

Similar behaviour of the SRR was observed with the alkaline NaOH, as to be expected as the origin of the resonator perturbation was due to Q factor change due to ionic conductivity change, this time with increasing [OH^-].

The resonant frequency was again insensitive to the pH level, as shown in Figure 5.26, while the quality factor (Q) was sensitive for pH change and decreased with the pH level increase towards higher alkalinity, as shown in Figure 5.27.

Again, plotting the dimensionless parameter $\Delta f/\Delta f_B$ as a function of pH (as in Figure 5.28) and performing an SPSS significance test yields a p-value of less than 0.05, indicative of the excellent correlation.

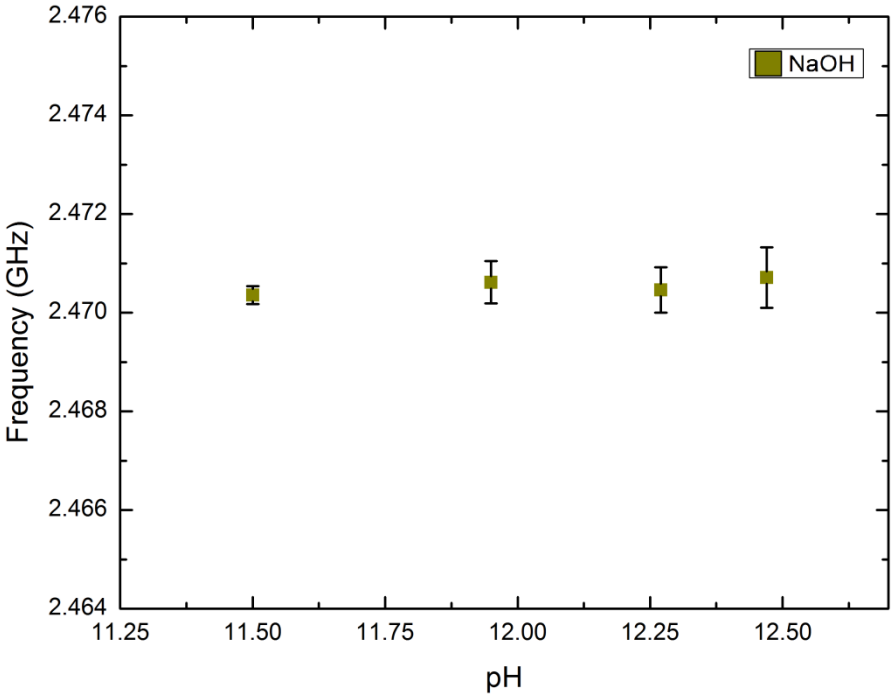

Figure 5.26 Resonant frequency response vs. pH for NaOH

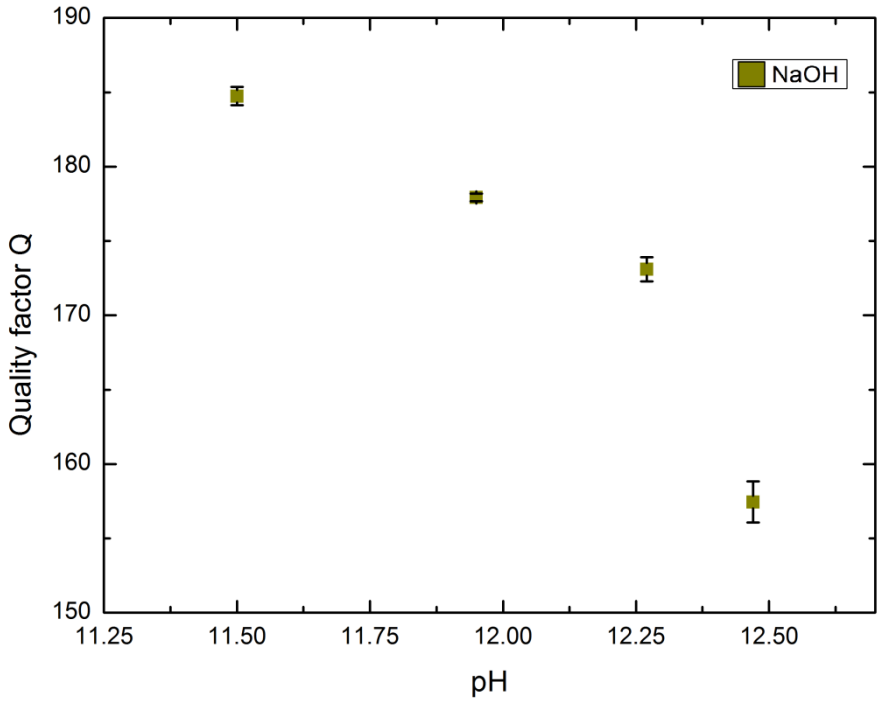

Figure 5.27 Quality factor Q change vs. pH for NaOH

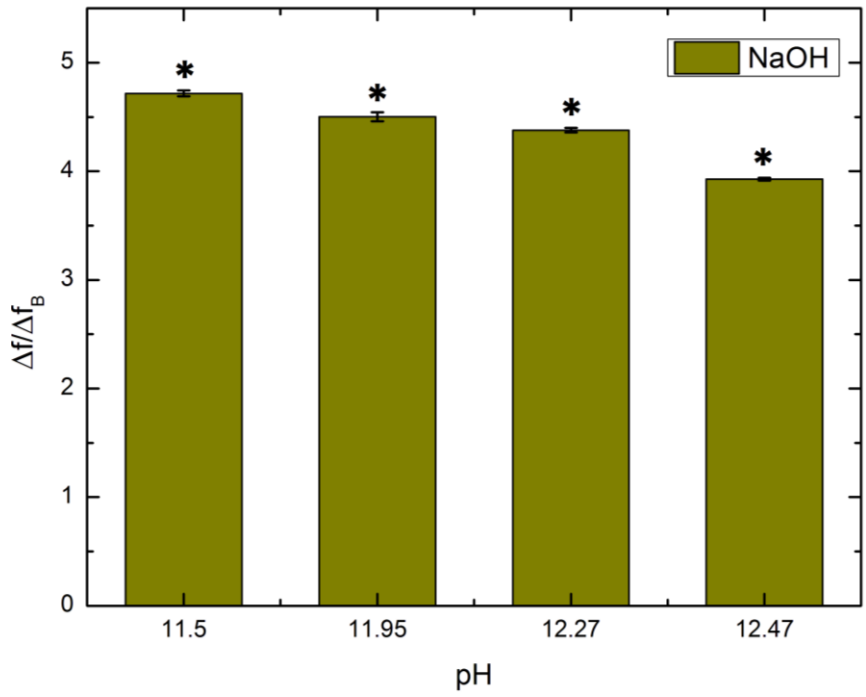

Figure 5.28 Δf/ΔBW vs. pH for NaOH. (*) means the difference is significant ($p < 0.05$) between the pH groups.

Although the SRR is able to measure pH of both acid and alkaline solutions non-invasively (i.e. with the solution in a plastic tube) with a high degree of accuracy, it is not able to deduce absolutely whether an unknown liquid is acid or alkaline. The simple reason for this is that it measures changes in ionic concentration through changes in ionic conductivity, and both increasing acidity and alkalinity will produce the same sorts of reductions in Q. However, if the starting pH of a solution is known, we have shown that the SRR is then capable of resolving very small subsequent pH changes, in a non-invasive way without the use of electrodes (which is the critical point), with an error of less than ±0.01.

Table 5.3

Experimental results for HCl and NaOH

Solution	pH Value	Measured fo (GHz)	Measured fr (GHz)	Measured Unloaded Quality (Q_o)	Measured Loaded Quality (Q_L)	Measured Unloaded f_{B0} (MHz)	Measured Loaded f_{BL} (MHz)	$\Delta f/\Delta f_B$	Error
HCl	1.1	2.527	2.471	1858	70	1.36	35.30	1.65	0.03
HCl	1.4	2.527	2.472	1858	109	1.36	22.66	2.67	0.04
HCl	1.8	2.527	2.470	1858	157	1.36	15.73	4.00	0.07
HCl	2.3	2.527	2.470	1858	171	1.36	14.44	4.36	0.06
NaOH	11.5	2.527	2.470	1858	185	1.36	13.35	4.75	0.03
NaOH	11.95	2.527	2.470	1858	178	1.36	13.88	4.55	0.04
NaOH	12.27	2.527	2.470	1858	172	1.36	14.36	4.38	0.02
NaOH	12.47	2.527	2.471	1858	157	1.36	15.73	3.96	0.01

5.9. Saline Test Results

There is a wide demand for highly sensitive and stable NaCl sensors for chemical and metal industries, food processing, and biological research. Aqueous NaCl solutions play a major role in many chemical processes in many chemical and biological systems. Sensitive detection of NaCl concentration in water is a helpful tool for studying the electrical and biological properties of samples. Commercial development of these tools has allowed measurement of NaCl concentration with sufficient accuracy. However, the tools are largely restricted to monitoring patterns and trends and are invasive, relatively expensive and time consuming. Accordingly, techniques with high sensitivity and accuracy for the detection of NaCl concentration using non-invasive and contactless technology are of importance in biosensor construction [128].

The dielectric properties of aqueous electrolyte solutions are of major importance for our understanding of the hydration and behaviour of ions, specifically for our knowledge of related elementary mechanisms in liquids, such as electric conductivity. Also, there is interest in the interaction between electromagnetic waves and the saline solutions initiated from a variety of applications, including the use of microwaves as sensors in the measurements of the water content in soils and in the non-invasive moisture determination of many liquids and materials [129].

Microwave sensors are widely utilized for monitoring the concentration of various mixture solutions. This parameter must be determined with high accuracy for different applications, such as food and pharmaceutical industries, chemical processing, environmental monitoring etc., where the content of substances in water is a critical variable [130].

Different concentration samples of NaCl (Sodium chloride) dissolved in deionized water have been prepared and tested at 25^0C; the results are listed in Table 5.4. As seen from Figures 5.29 and 5.30 for the change of resonance frequency and quality factor Q against NaCl concentration, the resonance frequency doesn’t change significantly with lower concentrations, when there is small increment in the concentration level. On the other hand, the quality factor Q decreases with increases in the concentration level, even at very low levels of concentration with small increments.

As has already been discussed in the context of pH, ionic conductivity usually introduces losses into a material. The dielectric loss of a material can be described as a function of both dielectric loss (ε_{2d}) and conductivity (σ):

$$\varepsilon_2 = \varepsilon_{2d} + \frac{\sigma}{\omega\varepsilon_0} \tag{5.32}$$

The conductivity of a material may arise due to many different conduction mechanisms. The most common one in moist materials is ionic conductivity, where ε_2 at low frequencies is dominated by the effect of electrolytic conduction caused by free ions in the presence of a solvent, water being a prime example. The effect of ionic conductivity on the dielectric loss term is inversely proportional to operating frequency, whilst has little effect on the overall polarisation as can be seen by equation (5.32).

The SRR sensor shows high sensitivity to the concentration of NaCl in deionized water, where the NaCl concentration level affects the imaginary part of the dielectric permittivity, leading to reduced Q. However, the real part of permittivity is less sensitive, as can be seen by the much smaller frequency shift.

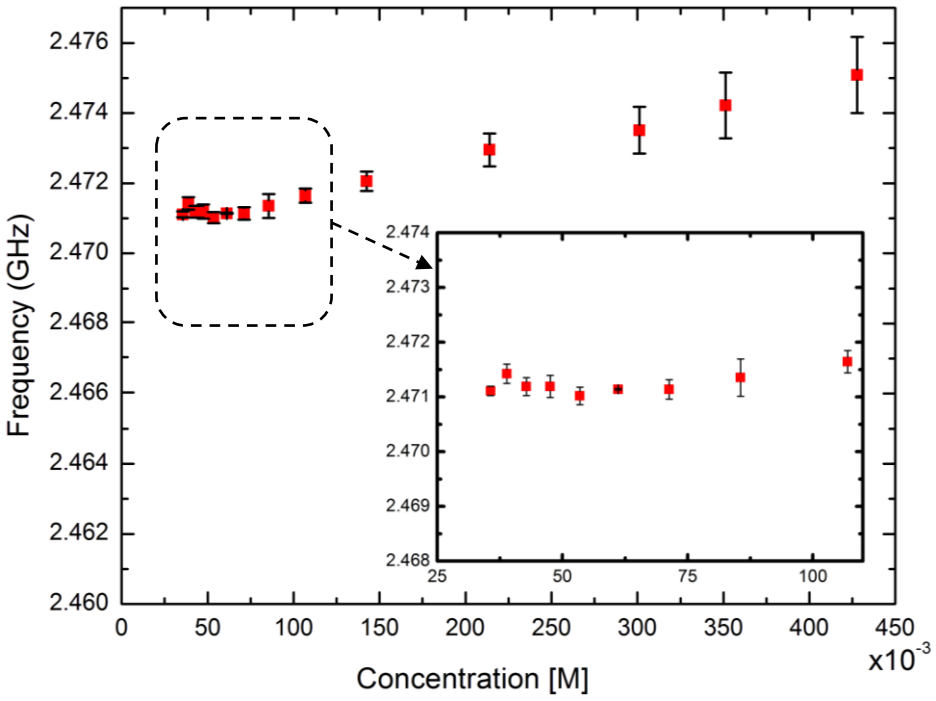

Figure 5.29 Resonant frequency change against NaCl concentration.

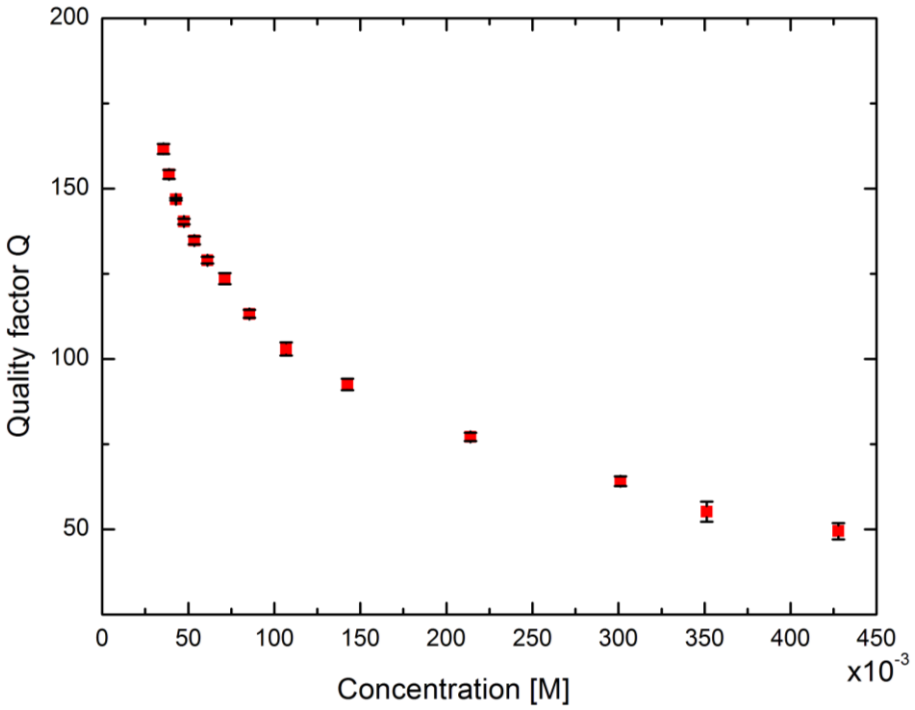

Figure 5.30 Quality factor change against NaCl concentration.

They are again significant ($p < 0.05$) variations of $\Delta f/\Delta f_B$ against the concentration level, and the SRR sensor is very sensitive for small change in salt concentration, as shown in Figure 5.31.

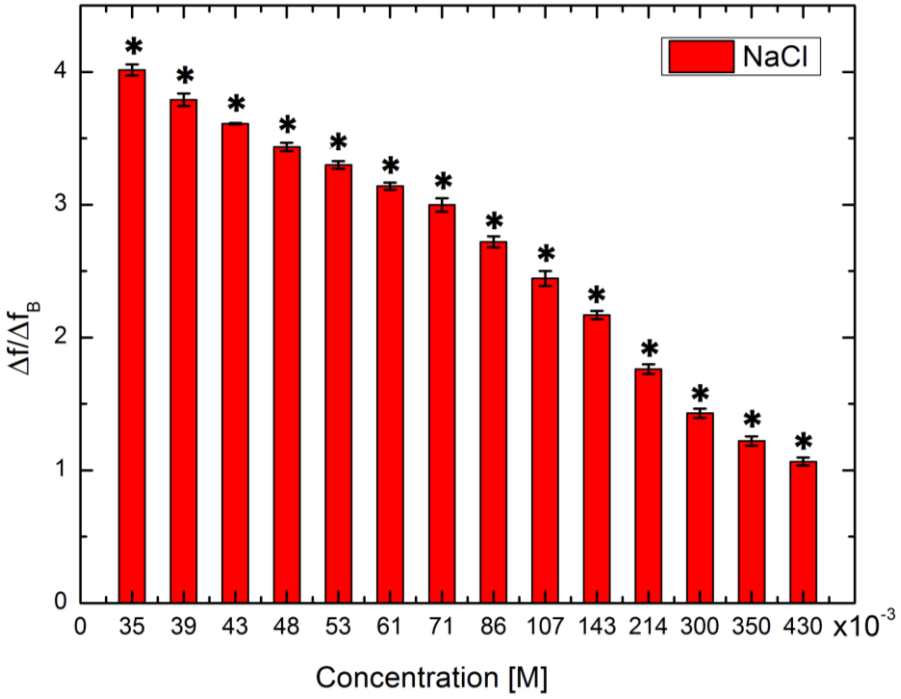

Figure 5.31 $\Delta f/\Delta f_B$ vs. NaCl concentration. (*) means the difference is significant ($p < 0.05$) between different concentrations.

Table 5.4
Experimental results for saline

Solution	NaCl Concentration [M]	Measured f (GHz)	Unloaded Quality (Q_o)	Loaded Quality (Q_L)	Unloaded f_{B0} (MHz)	Loaded f_{BL} (MHz)	$\Delta f/\Delta f_B$	Error
Saline	0	2.467	1858	184	1.36	13.39	4.96	0.065
Saline	0.035	2.471	1858	152	1.36	16.26	4.01	0.041
Saline	0.039	2.471	1858	148	1.36	16.65	3.74	0.046
Saline	0.043	2.471	1858	147	1.36	16.79	3.60	0.006
Saline	0.048	2.471	1858	141	1.36	17.49	3.47	0.032
Saline	0.053	2.471	1858	135	1.36	18.34	3.31	0.029
Saline	0.061	2.471	1858	128	1.36	19.30	3.11	0.027
Saline	0.071	2.471	1858	122	1.36	20.30	2.94	0.051
Saline	0.086	2.471	1858	115	1.36	21.40	2.75	0.042
Saline	0.110	2.471	1858	105	1.36	23.63	2.50	0.056
Saline	0.140	2.472	1858	94	1.36	26.17	2.20	0.031
Saline	0.210	2.473	1858	79	1.36	31.47	1.80	0.037
Saline	0.312	2.473	1858	64	1.36	38.65	1.43	0.035
Saline	0.351	2.474	1858	55	1.36	44.98	1.22	0.035
Saline	0.430	2.475	1858	49	1.36	50.10	1.06	0.030

5.10. SRR For Microfluidic Sensing

In this chapter, a novel split ring resonator has been proposed as a microfluidic sensor. The two main advantages, both of which increase sensitivity for dielectric measurement, are its low volume over which the electric field energy is concentrated (effectively the gap region, only about 10 mm^3) and the low amount of electric field depolarisation within the sample when it is in the parallel geometry. It has been tested for dielectric property measurement with some common solvents; water, methanol ethanol and chloroform. The sensor was able to efficiently characterize the dielectric properties of the solvents, where there was excellent agreement between simulated and experimental results.

Furthermore, the sensor has been tested as a pH meter with hydrochloric acid (HCl) and sodium hydroxide (NaOH). From the experimental results, the proposed SRR was very sensitive to the pH level for both HCL and NaOH in terms of change in quality factor (Q) change. It means the sensor can specify and track changes in the acidity or alkalinity of the solution provided a starting point (on the acid or alkaline side) is given. Also, saline solutions (NaCl dissolved in water) of different concentrations were incorporated into the tests, where it was found that the quality factor (Q) decreased with the increases in salt concentration, whilst the resonant frequency was less sensitive to changes in salinity.

CHAPTER SIX
HIGH POWER SYSTEM DESIGN

6.1. Introduction

A special pulsed microwaving delivery system has been designed and built to deliver both high and low power microwave for sample activation (thermal, or non-thermal when pulsed). Figure 6.1 shows the schematic for the whole system incorporating the split ring resonator. It is built from TELEMAKUS and Mini-Circuits equipment, a variable attenuator, and power amplifier. All of these are controlled by a laptop through LabVIEW software. A programmable syringe pump (Aladdin-220, World Precision Instruments, UK) is also used to keep a constant flow rate. The whole circuit is shown in detail in Figure 6.2.

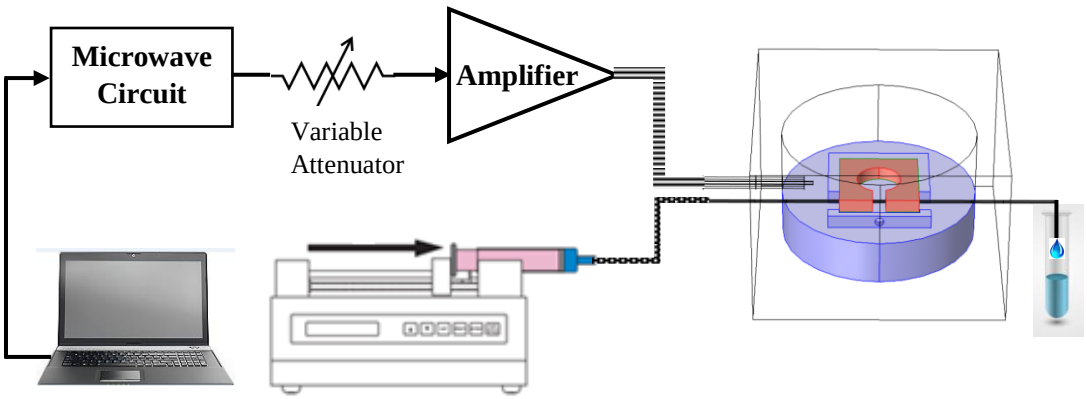

Figure 6.1 Schematic of the whole system, controlled by PC using LabVIEW software.

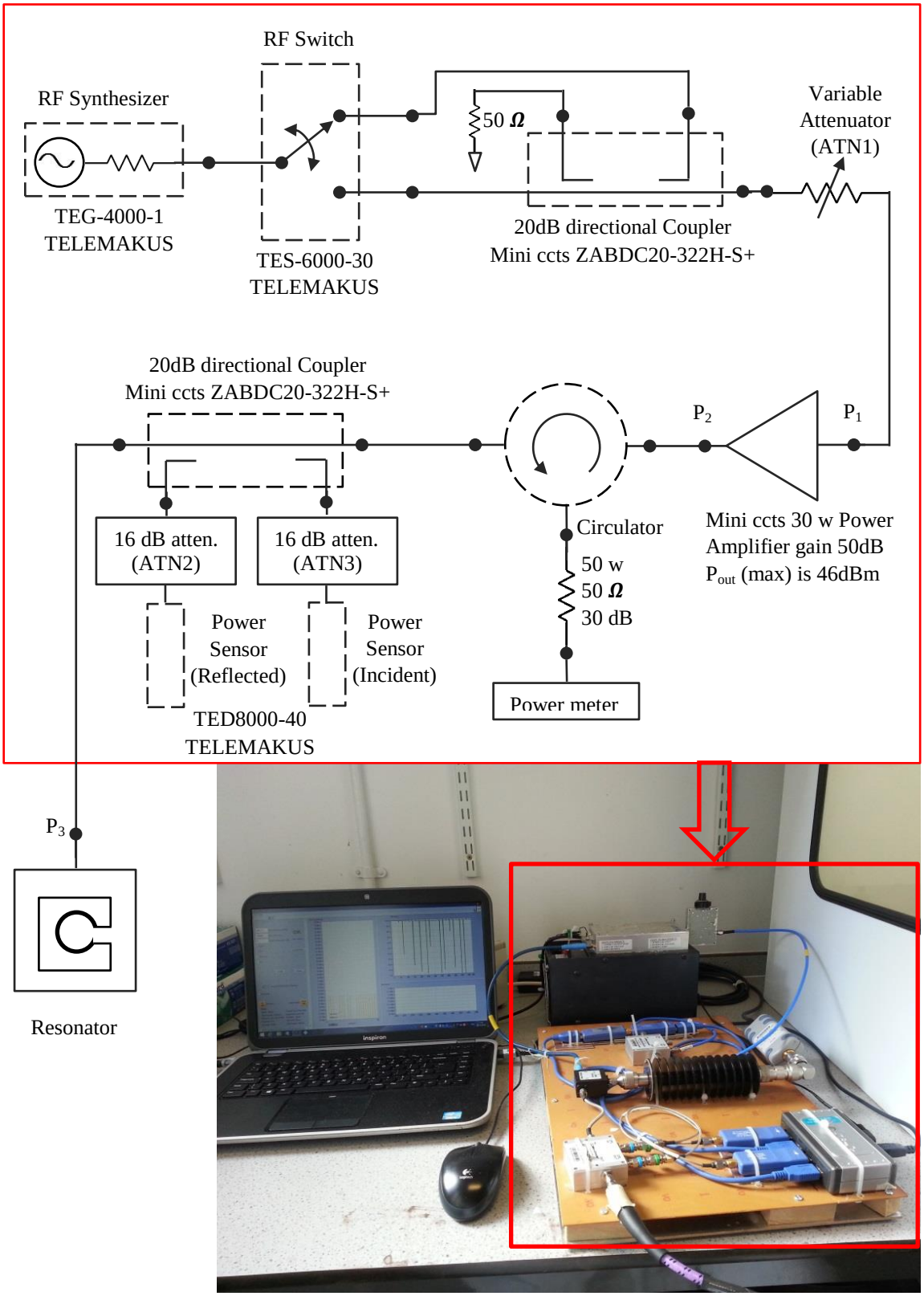

Figure 6.2 Microwaving circuit, controlled by PC via LabVIEW software.

6.2. Microwave Circuit Operation

The RF synthesizer generates an RF signal at low power level ~0.001 W (0 dBm) and there is an RF switch to modulate the signal. A directional coupler is used to split the signal, consisting of a four-port waveguide junction, as shown in Figure 6.3. It has a primary waveguide (port 1-port 2) and a secondary, coupled, waveguide (port 3-port 4). When all ports are terminated in their characteristic impedances, there is free transmission of power, without reflection between port 1 and port 2, and there is no transmission of power between port 1 and port 3 or between port 2 and port 4 because no coupling exists between these two pairs of ports. The level of coupling between port 1 and port 4 and between port 2 and port 3 depends on the structure of the coupler. The characteristics of a directional coupler can be expressed in terms of its coupling factor and its directivity. Assuming that the wave is propagating from port l to port 2 in the primary line, the coupling factor and the directivity are characterized individually by [131]:

$$\text{Coupling factor (dB)} = 10\log_{10}\frac{P_1}{P_4} \tag{6.1}$$

$$\text{Directivity (dB)} = 10\log_{10}\frac{P_4}{P_3} \tag{6.2}$$

P_1= power input to port 1
P_3= power input to port 3
P_4= power input to port 4

It should be stressed again that port 2, port 3, and port 4 are terminated in their characteristic impedances. The coupling factor is a measure of the ratio of power levels in the primary and secondary waveguides. Consequently if the coupling factor is known, a fraction of power measured at port 4 may be used to determine the power input at port 1.

This is highly significant for microwave power measurements because no disturbance can occurs in the primary line. The directivity is a measure of how well the forward traveling wave in the primary waveguide couples only to a specific port of the

secondary waveguide. Perfect or ideal directional couplers should have infinite directivity. In other words, the power at port 3 must be zero because port 2 and port 4 are perfectly matched. Actually, our designed directional couplers have a directivity of 20 dB (Mini ccts ZABDC20-322H-S+).

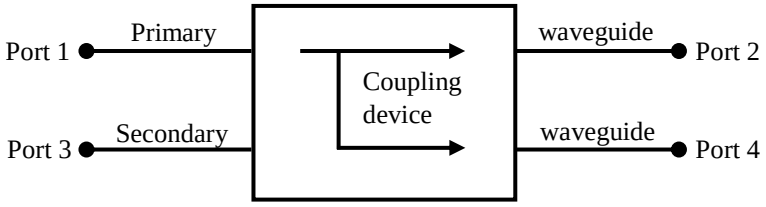

Figure 6.3 Directional coupler [131].

A power amplifier is used for high power amplification (ZHL-30W-252-S+, Mini ccts) and variable attenuator to adjust the required input power level.

A microwave circulator is utilized in the circuit design to protect the power amplifier from the reflected power. A microwave circulator is a multiport waveguide junction in which the microwave signal flows only in one direction from port 1 to port 2 as shown in Figure 6.4. The component chosen here is the RACAL MESL Circulator, with -20 dB isolation.

The junction circulator's basic operational principle is based on two counter-rotating wave components or modes. As shown in Figure 6.4, the two modes must propagate at different velocities for circulator action to occur. For coupling from port 1 to port 2, the phase difference between the clockwise CW(+) and counterclockwise CW(-) modes must be $N2\pi$:

$$2\beta_{-}L - \beta_{+}L = 2N\pi \tag{6.3}$$

where β is the phase constant of the positive or negative mode, keeping in mind that the negative wave must travel twice the distance the positive wave travels to reach port 2. N denotes any integer and L is the distance crossed by a wave. For port 3 to be decoupled or nulled, the two wave components reaching this port must differ in phase by an odd multiple of π, i.e.

$$-\beta_{-}L + 2\beta_{+}L = (2M - 1)\pi \tag{6.4}$$

where M is any integer. By solving (6.3) and (6.4) simultaneously, we get

$$\beta_{-}L = \frac{4N + 2M - 1}{3}\pi \tag{6.5}$$

$$\beta_{+}L = \frac{2N + 4M - 2}{3}\pi \tag{6.6}$$

When (6.5) and (6.6) are satisfied, we have perfect circulation [132].

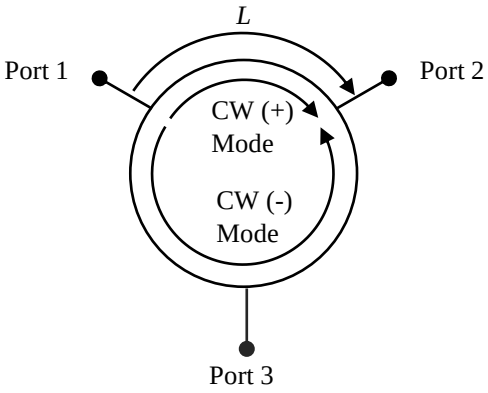

Figure 6.4 Circulator symbol and rotating modes [132].

The power meter attached to the circulator in Figure 6.2 is an additional way of accessing the reflected wave, and allows us to measure and observe the reflected power in the pulse. The power meter is fast enough to show how the reflection coefficient changes during the pulse, and gives us some additional information.

Two USB power sensors (TED8000-40 TELEMAKUS) are used to measure the incident and reflected powers.

Measurements have been recorded in Table 6.1 and two cases have been considered in these measurements: when the attenuator is 20 dB, and when there is no attenuator. The delivered power then ranges from 1 Watt to maximum of 30 Watts, depending on the attenuator value, and then it can be set according to the required power level.

Table 6.1

Power measured values

Power level	ATN1 (dB)	ATN2 (dB)	ATN3 (dB)	P_1 (dBm)	P_2 (dBm)	P_3 (dBm)
High (30 W)	0	16	16	0	45	44.5
Low (1 W)	20	0	0	-20	30.5	30

In terms of power absorption, the maximum internal electric field of a water sample within the SRR (or any resonant cavity) occurs when the sample is oriented parallel with the applied electric field. So, maximum power has been absorbed by the water sample as shown in Figure 6.5, which shows simulation results using COMSOL Multiphysics software.

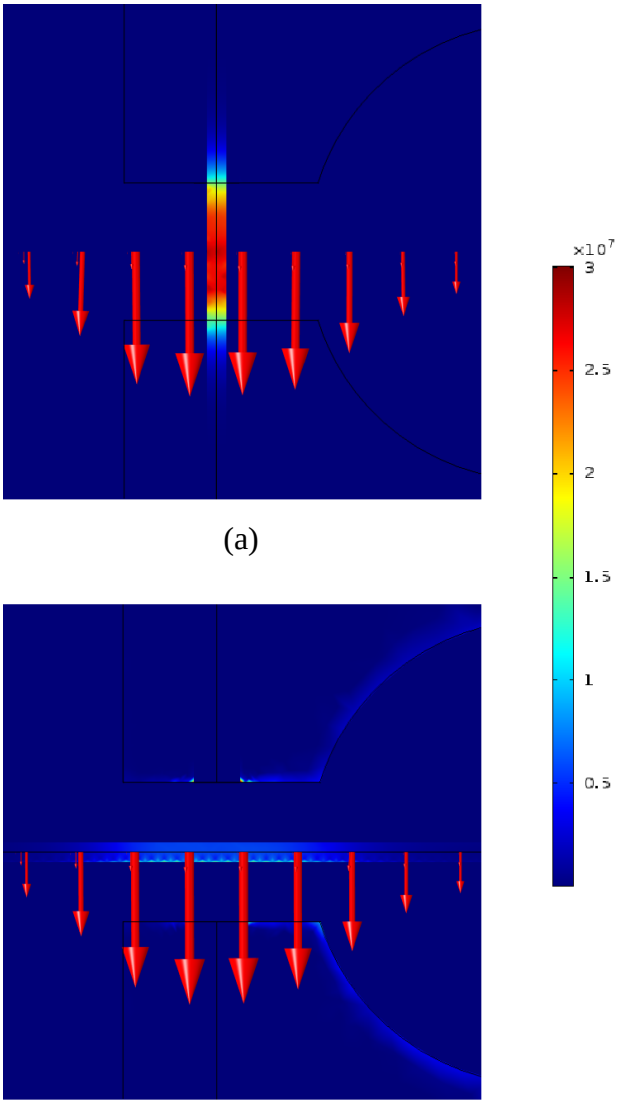

(a)

(b)

Figure 6.5 Simulation results for the power dissipation density (W/m^3) when an FEP tube filled with water placed in two orientations: (a) parallel, and (b) perpendicular with applied electric field in the gap of the split ring resonator.

6.3. Power Delivery Efficiency

There is a significant variation of the dielectric constant of polar liquids, such as water, with temperature due to the effect of heat on orientational polarization. The complex dielectric constant describes the collective motion of the molecular dipole moments under the influence of an electric field. In liquid water, the molecules are connected by a disordered network of hydrogen bonds, in which a hydrogen atom of one molecule is

attracted to the oxygen atom of another molecule that is located within a distance of a few angstroms [133], [134].

If the water temperature is increased, this will decrease the strength and extent of the hydrogen bonding in water; so reducing the frictional forces between water molecules and accordingly these molecules can rotate more easily. As a result, the permittivity decreases with temperature increasing [135]-[139].

6.3.1. Power Delivery Efficiency of The Split Ring Resonator

The efficiency of the split ring resonator has been measured in terms of incident and reflected power using DI-water sample. A programmable syringe pump has been set to control a constant flow rate. The resonant frequency was found to be 2413.25 MHz at room temperature (25^0C) at critical coupling for maximum power transfer requirement. Figure 6.6 shows the efficiency when the flow rate is constant at 1 ml/hr but the delivered power varies from 0.1 Watt to 1 Watt. It can be seen that efficiency is inversely proportional with the delivered power level. The higher microwave power, the higher the increase in water temperature, causing a shift in resonant frequency and an increase in the Q factor. This degrades the efficiency since the input impedance match is affected by the temperature change, which is particularly so in a high Q resonator such as this.

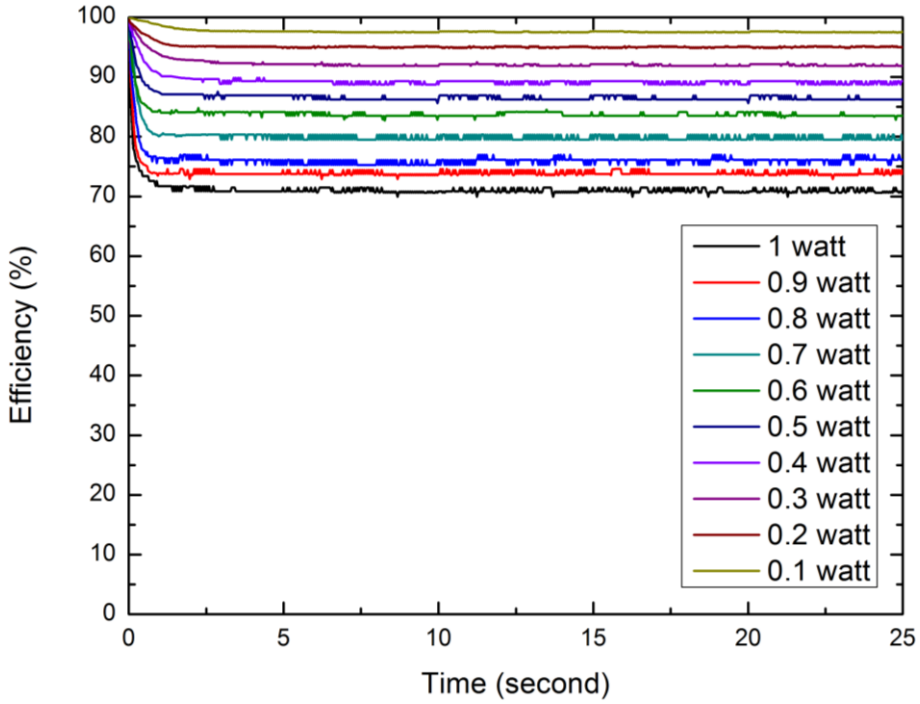

Figure 6.6 Delivered power efficiency of the split ring resonator, when the flow rate is constant at 1 ml/hr and different power levels.

Referring to the power reflection coefficient stated in CHAPTER FOUR equation (4.36), which is:

$$|S_{11}|^2 = \frac{(1-\mathrm{g})^2 + 4Q_o^2\left(\frac{f-f_o}{f_o}\right)^2}{(1+\mathrm{g})^2 + 4Q_o^2\left(\frac{f-f_o}{f_o}\right)^2} \tag{4.36}$$

At critical coupling, g ≈ 1. Assuming that the resonance frequency f_o changes to f_1, then:

$$f_o \rightarrow f_1 = f_o + \Delta f \tag{6.7}$$

$$\text{efficiency } (e) = (1 - |S_{11}|^2) \times 100\% \tag{6.8}$$

By substituting equation (4.36) into (6.8):

$$\text{efficiency } (e) = \left(1 - \frac{(1-\mathrm{g})^2 + 4Q_o^2\left(\frac{f-f_o}{f_o}\right)^2}{(1+\mathrm{g})^2 + 4Q_o^2\left(\frac{f-f_o}{f_o}\right)^2}\right) \times 100\% \tag{6.9}$$

$$\text{efficiency } (e) = \left(\frac{4\text{g}}{(1+\text{g})^2 + 4Q_o^2 \left(\frac{f - f_o}{f_o} \right)^2} \right) \times 100\% \tag{6.10}$$

Now, at initial state ($f = f_o$), which leads to initial efficiency (e_0):

$$e_0 = \frac{4\text{g}}{(1+\text{g})^2} \times 100\% \tag{6.11}$$

$\text{e}_0 \approx 100\%$, as $\text{g} \approx 1$ at critical coupling.

When the resonance frequency changes $f \rightarrow f_1$ due to heating, then the efficiency changes to e_1:

$$e_1 = \left(\frac{4\text{g}}{(1+\text{g})^2 + 4Q_o^2 \left(\frac{f_1 - f_o}{f_o} \right)^2} \right) \times 100\% \tag{6.12}$$

$$\frac{1}{e_1} - \frac{1}{e_0} = \frac{Q_o^2}{\text{g}} \left(\frac{f - f_o}{f_o} \right)^2 \tag{6.13}$$

Substituting for $\text{g} = 1$,

$$\frac{1}{e_1} - \frac{1}{e_0} = Q_o^2 \left(\frac{\Delta f}{f_o} \right)^2 \tag{6.14}$$

After mathematical simplifications, the change in resonant frequency due to increases in water temperature due to heating, in terms of reflected and incident power (efficiency) will be:

$$\Delta f = \frac{f_o}{Q_o} \sqrt{\frac{1}{e_1} - \frac{1}{e_0}} \tag{6.15}$$

The change in resonance frequency Δf in Table 6.2 has been calculated when the power increased from 0.1 to 1 Watt and after setting values of f_o and Q_o to 2413.25 MHz and 250 respectively. It can be seen from Figure 6.7 which is plotted according to equation (6.15), the relationship between the change in resonance frequency Δf and $\sqrt{\frac{1}{e_1} - \frac{1}{e_0}}$ is linear.

Table 6.2

Change in the resonance frequency with input power using the split ring resonator.

Power Level (Watt)	Efficiency e_0 (%)	Efficiency e_1(%)	$\sqrt{\frac{1}{e_1}-\frac{1}{e_0}}$	Δf (MHz)
0.1	100	98±0.17	0.158	1.52±0.06
0.2	100	95±0.20	0.229	2.21±0.07
0.3	100	92±0.31	0.293	2.83±0.11
0.4	100	89±0.33	0.348	3.36±0.12
0.5	100	87±0.35	0.395	3.81±0.13
0.6	100	84±0.39	0.441	4.26±0.15
0.7	100	80±0.43	0.502	4.84±0.18
0.8	100	76±0.47	0.563	5.43±0.20
0.9	100	74±0.51	0.595	5.74±0.23
1	100	71±0.58	0.640	6.17±0.27

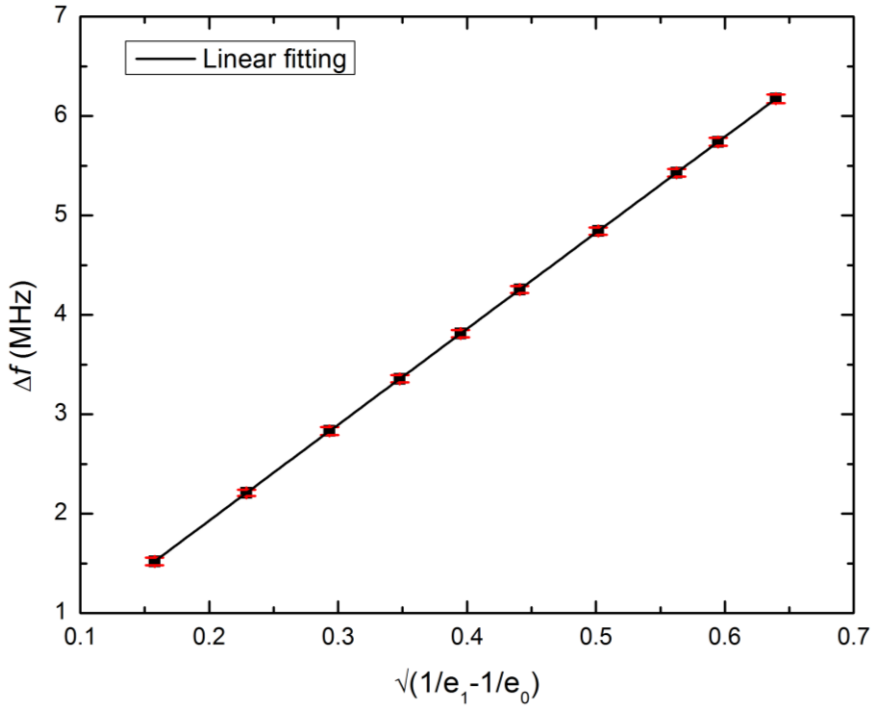

Figure 6.7 Change in resonance frequency vs change in efficiency ($\sqrt{(1/e_1-e_0)}$.

The relationship between the power level and efficiency is shown in Figures 6.8. It can be seen that efficiency is inversely proportional with the power level. Efficiency decreases with the higher power levels due to increasing water temperature, which increases the resonance frequency more, as shown in Figure 6.9 which presents the relationship between the power level with the change in resonance frequency Δf.

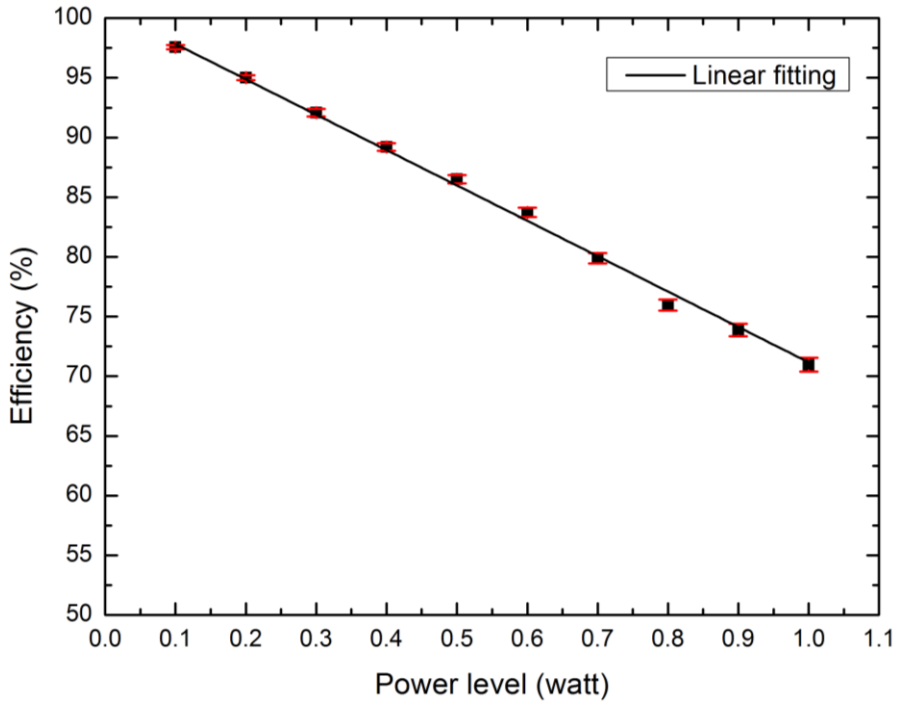

Figure 6.8 Delivered power efficiency vs the power level.

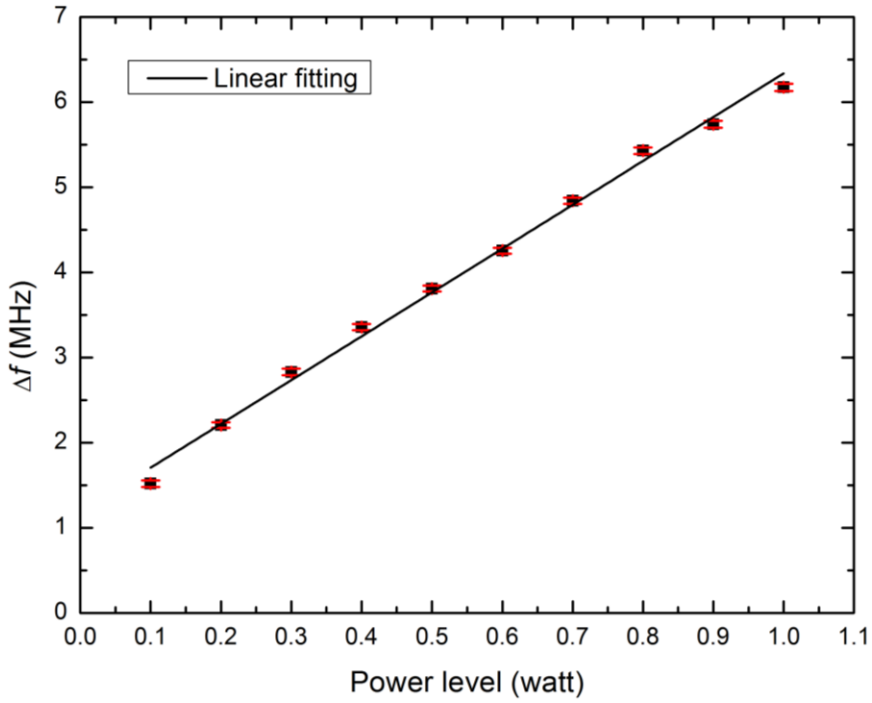

Figure 6.9 Change in resonance frequency vs the power level.

On the other hand, Figure 6.10 presents the efficiency when the delivered power is fixed at 1 Watt but at different flow rates. Higher efficiency is observed when the flow rate is faster, because the temperature rises are less since the heat is removed by the flowing water. Delivered power efficiency is found to be directly proportional with the flow rate.

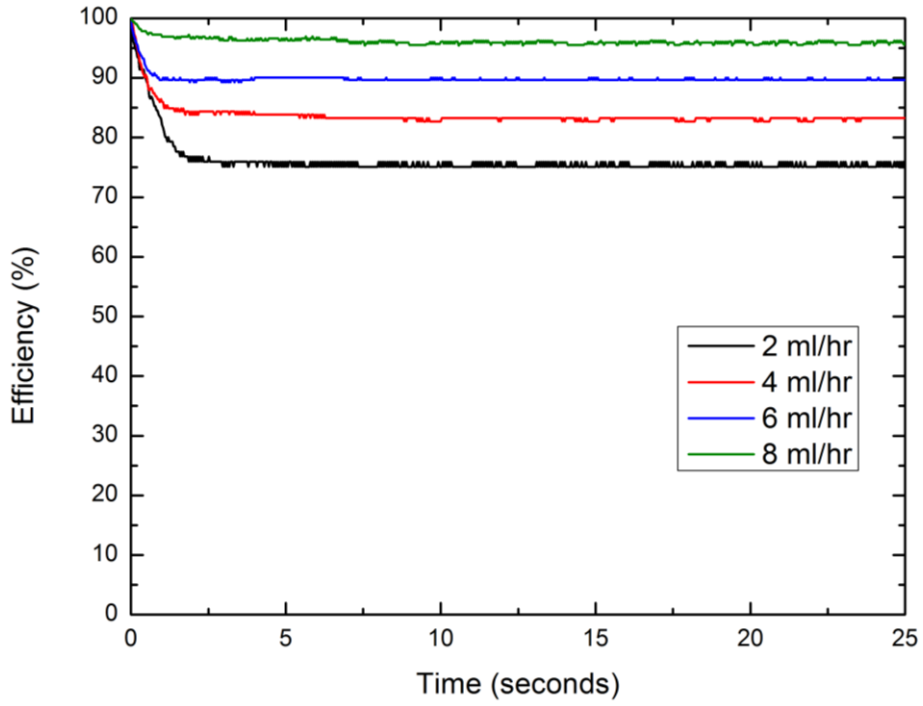

Figure 6.10 Delivered power efficiency, when the delivered power is fixed at 1 Watt and different flow rates.

6.3.2. Power Delivery Efficiency of The Cylindrical Cavity Resonator

The delivered efficiency of the microwave power using the cylindrical cavity resonator, which described and simulated in CHAPTER FOUR section 4.8 has been measured in terms of transmitted and reflected power using a DI-water sample. The same heating circuit described earlier and shown in Figure 6.2 has been used to deliver 30 Watts to the cylindrical cavity resonator. The programmable syringe pump has not been utilized here as measurements have been recorded in a static situation and 0.2 ml mini-microtube from alpha laboratories has been used for sample holding, as shown in Figure 6.11, with the water volume fixed at 170 µl. This is the condition used for the first attempts at the release of DNA from bacterial samples, described in the next chapter. The resonant frequency was 2426.25 MHz at 25^0C at critical coupling for maximum power transfer requirement.

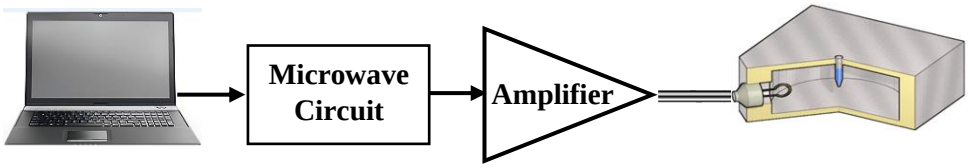

Figure 6.11 Schematic of the whole microwaving system using the cavity applicator.

Figure 6.12 shows the efficiency decreased with time after microwave power was switched on since the sample water is in a static situation and so heats rapidly.

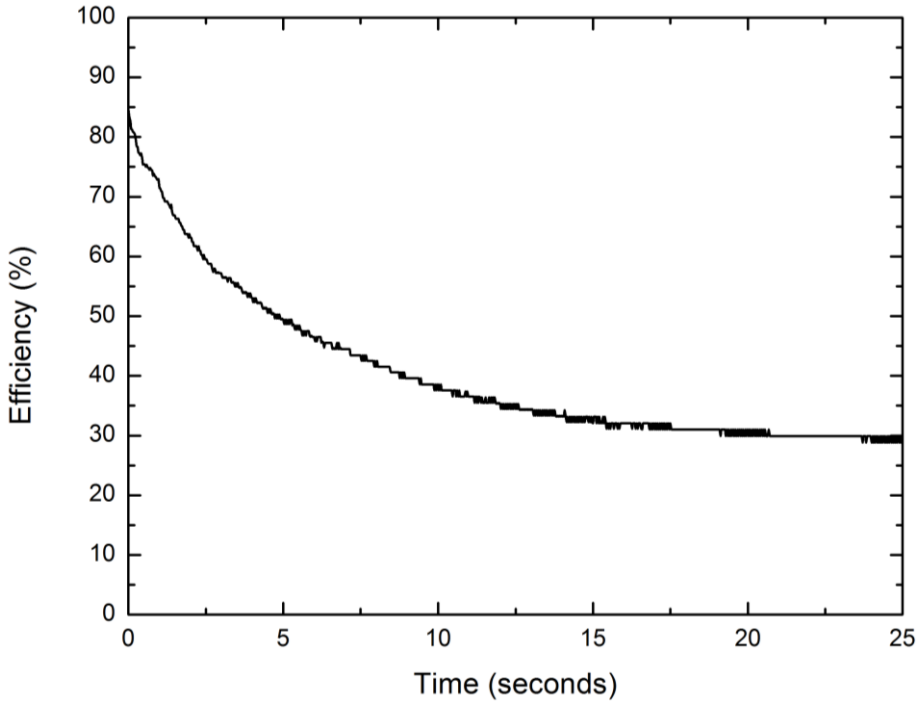

Figure 6.12 Delivered power efficiency using cavity applicator with a water sample and 30 Watt continuous microwave power under (initial) critical coupling.

Using equation (6.15), the change in resonance frequency Δf is calculated and shown in Figure 6.13 after setting values of f_o and Q_o to 2426.25 MHz and 350 respectively. The change in the frequency becomes bigger with time as the sample absorbs more microwave power and consequently heats rapidly.

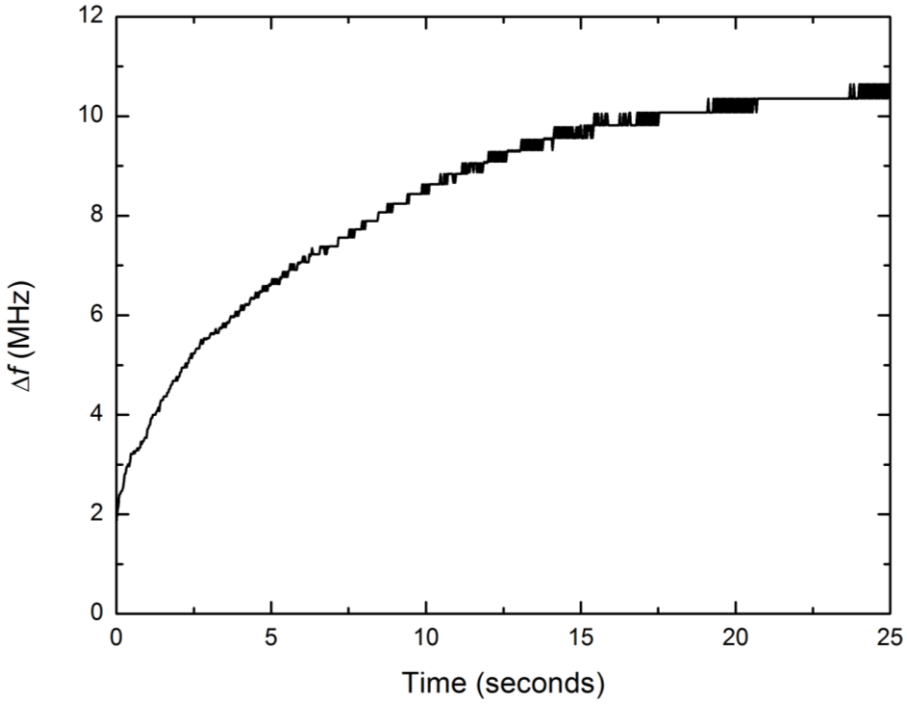

Figure 6.13 Change in resonance frequency vs time when the cavity applicator used at 30 Watt and 2426.25 MHz resonant frequency at (initial) critical coupling.

6.4. Scale Down From Cavity to Split Ring Resonator

For scaling the microwave cavity to the split ring, let us consider the microwave cavity with load inside it as shown in Figure 6.14. Owing to the huge reduction in effective volume, we expect to get similar values of electric field in the SRR's gap region for much lower power levels when compared to those on-axis in the cylindrical cavity resonator when 30 Watts are used. This is our aim, so that we can reduce the microwave power requirement for treatment of microfluidic samples, thus opening up the possibility of incorporating the SRR into a battery operated, hand-held device for bacterial DNA detection (CHAPTER SEVEN).

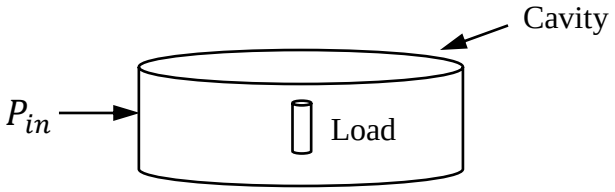

Figure 6.14 Sample load inside the microwave cylindrical cavity.

To calculate the reduction in input power needed, note first that the input power to a sample loaded, critically coupled cavity divides between the power dissipated in the cavity and the power dissipated in the sample as follows (from the fundamental definition of Q factor)

$$P_{in} = P_{cavity} + P_{load} \tag{6.16}$$

$$P_{load} = P_{in}\left(1 - \frac{Q_s}{Q_o}\right) \tag{6.17}$$

Here Q_s is the quality of the cavity resonator with sample load, and Q_o is the quality when it is empty. The time-averaged power dissipated in the sample is:

$$\langle P_{load} \rangle = \frac{1}{2}\, \varepsilon_2\, \varepsilon_o\, \omega\, E_{in}^2\, V_s \tag{6.18}$$

E_{in}^2 is the average electric field energy inside sample load, V_s is the sample volume.

$$E_{in}^2 = \frac{2\,\langle P_{load} \rangle}{\varepsilon_2\, \varepsilon_o\, \omega\, V_s} \tag{6.19}$$

$$E_{in}^2 = \frac{2\, P_{in}}{\varepsilon_2\, \varepsilon_o\, \omega\, V_s}\left(1 - \frac{Q_s}{Q_o}\right) \tag{6.20}$$

Since $Q_s \ll Q_o$, then equation (6.20) can be written as follows:

$$E_{in}^2 = \frac{P_{in}}{\pi f_o \varepsilon_2\, \varepsilon_o\, V_s} \quad , E_{in} = \sqrt{\frac{P_{in}}{\pi f_o \varepsilon_2\, \varepsilon_o\, V_s}} \tag{6.21}$$

where $\omega = 2\pi f_o$

The calculated electric field inside the 170 µl water sample at resonant frequency of 2426.25 MHz as the input power varies from 0 Watt to 30 Watt is shown in Figure 6.15. The maximum value is around 1.7×10^4 V/m at 30 Watt.

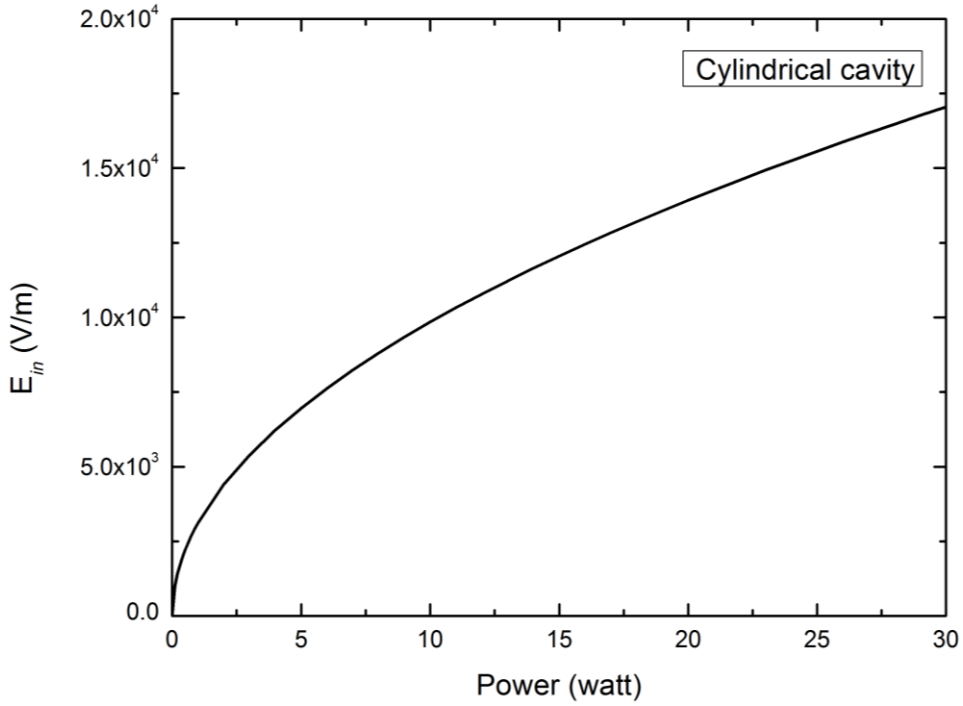

Figure 6.15 Electric field inside water sample vs input power to the cavity at 2426.25 MHz resonant frequency.

Now, the electric field inside a water sample using the split ring resonator is calculated and plotted against the input power as shown in Figure 6.16. The electric field increases when the input power to the split ring increases but in the split ring case the power is needed is much less than in the case of cylindrical cavity for the same values of electric field. It can be seen that the input power to the split ring resonator of only 0.1 Watt can produce electric field inside water sample equivalent to that of 30 Watt when using the cylindrical cavity. This is an important step towards system miniaturization with minimum power consumption, allowing the microwave resonant cavity can be scaled down to the split ring as shown in Figure 6.17 for microwave treatment achieving the same electric field. Of course, the sample volume is also scaled down, but this causes little issue if a certain volume of sample needs to be collected as the sample can be within a flow scenario.

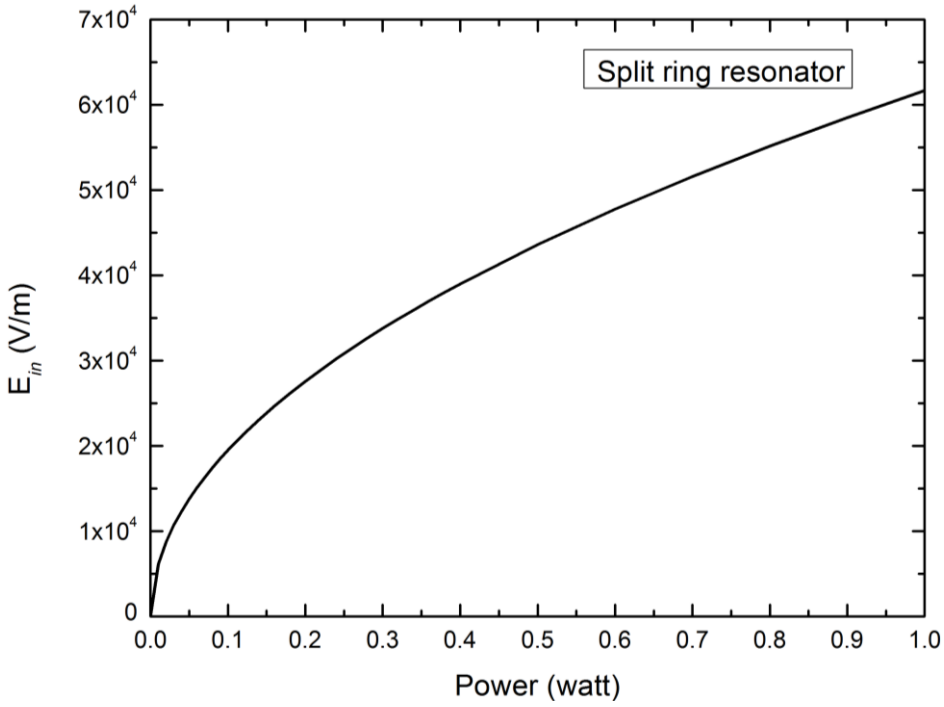

Figure 6.16 Electric field inside water sample vs input power to the split ring at 2413.25 MHz resonant frequency.

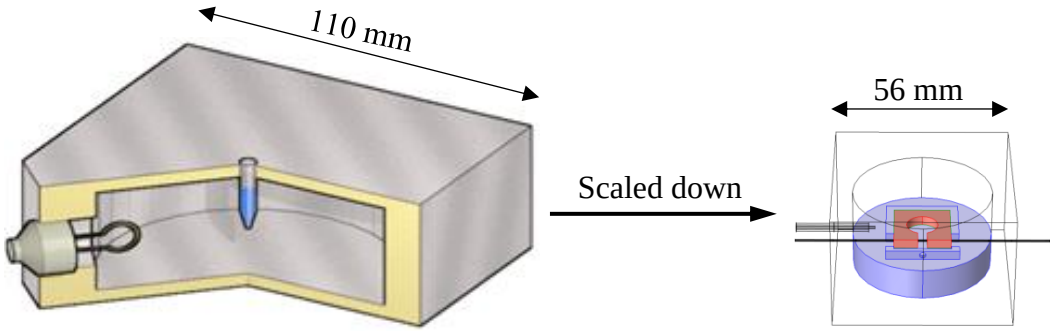

Figure 6.17 Schematic of cylindrical cavity scaling to split ring resonator.

6.5. Split Ring Resonator Versus Cylindrical Cavity Resonator

The efficiency of the SRR in heating applications under dynamic conditions is promising as the power consumption is minimum compared with the larger cavity where approximately all the applied power is absorbed by the MUT due to minimum depolarization effect, the dynamic conditions here play a very important role in minimising the effects of temperature and allowing efficiency to be maintained higher in terms of incident and reflected power, two important parameters can be adjusted here according to the required application such as power level, and flow rate.

CHAPTER SEVEN
SPLIT RING RESONATOR FOR HEALTHCARE APPLICATIONS

7.1. Introduction

Recently, microwave technologies have received significant attention for use in biological sample detection and analysis. This is mainly due to a strong desire to find new methods for the accurate, quick and cost-efficient characterization of bimolecular specimens [140], [141].

DNA detection is an important research area in almost every field of modern life science and is relevant for applications such as drug discovery, clinical analysis, and food quality [142]-[144]. On the other hand, the DNA detection at various electromagnetic frequencies depends on the dielectric properties of this biomolecule [145]. There is large number of DNA extraction methods; each one has its own advantages and disadvantages. Many of these methods include a variable number of reagents, chemicals, heat, enzymes, equipment, etc. [146]-[148].

Rather than using EM techniques to directly detect DNA, our resonant applicator system uses the split ring resonator (SRR) for highly targeted delivery of microwave energy to an aqueous sample in the parallel E field orientation in the gap region. DNA release is spontaneous, and we use novel DNA probes to capture and detect the presence of pathogen specific DNA. We focused our studies on the detection of the bacteria *Clostridium difficile*, which is a major cause of hospital and community acquired infections.

Clostridium difficile is a spore forming, toxin-producing bacterium which is currently the principal cause of healthcare associated diarrhoea in the world. There were 284,875 infections in the USA in 2007 while in the UK during the same period the pathogen was linked to the death of 8,324 individuals. The bacterium currently presents a considerable challenge to healthcare professionals and has stimulated researchers to develop

improved diagnostics and medical countermeasures [149]. Recent statistics for 2015 showed that *Clostridium difficile* (*C. difficile*) caused almost 500,000 infections among patients in the USA in a single year, according to a study released by the U.S. department of health and human services Center for Disease Control and Prevention (CDC) [150], and more than 14,000 infections in the UK according to Office of National Statistics [151] .

The structure of the *C. difficile* spore is not easy to break it open and release the target DNA and enhance the need to develop an optimised microwave protocol.

7.2. Microwaving Protocols

Three protocols of microwaving have been used: continuous power (100% duty cycle), pulsing with 10% duty cycle (the ON time is set to 100 ms and so OFF is for 900 ms per pulse), and pulsing with 3% duty cycle (the ON time is set to 30 ms and so OFF is for 970 ms per pulse). The pulse cycle is illustrated in Figure 7.1, in terms of which the pulse duty cycle is (T_{on}/T_1)*100%. All the microwaving protocols used an excitation frequency of approximately 2413 MHz, with the SRR critically coupled for maximum power transfer.

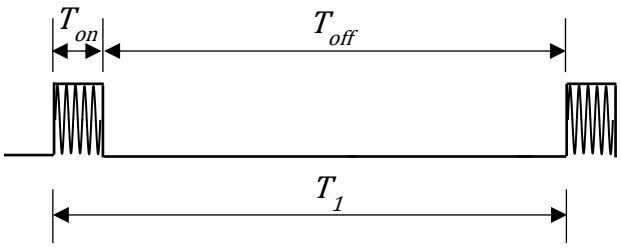

Figure 7.1 Pulse duration and repetition frequency.

For pulse powered, the energy transfer rate is averaged over the pulse width, T_{on}

$$P_p = \frac{1}{T_{on}} \int_0^{T_{on}} e(t) \cdot i(t)\, dt \tag{7.1}$$

where $e(t)$and $i(t)$are voltage and current respectively.

7.3. Efficiency of Cylindrical Cavity

The efficiency of the cylindrical cavity has been measured in terms the ratio of incident and reflected power using a water sample (170 µl) for the three microwaving protocols ; continuous power (100% duty cycle), pulsing with 10% duty cycle, and pulsing with 3% duty cycle as shown in Figure 7.2. The drive power level used here was 30 W and the cavity was firstly critically coupled at room temperature, with an excitation frequency of approximately 2426 MHz.

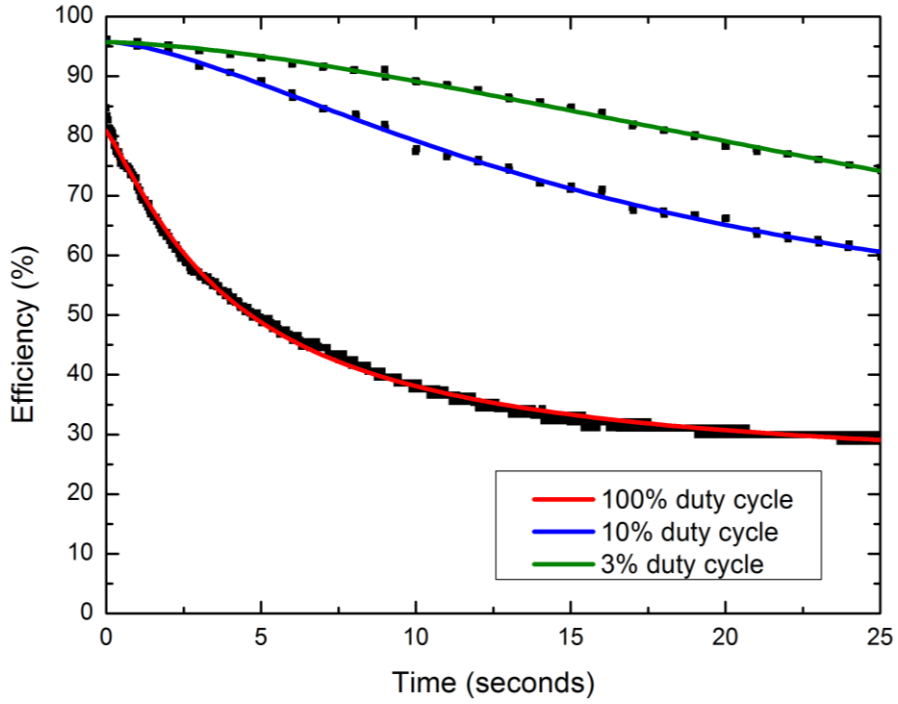

Figure 7.2 Delivered power efficiency for the three microwaving protocols using the cylindrical microwave cavity.

7.4. Qubit Detection Tool

Before presenting the results for the liberation of DNA from *C. difficile* spores by microwaving, the method for DNA detection will be presented briefly, namely the Qubit 3.0 Fluorometer from Life Technologies, shown in Figure 7.3. This is an analytical instrument that accurately measures DNA, RNA, and protein using the highly

sensitive fluorescence-based Qubit quantitation assays. The fluorescent dyes used in these assays emit signals only when bound to specific target molecules, even at low concentrations, thus minimizing the effects of contaminants, including degraded DNA or RNA. The integrated design of the instrument and assays results in quantitation that is far more sensitive than UV absorbance.

Figure 7.3 Qubit Fluorometer instrument

The instrument works with Invitrogen Qubit assay kits to enable greater sensitivity and accuracy. Qubit Assay Kits provide concentrated assay reagent, dilution buffer, and pre-diluted standards. The reagent can simply be diluted using the buffer provided, the sample is then added (any volume between 1 μL and 20 μL is acceptable), and then the reading of concentration using the Qubit 3.0 Fluorometer is displayed, as shown schematically in Figure 7.4. The assay is performed at room temperature, and the signal is stable for 3 hours. The Qubit is able to detect ssDNA (single stranded) and dsDNA (double stranded) separately.

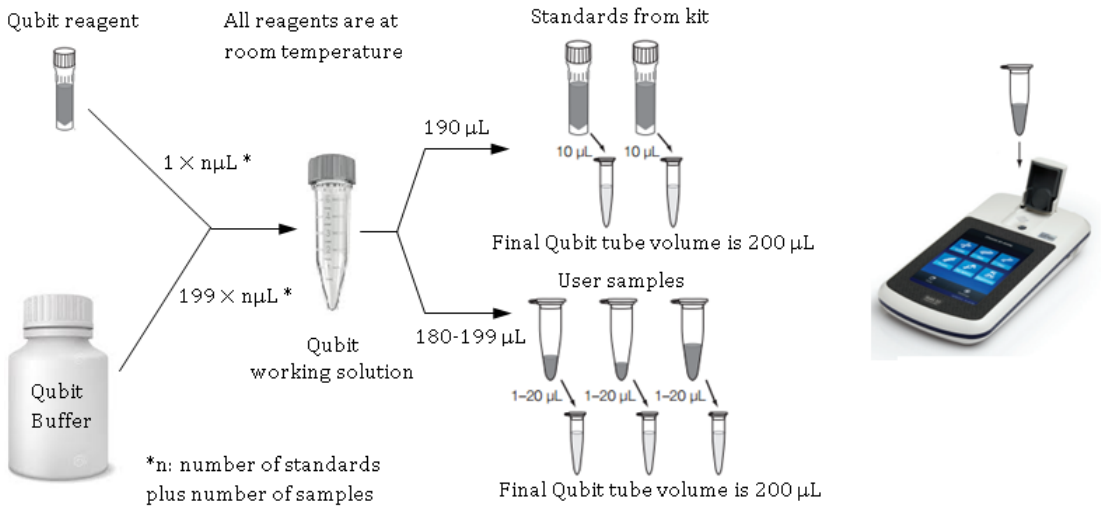

Figure 7.4 Workflow for the Qubit assays using the Qubit Fluorometer.

7.5. Microwave of *C. difficile* Spores Using Cylindrical Cavity

This cavity has been used to liberate the DNA from purified spores of two strains of *C. difficile*; toxigenic DS1813 and non-toxigenic DS1684 at a concentration of 1×10^6 spores/ml at 30 Watt and 2426.25 MHz for 4 seconds exposure time. Purified spores of *C. difficile* DS1813 and DS1684 have been prepared by the author in Cardiff School of Pharmacy's category 2 laboratories according to the method described in [152] and then diluted to the required concentration using DI-water.

The Qubit instrument was used to measure how much DNA was released, with 6 µl samples taken for each detection test, for both dsDNA and ssDNA.

Figure 7.5 and Figure 7.6 show the detection results for ssDNA and the significance results according to SPSS software analysis for DS1813 and DS1684 respectively; the highest and lowest standards values are 18,081 ng/ml and 167.72 ng/ml respectively. It can been seen from the results of both DS1813 and DS1684 that microwaving *C. difficile* spores releases DNA, and there is a significant increase in the amount of ssDNA before and after microwaving when using 10% duty cycle.

The concentrations of dsDNA were too low to measure using the Qubit tool, so it is likely that dsDNA is being broken down into ssDNA by the action of the microwaves.

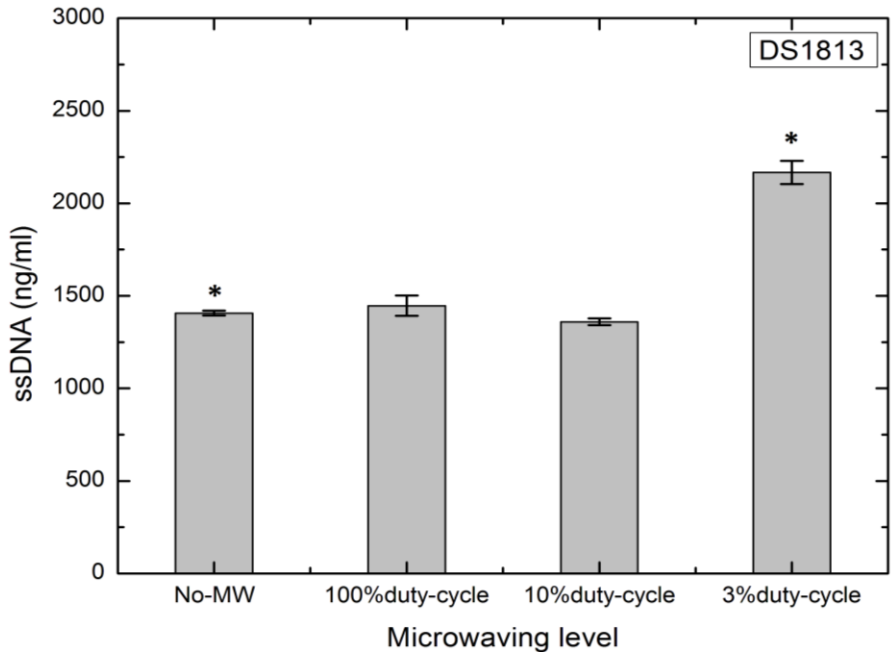

Figure 7.5 ssDNA for purified DS1813 using cylindrical cavity, concentration of 1×10^6 spores/ml. (*) means the difference is significant ($p < 0.05$).

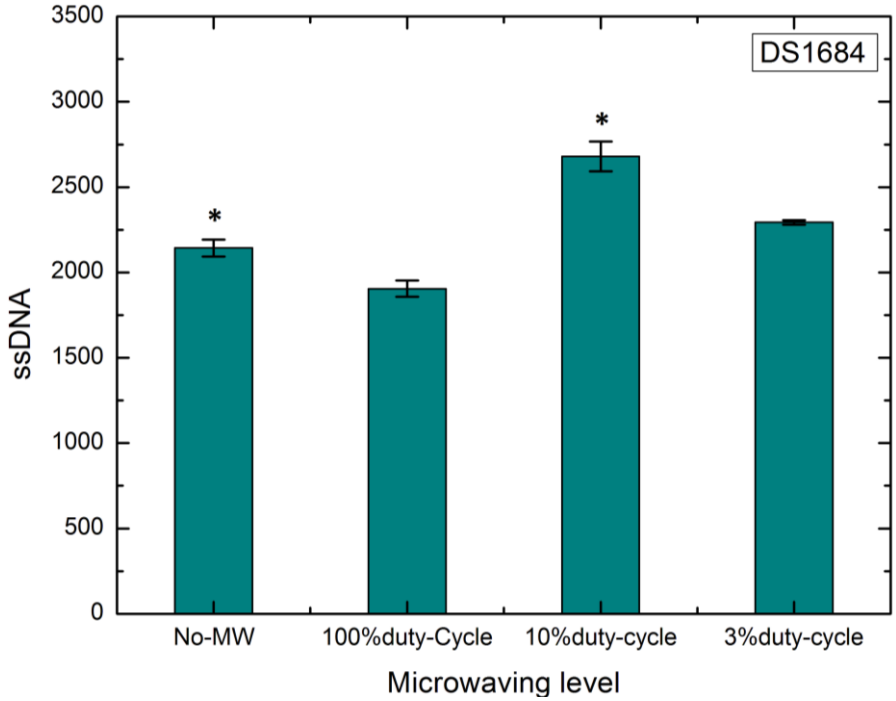

Figure 7.6 ssDNA for purified DS1684 using cylindrical cavity, concentration of 1×10^6 spores/ml. (*) means the difference is significant ($p < 0.05$).

7.6. Efficiency of The Split Ring Resonator

The efficiency of the SRR has been measured in terms of the incident and reflected power using water sample for the three protocols of microwaving: continuous power (100% duty cycle), pulsing with 10% duty cycle, and pulsing with 3% duty cycle as shown in Figure 7.7. A programmable syringe pump has been set to keep constant sample flow rate at 0.75 ml/hr; the results are presented in Table 7.3.

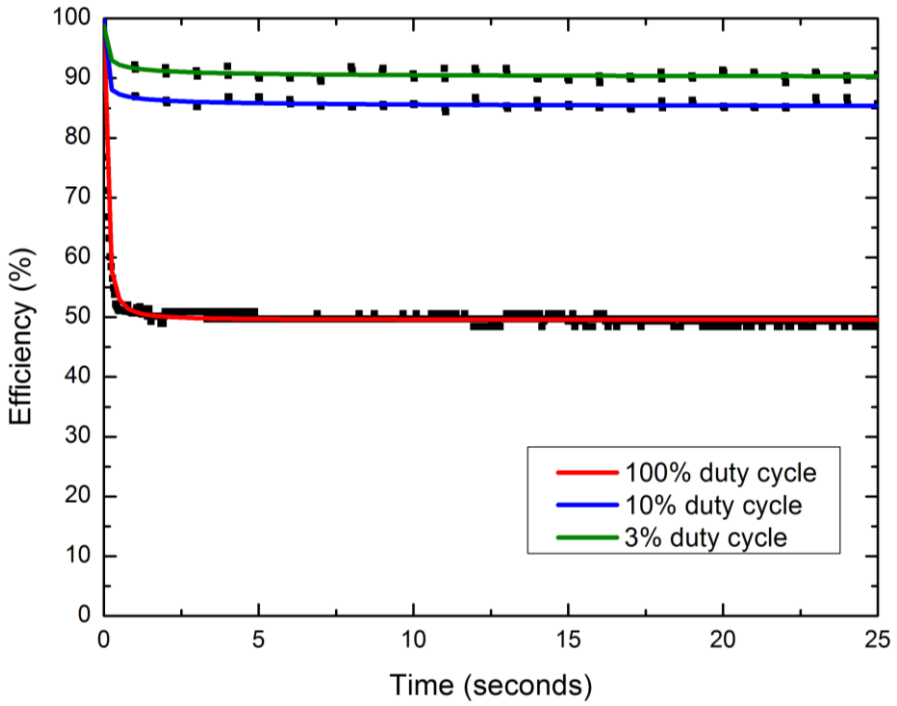

Figure 7.7 Delivered power efficiency for different microwaving protocols.

It can be seen that the efficiency at 3% duty cycle is better than 10% duty cycle and better than 100% duty cycle. The efficiency is related to temperature of the water, hence the 3% duty cycle does not cause as much heat as 10% duty cycle or 100% duty cycle. An increased temperature means decreases in both the real and imaginary parts of the complex permittivity of the water; these cause an increased resonant frequency and an increased Q factor. Since critical coupling is set for the flowing sample at room temperature, at a fixed excitation frequency throughout, the condition can't then be

maintained as the sample heats and so moves off resonance, and becomes over-coupled due to the increased Q.

The change in resonance frequency Δf in Table 7.3 has been calculated according to the derived equation (6.15) in CHAPTER SIX.

Table 7.3
Change in the resonant frequency

Microwaving Level	Efficiency e_0 (%)	Efficiency e_1(%)	Δf (MHz)
100 %	100	50±1	9.71±1.10
10 %	100	86±1	3.96±0.25
3 %	100	91±1	3.12±0.26

Furthermore, S_{11} has been measured as shown in Figure 7.8 for the three microwaving protocols. Using COMSOL software with the aid of parameters listed in Table 7.4 [153] which have been used as input parameters for the relative permittivity of Debye model equation, the rise in water temperature has been extracted and are presented in Table 7.5.

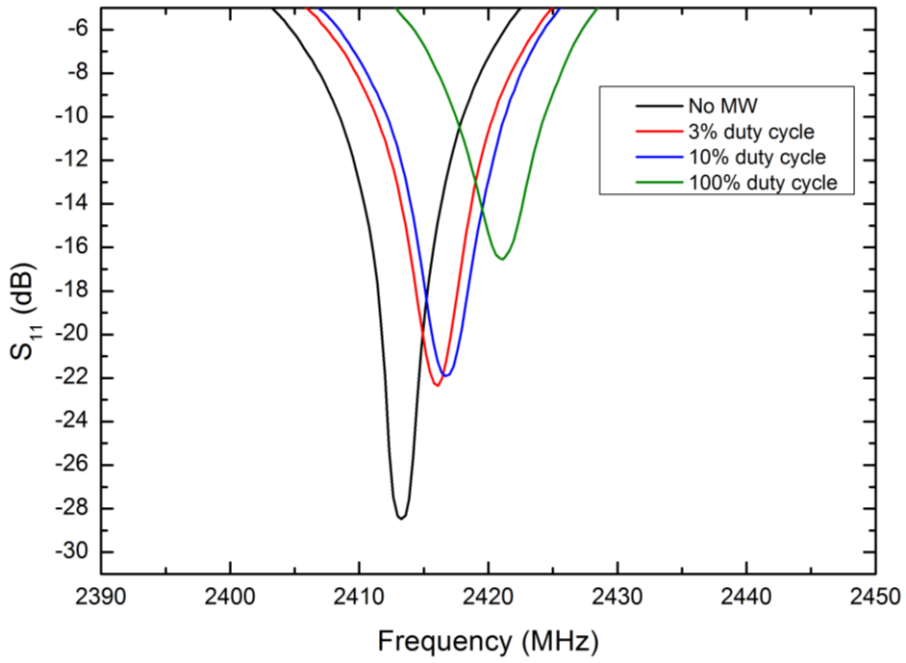

Figure 7.8 Measured reflection coefficient $|S_{11}|$ at 2.413 GHz, before microwaving and after applying 1 Watt at constant flow rate at 0.75 ml/hr with 3%, 10%, and 100% duty cycles.

Table 7.4

Parameters of the Debye relaxation spectral function (equation 4.59) for water at various temperatures

T (^{0}C)	$\varepsilon_s \pm \Delta\varepsilon_s$	$\varepsilon_\infty \pm \Delta\varepsilon_\infty$	$\boldsymbol{\tau}$ (ps)
-4.1	89.25±0.2	5.9±0.3	21.1±0.2
0	87.9±0.2	5.7±0.2	17.7±0.1
5	85.8±0.2	5.7±0.2	14.9±0.1
10	83.9±0.2	5.5±0.2	12.7±0.1
15	82.1±0.2	6.0±0.5	10.8±0.2
20	80.2±0.2	5.6±0.2	9.4±0.05
25	78.4±0.05	5.2±0.1	8.3±0.02
30	76.6±0.2	5.2±0.4	7.3±0.05
35	74.9±0.2	5.1±0.3	6.5±0.05
40	73.2±0.2	3.9±0.3	5.8±0.05
50	69.9±0.2	4.0±0.3	4.8±0.05
60	66.7±0.2	4.2±0.3	4.0±0.05

Table 7.5

Simulated temperature according to measured resonant frequency with the aid of Debye relaxation parameters

MW	Temperature	Frequency Fr (MHz)		Debye relaxation parameters		
		Experimental	Simulated	ε_s	ε_∞	$\boldsymbol{\tau}$ (ps)
Non	25 ^{0}C	2413.25	2413.26	78.36	5.2	8.27
100%	50 ^{0}C	2421.13	2421.20	69.89	4.0	4.75
10%	30 ^{0}C	2416.69	2416.94	76.56	5.2	7.28
3%	(25-30) ^{0}C	2416.10	2416.40	77.13	5.2	7.77

7.7. Microwave Irradiation of *C. difficile* Spores Using the Split Ring

Purified spores of *C. difficile* DS1813 and DS1684 at concentration level of 1×10^5 spores/ml were microwaved using split ring cavity resonator at 1 Watt and 2413 MHz. A programmable syringe pump, which has been described earlier in section 6.1 CHAPTER SIX (Figures 6.1 and 6.2) has been used to keep constant flow rate of 0.75 ml/hour. Each sample of *C. difficile* was introduced to the SRR via FEP tubing (Fluorinated Ethylene Propylene), 0.77mm O.D. × 0.4mm I.D.

Three protocols have been applied in microwaving: continuous power (100% duty cycle), pulsing of 10% duty cycle, and pulsing of 3% duty cycle. The Qubit tool has been used to measure how much DNA has been released. 6 µl has been taken from each sample for each detection test, for both double and single stranded DNA (denoted dsDNA and ssDNA, respectively). Figure 7.9 and Figure 7.10 show the detection results and the significance results according to SPSS software analysis for ssDNA for DS1813 and DS1684 respectively; the highest and lowest standards values are 14800 ng/ml and 110.21 ng/ml respectively. It can be seen from the results of both DS1813 and DS1684 that microwaving *C. difficile* spores releases DNA. There is a significant increase in the amount of ssDNA before and after microwaving when using 10% duty cycle according to SPSS software analysis. For the dsDNA as observed in section 7.5, the concentrations were too low to measure using the Qubit tool; we conclude from this that the microwaves are likely to be breaking the dsDNA into ssDNA.

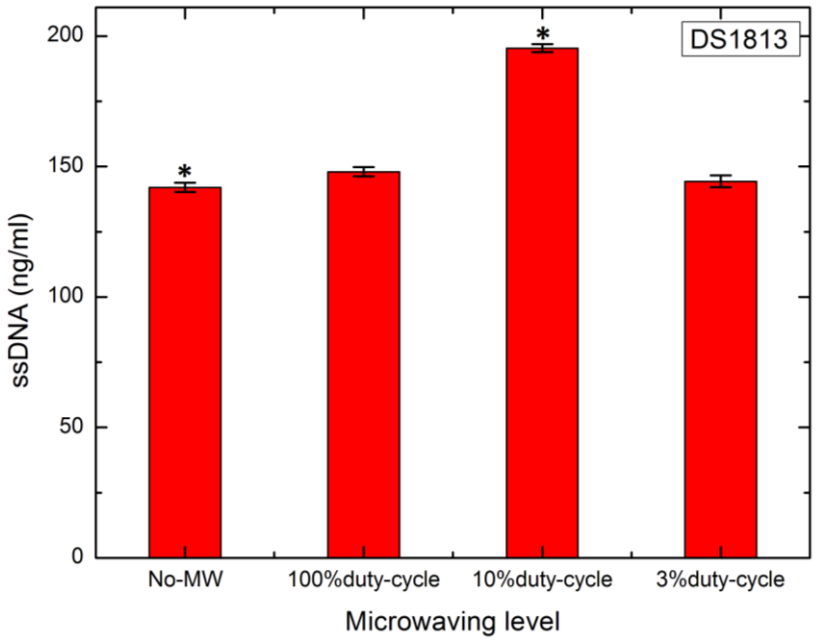

Figure 7.9 ssDNA for purified DS1813, concentration of 1×10^5 spores/ml. (*) means the difference is significant ($p < 0.05$).

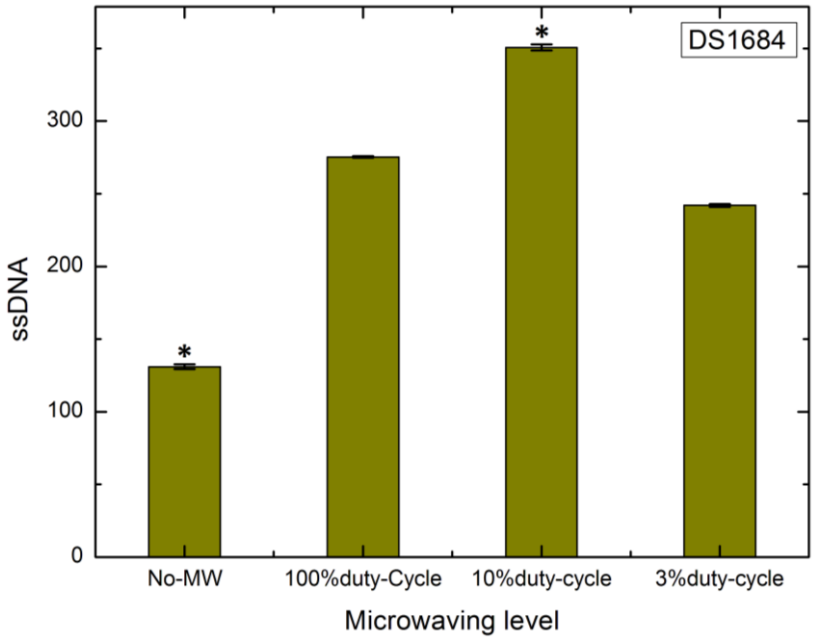

Figure 7.10 ssDNA for purified DS1684, concentration of 1×10^5 spores/ml. (*) means the difference is significant ($p < 0.05$).

A further experiment using a 10 fold higher concentration of purified spores of *C. difficile* DS1813 and DS1684 was performed; the concentration level was 1×10^6 spores/ml for the both strains. Also, the same three microwaving protocols have been applied at 1 Watt power level. Again, 6 µl has been taken from each sample for each detection test for dsDNA and ssDNA. The highest and lowest standards values are 21963 ng/ml and 110.21 ng/ml respectively. Figure 7.11 and Figure 7.12 the detection results and the significance results according to SPSS software analysis for ssDNA for DS1813 and DS1684, respectively. For the dsDNA, the concentrations were again too low to be measured by the Qubit instrument, again implying that the microwaves were breaking dsDNA into ssDNA. According to the results for both DS1813 and DS1684, after microwaving *C. difficile* spores there is significant increase in the amount of ssDNA before and after microwaving when using 10% duty cycle.

As expected, with the higher concentration of spores there is a far greater concentration of DNA released into solution. A comparison results are listed in Tables 7.6 and 7.7 for DS1813 and DS1684 respectively, each measurements has been repeated three times.

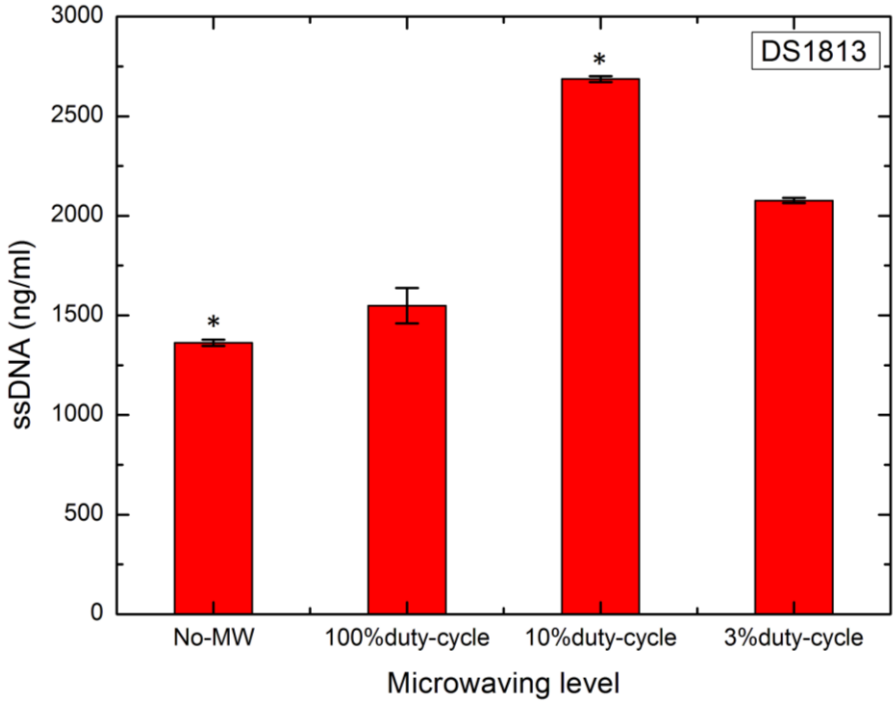

Figure 7.11 ssDNA for purified DS1813, concentration of 1×10^6 spores/ml. (*) means the difference is significant ($p < 0.05$).

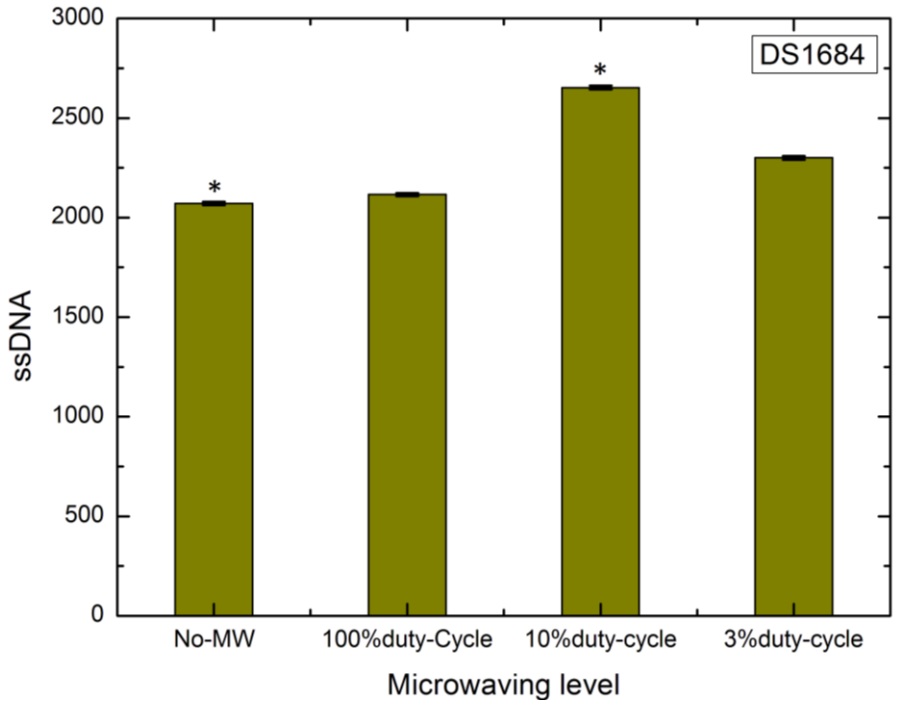

Figure 7.12 ssDNA for purified DS1684, concentration of 1×10^6 spores/ml. (*) means the difference is significant ($p < 0.05$).

Table 7.6
Comparison between released ssDNA of DS1813 using split ring resonator for two concentrations

Average released ssDNA (ng/ml) for DS1813				
concentration (spores/ml)	Before MW	After MW 100% duty Cycle	After MW 10% duty cycle	After MW 3% duty cycle
1×10^5	142	148	195	144
1×10^6	1362	1549	2686	2077

Table 7.7
Comparison between released ssDNA of DS1684 using split ring resonator for two concentrations

Average released ssDNA (ng/ml) for DS1684				
concentration (spores/ml)	Before MW	After MW 100% duty Cycle	After MW 10% duty cycle	After MW 3% duty cycle
1×10^5	131	275	351	242
1×10^6	2071	2116	2653	2360

7.8. Summarized Results of the SRR and The Cylindrical Cavity

From results of the SRR, we conclude that microwaving at 10% duty cycle is the most effective and better than other protocols according to the concentration of released ssDNA, while the fact that dsDNA was not detectable is likely to be due to the microwaves converting the dsDNA into ssDNA almost completely. Lower power levels of 1 Watt have been used in an attempt to extract dsDNA but unfortunately there was still no significant dsDNA released possibly due to fact that the power levels were insufficient to disrupt the structure of the spore.

From the cylindrical microwave cavity results, it has been noticed that 3% duty cycle is significant in ssDNA liberation with DS1813 while the 10% duty cycle is the most significant for microwaving DS1684. The dsDNA was not detectable (concentration too low to measure and below the lowest standard of the Qubit instrument). Hence, both split ring resonator and the cylindrical cavity have been shown to be effective for rapid release of ssDNA from *C. difficile*, but some optimisation needs be done with the SRR in particular, relating to optimised flow rates for a hand-held DNA detector.

CHAPTER EIGHT
CONCLUSIONS AND FUTURE WORK

8.1. Conclusions

This thesis has presented new and improved sensing method for microfluidic samples using microwave technology based on the interaction between microwave electric field and the material under test (MUT). This interaction has been discussed in detail as the design of new sensors requires good understanding of a material's response to microwave irradiation. In this field, new types of resonators have been designed and manufactured to achieve both high sensitivity as well as high efficiency of power transfer, which is required for material thermal processing and excitation.

The conclusions can be summarized according to thesis's chapters and as following:

A. Chapter two:

Background behind the fundamental microwave technologies and their sensing capabilities was provided, specifically those relevant to dielectric properties characterization. The main methods used have been reviewed, with the advantages and disadvantages of each in terms of operating frequency, measurement accuracy, environment temperature, and sample shape and size provided. Sensors are divided into resonant and non-resonant types based on the sensing operation. Furthermore, thermal material processing using microwaves driven by the electric field component and the ability of microwaves to heat the material efficiently has been discussed and supported by some application examples. This efficiency arises from the volumetric heating, i.e., microwaves heat material from inside and the heating is not based on classical thermal convection. Microwave heating or drying provides a number of advantages and can be summarized as: (i) it depends on energy transfer instead of heat transfer; (ii) it provides contactless heating; (iii) it involves quick start-up and stopping; (iv) heating is from the interior of the material body; and (v) it is safe, since the microwave energy is a nonionizing electromagnetic radiation with frequencies in the range of 300 MHz to 300 GHz. In this context, some examples have been presented for the use of microwave heating in selective applications.

Finally, in this chapter, some literatures related to microwave cavities and split ring resonators have been presented for selected applications.

B. Chapter Three:

The interaction between dielectric materials and the electromagnetic E field at microwave frequencies has been discussed. This interaction mainly depends on the type of dielectric material, and the polarization and depolarization effects that result. Although the relationship between internal electric field (E_{in}) inside material and the applied electric field (E_0) depends strongly on the material's dielectric constant (relative permittivity), there is another very important parameter which is the depolarization factor (N): it is a dimensionless parameter, whose value depends on the dielectric material shape and also on the direction of the applied electric field (E_0) with respect to the dielectric material. The depolarization factor can be considered as a key factor in the design for high sensitivity sensors and efficient microwave applicators, where it should be minimised (ideally close to zero),

C. Chapter Four:

The re-entrant microwave cavity (RMC) is a very attractive sensor for dielectric characterisation of small liquid volumes (of 7 mm^3 and less) due to the high concentration of electric field in its gap region. It is also easy to manufacture, and retains a high quality factor Q (of a few thousand) even when machined from aluminium metal. Whilst the electric field is very high in the narrow gap region, the associated magnetic field is small and spread over a much larger volume, leading to low surface loss on the metal surfaces it is exposed to, hence the high Q. These desirable features (high Q, high concentration of electric field in the gap) contribute to a high performance dielectric sensor and applicator.

The designed and machined re-entrant cavities (at 900 MHz and 2.4 GHz) showed very good sensitivity for solvent characterisation in micro-volumes. They work as sensitive sensors not only for the fluid type but also for characterising mixtures (including dissolved impurities) and multiphase flows; this makes the RMC very suitable for a wide range of applications in industrial, medical, and pharmaceutical applications. The resonant frequency and quality factor were both dependent on the type and

concentration of dissolved impurities. Furthermore, the RMC was also demonstrated for characterising segmented flows, when there are two immiscible liquids (water and oil) flowing in sequence through the re-entrant cavity sensor; the resonant frequency and quality factor were changed rapidly according to segment type, owing to the rapid drop-off of electric field intensity outside of the gap region. There was very good agreement between simulation (carried out using COMSOL Multiphysics) and experimental results.

D. Chapter Five:

A novel split ring resonator has been designed and machined from copper with PTFE dielectric base, sitting in specially designed aluminium cavity to reduce the effects on the resonant frequency from any external interferences and to improve the quality factor. Depolarizations effect have been considered in the split ring design by drilling a hole for the sample tube insertion allowing fluid to pass in parallel with electric field generated in the split ring gap. The depolarization factor (*N*) in that case is approximately equal to zero, which means the internal electric field is approximately equal to applied electric field ($E_{in} \approx E_0$). Compared with the orthogonal case, when the cylindrical sample under test (SUT) crosses the applied electric field perpendicularly (*N* ≈1/2), the internal electric field will be much less than the applied field ($E_{in} \approx 0.025E_0$ for an aqueous sample). This mathematical result has been demonstrated experimentally and by simulation software (COMSOL Multiphysics). So, it is necessary to avoid depolarization effect to increase the split ring sensitivity on one hand, and achieving higher power absorption for heating purposes on the other. The split ring resonator structure has been tested with common solvents (water, methanol, ethanol, and chloroform); the experimental results are in very good agreement with the simulation results.

Also, the sensor sensitivity has been tested with different pH readings of well-known acids and alkalines: hydrochloric acid (HCl) and sodium hydroxide (NaOH). The experimental results showed that our novel split ring resonator was very sensitive to the pH level for both HCl and NaOH in terms of quality factor (Q) change, while the resonant frequency change was not sensitive enough for the pH change. According to

SPSS software statistical data analysis, the changes in quality factor were significant ($p<0.05$) between the pH groups for both HCl and NaOH.

Furthermore, saline solutions (NaCl dissolved in water) were included in the test of the split ring resonator sensitivity test with different salt concentrations. It has been found that the quality factor (Q) decreased with increasing salt concentration, while the resonance frequency was not sensitive to saline concentration. Also the results have been confirmed by SPSS, where the change was significant ($p<0.05$) between the different concentrations.

E. Chapter Six:

For the heating application (thermal material processing) under dynamic conditions, a special microwaving system has been designed and built, that both allows the efficient and precise delivery and measurement of microwave electric field, as well as a programmable syringe pump to maintain a constant flow rate through the resonant sensor/applicator. All components are controlled using LabVIEW software. The power delivery efficiency has been recorded in terms of incident and reflected power from the split ring resonator. The delivered power efficiency reduces with increased applied power level as higher power raises the water temperature, causing lower permittivity which leads to larger shift in resonant frequency and hence changes the impedance match condition for critical coupling. Also, the delivered power efficiency is found to be directly proportional with flow rate speed, where a faster flow rate acts as an effective heat sink, giving only slight increases of resonance frequency. An equation to calculate the shift in resonance frequency from the efficiency of the delivered power has been derived and applied to this situation to estimate the temperature rise for different pulse duty cycles in chapter seven.

F. Chapter Seven:

Microwave technologies have recently become more attractive for applications in the biological area: for sample detection, analysis, and thermal processing. Microwaves offer numerous advantages such as high accuracy, high speed and low cost.

The designed split ring resonator has been utilized with a microwave heating system described in CHAPTER FIVE to release the DNA from a bacterium called *Clostridium difficile*.

Before proceeding with bacteria microwaving experiments, water samples have been tested with different microwaving protocols: i) continuous microwaving, 100% duty cycle, ii) pulsing microwaving at 10% duty cycle iii) pulsing microwaving at 3% duty cycle. The shift in resonance frequency has been recorded and calculated and used to simulate the increasing in temperature using COMSOL Multiphysics and Debye model with 1 Watt power level. As expected, the highest temperatures were obtained in the order of: 100% duty cycle, 10% duty cycle, and 3% duty cycle.

Two strains of *C. difficile* were used in these experiments DS1813 and DS1684 to represent the structural diversity of this species of pathogen. The same three microwaving protocols have been used with a power level of 1 Watt and 0.35 ml/hr constant flow rate controlled by the programmable syringe pump. The results for the released ssDNA showed that microwaving using pulsing at 10% duty cycle is better than other protocols according to the Qubit detection device. Also the results have been confirmed by SPSS statistical data analysis, showing significant DNA release when using 10% duty cycle microwaving, while other microwaving methods were not statistically significant for ssDNA detection. Importantly, this implies that the heat was not the cause of DNA release but it is the direct effect of the microwave electric field, possibly similar to the effect of electrophoresis for low frequency electric field application.

8.2. Future Work

Some recommendations and suggestions for future work are listed below:

1) For the both re-entrant cavity and split ring resonator, the active gap area where the electric field is maximum can optimized to improve sensing. For example by designing the internal posts (for the re-entrant cavity), and the opposite faces (of the split ring) could be more sharp or tapered instead of flat opposite faces as

shown in Figure 8.1, and then test the sensor in both static and dynamic situations for pure liquids, mixture, and multi-segment flow.

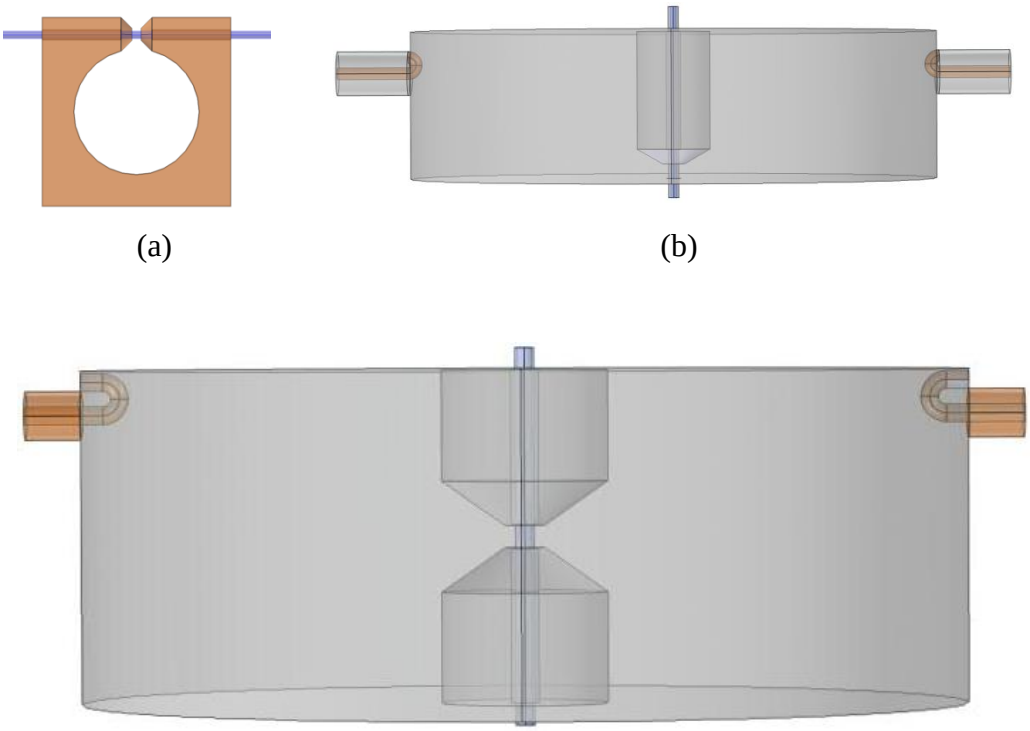

(a) (b)

(c)

Figure 8.1 Suggested structure design for future work, (a) split ring resonator, (b) single post re-entrant cavity, and (c) double post re-entrant cavity.

2) All experiments and measurements were performed and recorded in room temperature environment; it is recommended for future works that such experiments are conducted with an arrangement or by modifying the system design to monitor the sample temperature by using, for example, an optical fibre temperature probe.

3) Modifying the microwave power delivery circuit, especially the split ring resonator, for very low power consumption. This would miniaturize the whole system to become more suitable for a hand held device for both sensing and heating applications.

4) The developed sensors have considerable potential to be utilized in pharmaceutical applications, such as monitoring or measuring medicines and drugs concentration as the presented sensors in this research have the potential and sensitivity to mixture type and its concentration.

5) There are still some parameters that need to be optimized in the use of split ring for DNA liberation; these parameters are mainly: flow rate, power level, and the pulse duration when using pulsed microwaving. For example changing the whole period time (T_1) or (T_{off}) as shown in Figure 8.2, instead of only T_{on} as in the experiments presented here.

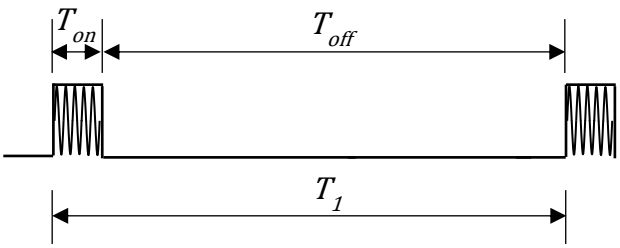

Figure 8.2 Microwave pulsing periods

6) Using the split ring sensor in sensing to UV curing of Trimethylolpropane triacrylate (TMPTA) as shown in Figure 8.3, where the resonance frequency of the split ring increases when the TMPTA hardens. Some data has already been accumulated successfully on this technique, as a proof-of-principle.

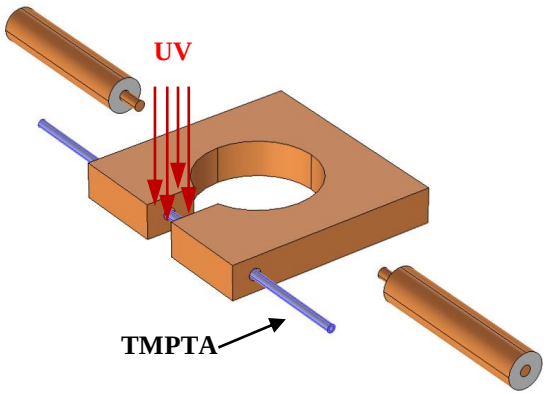

Figure 8.3 Proposed UV curing sensing using split ring resonator.

References

[1] S. F. Adam, *Microwave theory and applications*, 2nd ed.: Longman Higher Education, 1970.

[2] D. F. Stein, R. H. Edgar, M. F. Iskander, D. L. Johnson, S. M. Johnson, C. G. Lob, J. M. Shaw, W. H. Sutton, and P. K. Tien, *Microwave processing of materials*, Washington, D.C. 1994: National Academy of Sciences.

[3] R. J. Meredith, *Engineers' handbook of industrial microwave heating*, London, United Kingdom: Institution of Electrical Engineers, 1998.

[4] A. S. Khan, *Microwave engineering concepts and fundamentals*: CRC Press, 2014.

[5] A. C. Metaxas, and R. J. Meredith, *Industrial microwave heating*, United Kingdom: Institution of Engineering and Technology, 1983.

[6] D. M. Pozar, *Microwave engineering*, United States of America: JohnWiley &Sons, Inc., 2011.

[7] S. J. Orfanidis, *Electromagnetic waves and antennas*, 2002.

[8] Y. Zhao, Y. Li, B. Pan, S.-H. Kim, Z. Liu, M. M. Tentzeris, J. Papapolymerou, and M. G. Allen, "RF evanescent-mode cavity resonator for passive wireless sensor applications," *Sensors and Actuators A: Physical*, vol. 161, no. 1-2, pp. 322-328, 2010.

[9] C. Elbuken, T. Glawdel, D. Chan, and C. L. Ren, "Detection of microdroplet size and speed using capacitive sensors," *Sensors and Actuators A: Physical*, vol. 171, no. 2, pp. 55-62, 2011.

[10] T. Chretiennot, D. Dubuc, and K. Grenier, "A microwave and microfluidic planar resonator for efficient and accurate complex permittivity characterization of aqueous solutions," *IEEE Transactions on Microwave Theory and Techniques*, vol. 61, no. 2, pp. 972-978, 2013.

[11] L. F. Chen, C. K. Ong, C. P. Neo, V. V. Varadan, and V. K. Varadan, *Microwave electronics material measurements and characterization*: John Wiley and Sons, Ltd, 2004.

[12] A.-H. Boughriet, C. Legrand, and A. Chapoton, "Noniterative stable transmission/reflection method for low-loss material complex permittivity determination," *IEEE Transactions on Microwave Theory and Techniques*, vol. 45, no. 1, pp. 52-57, 1997.

[13] B. Akuthota, R. Zoughi, and K. E. Kurtis, "Determination of dielectric property profile in cement-based materials using microwave reflection and transmission properties," in Instrumentation and measurement technology conference, 2004 IMTC 04. Proceedings of the 21st IEEE, 2004, pp. 327-332.

[14] K. C. Yaw, "Measurement of dielectric material properties," *Rohde & Schwarz Application Note*.

[15] J. Baker-Jarvis, "Transmission/Reflection and short circuit line permittivity measurements," *NIST Technical Note*, 1990.

[16] J. Baker-Jarvis, E. J. Vanzura, and W. A. Kissick, “Improved technique for determining complex permittivity with the transmission /reflection method ” *IEEE Transactions on Microwave Theory and Techniques,* vol. 38, no. 8, pp. 1096-1103, 1990.

[17] A. Galoić, B. Ivšić, and D. Bonefačić, “Sensitivity of transmission-reflection based method for textile material characterization ” in Radioelektronika (Radioelektronika), 2016 26th International Conference, 2016.

[18] D. A. Houtz, D. Gu, and D. K. Walker, “An improved two-port transmission line Permittivity and permeability determination method with shorted sample,” *IEEE Transactions on Microwave Theory and Techniques,* vol. 64, no. 11, pp. 3820 - 3827, 2016.

[19] S. Panda, N. K. Tiwari, and M. J. Akhtar, “Computationally intelligent sensor system for microwave characterization of dielectric sheets,” *IEEE Sensors Journal,* vol. 16, no. 20, pp. 7483 - 7493, 2016.

[20] K. Folgero, “Broad-band dielectric spectroscopy of low-permittivity fluids using one measurement cell,” *IEEE Transactions on Instrumentation and Measurement* vol. 47, no. 4, pp. 881- 885, 1998.

[21] A. technologies, “Basics of measuring the dielectric properties of materials,” *Agilent technologies Application Note*.

[22] M. S. Venkatesh, and G. S. V. Raghavan, “An overview of dielectric properties measuring techniques,” *Canadian biosystems engineering,* vol. 47, 2005.

[23] R. Zajíček, L. Oppl, and J. Vrba, “Broadband measurement of complex permittivity using reflection method and coaxial probes,” *Radio engineering,* vol. 17, no. 1, pp. 14-19, 2008.

[24] T. P. Marsland, and S. Evans, “Dielectric measurements with an open-ended coaxial probe,” *IEE Proceedings-microwaves, antennas and propagation,* vol. 134, no. 4, pp. 341 - 349, 1987.

[25] J. P. Grant, R. N. Clarke, G. T. Symm, and N. M. Spyrou, “A critical study of the open-ended coaxial line sensor technique for RF and microwave complex permittivity measurements,” *J. Phys. E: Sci. Instrum,* vol. 22, pp. 757-770, 1989.

[26] R. Olmi, M. Bini, A. Ignesti, and C. Riminesi, “Non-destructive permittivity measurement of solid materials,” *Meas. Sci. Technol.,* vol. 11, no. 11, pp. 1623–1629, 2000.

[27] D. Misra, M. Chabbra, B. R. Epstein, M. Microtznik, and K. R. Foster, “Noninvasive electrical characterization of materials at microwave frequencies using an open-ended coaxial line: test of an improved calibration technique,” *IEEE Transactions on Microwave Theory and Techniques,* vol. 38, no. 1, pp. 8 - 14, 1990.

[28] J. R. Mosig, J.-C. E. Besson, M. Gex-Fabry, and F. E. Gardiol, “Reflection of an open-ended coaxial line and application to nondestructive measurement of materials,” *IEEE Transactions on Instrumentation and Measurement,* vol. IM-30, no. 1, pp. 46 - 51, 1981.

[29] P. Mehta, K. Chand, D. Narayanswamy, D. G. Beetner, R. Zoughi, and W. V. Stoecker, "Microwave reflectometry as a novel diagnostic tool for detection of skin cancers," *IEEE Transactions on Instrumentation and Measurement,* vol. 55, no. 4, pp. 1309 - 1316, 2006.

[30] K. M. Donnell, A. McClanahan, and R. Zoughi, "On the Crack Characteristic Signal From an Open-Ended Coaxial Probe," *IEEE Transactions on Instrumentation and Measurement,* vol. 63, no. 7, pp. 1877-1879, 2014.

[31] H. Maftooli, H. R. Karami, S. H. H. Sadeghi, and R. Moini, "Output signal prediction of an open-ended coaxial probe when scanning arbitrary-shape surface cracks in metals," *IEEE Transactions on Instrumentation and Measurement,* vol. 61, no. 9, pp. 2384 - 2391, 2012.

[32] G. L. Friedsam, and E. M. Biebl, "A broadband free-space dielectric properties measurement system at millimeter wavelengths," *IEEE Transactions on Instrumentation and Measurement,* vol. 46, no. 2, pp. 515 - 518, 1997.

[33] D. K. Ghodgaonkar, V. V. Varadan, and V. K. Varadan, "Free-space measurement of complex permittivity and complex permeability of magnetic materials at microwave frequencies," *IEEE Transactions on Instrumentation and Measurement,* vol. 39, no. 2, pp. 387 - 394, 1990.

[34] J. Hammler, A. J. Gallant, and C. Balocco, "Free-space permittivity measurement at terahertz frequencies with a vector network analyzer," *IEEE Transactions on Terahertz Science and Technology,* vol. 6, no. 6, pp. 817- 823, 2016.

[35] A. M. Hassan, J. Obrzut, and E. J. Garboczi, "A Q-band free-space characterization of carbon nanotube composites," *IEEE Transactions on Microwave Theory and Techniques* vol. 64, no. 11, pp. 3807 - 3819, 2016.

[36] S. Trabelsi, and S. O. Nelson, "Nondestructive sensing of physical properties of granular materials by microwave permittivity measurement," *IEEE Transactions on Instrumentation and Measurement,* vol. 55, no. 3, pp. 953 - 963, 2006.

[37] D. K. Ghodgaonkar, V. V. Varadan, and V. K. Varadan, "A free-space method for measurement of dielectric constants and loss tangents at microwave frequencies," *IEEE Transactions on instrumentation and measurement,* vol. 37, no. 3, pp. 789 - 793, 1989.

[38] A. K. Jha, and M. J. Akhtar, "A generalized rectangular cavity approach for determination of complex permittivity of materials," *IEEE transactions on instrumentation and measurement,* vol. 63, no. 11, pp. 2632-2641, 2014.

[39] R. G. Carter, "Accuracy of microwave cavity perturbation measurements," *IEEE Microwave Theory and Techniques,* vol. 49, no. 5, pp. 918 - 923, 2001.

[40] K. B. Yu, S. G. Ogourtsov, V. G. Belenky, A. B. Maslenikov, and A. S. Omar, "Accurate microwave resonant method for complex permittivity measurements of liquids," *IEEE Transactions on microwave theory and techniques,* vol. 48, no. 11, 2000.

[41] A. Porch, "TM010 microwave cavity for materials measurements", 2010.

[42] B. Clarke, A. Gregory, D. Cannell, M. Patrick, S. Wylie, I. Youngs, and G. Hill, *A guide to characterisation of dielectric materials at RF and microwave frequencies*, The institute of measurement and control/National Physica Laboratory NPL, 2003.

[43] F. Bordoni, L. Yinghua, B. Spataro, F. Feliciangeli, F. Vasarelli, G. Cardarilli, and B. A. a. R. Scrimaglio, "A microwave scanning surface harmonic microscope using a re-entrant resonant cavity," *Meas. Sci. Technol*, vol. 6, no. 8, pp. 1208-1214, 1995.

[44] Z. X. Xia, Y. J. Cheng, and Y. Fan, "Frequency-reconfigurable TM010-mode reentrant cylindrical cavity for microwave material processing," *Journal of Electromagnetic Waves and Applications*, vol. 27, no. 5, pp. 605-614, 2013.

[45] E. Musonda, and I. C. Hunter, "Microwave bandpass filters using re-entrant resonators," *IEEE Transactions on Microwave Theory and Techniques*, vol. 63, no. 3, pp. 954 - 964, 2015.

[46] X. Liu, L. P. B. Katehi, W. J. Chappell, and D. Peroulis, "High-Q tunable microwave cavity resonators and filters using SOI-based RF MEMS tuners," *Journal of Microelectromechanical Systems*, vol. 19, no. 4, pp. 774 - 784, 2010.

[47] J. Baker-Jarvis, R. G. Geyer, J. H. Grosvenor, M. D. Janezic, C. A. Jones, B. Riddle, C. M. Weil, and J. Krupka, "Dielectric characterization of low-loss materials a comparison of techniques " *IEEE Transactions on Dielectrics and Electrical Insulation*, vol. 5, no. 4, pp. 571 - 577, 1998.

[48] A. Porch, D. Slocombe, J. Beutler, P. Edwards, A. Aldawsari, T. Xiao, V. Kuznetsov, H. Almegren, S. Aldrees, and N. Almaqati, "Microwave treatment in oil refining," *Applied Petrochemical Research*, vol. 2, no. 1-2, pp. 37-44, 2012.

[49] V. A. Sydoruk, F. Fiorani, S. Jahnke, and H.-J. Krause, "Design and characterization of microwave cavity resonators for noninvasive monitoring of plant water distribution," *IEEE Transactions on Microwave Theory and Techniques*, vol. 64, no. 9, pp. 2894 - 2904, 2016.

[50] E. Bourdel, D. Pasquet, P. Denorme, and A. Roussel, "Measurement of the moisture content with a cylindrical resonating cavity in TM010 mode," *IEEE Transactions on Instrumentation and Measurement*, vol. 49, no. 5, pp. 1023 - 1028, 2000.

[51] G. Gennarelli, S. Romeo, M. R. Scarfì, and F. Soldovieri, "A microwave resonant sensor for concentration measurements of liquid solutions," *IEEE Sensors Journal*, vol. 13, no. 5, pp. 1857-1864, 2013.

[52] J. Sheen, and Yun-Lin, "Microwave measurements of dielectric properties using a closed cylindrical cavity dielectric resonator," *IEEE Transactions on Dielectrics and Electrical Insulation*, vol. 14, no. 5, pp. 1139-1144, 2007.

[53] J. H. Goh, A. Mason, A. I. Al-Shamma'a, M. Field, M. Shackcloth, and P. Browning, "Non invasive microwave sensor for the detection of lactic acid in cerebrospinal fluid (CSF)," *Journal of Physics: Conference Series*, vol. 307, pp. 012017, 2011.

[54] D. J. Rowe, S. al-Malki, A. A. Abduljabar, A. Porch, D. A. Barrow, and C. J. Allender, "Improved split-ring resonator for microfluidic sensing," *IEEE Transactions on Microwave Theory and Techniques* vol. 62, no. 3, pp. 689 - 699 2014.

[55] A. A. Abduljabar, D. J. Rowe, A. Porch, and D. A. Barrow, "Novel microwave microfluidic sensor using a microstrip split-ring resonator," *IEEE Transactions on Microwave Theory and Techniques* vol. 62, no. 3, pp. 679 - 688 2014.

[56] N. Yoshikawa, "Recent studies on fundamentals and application of microwave processing of materials, advances in induction and microwave heating of mineral and organic materials," *InTech*, 2011.

[57] J. A. Menéndez, A. Arenillas, B. Fidalgo, Y. Fernández, L. Zubizarreta, E. G. Calvo, and J. M. Bermúdez, "Microwave heating processes involving carbon materials," *Fuel Processing Technology*, vol. 91, no. 1, pp. 1-8, 2010.

[58] K. E. Haque, "Microwave energy for mineral treatment processes-a brief review," *International journal of mineral processing*, vol. 57, no. 1, pp. 1–24, 1999.

[59] R. S. Vilayannur, V. M. Puri, and R. C. Anantheswaran, "Size and shape effect on non-uniformity of temperature and moisture distributions in microwave heated food materials: part 11 experimental validation," *Journal of food process engineering*, vol. 21, no. 3, pp. 235–248, 1998.

[60] D. Luan, and Y. Wang, "Heating pattern of frozen food affected by microwave oven frequency " in Microwave symposium (MMS), 2015.

[61] H. S. Ku, EliasSlares, and J. RBall, "Review - microwave processing of materials: part I," *HKIE Transactions*, vol. 8, no. 3, 2001.

[62] Y. Nikawa, "Microwave diagnosis using MRI and image of capillary blood vessel," in Microwave conference, 2009. APMC 2009. Asia Pacific, 2009.

[63] J. Vrba, L. Oppl, B. Vrbova, J. Vrba, D. Vrba, D. Havelka, K. Cervinkova, L. Vojackova, I. Merunka, and O. Fiser, "Microwaves in medical diagnostics and treatment," in Radioelektronika (RADIOELEKTRONIKA), 2014 24th International Conference, 2014.

[64] C.-F. Huang, Y.-W. Tien, C.-Y. Chen, and X.-Z. Lin, "Design techniques for antenna needles used in microwave hyperthermia therapy for tumor treatment " in Antennas and propagation in wireless communications (APWC), 2014 IEEE-APS topical conference on, 2014.

[65] D. M. Hagl, D. Popovic, S. C. Hagness, J. H. Booske, and M. Okoniewski, "Sensing volume of open-ended coaxial probes for dielectric characterization of breast tissue at microwave frequencies," *IEEE Transactions on Microwave Theory and Techniques*, vol. 51, no. 4, pp. 1194 - 1206, 2003.

[66] P. T. Nguyen, A. Abbosh, and S. Crozier, "Microwave hyperthermia for breast cancer treatment using electromagnetic and thermal focusing tested on realistic breast models and antenna arrays," *IEEE Transactions on antennas and propagation* vol. 63, no. 10, pp. 4426 - 4434, 2015.

[67] I. Merunka, O. Fiser, L. Vojackova, J. Vrba, and D. Vrba, “Array of balanced antipodal vivaldi antennas used for microwave hypertermia treatment of neck cancer ” in Radioelektronika (RADIOELEKTRONIKA), 2014 24th international conference, 2014.

[68] Y. Kanai, T. Tsukamoto, Y. Saitoh, M. Miyakawa, and T. Kashiwa, “Analysis of a hyperthermic treatment using a reentrant resonant cavity applicator for a heterogeneous model with blood flow,” *IEEE Transactions on Magnetics* vol. 33, no. 2, pp. 2175 - 2178, 1997.

[69] A. Sanpanich, C. Khongkhanon, Y. Kajornpredanon, S. Thanangkul, C. Apaiwong, W. Sroykham, K. Petsarb, C. Phairoh, W. Angkhananuwat, and P. Phasukkit, “Thermal ablation for cancer treatment by using microwave energy in a simple lung model,” in Biomedical engineering international conference (BMEiCON), 2014 7th, 2015.

[70] S. M. Janković, M. Z. Milošev, and M. L. Novaković, “The effects of microwave radiation on microbial cultures,” *Hospital pharmacology, international multidisciplinary journal,* vol. 1, no. 2, pp. 102-108, 2014.

[71] Q. Wu, “Effect of high-power microwave on indicator bacteria for sterilization,” *IEEE Transactions on biomedical engineering,* vol. 43, no. 7, pp. 752-754, 1996.

[72] M. E. Sosa-Morales, L. Valerio-Junco, A. López-Malo, and H. S. García, “Dielectric properties of foods: Reported data in the 21st Century and their potential applications,” *LWT - Food Science and Technology,* vol. 43, no. 8, pp. 1169-1179, 2010.

[73] A. P. Gregory, and R. N. Clarke, “A review of RF and microwave techniques for dielectric measurements on polar liquids,” *IEEE Transactions on Dielectrics and Electrical Insulation* vol. 13, no. 4, pp. 727-743, August 2006, 2006.

[74] M. S. Venkatesh, and G. S. V. Raghavan, “An Overview of Microwave Processing and Dielectric Properties of Agri-food Materials,” *Biosystems Engineering,* vol. 88, no. 1, pp. 1-18, 2004.

[75] Gabriel Galindo-Romera, F. J. Herraiz-Martínez, M. Gil, and J. J. Martínez-Martínez, “Submersible printed split-ring resonator-based sensor for thin-film detection and permittivity characterization,” *IEEE Sensors Journal,* vol. 16, no. 10, pp. 3587-3596, 2016.

[76] M. Mehdizadeh, *Microwave/RF applicators and probes for material heating, sensing, and plasma generation,* Second ed.: Elsevier Inc., 2010.

[77] A. P. Gregory, and R. N. Clarke, “A review of RF and microwave techniques for dielectric measurements on polar liquids,” *IEEE Transactions on Dielectrics and Electrical Insulation,* vol. 13, no. 4, pp. 727-743, 2006.

[78] A. Porch, "Advanced HF electronic materials," 2014.

[79] W. Gao, Z. Li, and N. Sammes, *An introduction to electronic materials for engineers,* 2nd ed.: World Scientific Publishing Co. Pte. Ltd., 2011.

[80] M. A. Laughton, and D. F. Warne, *Electrical engineer's reference book*, 16th ed., 2003.
[81] G. K. Banerjee, *Electrical and electronics engineering materials*: PHI learning private limited, 2015.
[82] S. K. Nayak, and K. P. Bhuvana, *Engineering physics*: Tata McGraw Hill Education Private Limited, 2012.
[83] S. A. Holgate, *Understanding solid state physics*: CRC Press Taylor&Francis Group, 2010.
[84] Andre Vander Vorst, Arye Rosen, and Y. Kotsuka, *RF microwave interaction with biological tissues*: Wiley-IEEE Press, 2006.
[85] A. R. V. Hippel, *Dielectric materials and applications*, USA: The technology press of M.I.T., 1954.
[86] F. T. Ulaby, and U. Ravaioli, *Fundamentals of applied electromagnetics*, Seventh ed.: Pearson Education, Inc., 2010.
[87] Olivier Klein, Steve Donovan, Martin Dressel, and G. Gruner, "Microwave cavity perturbation technique: part I: principles," *International Journal of Infrared and Millimeter Waves*, vol. 14, no. 12, pp. 2423-2457, 1993.
[88] A. Technologies, "Basics of measuring the dielectric properties of materials," Agilent, ed., Agilent Technologies, 2014.
[89] K. Fenske, and D. Misra, "Dielectric materials at microwave frequencies," *Applied microwave and wireless*.
[90] A. P. Gregory, and R. N. Clarke, "Tables of the complex permittivity of dielectric reference liquids at frequencies up to 5 GHz," *National Physica Laboratory NPL*, 2012.
[91] F. Buckley, and A. A. Maryott, "Tables of dielectric dispersion data for pure liquids and dilute solutions," *National Bureau of Standards Circular*, 1958.
[92] S. Donovan, O. Klein, M. Dressel, K. Holczer, and G. Gruner, "Microwave cavity perturbation technique: part II: experimental scheme," *International Journal of lnfrared and Millimeter Waves*, vol. 14, no. 12, pp. 2459-2487, 1993.
[93] N. Kittiamornkul, K. Chamnongthai, K. Jirasereeamornkul, and K. Higuchi, "A system of microwave cylindrical cavity resonator for granular material dielectric measurement using two waveguide transmitters," in SICE Annual Conference, Taipei, Taiwan, 2010, pp. 1888-1891.
[94] S. Begley, *Electromagnetic properties of materials: characterization at microwave frequencies and beyond*, Agilent Technologies, 2009.
[95] E. G. Nyfors, "Cylindrical microwave resonator sensors for measuring materials under flow," Dissertation for the degree of Doctor of Science in Technology, Electrical and Communications Engineering, Helsinki University of Technology, Finland, 2000.
[96] M. J. Lancaster, *Passive microwave device applications of high-temperature superconductors*, Cambridge university: Cambridge university press, 1997.

[97] S. K. Chatterjee, “Microwave cavity resonators. Some perturbation effects and their applications,” *Journal of the British Institution of Radio Engineers,* vol. 13, no. 10, pp. 475 - 484, 1953.

[98] R. A. Waldron, “Perturbation theory of resonant cavities,” *Proceedings of the IEE - Part C: Monographs,* vol. 107, no. 12, pp. 272 - 274, 1960.

[99] K. Chang, *RF and microwave wireless systems*: John Wiley & Sons, Inc. All, 2000.

[100] S. Li, C. Akyel, and R. G. Bosisio, “Precise calculations and measurements on the complex dielectric constant of lossy materials using TM010 cavity perturbation techniques,” *IEEE Microwave Theory and Techniques Society,* vol. 29, no. 10, pp. 1041 - 1048, 1981.

[101] W. Che, Z. Wang, Y. Chang, and P. Russer, “Permittivity measurement of biological materials with improved microwave cavity perturbation technique,” in Microwave Conference, EuMC 2008. 38th European, 2008, pp. 905 - 908.

[102] K. Zhang, and D. Li, *Electromagnetic theory for microwaves and optoelectronics,* Second ed., Springer-Verlag Berlin Heidelberg New York: Springer, 1998.

[103] M. Giordanot, F. Momot, and A. Sotgiuts, “On the design of a re-entrant square cavity as resonator for low-frequency ESR spectroscopy,” *Journal of Physics E: Scientific Instruments,* vol. 16, no. 8, pp. 774-779, 1983.

[104] S. Bonde, R. D’Silva, V. Gupte, M. John, F. Fernandes, and A. Kotrashetti, “2.4 GHz cavity notch filter for UWB radio,” in India Conference (INDICON), 2011 Annual IEEE, Hyderabad, 2011, pp. 1 - 4.

[105] Y. Shindo, Kawasaki, K. Kato, K. Tsuchiya, T. Yabuhara, T. Shigihara, R. Iwazaki, T. Uzuka, and H. Takahashi, “Heating properties of re-entrant resonant applicator for brain tumor by electromagnetic heating modes,” in Engineering in Medicine and Biology Society, 2007. EMBS 2007. 29th Annual International Conference of the IEEE, Lyon, 2007, pp. 3609 - 3612.

[106] J. Krupka, R. G. Geyer, J. Baker-Jarvis, and J. Ceremuga, “Measurements of the complex permittivity of microwave circuit board substrates using split dielectric resonator and reentrant cavity techniques,” in Dielectric Materials, Measurements and Applications, Seventh International Conference, Bath, 1996, pp. 21 - 24.

[107] R. D. Harrington, R. C. Powell, and P. H. Haas, “A re-entrant cavity for measurement of complex permeability in the very-high-frequency region,” *Research of the National Bureau of Standards,* vol. 56 No. 3, pp. 129-134, 1956.

[108] J. J. Barroso, P. J. Castro, J. P. L. Neto, and O. D. Aguiar, “Reentrant cylindrical cavities,” in Microwave and Optoelectronics, 2005 SBMO/IEEE MTT-S International Conference, 2005, pp. 129 - 132.

[109] K. Fujisawa, “General treatment of klystron resonant cavities,” *Microwave Theory and Techniques, IRE Transactions (IEEE Transactions on Microwave Theory and Techniques),* vol. 6, no. 4, pp. 344 - 358, 1958.

[110] D. R. Hamilton, J. K. Knipp, and J. B. H. Kuper, *Klystrons and microwave triodes*, p.^pp. 533: Boston Technical Publishers, Inc., 1964.
[111] J. W. Gewartowski, and H. A. Watson, *Principles of electrontubes*: D. Van Nostrand Company, INC., 1965.
[112] A. C. Raptis, and K. E. Lonngren, "Microwave cavities for plasma diagnostics," *Journal of the Microwave power and Electromagnetic Energy,* vol. 4, no. 3, pp. 182-187, 1969.
[113] W. Xi, W. R. Tinga, W. A. G. Voss, and B. Q. Tian, "New results for coaxial re-entrant cavity with partially dielectric filled gap," *IEEE transactions on microwave theory and techniques,* vol. 40, no. 4, pp. 747-753, 1992.
[114] M. Peichl, T. Albers, and S. Dill, "Detection of small impurities in bulk material by MMW radar," in Radar Symposium (IRS), 2015 16th International.
[115] J. Mateu, N. Orloff, M. Rinehart, and J. C. Booth, "Broadband permittivity of liquids extracted from transmission line measurements of microfluidic channels," in Microwave Symposium, 2007. IEEE/MTT-S International, 2007, pp. 523-526.
[116] T. Chen, D. Dubuc, M. Poupot, J.-J. Fournie, and K. Grenier, "Accurate nanoliter liquid characterization up to 40 GHz for biomedical applications: toward noninvasive living cells monitoring," *IEEE Transactions on Microwave Theory and Techniques,* vol. 60, no. 12, pp. 4171-4177, 2012.
[117] D. J. Griffiths, and R. College, *Introduction to electrodynamics*, 3rd ed., New Jersey, USA: Prentice Hall, 1999.
[118] A. Sihvola, "Dielectric Polarization and Particle Shape Effects," *Journal of Nanomaterials,* vol. 2007, pp. 1-9, 2007.
[119] R. E. Collin, *Field theory of guided waves*: McGraw-Hill Book Company, Inc., 1960.
[120] N. E. Engtsson, and T. Ohlsson, "Microwave heating in the food industry," *Proceedings of the IEEE,* vol. 62, no. 1, pp. 44 - 55, 1974.
[121] S. Das, A. K. Mukhopadhyay, S. Datta, and D. Basu, "Prospects of microwave processing: An overview " *Bulletin of Materials Science,* vol. 32, no. 1, pp. 1-13, 2009.
[122] O. Sydoruk, E. Tatartschuk, E. Shamonina, and L. Solymar, "Analytical formulation for the resonant frequency of split rings," *Journal of Applied Physics,* vol. 105, no. 1, pp. 014903, 2009.
[123] K. Chang, and L.-H. Hseih, *Microwave ring circuits and related structures*, Second ed., New Jersey, USA: Wiley, 2004.
[124] W. L. Kinney, A. N. Brecheisen, and V. W. Lambou, *Surface water quality parameters for monitoring oil shale development*: Environmental protection agency, USA, 1979.
[125] E. R. Weiner, *Applications of environmental chemistry*, USA: CRC Press, LLC, 2000.

[126] K. Kupfer, *Electromagnetic aquametry: electromagnetic wave interaction with water and moist substances*, Germany: Springer-Verlag Berlin Heidelberg 2005.
[127] F. Daschner, and R. Knöchel, "Dielectric microwave sensors with multivariate calibration," *Advances in radio science,* vol. 1, pp. 9-13, 2003.
[128] A. Babajanyan, J. Kim, S. Kim, K. Lee, and B. Friedman, "Sodium chloride sensing by using a near-field microwave microprobe," *Applied Physics Letters,* vol. 89, no. 18, pp. 183504, 2006.
[129] K. Nörtemann, J. Hilland, and U. Kaatze, "Dielectric properties of aqueous NaCl solutions at microwave frequencies," *J. Phys. Chem.*, vol. 101, no. 37, pp. 6864-6869, 1997.
[130] B. Kapilevich, and B. Litvak, "Microwave sensor for accurate measurements of water solution concentrations," *Asia-Pacific Microwave Conference*, 2007.
[131] S. Y. Liao, *Microwave devices and circuits*, Third ed.: Pearson Education, 2003.
[132] D. K. Linkhart, *Microwave circulator design*, Second ed.: Artech House, 2014.
[133] N. J. English, and J. M. D. MacElroy, "Hydrogen bonding and molecular mobility in liquid water in external electromagnetic fields," *The Journal of Chemical Physics*, vol. 119, no. 22, pp. 11806, 2003.
[134] P. W. Rosenkranz, "A model for the complex dielectric constant of supercooled liquid water at microwave frequencies," *IEEE Transactions on Geoscience and Remote Sensing*, vol. 53, no. 3, pp. 1387-1393, 2015.
[135] Martin Chaplin, "Water's hydrogen bond strength," *London South Bank University*, 2007.
[136] U. Kaatze, R. Behrends, and R. Pottel, "Hydrogen network fluctuations and dielectric spectrometry of liquids," *Journal of Non-Crystalline Solids,* vol. 305, pp. 19–28, 2002.
[137] K. Okada, M. Yao, Y. Hiejima, H. Kohno, and Y. Kajihara, "Dielectric relaxation of water and heavy water in the whole fluid phase," *The Journal of Chemical Physics*, vol. 110, no. 6, pp. 3026, 1999.
[138] A. Catenaccio, Y. Daruich, and C. Magallanes, "Temperature dependence of the permittivity of water," *Chemical Physics Letters,* vol. 367, pp. 669–671, 2003.
[139] W. J. Ellison, "Permittivity of Pure Water, at Standard Atmospheric Pressure, over the Frequency Range 0–25 THz and the Temperature Range 0–100 °C," *Journal of Physical and Chemical Reference Data*, vol. 36, no. 1, pp. 1, 2007.
[140] H.-J. Lee, H.-S. Lee, K.-H. Yoo, and J.-G. Yook, "DNA sensing using split-ring resonator alone at microwave regime," *Journal of Applied Physics*, vol. 108, no. 1, pp. 014908, 2010.
[141] C. Dalmay, A. Pothier, P. Blondy, M. Cheray, F. Lalloue, and M.-O. Jauberteau, "RF biosensor based on microwave filter for biological cell characterisation," *Proceedings of the 39th European Microwave Conference*, pp. 41-44, 2009.
[142] D. Berdat, A. Marin, F. Herrera, and M. A. M. Gijs, "DNA biosensor using fluorescence microscopy and impedance spectroscopy," *Sensors and Actuators B: Chemical*, vol. 118, no. 1-2, pp. 53-59, 2006.

[143] Y.-S. Liu, P. P. Banada, S. Bhattacharya, A. K. Bhunia, and R. Bashir, "Electrical characterization of DNA molecules in solution using impedance measurements," *Applied Physics Letters,* vol. 92, no. 14, pp. 143902, 2008.

[144] Vijayalakshmi Velusamy, Khalil Arshak, Cathy Yang, Lei Yu, Olga Korostynska, Kamila Oliwa, and C. Adley, "Label-free detection of Bacillus cereus DNA hybridization using electrochemical impedance spectroscopy for food quality monitoring application," in Sensors Applications Symposium (SAS), 2010 IEEE, 2010, pp. 135-138.

[145] R. Holzel, "Dielectric and dielectrophoretic properties of DNA," *IET Nanobiotechnol,* vol. 3, no. 2, pp. 28-45, 2009.

[146] M. Gross-Bellari, P. Oudet, and P. Chambon, "Isolation of high-molecular-weight DNA from mammalian cells " *European journal of biochemistry EJB,* vol. 36, no. 1, pp. 32-38 1973.

[147] L. A. Porteous, J. L. Armstrong, R. J. Seidler, and L. S. Watrud, "An effective method to extract DNA from environmental samples for polymerase chain reaction amplification and DNA fingerprint analysis " *Current microbiology* vol. 29, no. 5, pp. 301-307 1994.

[148] E. A. Nelson, E. A. Palombo, and S. R. Knowles, "Comparison of methods for the extraction of bacterial DNA from human faecal samples for analysis by real-time PCR " *Current research, technology and education topics in applied microbiology and microbial biotechnology*, vol. 2, pp. 1479-1485, 2010.

[149] L. T. Joshi, B. L. Mali, C. D. Geddes, and L. Baillie, "Extraction and sensitive detection of toxins A and B from the human pathogen Clostridium difficile in 40 seconds using microwave-accelerated metal-enhanced fluorescence," *PLoS One,* vol. 9, no. 8, pp. e104334, 2014.

[150] CDC, "2015 health security report," *U.S. deparmnet of health and human services Centers for Disease Control and Prevention*, 2015.

[151] https://www.gov.uk/government/statistics/clostridium-difficile-infection-annual-data. "Clostridium difficile infection: annual data," 2017.

[152] J. A. Sorg, and A. L. Sonenshein, "Bile salts and glycine as cogerminants for Clostridium difficile spores," *J Bacteriol,* vol. 190, no. 7, pp. 2505-12, Apr, 2008.

[153] U. Kaatze, "Complex permittivity of water as a function of frequency and temperature," *J. Chem. Eng. Data,* vol. 34, no. 4, pp. 371-374 1989.